

Effect of Turbulence Intensity and Variability on Model-Based Biodynamic Feedthrough Mitigation with Touchscreen Dragging Tasks

Technische Universiteit Delft

G. Leto



Effect of Turbulence Intensity and Variability on Model-Based Biodynamic Feedthrough Mitigation with Touchscreen Dragging Tasks

by

G. Leto

to obtain the degree of Master of Science
in Aerospace Engineering
at the Delft University of Technology,
to be defended publicly on Wednesday July 12, 2023 at 1:00 PM.

Student number:	4577442	
Project duration:	January 6, 2021 – July 12, 2023	
Thesis committee:	Dr. ir. D. M. Pool,	TU Delft, supervisor
	Prof. dr. ir. M. Mulder,	TU Delft, supervisor and chair
	Dr. O. A. Sharpanskykh,	TU Delft, examiner
	Dr. ir. A. C. in 't Veld,	TU Delft, additional

An electronic version of this thesis is available at <http://repository.tudelft.nl/>.
Cover photo courtesy of D. M. Pool and Y. Vardar.

Acknowledgements

The thesis that you are about to read has been for me a scope, a iceberg blocking my way, but also a wonderful ship with which I explored myself as a researcher in the field of cybernetics.

As this journey is about to end, my deepest thanks goes to Daan, who supervised me with such patience and competence, guiding me in the right direction while leaving me the freedom to explore this field by myself. Digging into the rabbit holes head first has been a pleasure, though I promise my best efforts will go into jumping across them, next time. Your encouragements have meant a lot to me. Thanks Max, your teachings, supervision and encouragements, that I really appreciated. I owe a lot to Olaf, who helped and supervised me while conducting the experiment in the SIMONA Research Simulator. Thanks for your kind words and encouragements at the end of the trials, they mean a lot to me. To Andries and Ferdinand, thank you for your technical support, kindness, and constant availability.

To the touchscreen research group, you have my gratitude (especially you, Alex!), for enabling me to share progress and knowledge together, greatly enriching this experience.

Thanks to everybody at the Control and Simulation department for keeping up with my rants about the weather and making lunch time fun time. In particular, to those with whom I crossed paths in SIM008, Arne, Berna, Lukas, Raoul, Till, Lauren, Matteo, Wouter, Roemer, Mitchel and Jorne.

Thanks Melissa for all your support and enthusiasm in whatever trip (which to me felt like an adventure) I came up with.

Thanks Yovanka for answering all my texts despite us been so far apart (yeah, I know you are one hour away by plane, but it does feel like we are on opposite sides of the planet, doesn't it?).

Thanks to Saru, Lulu and Atiqah, to Tom, Omar and Vinicius, to Tullio and Guido, to Rick and Chee, to Joshua and Midas, all people who have been in my heart during my studies, even though we all went different ways.

Most of all, thanks to my mom, my dad, my brother (and my two lovely cats) who have constantly supported me with all their might, and always will.

In the hope you enjoy reading my master thesis,

*G. Leto
Delft, July 2023*

Contents

List of Figures	iv
List of Tables	vii
Nomenclature	ix
1 Introduction	1
I Paper	3
II Preliminary Report	33
2 Preliminary Research Questions	34
3 Touchscreens and Biodynamic Feedthrough	35
3.1 Touchscreen technologies	35
3.1.1 Touchscreen interfaces in control applications	36
3.1.2 Requirements for touchscreen interfaces in aviation	37
3.2 Biodynamic feedthrough	37
3.2.1 Manual control in dynamic environments	37
3.2.2 Open-loop and closed-loop biodynamic feedthrough	39
3.2.3 Framework for biodynamic feedthrough mitigation	39
3.3 Biodynamic feedthrough occurring with touchscreens	40
3.3.1 Measuring touchscreen interfaces performance	40
3.3.2 Touchscreens in dynamic environments.	41
3.3.3 Mitigation of biodynamic feedthrough in touchscreens	41
3.4 Biodynamic feedthrough model identification on touchscreens	47
3.5 Summary and research gaps	50
4 Turbulence	53
4.1 Turbulence mechanisms	53
4.2 The statistical approach	54
4.2.1 Statistical description of turbulence	54
4.2.2 Energy spectral density and power spectral density	55
4.3 Introduction to turbulence modeling	56
4.3.1 Coordinate system	56
4.3.2 General assumptions for turbulence modeling	56
4.3.3 Turbulence inputs required from the aircraft model	57
4.3.4 Power spectral density models	58
4.4 Turbulence models	60
4.4.1 Gaussian turbulence models.	60
4.4.2 Non-Gaussian turbulence models	60
4.5 Validity of the models in the Earth's atmosphere	64
4.6 Turbulence in touchscreen biodynamic feedthrough research	65
4.7 Summary and research gaps	66
5 Introduction to the Preliminary Research	69
6 Biodynamic Feedthrough Identification	71
6.1 Effect of different cost functions	71
6.2 Time domain identification of biodynamic feedthrough	72
6.2.1 Implementation	73
6.2.2 Performance comparison of the time and frequency domain identification	73

6.3 Summary	75
7 Design of the Experimental Conditions	76
7.1 Baseline turbulent flight conditions	76
7.2 Verification of the patchy turbulence model	77
7.2.1 Verification of the original description of the model	77
7.2.2 Verification of the previous implementations of the model	82
7.3 Controller development	84
7.3.1 Controller structure	85
7.3.2 Controller tuning	86
7.3.3 Controlled aircraft responses to turbulence	87
7.4 Design of experimental conditions.	88
7.4.1 Influence of the turbulence parameters on the aircraft motion	88
7.4.2 Selection of the turbulence parameters and filter settings	92
7.5 Overview of the experimental conditions	95
7.6 Summary	100
8 Research Plan	102
8.1 Research questions	102
8.2 Experimental set-up	102
8.2.1 Control variables	102
8.2.2 Independent variables	103
8.2.3 Dependent variables	103
8.2.4 Procedure.	103
8.3 Hypothesis	104
9 Conclusions	105
Appendices to Preliminary Report	106
A Equations of the Linear Filters of the Turbulence Models	107
A.1 Gaussian turbulence model	107
A.2 Patchy turbulence model.	108
B Equations of the Proposed Corrected Patchy Turbulence Model	111
III Appendices to Paper	114
C Experiment Briefing and Consent Form	115
D Baseline Conditions Compared to Khoshnewiszadeh and Pool	119
E Variability in Biodynamic Feedthrough Across Participants	120
F Model Identification of G3 Condition with Fixed and Variable Time Delay	126
G Biodynamic Feedthrough Model Parameters	128
H Individual Runs Cancellation Results	141
I Performance in Gaussian and Patchy Turbulence at Medium and Low Intensity	148
Bibliography	150

List of Figures

3.1	Frequency response of the fingertip.	38
3.2	Accuracy in the BDFT estimate and modeling.	44
3.3	Performance of BDFT mitigation across all participants for the OSFA and SA models.	45
3.4	Average and spread of the BDFT model parameters across participants, for the HOR and VER motion conditions.	46
3.5	Cancellation of the discrete input signal.	46
3.6	Drag latency of Iiyama ProLite TF1534MC-B1X as a function of input speed.	47
3.7	Quasi-linear model of the human operator and BDFT model-based mitigation model.	47
3.8	PSD of the TSC target and motion disturbance signals.	48
3.9	Example of the target trajectory in the continuous tracking task on the TSC.	48
4.1	Energy cascade leading to the generation of gradually smaller eddies after the occurrence of a first instability.	53
4.2	Illustration of a one dimensional energy spectrum for fully developed turbulence.	54
4.3	Shape of the energy spectrum $E(\Omega)$ for eddies of fixed size l	54
4.4	Statistical description of the turbulence velocity field.	55
4.5	Definition of turbulence velocities.	56
4.6	Definition of longitudinal and lateral correlations between velocities u and u' , at distance ξ from one another.	58
4.7	Difference between the von Kármán and Dryden spectra.	59
4.8	Schematic of linear filtering of white noise.	60
4.9	Comparison between the PDF measured from real turbulence and the PDF of Gaussian turbulence.	61
4.10	Schematic for the <i>patchy turbulence model</i>	61
4.11	Gaussian and modified Bessel PDF, differing by their Kurtosis K	62
4.12	Graphical interpretation of R , showing the turbulence velocity for short patches and long patches.	63
4.13	Schematic for the <i>intermittent turbulence model</i>	63
4.14	The Kurtosis of the PDF of the turbulence velocity gradient $K_{\Delta w}$ plotted against the Kurtosis of the PDF of the turbulence velocity K_w , for the <i>patchy turbulence model</i> , the <i>intermittent turbulence model</i> and for data measured in turbulence.	64
4.15	RMS of the turbulence velocity as a function of the altitude, for altitudes above 2000 ft.	66
5.1	Schematic of the steps required for the simulation of experimental conditions.	69
6.1	Performance of different cost functions with the SA model, VER case.	72
6.2	Performance of different cost functions with the OSFA model, VER case.	73
6.3	Performance of the time domain and the frequency domain identification, VER case.	74
6.4	Comparison between the SA models obtained with the frequency domain approach and the time domain approach, VER case.	74
6.5	Comparison between the model parameters of the SA and OSFA models, identified from a time and frequency domain approach, for the heave-vertical TSC input (VER) case and the sway-lateral TSC input (HOR) case.	75
7.1	Influence of the patchy turbulence model gains and their ratio on the PSD of the longitudinal and vertical turbulence velocities.	78
7.2	PSDs of the turbulence velocity u_g and the construction signal $c(t)$, and the analytical spectrum of u_g , for Gaussian and non-Gaussian turbulence.	81

7.3	PSDs of the turbulence velocity $\hat{u}_{g_{asym}}$ and the construction signal $c(t)$ from the <i>original patchy turbulence model</i> , and the analytical spectrum of $\hat{u}_{g_{asym}}$, for Gaussian and non-Gaussian turbulence.	82
7.4	PSDs of the turbulence velocity $\hat{u}_{g_{asym}}$ and the construction signal $c(t)$ from the <i>patchy turbulence model with the proposed corrections</i> , and the analytical spectrum of $\hat{u}_{g_{asym}}$, for Gaussian and non-Gaussian turbulence.	83
7.5	Comparison between Jacobson's patchy turbulence model implementation and the proposed corrected model, showing quantities made dimensional.	84
7.6	Aircraft responses to Jacobson's patchy turbulence in comparison with responses to the proposed corrected patchy turbulence.	85
7.7	Pitch rate feedback controller and roll damper.	86
7.8	Comparison between velocity, altitude and Euler angles of the uncontrolled and the controlled simulated aircraft.	88
7.9	Comparison between the uncontrolled and the controlled aircraft responses, with first iteration tuning. The highlighted parts show the transient response taken as reference for the tuning criteria.	89
7.10	Second tuning step, varying K_q	90
7.11	Comparison between the controlled aircraft responses with the highest and lowest possible values for gain K_q	91
7.12	Comparison between the controlled aircraft responses obtained with the first and second round of tuning.	92
7.13	Effect on the aircraft specific forces of variations in σ_g (Gaussian turbulence: $L_{ug} = 300$ m, $Q = 0$ and $R = 0.01$).	93
7.14	Effect on the turbulence velocity components and on the vertical specific force of variations in L_{ug} (Gaussian turbulence: $\sigma_g^2 = 1$ m ² /s ² , $Q = 0$ and $R = 0.01$).	94
7.15	Effect on the turbulence velocity components and on the aircraft specific forces of variations in R	95
7.16	Heave Gouverneur analysis for different values of R	96
7.17	Heave Gouverneur analysis, design point $K_{heave} = 1$, $\omega_{heave} = 0.9$ rad/s.	96
7.18	Vertical specific force of the aircraft at the pilot station (PS) and vertical acceleration of the simulator at the upper gimbal point (UGP).	97
7.19	Frequency bin averaged PSD of the vertical acceleration of the aircraft at the Pilot Station (PS) and of the vertical acceleration of the simulator at the Upper Gimbal Point (UGP).	98
7.20	Detail of the time traces of the Multisine, Patchy and Gaussian motion disturbances, $V_{metric} = 0.75$ m/s ²	98
7.21	Frequency bin averaged PSD of the multisine, patchy and Gaussian motion disturbances, $V_{metric} = 0.75$ m/s ²	99
7.22	Simulated BDFT component of the vertical input for the multisine, Gaussian and patchy turbulence conditions.	99
7.23	Average standard deviation of the involuntary component of the vertical input signal occurring with heave multisine motion disturbance, observed in Khoshnewiszadeh's experiment [1], together with the one simulated for each experimental condition.	100
7.24	Frequency bin averaged PSD of the multisine, patchy and Gaussian motion disturbances, at the three levels of intensity: $V_{metric} = 0.75, 0.5, 0.25$ m/s ²	101
B.1	Schematic for the proposed corrected <i>patchy turbulence model</i>	111
D.1	Median and spread of the parameters of the $H_{BDFT/M}(j\omega)$ models of this study and of Khoshnewiszadeh and Pool.	119
D.2	BDFT estimates and BDFT models frequency response of individual participants of this study and of Khoshnewiszadeh and Pool.	119
E.1	Participant 1, variability in measured BDFT for the identification M3 dataset.	120
E.2	Participant 2, variability in measured BDFT for the identification M3 dataset.	120
E.3	Participant 3, variability in measured BDFT for the identification M3 dataset.	121
E.4	Participant 4, variability in measured BDFT for the identification M3 dataset.	121

E.5	Participant 5, variability in measured BDFT for the identification M3 dataset.	121
E.6	Participant 6, variability in measured BDFT for the identification M3 dataset.	121
E.7	Participant 7, variability in measured BDFT for the identification M3 dataset.	122
E.8	Participant 8, variability in measured BDFT for the identification M3 dataset.	122
E.9	Participant 9, variability in measured BDFT for the identification M3 dataset.	122
E.10	Participant 10, variability in measured BDFT for the identification M3 dataset.	122
E.11	Participant 11, variability in measured BDFT for the identification M3 dataset.	123
E.12	Participant 12, variability in measured BDFT for the identification M3 dataset.	123
E.13	Participant 13, variability in measured BDFT for the identification M3 dataset.	123
E.14	Participant 14, variability in measured BDFT for the identification M3 dataset.	123
E.15	Participant 15, variability in measured BDFT for the identification M3 dataset.	124
E.16	Participant 16, variability in measured BDFT for the identification M3 dataset.	124
E.17	Participant 17, variability in measured BDFT for the identification M3 dataset.	124
E.18	Participant 18, variability in measured BDFT for the identification M3 dataset.	124
E.19	Participant 19, variability in measured BDFT for the identification M3 dataset.	125
E.20	Participant 20, variability in measured BDFT for the identification M3 dataset.	125
E.21	Participant 21, variability in measured BDFT for the identification M3 dataset.	125
F.1	Median and spread of the parameters of the $H_{BDFT/G3}(j\omega)$ models with fixed and variable time delay τ_{BDFT}	126
F.2	Performance of the SA $H_{BDFT/G3}$ models with fixed and variable time delay τ_{BDFT}	127
F.3	Performance of the OSFA $H_{BDFT/G3}$ models with fixed and variable time delay τ_{BDFT}	127
G.1	Participant 1, identification dataset M1.	137
G.2	Participant 1, identification dataset M2.	138
G.3	Participant 1, identification dataset M3.	139
G.4	Participant 1, identification dataset G3.	140
H.1	Participant 1, evaluation dataset M1.	145
H.2	Participant 1, evaluation dataset M2.	146
H.3	Participant 1, evaluation dataset M3.	146
H.4	Participant 1, evaluation dataset G3.	147
H.5	Participant 1, evaluation dataset P3.	147
I.1	Performance of the OSFA, SA and IR $H_{BDFT/G2}$ models for the identification of BDFT from the G2 data.	148
I.2	Performance of the OSFA, SA and IR $H_{BDFT/G1}$ models for the identification of BDFT from the G1 data.	148
I.3	Cancellation performance of model $H_{BDFT/G3}$ on BDFT occurring in G3 conditions, of model $H_{BDFT/G2}$ on BDFT occurring in G2 conditions and of model $H_{BDFT/G1}$ on BDFT occurring in G1 conditions.	149
I.4	Cancellation performance of model $H_{BDFT/M3}$ on BDFT occurring in G3 conditions, of model $H_{BDFT/M2}$ on BDFT occurring in G2 conditions and of model $H_{BDFT/M1}$ on BDFT occurring in G1 conditions.	149
I.5	Cancellation performance of model $H_{BDFT/G3}$ on BDFT occurring in P3 conditions, of model $H_{BDFT/G2}$ on BDFT occurring in P2 conditions and of model $H_{BDFT/G1}$ on BDFT occurring in P1 conditions.	149
I.6	Cancellation performance of model $H_{BDFT/M3}$ on BDFT occurring in P3 conditions, of model $H_{BDFT/M2}$ on BDFT occurring in P2 conditions and of model $H_{BDFT/M1}$ on BDFT occurring in P1 conditions.	149

List of Tables

3.1	Parameters for the fingertip model when impinging 0.5 N on the probe.	39
3.2	Dependency of the fingertip model parameters on the normal force impinged on the surface.	39
3.3	Experimental conditions and input directions for which a BDFT model can be estimated accurately.	44
3.4	Initial conditions and constraints for BDFT model fitting.	49
3.5	Values used for construction of the target signal for the TSC tracking task.	49
3.6	Values for construction of the motion disturbance signal used in place of turbulence. . .	50
4.1	Jacobson's turbulence conditions, defined by the RMS accelerations.	65
4.2	Standard deviation of low altitude turbulence of different intensity for horizontal σ_{u_g} , vertical σ_{w_g} and lateral σ_{v_g} turbulence velocities.	66
7.1	Influence of the gains and their ratio on Kurtosis K_w and on intensity σ_w^2 of the longitudinal and vertical turbulence velocities.	78
7.2	Intensity σ_w^2 and Kurtosis K_w of the antisymmetric turbulence components, depending on the model used.	80
7.3	Values of the Kurtosis associated to parameter Q , $K(Q)$ calculated with Equation 4.12, K_w measured from a 9000 seconds simulation and K_w measured from a 90 seconds simulation of the vertical component of the turbulence velocity.	90
7.4	Experimental conditions to be used in the upcoming experiment.	97
8.1	Experimental conditions matrix.	103
A.1	Constants used for modeling the antisymmetric turbulence components, as a function of $B = \frac{b}{2L_{u_g}}$	108
G.1	Participant 1, parameters identification in time domain.	128
G.2	Participant 1, identification performance in %, time domain.	128
G.3	Participant 2, parameters identification in time domain.	129
G.4	Participant 2, identification performance in %, time domain.	129
G.5	Participant 3, parameters identification in time domain.	129
G.6	Participant 3, identification performance in %, time domain.	129
G.7	Participant 4, parameters identification in time domain.	129
G.8	Participant 4, identification performance in %, time domain.	130
G.9	Participant 5, parameters identification in time domain.	130
G.10	Participant 5, identification performance in %, time domain.	130
G.11	Participant 6, parameters identification in time domain.	130
G.12	Participant 6, identification performance in %, time domain.	130
G.13	Participant 7, parameters identification in time domain.	131
G.14	Participant 7, identification performance in %, time domain.	131
G.15	Participant 8, parameters identification in time domain.	131
G.16	Participant 8, identification performance in %, time domain.	131
G.17	Participant 1, parameters identification in time domain.	131
G.18	Participant 9, identification performance in %, time domain.	132
G.19	Participant 10, parameters identification in time domain.	132
G.20	Participant 10, identification performance in %, time domain.	132
G.21	Participant 11, parameters identification in time domain.	132

G.22 Participant 11, identification performance in %, time domain.	132
G.23 Participant 12, parameters identification in time domain.	133
G.24 Participant 12, identification performance in %, time domain.	133
G.25 Participant 13, parameters identification in time domain.	133
G.26 Participant 13, identification performance in %, time domain.	133
G.27 Participant 14, parameters identification in time domain.	133
G.28 Participant 14, identification performance in %, time domain.	134
G.29 Participant 15, parameters identification in time domain.	134
G.30 Participant 15, identification performance in %, time domain.	134
G.31 Participant 16, parameters identification in time domain.	134
G.32 Participant 16, identification performance in %, time domain.	134
G.33 Participant 17, parameters identification in time domain.	135
G.34 Participant 17, identification performance in %, time domain.	135
G.35 Participant 18, parameters identification in time domain.	135
G.36 Participant 18, identification performance in %, time domain.	135
G.37 Participant 19, parameters identification in time domain.	135
G.38 Participant 19, identification performance in %, time domain.	136
G.39 Participant 20, parameters identification in time domain.	136
G.40 Participant 20, identification performance in %, time domain.	136
G.41 Participant 21, parameters identification in time domain.	136
G.42 Participant 21, identification performance in %, time domain.	136
H.1 Participant 1, individual run cancellation results in %.	141
H.2 Participant 2, individual run cancellation results in %.	141
H.3 Participant 3, individual run cancellation results in %.	141
H.4 Participant 4, individual run cancellation results in %.	142
H.5 Participant 5, individual run cancellation results in %.	142
H.6 Participant 6, individual run cancellation results in %.	142
H.7 Participant 7, individual run cancellation results in %.	142
H.8 Participant 8, individual run cancellation results in %.	142
H.9 Participant 9, individual run cancellation results in %.	143
H.10 Participant 10, individual run cancellation results in %.	143
H.11 Participant 11, individual run cancellation results in %.	143
H.12 Participant 12, individual run cancellation results in %.	143
H.13 Participant 13, individual run cancellation results in %.	143
H.14 Participant 14, individual run cancellation results in %.	144
H.15 Participant 15, individual run cancellation results in %.	144
H.16 Participant 16, individual run cancellation results in %.	144
H.17 Participant 17, individual run cancellation results in %.	144
H.18 Participant 18, individual run cancellation results in %.	144
H.19 Participant 19, individual run cancellation results in %.	145
H.20 Participant 20, individual run cancellation results in %.	145
H.21 Participant 21, individual run cancellation results in %.	145

Nomenclature

List of Abbreviations

ABL	Atmospheric Boundary Layer
BDFT	Biodynamic Feedthrough
CDU	Control Display Unit
CG	Centre of Gravity
CW16	Classical Washout 16
DASMAT	Delft University Aircraft Simulation Model and Analysis Tool
DERP	Design Eye Reference Point
EASA	European Union Aviation Safety Agency
ESD	Energy Spectral Density
FTIP	Fingertip
HOR	Experimental condition with sway motion disturbance causing BDFT on the lateral TSC inputs
ID	Index of Difficulty
MT	Movement Time
OSFA	One-Size-Fits-All model
PDF	Probability Density Function
PFD	Primary Flight Display
PS	Pilot Station
PSD	Power Spectral Density
RMS	Root-Mean-Square
SA	Subject Averaged model
SIMONA	International Research Institute for Simulation, Motion & Navigation
SRS	SIMONA Research Simulator
TSC	Touchscreen
UGP	Upper Gimbal Point
VAF	Variance Accounted For
VER	Experimental condition with heave motion disturbance causing BDFT on the vertical TSC inputs

List of Symbols

$a(t)$	Gaussian stochastic process, filtered with $H_a(j\omega)$	$\sqrt{\text{m/s}}$ or - or $\sqrt{\text{rad}}$
A_d	Amplitudes of the components of the disturbance forcing function	m
$a_{FL/V}$	Coefficient in the V -metric adapted Fitts' law and Finger-Fitts' law	-
a_{FL}	Coefficient in the Fitts' law and Finger-Fitts' law	-
A_t	Amplitudes of the components of the target forcing function	mm
B	Span loading, $\frac{b}{2L_{ug}}$	-
b	Span	m
$b(t)$	Gaussian stochastic process, filtered with $H_b(j\omega)$	$\sqrt{\text{m/s}}$ or - or $\sqrt{\text{rad}}$
b_{BDFT}	Damping coefficient of the BDFT model	kg/s
$b_{FL/V}$	Coefficient in the V -metric adapted Fitts' law and Finger-Fitts' law	-
b_{FL}	Coefficient in the Fitts' law and Finger-Fitts' law	-
b_{FTIP}	Fingertip viscosity	Ns/m
c	Chord length	m
$c(t)$	Gaussian stochastic process, filtered with $H_c(j\omega)$	m/s or - or rad
$C_{\mathbf{u}'\mathbf{u}'}(\tau)$	Auto-covariance function of the stochastic turbulence velocity	m^2/s^2
$c_{FL/V}$	Coefficient in the V -metric adapted Fitts' law and Finger-Fitts' law	-
$d_{FL/V}$	Coefficient in the V -metric adapted Fitts' law and Finger-Fitts' law	-
$E(\Omega)$	One dimensional energy spectrum per unit mass	Jm/kg
$f''_{d_{faded}}(t)$	Second derivative of the disturbance forcing function with fading	m/s^2
$f''_d(t)$	Second derivative of the disturbance forcing function	m/s^2
$f'_d(t)$	First derivative of the disturbance forcing function	m/s
$f_d(t)$	Disturbance forcing function	m
$f_t(t)$	Target forcing function	mm
G_{BDFT}	Gain of the BDFT model	mm/ms^{-2}
$g_d(t)$	Fading function	-
$g''_d(t)$	Second derivative of the fading function	$1/\text{s}^2$
$g'_d(t)$	First derivative of the fading forcing function	1/s
$\hat{H}_{BDFT}(j\omega_d)$	Estimated BDFT dynamics	mm/ms^{-2}
h	Altitude	m or ft
$H(s)$	Aircraft platform	
$H_a(j\omega)$	Linear filter shaping signal $a(t)$, patchy turbulence model	units of $a(t) * \sqrt{1/\text{Hz}}$
$H_b(j\omega)$	Linear filter shaping signal $b(t)$, patchy turbulence model	units of $b(t) * \sqrt{1/\text{Hz}}$
$H_c(j\omega)$	Linear filter shaping signal $c(t)$, patchy turbulence model	units of $c(t) * \sqrt{1/\text{Hz}}$
$H_w(j\omega)$	Linear filter shaping signal $w(t)$, Gaussian turbulence model	units of $w(t) * \sqrt{1/\text{Hz}}$

$H_{\alpha_{gasy}}(j\omega)$	Linear filter shaping signal α_{gasy}	$\text{rad}\sqrt{1/\text{Hz}}$
$H_{\hat{u}_{gasy}}(j\omega)$	Linear filter shaping signal \hat{u}_{gasy}	$\sqrt{1/\text{Hz}}$
$H_{a_{\alpha_{gasy}}}(j\omega)$	Linear filter shaping signal $a(t)$ for turbulence component α_{gasy}	$\sqrt{\text{rad}/\text{Hz}}$
$H_{a_{\hat{u}_{gasy}}}(j\omega)$	Linear filter shaping signal $a(t)$ for turbulence component \hat{u}_{gasy}	$\sqrt{1/\text{Hz}}$
$H_{a_{u_g}}(j\omega)$	Linear filter shaping signal $a(t)$ for turbulence component u_g	$\sqrt{\text{ms}^{-1}/\text{Hz}}$
$H_{a_{v_g}}(j\omega)$	Linear filter shaping signal $a(t)$ for turbulence component v_g	$\sqrt{\text{ms}^{-1}/\text{Hz}}$
$H_{a_{w_g}}(j\omega)$	Linear filter shaping signal $a(t)$ for turbulence component w_g	$\sqrt{\text{ms}^{-1}/\text{Hz}}$
$H_{BDFT}(s)$	Transfer function describing BDFT dynamics	mm/ms^{-2}
$H_{b_{\alpha_{gasy}}}(j\omega)$	Linear filter shaping signal $b(t)$ for turbulence component α_{gasy}	$\sqrt{\text{rad}/\text{Hz}}$
$H_{b_{\hat{u}_{gasy}}}(j\omega)$	Linear filter shaping signal $b(t)$ for turbulence component \hat{u}_{gasy}	$\sqrt{1/\text{Hz}}$
$H_{b_{u_g}}(j\omega)$	Linear filter shaping signal $b(t)$ for turbulence component u_g	$\sqrt{\text{ms}^{-1}/\text{Hz}}$
$H_{b_{v_g}}(j\omega)$	Linear filter shaping signal $b(t)$ for turbulence component v_g	$\sqrt{\text{ms}^{-1}/\text{Hz}}$
$H_{b_{w_g}}(j\omega)$	Linear filter shaping signal $b(t)$ for turbulence component w_g	$\sqrt{\text{ms}^{-1}/\text{Hz}}$
$H_{c_{\alpha_{gasy}}}(j\omega)$	Linear filter shaping signal $c(t)$ for turbulence component α_{gasy} (corrected), rad (non corrected)	$\text{rad}\sqrt{1/\text{Hz}}$
$H_{c_{\hat{u}_{gasy}}}(j\omega)$	Linear filter shaping signal $c(t)$ for turbulence component \hat{u}_{gasy} (non corrected)	$\sqrt{1/\text{Hz}}$ (corrected), -
$H_{c_{u_g}}(j\omega)$	Linear filter shaping signal $c(t)$ for turbulence component u_g	$\text{m}/\text{s}\sqrt{1/\text{Hz}}$
$H_{c_{v_g}}(j\omega)$	Linear filter shaping signal $c(t)$ for turbulence component v_g	$\text{m}/\text{s}\sqrt{1/\text{Hz}}$
$H_{c_{w_g}}(j\omega)$	Linear filter shaping signal $c(t)$ for turbulence component w_g	$\text{m}/\text{s}\sqrt{1/\text{Hz}}$
$H_{u_g}(j\omega)$	Linear filter shaping signal u_g	$\text{m}/\text{s}\sqrt{1/\text{Hz}}$
$H_{v_g}(j\omega)$	Linear filter shaping signal v_g	$\text{m}/\text{s}\sqrt{1/\text{Hz}}$
$H_{w_g}(j\omega)$	Linear filter shaping signal w_g	$\text{m}/\text{s}\sqrt{1/\text{Hz}}$
I	Gaussian white noise, input to $H_a(j\omega)$	-
$I_{\alpha_g}(0, B)$	Constant used for $I_{\alpha_g}(\omega, B)$	rad^2
$I_{\alpha_g}(\omega, B)$	Auto-PSD of α_{gasy}	rad^2/Hz
$I_{\hat{u}_g}(0, B)$	Constant used for $I_{\hat{u}_g}(\omega, B)$	-
$I_{\hat{u}_g}(\omega, B)$	Auto-PSD of \hat{u}_{gasy}	$1/\text{Hz}$
II	Gaussian white noise, input to $H_b(j\omega)$	-
III	Gaussian white noise, input to $H_c(j\omega)$	-

$J(\delta)$	Cost function used for the optimization of the BDFT model parameters	-
K_ϕ	Proportional gain for ϕ	-
K_θ	Proportional gain for θ	1/s
K_q	Proportional gain for q	s
$K_{\Delta w}$	Kurtosis of the PDF of the gradient of the turbulence velocity $w(t)$	-
k_{BDFT}	Stiffness of the BDFT model	kg/s ²
k_{FTIP}	Fingertip stiffness	N/mm
K_{heave}	Gain for the high pass motion filter in heave	-
K_w	Kurtosis of the PDF of the turbulence velocity $w(t)$	-
L	Integral length scale of turbulence	m
l	Eddy size	m
L_{u_g}	Integral length scale of turbulence in the longitudinal direction	m
L_{v_g}	Integral length scale of turbulence in the lateral direction	m
m_{BDFT}	Mass of the BDFT model	kg
m_{FTIP}	Fingertip mass	g
N	Number of data points	-
n	Remnant component of the TSC input signal	mm
N_d	Number of components of the disturbance forcing function	-
n_d	Number of periods that fit in the measurement time of a component of the disturbance forcing function	-
n_{FTIP}	Normal force impinged on a surface by the FTIP	N
N_t	Number of components of the target forcing function	-
n_t	Number of periods that fit in the measurement time of a component of the target forcing function	-
\dot{p}	Aircraft roll acceleration	rad/s ²
p	Aircraft roll rate	rad/s
\dot{q}	Aircraft pitch acceleration	rad/s ²
Q	σ_u/σ_c	-
q	Aircraft pitch rate	rad/s
q_e	Roll rate error	rad/s
q_{ref}	Roll rate reference	rad/s
\dot{r}	Aircraft yaw acceleration	rad/s ²
R	Parameter for the patch length, defines as the ratio between the corner frequencies of $H_a(j\omega)$ and $H_b(j\omega)$	-
r	Aircraft yaw rate	rad/s

$S_{\mathbf{u}'\mathbf{u}'}(\omega)$	Auto-PSD of the stochastic turbulence velocity	$\text{m}^2\text{s}^{-2}/\text{Hz}$
$S_{f_d f_d}(\omega_d)$	Auto-PSD of the acceleration disturbance	$\text{m}^2\text{s}^{-4}/\text{Hz}$
$S_{f_d u}(\omega_d)$	Cross-PSD of acceleration disturbance and the TSC input signal	$\text{ms}^{-2}\text{mm}/\text{Hz}$
$S_{kk}(\omega)$	Constant auto-PSD of a white noise signal	-
$S_{u_g u_g}(\omega)$	Auto-PSD of u_g	$\text{m}^2\text{s}^{-2}/\text{Hz}$
$S_{v_g v_g}(\omega)$	Auto-PSD of v_g	$\text{m}^2\text{s}^{-2}/\text{Hz}$
$S_{w_g w_g}(\omega)$	Auto-PSD of w_g	$\text{m}^2\text{s}^{-2}/\text{Hz}$
$S_{ww}(\omega)$	Auto-PSD of a signal shaped with linear filter $H_w(j\omega)$	$\text{m}^2\text{s}^{-2}/\text{Hz}$
$SF x_s$	Aircraft specific forces in the longitudinal axis	g
$SF y_s$	Aircraft specific forces in the lateral axis	g
$SF z_s$	Aircraft specific forces in the vertical axis	g
t	Time	s
T_m	Experimental measurement time	s
t_{fade}	Fading time	s
\dot{u}_g	Dimensionless derivative of the longitudinal gust velocity	-
\dot{u}_g	Derivative of the longitudinal turbulence velocity	m/s^2
$\hat{u}_{g_{asym}}$	Dimensionless longitudinal gust velocity varying along the wingspan	-
\hat{u}_g	Dimensionless longitudinal gust velocity	-
\mathbf{u}	Velocity vector of a turbulent flow	m/s
\mathbf{u}'	Time dependent component of the flow velocity vector	m/s
$\bar{\mathbf{u}}$	Mean flow velocity vector	m/s
u	TSC input signal	mm
$u(t)$	Non Gaussian stochastic process, product of $a(t)$ and $b(t)$	m/s
u^{can}	Canceled voluntary component of the TSC input	mm
u^{cog}	Voluntary component of the TSC input	mm
u^{meas}	Involuntary component of the TSC input	mm
u^{mod}	Modeled involuntary component of the TSC input	mm
u_g	Longitudinal component of the stochastic turbulence velocity	m/s
$u_{g_{asym}}$	Dimensional longitudinal gust velocity varying along the wingspan	m/s
\dot{v}_g	Derivative of the lateral turbulence velocity	m/s^2
V	Airspeed	m/s
v_g	Lateral component of the stochastic turbulence velocity	m/s
V_{metric}	Total magnitude of the RMS accelerations of a vehicle	m/s^2
\dot{w}_g	Derivative of the vertical turbulence velocity	m/s^2

$w(t)$	General turbulence velocity vector output of turbulence models	m/s
w_g	Vertical component of the stochastic turbulence velocity	m/s
W_a	Constant PSD of the white noise used to generate signal $a(t)$	-
W_b	Constant PSD of the white noise used to generate signal $b(t)$	-
W_c	Constant PSD of the white noise used to generate signal $c(t)$	-
W_k	Constant PSD of the white noise used to generate turbulence velocities through linear filtering	-
\ddot{x}	Aircraft horizontal acceleration	m/s ²
\mathbf{x}	Position vector of a particle in the flow	m
\ddot{y}	Aircraft lateral acceleration	m/s ²
\ddot{z}	Aircraft vertical acceleration	m/s ²
$Z_{FTIP}(j\omega)$	Fingertip impedance	Ns/m
$\dot{\alpha}_g$	Rate of the gust angle of attack	rad
α	Coefficient relating the FTIP parameters with the impinged normal force	-
α_{gasymp}	Gust angle of attack varying along the wingspan	rad
α_g	Gust angle of attack	rad
β	Coefficient relating the FTIP parameters with the impinged normal force	-
β_g	Gust sideslip angle	rad
$\dot{\beta}_g$	Rate of the gust sideslip angle	rad
δ	Set of BDFT model parameters	
δ_a	Aileron deflection	rad
δ_e	Elevator deflection	rad
ζ_{BDFT}	Damping ratio of the BDFT model	-
η	Kolmogorov microscale of turbulence	m
θ	Aircraft pitch angle	rad
θ_e	Pitch error	rad
θ_{ref}	Pitch reference	rad
ξ	Position increment vector	m
σ_g^2	Isotropic variance of the turbulence velocity	m ² /s ²
$\sigma_{\alpha_g}^2$	σ_g^2/V^2	-
$\sigma_{\dot{u}_g}^2$	σ_g^2/V^2	-
σ_c	Standard deviation of $c(t)$	m/s
σ_{u_g}	Standard deviation of the longitudinal component of the turbulence velocity u_g	m/s
$\sigma_{u_g}^2$	Variance/Intensity of the longitudinal component of the turbulence velocity u_g	m ² /s ²

σ_u	Standard deviation of $u(t)$	m/s
σ_{v_g}	Standard deviation of the lateral component of the turbulence velocity v_g	m/s
$\sigma_{v_g}^2$	Variance/Intensity of the lateral component of the turbulence velocity v_g	m ² /s ²
σ_{w_g}	Standard deviation of the vertical component of the turbulence velocity w_g	m/s
$\sigma_{w_g}^2$	Variance/Intensity of the vertical component of the turbulence velocity w_g	m ² /s ²
σ_w^2	Variance/Intensity of the turbulence velocity $w(t)$	m ² /s ²
τ	Time increment	s
τ_1	Constant used for $I_{\hat{u}_g}(\omega, B)$	-
τ_2	Constant used for $I_{\hat{u}_g}(\omega, B)$	-
τ_3	Constant used for $I_{\hat{u}_g}(\omega, B)$	-
τ_4	Constant used for $I_{\alpha_g}(\omega, B)$	-
τ_5	Constant used for $I_{\alpha_g}(\omega, B)$	-
τ_6	Constant used for $I_{\alpha_g}(\omega, B)$	-
τ_{BDFT}	Time delay of the BDFT model	s
ϕ	Aircraft roll angle	rad
ϕ_e	Roll error	rad
ϕ_d	Phases of the components of the disturbance forcing function	rad
ϕ_{ref}	Roll reference	rad
ϕ_t	Phases of the components of the target forcing function	rad
ψ	Aircraft yaw angle	rad
Ω	One dimensional wavenumber	rad/m
ω	Radial frequency	rad/s
ω_m	Base frequency for BDFT experiment	rad/s
ω_{BDFT}	Natural frequency of the BDFT model	rad/s
ω_d	Frequencies of the components of the disturbance forcing function	rad/s
ω_{heave}	Break frequency for the high pass motion filter in heave	rad/s
ω_t	Frequencies of the components of the target forcing function	rad/s
Ω	Three dimensional wavenumber	rad/m

Subscripts

d	Disturbance signal
fd	Component at the frequencies of the disturbance signal
k	Components of the multisine signals
RMS	Root-mean-square value

ty	Target signal on the y coordinates on the TSC
tz	Target signal of the z coordinates on the TSC
y	Component of the y coordinates on the TSC
z	Component of the z coordinates on the TSC

Mathematical Symbols and Constants

e	Euler's number
$E\{\cdot\}$	Expectation operator
j	Imaginary unit
K	Kurtosis of a probability density function
m_2	Second moment of a probability density function, variance
m_4	Fourth moment of a probability density function
s	Complex number
Var	Variance
μ	Mean
σ^2	Variance
σ_{skew}^2	Variance of the Skewness of a PDF
σ_K	Standard deviation of the Kurtosis of a PDF

Coordinate systems

x_s	Longitudinal axis of the aircraft fixed stability reference frame, positive forwards
y	Lateral axis of TSC coordinate system
y_s	Lateral axis of the aircraft fixed stability reference frame, positive to the right
z	Vertical axis of TSC coordinate system
z_s	Vertical axis of the aircraft fixed stability reference frame, positive downwards

Introduction

An aircraft's flight deck is the means through which a pilot interacts with the aircraft, gathering information about the aircraft's state, and performing control, communication and navigation tasks, alongside automation. In the early days of aviation, both indicators and controls were made with mechanical components [2]. As technology developed, mechanical indicators were eventually substituted by digital screens, where a compact and pre-integrated overview of the needed information is presented to the pilots [2]. Conversely, most of the control actions within the cockpit are still performed through mechanical controls [2].

Touchscreen (TSC) interfaces were first introduced in cockpits to provide more intuitive interaction with the Electronic Flight Bag, allowing the consultation of maps, pre-flight checklists and manuals, leaving aside safety critical tasks to be conducted in-flight, for which they were deemed inadequate [3]. With the progressive improvements in technology, especially in the latency of the response to touch inputs, TSCs are now being used in-flight for control of many subsystems, for example communication, navigation, power systems. Amongst others, Airbus¹ and Boeing² are notable examples of commercial aircraft manufacturers that already produce cockpits with TSC interfaces, Garmin³ and Thales⁴ do the same for private and military use. Most of these systems are still only implemented side by side with their mechanical counterparts, and the use of TSCs for safety critical tasks is still relatively uncommon, with exception of the SpaceX's Dragon capsule⁵, which uses TSC interfaces for the primary controls in space operations as a fail safe for automation.

Today, with the growth in air transport seen in the past decades and the overwhelming complexity of modern control systems and automation, the need has arisen to further aid the pilots in their jobs, by providing them with interfaces designed to increase their awareness of their surroundings, of the actions taken by the automation, and of any other constraint to their control behavior [3–5]. In this context, several studies have shown the potential of TSC interfaces to replace and modernize mechanical controls traditionally used for safety critical purposes [3, 5–10]. Nevertheless, some important issues have yet to be solved, especially when planning to use TSC technologies in dynamic environments such as an aircraft cockpit in turbulence: controlling a TSC requires the pilot to precisely touch the screen in the location of a (virtual) button, move along a slider or perform some other very specific gesture. This straightforward action becomes particularly difficult when the user is exposed to accelerations or vibrations, especially with an interface that presents itself to touch as a flat surface [11, 12]. In an aircraft, the accelerations caused by atmospheric turbulence affect the pilot's vision, cognitive efforts and motor movements, ultimately their ability to correctly and efficiently perform control tasks [13]. In addition, when *biodynamic feedthrough* (BDFT) occurs, i.e., when the accelerations of the vehicle propagate to the control manipulators through the pilot's body, involuntary components

¹<https://www.airbus.com/newsroom/press-releases/en/2019/12/airbus-begins-deliveries-of-first-a350s-with-touchscreen-cockpit-displays-option-to-customers.html>, [cited on 22 January 2022]

²<https://www.boeing.com/features/2016/07/777x-touchscreen-07-16.page>, [cited on 22 January 2022]

³<https://cirrusaircraft.com/wp-content/uploads/2014/11/Cirrus-Perspective-Touch-Plus-Brochure.pdf>, [cited on 22 January 2022]

⁴<https://www.thalesgroup.com/en/markets/aerospace/flight-deck-avionics-equipment-functions/flytx-tactile-large-display-flight-deck>, [cited on 22 January 2022]

⁵<https://medium.com/swlh/the-touchscreens-controlling-spacex-dragon-on-its-historic-mission-b0546d26053c>, [cited on 22 January 2022]

can be present in the control inputs [14]. Some research has already been done on TSC interfaces in dynamic environments, evaluating their usability, and identifying mitigation strategies for BDFT, with particular reference to model-based identification and cancellation of the involuntary components in the input signals [1, 15–17].

This thesis project aims to further investigate the applicability of model-based mitigation of BDFT for TSCs in cockpit environments, where the user is exposed to atmospheric turbulence. Part I of this report contains a paper detailing the results of the research performed in an experiment on a moving-base simulator. Part II discussed the preliminary research performed with the goal of designing the experiment. Part III contains appendices to the paper. The structure of the preliminary report contained in Part II is as follows. The research questions for a literature study in this field can be found in Chapter 2, a literature study on BDFT, TSCs, human body dynamics in vibrating environments and finger-TSC dynamics is reported in Chapter 3. A review of atmospheric turbulence and turbulence models is presented in Chapter 4, followed by the introduction to the second part of this report in Chapter 5, containing the details of the preliminary research performed with the goal of developing the human-in-the-loop simulator experiment to better understand BDFT occurring with TSCs in turbulence. Chapter 6 and Chapter 7 report the preliminary research conducted respectively on improving the methods for the identification of BDFT and on the development of experimental conditions for the simulator experiment. Finally, the proposed experiment plan is discussed in Chapter 8, followed by a conclusion in Chapter 9.



Paper

Effects of Turbulence Intensity and Variability on Biodynamic Feedthrough Modeling in Touchscreen Dragging Tasks

Giulia Leto*

Delft University of Technology, Delft, The Netherlands

Recent aircraft have seen the implementation of touchscreens (TSCs) on the flight deck, in sight of more intuitive and direct human-machine interactions. Biodynamic feedthrough (BDFT), i.e., the transfer of the aircraft's accelerations through the pilot's body to the control inputs, is however still cause for concern, preventing safe and reliable use of TSCs in turbulence. This paper describes a simulator experiment evaluating the performance in turbulent flight of model-based mitigation of BDFT occurring with TSC dragging task. Placing a TSC in front of the pilot, various motion perturbations were tested on the heave axis: multisine signals resembling turbulence, stationary (Gaussian) and variable (patchy) simulated turbulence, at three intensity levels. The results show that on average over 87% accuracy can be achieved in the identification of a personalized BDFT model at intensity of 0.75 and 0.5 m/s² (RMS heave accelerations), decreasing to 74% for RMS intensity of 0.25 m/s², symptom of a lower amount of feedthrough in the TSC input at low turbulence intensity. No model canceling over 70% of the BDFT components of the TSC inputs could be generalized across intensities, as the damping of the BDFT dynamics shows a 49% decrease between high and low intensities. In regards to BDFT mitigation in turbulence, models were identified from BDFT in Gaussian turbulence with accuracy comparable to models identified in multisine motion disturbances, with only 3.5% lower performance on average. Comparison between the Gaussian and patchy turbulence cases revealed a 4.7% higher BDFT mitigation performance for the former, connected to the time-varying nature of patchy turbulence. Finally, models generalizing BDFT dynamics across participants or experimental runs were found to always be outperformed by individual run models, giving up to 10% higher identification performance. These findings show that a model-based approach is promising with regards to BDFT mitigation in turbulence for TSC dragging tasks, but also that real-time identification and time-varying BDFT models might be needed to achieve consistently high mitigation performance in realistic variable turbulence.

Nomenclature

Abbreviations

BDFT	=	Biodynamic Feedthrough
CW	=	Classical Washout filter
FRF	=	Frequency Response Function
G	=	Gaussian condition
IR	=	Individual-Run
M	=	Multisine condition
NM	=	No Motion
OSFA	=	One-Size-Fits-All

Symbols

A	=	Sinusoid amplitude
CF	=	Crest Factor
CI	=	Cancellation Index
e	=	Error signal
f	=	Position forcing function

P	=	Patchy condition
PDF	=	Probability Density Function
PSD	=	Power Spectral Density
RMS	=	Root-Mean-Square
SA	=	Subject-Averaged
SNR	=	Signal-to-Noise Ratio
SRS	=	SIMONA Research Simulator
TSC	=	Touchscreen
u	=	TSC input signal
u^{BDFT}	=	BDFT component of the TSC input
\hat{u}^{BDFT}	=	Modeled BDFT component of the TSC input
u^{CANC}	=	Canceled TSC input signal
u^{COG}	=	Cognitive component of the TSC input

*MSc Student, Supervised by Dr. ir. D. M. Pool, Prof. Dr. ir. M. Mulder, Faculty of Aerospace Engineering, Control and Simulation Division, giuliam.letto@gmail.com, Kluyverweg 1, 2629 HS, Delft, The Netherlands.

f''	= Acceleration forcing function	V	= Velocity
G_{BDFT}	= Gain of the BDFT model	VAF	= Variance Accounted For
H_{BDFT}	= BDFT model	V_{metric}	= Intensity metric
\hat{H}_{BDFT}	= BDFT model estimates	\ddot{x}	= Surge accelerations
J	= Cost function	\ddot{y}	= Sway accelerations
K	= Kurtosis	\ddot{z}	= Heave accelerations
K_{heave}	= Gain of CW16 filter	δ	= BDFT model parameter array
L_{u_g}	= Turbulence length scale	ζ_{BDFT}	= Damping ratio of the BDFT model
N	= Number of points	μ	= Mean
n	= Remnant	ρ_u^2	= Relative remnant
n_{ty}, n_{tz}, n_d	= Integer factors of the sinusoid frequency	σ	= Standard Deviation
Q	= Kurtosis related parameter	σ_g^2	= Turbulence intensity
R	= Patch length parameter	τ_{BDFT}	= Time delay of the BDFT model
RV	= Run variability	ϕ	= Sinusoid phase
\tilde{S}	= Estimated PSD	ω	= Sinusoid frequency
S	= PSD	ω_{BDFT}	= Break frequency of the BDFT model
t	= Time	ω_{heave}	= Gain of CW16 filter
T_m	= Measurement time	ω_m	= Base frequency
Subscripts			
d	= Disturbance	y	= Horizontal component
i, j, k	= Indices	z	= Vertical/heave component
t	= Target		

I. Introduction

IN the past decade, the growth in air transport and the increased complexity and automation of aircraft control systems has driven aircraft manufacturers to research for safe and reliable flight deck interfaces able to increase the pilots' awareness of their surroundings, of the actions taken by the automation, and of any other constraint to the pilots' control behavior [1–3]. Touchscreens (TSC) have been identified as a promising design choice thanks to their potential use as direct manipulation interfaces, in which the aircraft's state and controls can be shown through representations mimicking real life, bridging the gap between the actions performed by the pilots and by the automation, their original intentions and the actual consequences on the aircraft state [4, 5]. Lightweight and flexible in their software, TSCs have already found a place on board a variety of aircraft, from commercial (Airbus* and Boeing†) to civil (Cirrus‡) and military (Thales§). Their use is, however, generally limited to the consultation of maps, pre-flight checklists and manuals, sometimes to the control of communication, navigation and power systems [2, 3].

A few important issues have yet to be solved before TSCs can be used for safety critical tasks, especially in dynamic environments such as an aircraft cockpit in turbulence: controlling a TSC requires the pilot to precisely touch the screen in the location of a (virtual) button, move along a slider or perform some other very specific gesture. This straightforward action becomes particularly difficult when the user is exposed to accelerations or vibrations, especially with an interface that lacks tactile feedback [6, 7]. The propagation of the accelerations of vehicle to the control manipulators through the pilot's body, called biodynamic feedthrough (BDFT), will cause involuntary touches to be registered as control inputs [8].

Some research has already been done on BDFT occurring with TSC interfaces in dynamic environments, identifying mitigation strategies for its effects [1, 6, 9–14]. Among these, are studies relating the amount of BDFT to the type of TSC used, concluding that error rates are greater with projected capacitive TSCs compared to resistive touch technologies, and worsening with decreasing screen size [1]. Similar studies investigated the effect of the location of the TSC with respect to the pilot: proposed TSC positions were overhead, in front, inboard and outboard of the pilot, with the frontal position giving lower error rates and the inboard causing the least fatigue [1, 6, 14–16]. Other studies looked at ways to further reduce the error rates, and in so mitigate BDFT. The use of interchangeable stencil overlays was proposed to

*airbus.com/en/newsroom/press-releases/2019-12-airbus-begins-deliveries-of-first-a350-xwbs-with-touchscreen, [cited on 28 March 2023]

†boeing.com/features/2016/07/777x-touchscreen-07-16.page, [cited on 28 March 2023]

‡cirrusaircraft.com/wp-content/uploads/2014/11/Cirrus-Perspective-Touch-Plus-Brochure.pdf, [cited on 28 March 2023]

§thalesgroup.com/en/markets/aerospace/flight-deck-avionics-equipment-functions/flytx-tactile-large-display-flight-deck, [cited on 28 March 2023]

separate the input areas for discrete interaction with TSCs [10, 17]. These have been shown not only to be ineffective in their purpose, but also to greatly compromise the flexibility of the TSC interfaces, with their only benefit being the introduction of tactile feedback to the otherwise flat TSC surface [10, 17]. Error rate performance of different activation methods was evaluated on tapping, dragging and sliding tasks, concluding however that none were suitable to guarantee a correct input selection, pending an evaluation on force touch systems [6]. Configurations with users gripping the edges of the display, or using a wrist or arm support were shown to be constraining and, in most cases, ineffective in reducing error rates [12]. An exception is ‘braced touch’, a configuration in which the users supports their hand directly on the display, which proved to be effective in combination with a double tap activation method [11].

The most promising BDFT studies on TSC, however, do not attempt to physically mitigate BDFT as in the works discussed above, but rather to predict it from knowledge of human biodynamics and a vehicle’s accelerations to cancel its effects at the software level [13, 14]. This *model-based BDFT mitigation* approach was shown to cancel above 70% of the involuntary component of inputs recorded in continuous dragging tasks, in conditions in which at least 0.5% of the variance of said input was caused by the occurrence of BDFT [14]. Although promising, this mitigation approach has only been tested on the BDFT data recorded from a multisine motion disturbance loosely mimicking the accelerations of an aircraft in turbulence, designed to enable the separation of the involuntary BDFT component and of the voluntary component of the control inputs [13, 14]. The effectiveness of the BDFT model in turbulent flight conditions has therefore yet to be quantified in regards to the broader and continuous frequency spectrum of turbulence. In addition, the methods and models used for the identification of BDFT are based on the assumptions of linearity and time-invariance, raising questions in regards to the applicability of the state-of-the-art procedures in actual turbulence, which is variable in nature. Finally, the approach has been proven able to reliably identify a model for the BDFT component of the input when the occurring BDFT is sufficiently strong [14]. Because the reliability of the model is crucial for the successful cancellation of BDFT, understanding the effect of motion intensity on the feedthrough becomes essential for the use of model-based cancellation in TSCs on board of aircraft cockpits.

The goal of this paper is therefore to evaluate the use of model-based mitigation of BDFT in turbulent conditions with continuous TSC dragging tasks, with particular interest in the effect of variability and intensity of turbulence. Results were achieved by means of an experiment with the SIMONA Research Simulator at Delft University of Technology, in which 21 volunteers were asked to track a target on a TSC placed directly in front of them, while exposed to motion disturbances in the heave axis: a multisine signal mimicking turbulence and two turbulent flight conditions, differing in their variability, each at three intensity levels. The parameters for a time-invariant BDFT model were identified both from the multisine and the invariant turbulence motion disturbances using time domain fitting algorithms, hypothesizing that the resulting models would effectively cancel BDFT at all motion intensity levels and with time-invariant turbulence, but would be unable to do so for the time-varying turbulent flight case due to the adaptations in the neuromuscular dynamics of the TSC user.

The structure of this paper is as follows: Section II.A introduces the dynamics behind model-based BDFT mitigation and the issues related to modeling BDFT in (simulated) turbulence, opposed to in multisine motion disturbances. The experimental set-up and experiment design are discussed in Section III, together with the hypothesis for the research. Results of the experiment are shown in Section IV and subsequently discussed in Section V. Finally, conclusions are drawn in Section VI.

II. Model-Based Biodynamic Feedthrough Mitigation

A. Biodynamic Feedthrough Mitigation Dynamics

Figure 1 schematically shows the working principle of model-based BDFT mitigation for the case of a human operator employed in a TSC dragging task in turbulent flight, and gives an impression of the effects that are investigated in this paper. The human operator exposed to an acceleration f_d'' (motion disturbance) while tracking a target with position f_t on a TSC is assumed to have quasi-linear dynamics: the position of the finger of the operator, i.e., the input u given to the TSC, is the superposition of a cognitive component u^{COG} , linearly related to the control task f_t , and a BDFT component caused by the transfer of the vehicle’s accelerations f_d'' through the body and limbs of the human, with a remnant n accounting for non-linearities, inevitably present in the control input when performing a voluntary task independently on the presence or lack thereof a motion disturbance [13, 14]. The dynamics just described are synthesized in Eq. (1).

$$u = u^{BDFT} + u^{COG} + n \quad (1)$$

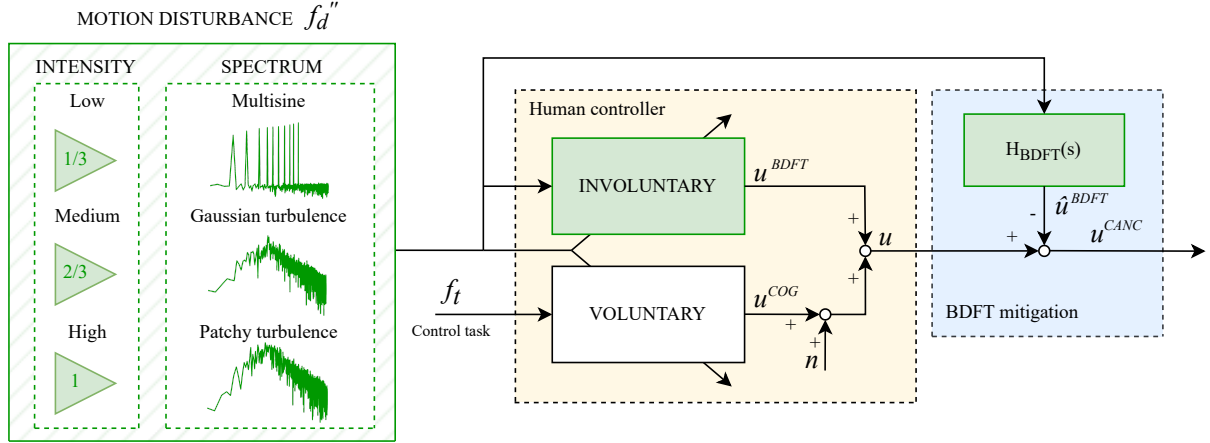


Fig. 1 Quasi-linear human controller dynamics and model-based BDFT mitigation dynamics. The arrow crossing the involuntary and voluntary blocks of the human controller indicate that these dynamics are assumed to adapt when changes in the motion disturbance occur. A graphical representation of the motion disturbances used in the experiment described in this paper is given on the left.

Using a BDFT model $H_{BDFT}(s)$, i.e., a transfer function between the vehicle's accelerations and the involuntary input to the TSC caused by such accelerations, the involuntary component u^{BDFT} can be estimated, and a canceled input signal u^{CANC} can be calculated and used as estimate of the voluntary component of the input u^{COG} , see Eq. (2) and the blue block of Figure 1.

$$u^{CANC} = u - \hat{u}^{BDFT} \quad (2)$$

The accuracy of the BDFT model $H_{BDFT}(s)$ is therefore essential for successful model-based mitigation of BDFT. To accurately identify a BDFT model however, both the control task and the motion disturbance have to be designed specifically for the purpose of identification, inevitably affecting the dynamics to be identified. In fact, to be able to separate the involuntary component of the input registered by a TSC from voluntary component and remnant, and relate the BDFT component of the input to the accelerations at which the human operator is exposed, the disturbance and the control forcing functions need to have discrete contributions to the frequency spectrum, easy to isolate, such as multisine signals [18]. Identification of BDFT occurring in realistic turbulence on the contrary is impeded by the impossibility of separating the BDFT components of the input from the remnant, as the spectrum of realistic turbulence is continuous. The identification of BDFT models in turbulence can no longer be separated from remnant contributions. On top of this inherent inaccuracy in BDFT modeling in turbulence, the intensity and the variation in intensity of turbulence are also bound to influence how model-based BDFT mitigation will perform. The human operator is likely to adapt his/her control behavior to maintain a good tracking performance when exposed to turbulence with different intensities or more or less variability, changing, as a consequence, the dynamics of BDFT. This adaptation is displayed in Figure 1 with arrows crossing the voluntary and involuntary dynamics blocks.

Before going further into the details of BDFT mitigation, a clarification should be made. For the case of a TSC, the control input u and the target signal f_t can be decomposed into a lateral component y and a vertical/longitudinal component z (depending on the orientation of the TSC). The schematic in Figure 1 describes the contributions to each of these components independently, and can be applied to both [13, 14].

B. Biodynamic Feedthrough Models

Previous research on BDFT occurring with TSCs showed that the lumped BDFT dynamics occurring with a multisine motion disturbance can be captured effectively using the model in Eq. (3), with its three components: an underdamped second-order system encompassing the neuromuscular dynamics, a gain G_{BDFT} capturing the magnitude of the BDFT and a time delay τ_{BDFT} accounting for propagation delays in the human body, as well as the latency in the

TSC processing systems [13].

$$H_{BDFT}(s) = G_{BDFT} \cdot \frac{\omega_{BDFT}^2}{s^2 + 2\zeta_{BDFT}\omega_{BDFT} \cdot s + \omega_{BDFT}^2} e^{-s\tau_{BDFT}} \quad (3)$$

An analysis of the data of the current experiment showed, however, that BDFT in TSCs behaves like an overdamped system in the majority of the cases. The use of an overdamped second-order model with the damping ratio fixed to 1 and an additional break frequency, described by Eq. (4), was considered to better capture changes in the slope occurring at high frequencies.

$$H_{BDFT}(s) = G_{BDFT} \cdot \frac{\omega_{BDFT/1} \cdot \omega_{BDFT/2}}{(s + \omega_{BDFT/1})(s + \omega_{BDFT/2})} e^{-s\tau_{BDFT}} \quad (4)$$

Figure 2 shows the BDFT estimates across four identification runs recorded at the high intensity multisine motion disturbance, for one of the participants showing overdamped BDFT dynamics.

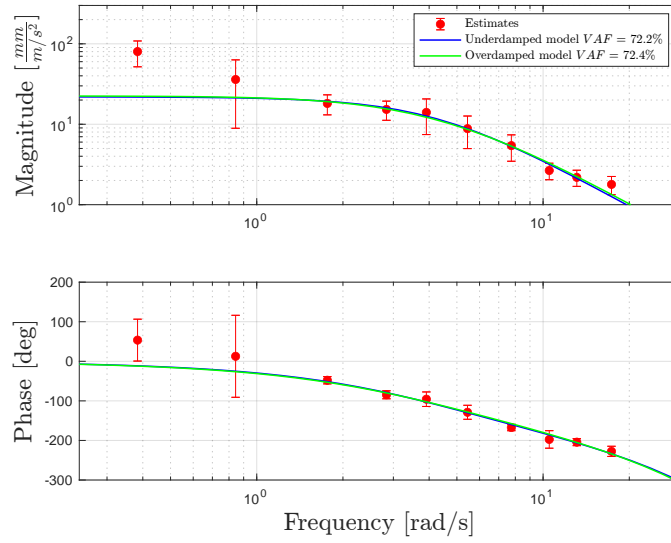


Fig. 2 Comparison between underdamped and overdamped BDFT models resulting from the averaged BDFT estimates of participant 16.

The figure shows that for the frequencies of the multisine signal, at which the model is being identified, there is no significant difference in the fit. Using the underdamped model, 72.2% of the BDFT component of the input is modeled for this participant, which becomes 72.4% using the overdamped model. It was therefore concluded that there will be no significant difference in the performance of either model for the cases in which overdamped dynamics are observed. To allow a direct comparison to the work of Khoshnawisadeh and Pool [13], the model in Eq. (3) is used for all further analysis.

C. Biodynamic Feedthrough Identification

Two methods can be used for the identification of the BDFT model: a frequency domain identification approach also used by Mobertz et al. [14] and Khoshnawisadeh and Pool [13] and a time domain approach as, for example, proposed in Zaai et al. [19]. In addition, three types of BDFT model are derived using different algorithms: the results of the identification performed on each run of the experiment is either used separately to evaluate BDFT identification performance with an Individual-Run (IR) model, or averaged for each participant resulting in a Subject-Averaged (SA) model. To further understand the capabilities of a BDFT model generalized to an averaged human controller, the One-Size-Fits-All (OSFA) model is used.

1. Frequency Domain Identification

In the frequency domain identification approach, the BDFT model in Eq. (3) is fitted to a non-parametric estimate of the BDFT frequency response function (FRF), computed from the cross-PSD of the multisine disturbance and the

input signal and the auto-PSD of the disturbance signal, as shown in Eq. (5).

$$\hat{H}_{BDFT}(j\omega_d) = \frac{S_{f_d''u}(\omega_d)}{S_{f_d''f_d''}(\omega_d)} \quad (5)$$

This estimate, although adding estimation errors to the fit, allows to visualize the frequency response of the estimated BDFT dynamics, giving great insight in the validity of the model structure. The model fit is performed using MATLAB's algorithm *fminsearch*, searching for a set of parameters δ which minimized the normalized magnitude of the error between the model H_{BDFT} and the estimate \hat{H}_{BDFT} . This cost function $J(\delta)$ is shown in Eq. (6).

$$J(\delta) = \sum_{k=1}^{Nd} \frac{|\hat{H}_{BDFT}(j\omega_d) - H_{BDFT}(j\omega_d|\delta)|}{|\hat{H}_{BDFT}(j\omega_d)|} \quad (6)$$

The initial guess and the constraints for the optimization of the parameters, the same for all motion intensities, are given in Table 1.

Table 1 Initial conditions and constraints for BDFT model fitting.

	G_{BDFT} [mm/(m/s ²)]	ω_{BDFT} [rad/s]	ζ_{BDFT} [-]	τ_{BDFT} [s]
Lower limit	0.0	0.0	0.0	0.0
Upper limit	150.0	50.0	2.0	2.0
Initial condition	20.0	6.0	0.6	0.1

2. Time Domain Identification

Time domain identification directly fits the model on the BDFT component of the input u^{BDFT} , separated from the voluntary components and from the remnant (this last only for the case of a multisine motion disturbance) using knowledge of the frequencies of target and disturbance signals and the Fourier Transform of the input u . The BDFT component of the input u^{BDFT} is then fed to a time domain estimator, which outputs a optimal set of parameters for the parametric model corresponding to a minimum error between the signal u^{BDFT} and the output of the BDFT model, \hat{u}^{BDFT} . For this study, a Maximum Likelihood Estimation method is used, the Gauss-Newton algorithm described by Zaal et al. [19].

3. Individual-Run, Subject-Averaged and One-Size-Fits-All Models

For each intensity of the multisine disturbance, a total of four measurement runs were recorded for identification of the model parameters. To understand how much of the BDFT component of the TSC input can be canceled with a model tailored to each of these run, the Individual-Run (IR) model is used, fitting the model in Eq. (3) separately to the data of each run, and evaluating its identification performance. Four IR models are therefore identified per participant per experimental condition. On the other hand, the Subject-Averaged (SA) model describes the average BDFT dynamics of each participant, functioning as a 'personalized' model. The algorithm used to obtain the parameters for this model depends on whether a time domain or a frequency domain identification approach are used. With the time domain approach, the parameters of the SA model are the average of the parameters of the IR model. With the frequency domain identification approach, the SA parameters are obtained by first calculating separately for each run the non-parametric estimates, then averaging the estimated, and finally fitting the averaged data to the BDFT model in Eq. (3). In this two-step identification method, averaging the estimates instead of directly averaging the IR parameters allows to reduce the error introduced during the non-parametric estimation of BDFT. Finally, the One-Size-Fits-All (OSFA) model is a generalized BDFT model, obtained averaging the parameters of the SA model of all the participants of the experiment.

III. Methods

The effect of turbulence intensity and variability on BDFT mitigation with a model-based approach were researched by means of an experiment in a moving-base simulator, in which participants were tasked with following a target on a

TSC, while exposed to heave motion disturbances. The experiment proposed here is based on an experiment originally designed by Mobertz et al. [14] and subsequently improved by Khoshnewisazadeh and Pool [13]. This chapter describes the experiment and the data analysis for the current experiment.

A. Apparatus

The experiment was conducted using the SIMONA Research Simulator (SRS), a six-degrees-of-freedom moving-base simulator, driven by hydraulic pumps, located at the Faculty of Aerospace Engineering at TU Delft, Figure 3. The SRS was equipped with a 15-inch Iiyama Pro-Lite TF1534MC-B1X TSC (1024x768 resolution, 1 pixel = 0.297 mm), located in place of the Primary Flight Display of the co-pilot, tilted from the vertical plane with an angle of 18 degrees upwards. The drag latency for this TSC and for the control task of this experiment is expected to be between 70-80 ms from test data analyzed by Khoshnewisazadeh and Pool [13] and Vrouwenfelder et al. [20].

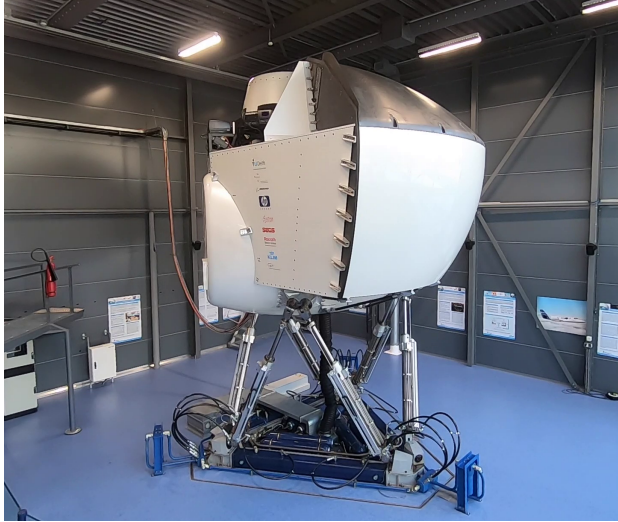


Fig. 3 SIMONA Research Simulator, TU Delft.



Fig. 4 Experiment set-up.

B. Forcing Functions

1. Control Task

Participants were tasked with a continuous pursuit dragging task, the same as previously used by Khoshnewisazadeh and Pool [13] in their experiment. The target was shown on the TSC with a pointer (a white triangle), its location highlighted with a vertical and an horizontal line intercepting at the coordinates of the pointer, see Figure 5. To provide visual feedback that their tracking effort was being recorded, a purple circle was shown on the screen at the location at the current registered touch location. Figure 5 also shows the coordinate system used in this paper, as well as a realization of the trajectory of the pointer, both of which were not shown to the participants of the experiment, but are included here for clarity. The y and z coordinates of the trajectory of the pointer were generated independently as sums of three sines with different frequencies, amplitudes and phases. The frequencies of the target signals were chosen among the integer multiples of the base frequency $\omega_m = 2\pi/T_m = 0.0767$ rad/s, derived from the measurement time $T_m = 81.92$ s, therefore preventing leakage. This measurement time, with

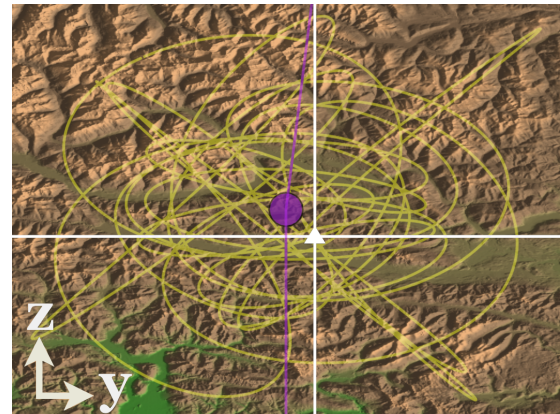


Fig. 5 Screen shown to the participants overlaid with a realization of the trajectory of the target (in yellow) and with a coordinate system.

a time resolution of 0.01 s leads to a number of data point which is a power of 2, characteristic that greatly reduces the computational time of the Fast Fourier Transform algorithms, and is therefore often employed in cybernetics research [13, 14, 19]. Eq. (7) describes a multisine signal built from sine components k with amplitude A_k , phase ϕ_k and frequency ω_k .

$$f(t) = \sum_{k=1}^N A_k \sin(\omega_k t + \phi_k) \quad (7)$$

The values used for the construction of f_{ty} and f_{tz} are shown in Table 2 together with the integers n_t used for the generation of frequencies ω_t . The spectra of the two signals are shown in Figure 6. The use of only three sinusoidal

Table 2 Values used for construction of the target signal for the TSC tracking task.

k	Target, f_{ty}				Target, f_{tz}			
	n_{ty}	ω_{ty}	A_{ty}	ϕ_{ty}	n_{tz}	ω_{tz}	A_{tz}	ϕ_{tz}
	[-]	[rad/s]	[mm]	[rad]	[-]	[rad/s]	[mm]	[rad]
1	3	0.230	32.767	1.445	2	0.153	22.771	0.308
2	7	0.537	39.777	0.000	13	0.997	39.775	-0.431
3	19	1.457	71.354	-1.825	17	1.304	47.511	-1.591

components for each signal was motivated by the need of keeping the task simple for the user to perform, while the amplitude of the sines was chosen to fully fill the available screen surface [14]. To prevent recognition of the signal, the lateral and vertical coordinates of the target were flipped, generating a total of four realizations of the target trajectory.

2. Motion Disturbances

In regards to the motion disturbance, three different types were used, in addition to a condition with no motion (NM) for calibration: multisine (M), Gaussian turbulence (G) and patchy turbulence (P). Each of the conditions with motion (M, G, P) was tested for three different motion intensities (1 = low, 2 = medium, 3 = high), for a total of ten experimental conditions. The intensity of the motion was quantified as the magnitude of the root-mean-square (RMS) accelerations to which participants were exposed, as previously proposed by Jacobson [21]: $V_{metric} = \sqrt{\ddot{x}_{RMS}^2 + \ddot{y}_{RMS}^2 + \ddot{z}_{RMS}^2}$. It should be noted that for this experiment, motion was only simulated in the heave axis to keep the amount of experimental conditions reasonable for performing the experiment in a single session. Heave was selected over sway and surge because the vertical accelerations caused by turbulence have higher peaks compared to lateral or horizontal accelerations, due to the larger projected surface exposed to the turbulent flow [22]. Consequently, for this experiment, $V_{metric} = \ddot{z}_{RMS}$.

The three intensity levels used were $V_{metric} = 0.75, 0.5, 0.25 \text{ m/s}^2$, implemented by multiplication of the high intensity motion disturbance signals with a gain (1, 2/3, 1/3 respectively, as visible in Figure 1). The highest intensity selected ($V_{metric} = 0.75 \text{ m/s}^2$) corresponds to the intensity of the multisine motion disturbance used in Mobertz et al. [14] and in Khoshnewiszadeh and Pool [13]. No higher intensities were tested due to the constraints of the motion space of the SRS. The medium and low intensities were chosen to correspond to the intensities used by Jacobson [21] in an experiment evaluating the performance of an extension of the Finger-Fitts' Law for use with TSCs in turbulent flight. The details of the construction of the motion disturbances are now discussed, starting from the multisine motion disturbance, used for identification and verification purposes, the same signal used in the works of Mobertz et al. [14] and of Khoshnewiszadeh and Pool [13].

a. Multisine Motion Disturbance

For the multisine condition, the vertical position of the simulator was generated from a sum-of-sines signal with a total of ten frequency components. These components were selected to cover as much as possible the range of frequencies at which humans are sensible, as well as to ensure that the accelerations generated from this position signal were not recognizable during the repeated simulations [13, 14]. The integers n_d , the frequencies ω_d , the amplitudes A_d and the phases ϕ_d used for each multisine component k are given in Table 3 [13, 14].

To use this signal on the SRS, both the position and the acceleration signals are required to have a zero starting value. For this reason, the position signal $f_d(t)$ constructed from the values in Table 3 was multiplied with a fade-in signal

Table 3 Values for construction of the position signal for the M3 motion disturbance.

k	n_d	Disturbance, f_d		
		ω_d	A_d	ϕ_d
		[-]	[m]	[rad]
1	5	0.383	$1.067 \cdot 10^{-1}$	-0.269
2	11	0.844	$8.069 \cdot 10^{-2}$	4.016
3	23	1.764	$4.019 \cdot 10^{-2}$	-0.806
4	37	2.838	$2.048 \cdot 10^{-2}$	4.938
5	51	3.912	$1.246 \cdot 10^{-2}$	5.442
6	71	5.446	$7.568 \cdot 10^{-3}$	2.274
7	101	7.747	$4.735 \cdot 10^{-3}$	1.636
8	137	10.508	$3.424 \cdot 10^{-3}$	2.973
9	171	13.116	$2.856 \cdot 10^{-3}$	3.429
10	226	17.334	$2.416 \cdot 10^{-3}$	3.486

with a fade-in time of 8 seconds, and then differentiated twice to get the acceleration $f_d''(t)$. Details on the fade-in signal can be found in Chapter 3.4 of Leto [23].

b. Gaussian and Patchy Motion Disturbances

The novelty of this experiment lies in the attempt to use model-based BDFT mitigation on TSC data collected in simulated flight conditions representative of real aircraft responses to turbulence. Two motion disturbances were derived from the simulation of the aircraft responses to turbulence, differing in their variability. These conditions were generated using the patchy turbulence model originally created by Van de Moesdijk [24, 25], in the version described in Chapter 7.2 of Leto [23]. The patchy turbulence model is a stochastic model which generates time traces for the components of an isotropic turbulence velocity field having Dryden spectra, tunable to present *patchiness*. Patchiness indicates that, in the flow field, areas of high and low energy alternate randomly, introducing spatial variability in the modeled turbulence compared to the conventional linear filtering with Dryden spectra: in practical terms, turbulence is modeled as subsequent patches, inhomogeneous from patch to patch, but carrying the assumptions of homogeneity and stationarity within each patch [24].

A total of four parameters are used to tune the patchy turbulence model. These are the isotropic turbulence intensity σ_g^2 and the longitudinal integral length scale L_{u_g} , influencing the power spectrum of the resulting turbulence, and Q and R , influencing its patchiness. Q , varying between 0 and $+\infty$, specifies the Kurtosis of the probability density function (PDF) of the components of the turbulence velocity field. With $Q = 0$, a Gaussian distributed turbulence velocity profile is obtained, with time-invariant characteristics. Setting $Q > 0$, the Kurtosis of the PDF is increased, leading to a higher occurrence of turbulence having high and low velocity (in magnitude), increasing its variability [25]. For reference, Kurtosis up to $K = 6$ has been observed in atmospheric turbulence [25]. Parameter R , varying between 0 and 1, is used by Van de Moesdijk [24] to model the variability of turbulence in the pilots' perception, specifying the scale of a patch of turbulence in comparison to the integral scale of the largest eddies in the turbulent flow [25]. In particular, $R = 1$ indicates short patches, which increase in length as R decreases [25].

For the experiment, model-based mitigation of BDFT was studied on two turbulence conditions: a time-invariant turbulence, having a Gaussian distributed PDF of the turbulence velocities, named the Gaussian condition (G) and a time-varying turbulence with patchy characteristic, the patchy condition (P). The parameter settings of the patchy turbulence model for the two conditions can be found in Table 4.

Both Gaussian and patchy turbulence conditions just mentioned led to an overall motion intensity of $V_{metric} = 0.75$ m/s², as simulated by the SRS. The selection of two different values for the turbulence intensity parameter σ_g^2 and of the motion filter settings (that will be described in the remainder of the section) are driven by the need of simulating motion with the selected V_{metric} .

The output of the turbulence model was filtered with a second-order low-pass filter with a cut-off frequency of 10 Hz, both because the Dryden spectra used for the turbulence model deviate from the spectra of actual turbulence at

Table 4 Input parameters for the patchy turbulence model to generate the Gaussian and patchy turbulence used in this experiment.

Condition	σ_g^2 [m ² /s ²]	L_{u_g} [m]	Q [-]	R [-]
Gaussian (G)	1	300	0	-
Patchy (P)	0.5	300	1.55	0.1

high frequencies [21, 26], and because of the physical limitations of the simulator, which would be damaged if exposed to high frequency motion. The symmetric components of the turbulence velocity field generated using the patchy turbulence model were then fed to a Cessna Citation 500 non-linear model based on the DASMAT architecture (see Van der Linden [27]) to simulate the vertical aircraft response to the designed turbulence. The antisymmetric turbulence velocity field was neglected, as it has negligible influence on symmetric aircraft motion. The aircraft model was then linearized for straight level flight at an altitude of 28,000 ft (8534.4 m), flying at a velocity of $V = 165$ m/s and having initial mass of 4,000 kg, similarly to Jacobson’s research [21].

The output of the aircraft model was passed through a motion filter, the classical washout filter (CW16), to simulate the vertical aircraft response with the SRS. Here, all motion except for the vertical accelerations was discarded, and these accelerations were filtered to remove the low frequency components of the motion using a third-order high-pass motion filter. To achieve this while avoiding confounds, the same set of settings for the filter were used for both the Gaussian and the patchy conditions. Of these settings, the damping ratio was fixed to 0.7, the first-order pole to 0.2 rad/s, following the specification in Gouverneur et al. [28]. The gain $K_{heave} = 1$ and break frequency of the second-order pole $\omega_{heave} = 0.9$ rad/s were selected after performing a simulator workspace analysis [28], in which the parameters were optimized to simulate as closely as possible the motion of the aircraft within the constraints of the actuation system of the simulator and of the selected highest overall motion intensity $V_{metric} = 0.75$ m/s². In the selection of the motion filter settings, the break frequency of the high-pass frequency was selected as low as possible within all other constraints, to simulate the motion at frequencies overlapping as much as possible the frequency band of the multisine. The details of the algorithm used can be found in Gouverneur et al. [28], while the details of the selection of the parameters of the turbulence model, aircraft model and filter settings can be found in Chapters 7.1 and 7.4 of Leto [23].

The spectra of the different disturbance signals are shown in Figure 6 together with the y and z target signals. In addition, Figure 7 zooms in on the time traces of the vertical acceleration for the three high intensity conditions. The higher turbulence variability of the patchy condition with respect to the Gaussian condition can be seen in the peaks present in the vertical acceleration (examples around 3, 10, 20 seconds), while the smoothness of the multisine disturbance clearly shows a lack of high frequency components in this signal. This difference is measurable calculating the crest factor CF : for the aircraft accelerations in response to Gaussian turbulence $CF = 3.23$, while for the patchy case $CF = 3.82$.

Summarizing, a total of 10 conditions are tested in this experiment, shown in Table 5. The M3 condition corresponds to the motion disturbance used by Khoshnewisadeh and Pool [13], and as such is also referred to as baseline. For the Gaussian conditions, a offset of maximum 0.02 m/s² can be observed in the exact value of V_{metric} calculated in the accelerations used during the experiment. This offset is due to the fact that the accelerations of the simulator for the turbulence cases were the output of an optimization on the parameters of the turbulence velocity field, those of the simulated aircraft and of the motion filters. Parameters outcome of the optimization resulting in V_{metric} close enough to the target were used, as an offset of 0.02 m/s² is believed to not influence results.

C. Participants

A total of 21 volunteers, 15 male and 6 female, were asked to take part in the experiment. Participants were all right handed, between 19 and 33 years of age ($\mu = 23.8$ years, $\sigma = 3.8$ years) with height between 1.67 and 2.03 m ($\mu = 1.78$ m, $\sigma = 0.08$ m) and weight between 51 and 102 kg ($\mu = 74.2$ kg, $\sigma = 12.8$ kg). All participants recalled having at least 8 years of experience using TSCs.

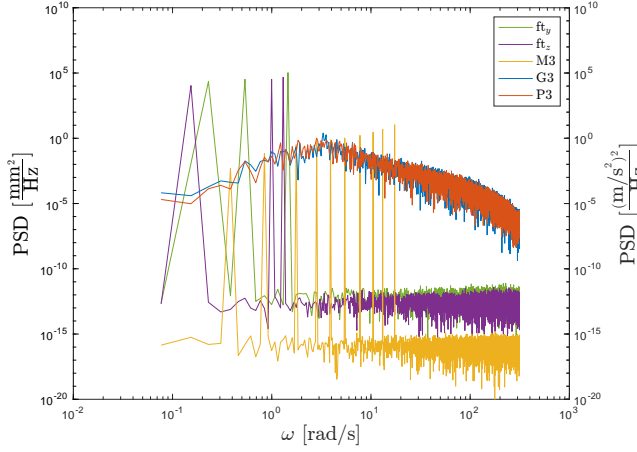


Fig. 6 PSD of the TSC target and motion disturbance signals; f_{ty} and f_{tyz} refer to the left axis with units mm^2/Hz ; M3, G3, P3 to the right axis, units $(\text{m/s}^2)^2/\text{Hz}$.

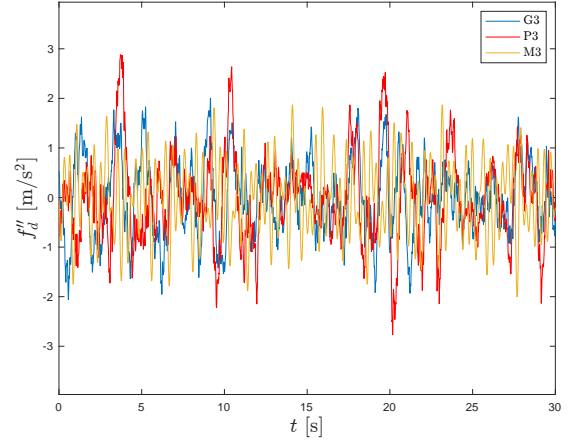


Fig. 7 Detail of the time traces of the multisine, patchy and Gaussian conditions, $V_{metric} = 0.75 \text{ m/s}^2$.

Table 5 Experimental conditions matrix.

Condition	Description	$V_{metric} [\text{m/s}^2]$
NM	No motion	-
M1	Multisine low intensity	0.25
M2	Multisine medium intensity	0.50
M3	Multisine high intensity	0.75
G1	Gaussian low intensity	0.24
G2	Gaussian medium intensity	0.48
G3	Gaussian high intensity	0.73
P1	Patchy low intensity	0.25
P2	Patchy medium intensity	0.50
P3	Patchy high intensity	0.75

D. Procedures

Participants were told that the experiment was performed to better understand the effects of turbulence on the use of TSCs in aircraft cockpits. No explicit details were given on the different motion conditions that would be tested, neither in regards to the intensity nor to the types of motion disturbances. They were instructed to perform the tracking tasks described in Section III.B, by following the white marker and lines with their index finger, and were told that the purple marker was shown to provide feedback. Participants were told to adjust their seating position and height before the start of the experimental runs to perform the tracking task with their backs upright and their arms in a natural (not too close, not outstretched) position with respect to the TSC.

Once a seating position was fixed, participants were told to maintain that position throughout the runs, and to try to match the same seating position after each break. In addition, participants were instructed to not lift their hand from the surface of the screen for the duration of the experimental runs. To reduce friction between the participant's skin and the TSC surface, preventing them from experiencing excessive fatigue, anti-static gloves were used. Noise-canceling headphones were used to mask the sounds made by the hydraulic pumps, preventing participants from predicting the simulator's accelerations.

Each participant was able to familiarize with the control task with and without motion and at different motion intensities during four training rounds (NM, M1, M2, M3). Subsequently, data were recorded for 16 trials to be used for the identification of the BDFT model and for 36 trials to be used for the evaluation of the cancellation performance. The

order of execution of the combined 52 identification and cancellation runs was randomized for each participant. To allow participants to rest, three breaks of 15 minutes were planned, for a total experiment duration of 3 hours. The 16 identification trials comprised of conditions M1, M2, M3 and NM, repeated four times each. The 36 evaluation trials comprised all conditions except for the NM condition (M1, M2, M3, G1, G2, G3, P1, P2, P3), again repeated four times each. For each repetition of the trials, the sign of one or both of the coordinates of the target signal on the TSC was flipped, reducing the chance that the participant could recognize and anticipate the movement of the target on the screen.

Participants were informed of the total (expected) duration of the experiment, of the three 15 minutes breaks and of the duration of each run. They were also told and encouraged to take short in-simulator breaks to rest their arms when needed, and of the possibility to take breaks outside of the simulator upon their request. Participants were instructed to give notice to the experimenter in case of motion sickness, ensuring that no data would be collected and used for the analysis if participants were experiencing excessive symptoms, such as nausea.

The experiment and procedures were approved by the 'Human Research Ethics Committee' of TU Delft (application number 1734), participants signed an informed consent form ensuring their understanding of the experiment procedures, of the safety and emergency procedures onboard the SRS, of their rights of withdrawal from the experiment and of the subsequent publication of the anonymized data in full or aggregated form. The informed consent form and experiment briefing can be found in Appendix C of Leto [23].

E. Hypotheses

The following hypotheses were formulated:

H1: Over 90% of the BDFT component of the TSC input occurring with the multisine motion disturbance at high intensity ($V_{metric} = 0.75 \text{ m/s}^2$) will be accounted for with personalized BDFT models.

The identification of BDFT with high motion intensity is conducted in the same physical set-up and with the same forcing functions as in the work of Khoshnawisadeh and Pool [13]. It is therefore expected that results for the identification of BDFT model for the baseline condition (M3), personalized to each participant, will be comparable to results reported by Khoshnawisadeh and Pool [13].

H2: The BDFT model identified for a higher motion intensity (V_{metric}) will overestimate BDFT when employed for mitigation at lower V_{metric} . Mitigating BDFT on data collected at a specific V_{metric} using a BDFT model identified at the same V_{metric} will lead to comparable performance independently of the magnitude of V_{metric} .

The main effect on BDFT of a decrease in the intensity of the disturbance motion is expected to be a decrease in the magnitude of the BDFT component of the TSC input. It can be hypothesized that the gain encoding the proportionality between motion disturbance input and BDFT output will be higher for the high motion intensity case compared to the ones for the medium and low motion intensity cases. Therefore, the BDFT model identified at high intensity will overestimate the amount of BDFT present in the TSC input recorded at medium and low intensities, and vice-versa. Since the identification and mitigation techniques and the type of data used at the high motion intensity are the same as the ones used for the lower motion intensities, it is hypothesized that BDFT mitigation tailored for each intensity will have comparable performance whether performed at high, medium or low intensities.

H3: A more compliant control behavior of the TSC operators, i.e., a lower natural frequency in their BDFT dynamics, will be observed with disturbances caused by Gaussian turbulence, when compared to the multisine disturbance. Effective model-based BDFT mitigation can still be obtained by adapting the model's parameters.

Comparing the time traces of the motion disturbances in Figure 7, a higher amount of high frequency motion is visible in the Gaussian and patchy cases when compared to the multisine, further confirmed in their power spectrum in Figure 6. These high frequency components continuously perturb the participants' control action. On the contrary, with the multisine disturbance, peaks of accelerations are perceived almost independently from one another, with smooth accelerations from one to the next. These considerations lead to hypothesize that, while exposed to the Gaussian motion disturbance, participants will relax their muscles to perform the tracking task without rigidly passing through all the high frequency components constantly perturbing their control action, more than under multisine conditions. Adaptation of the parameters of the existing model is expected to suffice to attain effective mitigation as defined by Mobertz et al. [14], as the accelerations caused by Gaussian turbulence are time-invariant [23].

H4: A time-varying neuromuscular adaptation will be observed with disturbances caused by patchy turbulence. Low performance will be observed with model-based BDFT mitigation using a time-invariant model.

The accelerations caused by patchy turbulence (turbulence of variable nature) present variations in time in their magnitude, shown visually using Figure 7 and quantified through a crest factor, see Section III.B.2.b. Consequently, it is expected that the participants exposed to such disturbance would adapt their control behavior throughout the

measurement time, to maintain a good performance in the tracking task. It was hypothesized that the dynamics of BDFT would be influenced by the adaptation of the voluntary control dynamics, and therefore that the current time-invariant BDFT model, unable to model the variations in the BDFT dynamics over time, would result in ineffective BDFT mitigation.

F. Dependent Measures

During the experiment, the lateral and vertical components of the TSC input given by the participants were collected with a sampling frequency of 100 Hz, together with the motion disturbances and target signals on the TSC. In addition, participants were asked to provide their age, weight, height and years of experience with TSCs, and to notify the experiment if contact with the screen was lost. From the collected data, a number of dependent measures were calculated to test the hypotheses:

- BDFT model parameters: G_{BDFT} , ω_{BDFT} , ζ_{BDFT} , τ_{BDFT} . These are used to investigate the effect of different motion disturbance intensities on the BDFT dynamics, as well as to understand differences in the BDFT dynamics of different participants. Although biased by the presence of remnant, the parameters are also used to assess the different BDFT dynamics occurring under multisine motion disturbance and under Gaussian and Patchy turbulence motion disturbances.
- Variance Accounted For VAF . This index is used to evaluate the performance of model-based BDFT mitigation, quantifying how much of the involuntary component of the input signal u^{BDFT} is modeled by the BDFT model. For the multisine case, in which $u^{BDFT} = u_{f_d}^{BDFT}$, the metric exploits the characteristic of the signal, in which disturbance components, control task components and remnant are clearly distinguishable:

$$VAF_M[\%] = \sum_{f_d''} \left(1 - \frac{Var(u_{f_d''}^{BDFT} - \hat{u}_{f_d''}^{BDFT})}{Var(u_{f_d''}^{BDFT})} \right) \times 100 \quad (8)$$

For the TSC vertical input recorded under Gaussian and Patchy turbulence, where it is not possible to separate the BDFT component of the input from the remnant, BDFT mitigation performance is evaluated on all frequencies except for the lateral and vertical target frequencies. To approximate and somewhat compensate for the contribution of the remnant, the TSC input recorded in static conditions at these frequencies u_f^{NM} is subtracted from the TSC input signal u_f recorded in Gaussian and Patchy conditions.

$$VAF_{G/P}[\%] = \sum_{f \neq f_{ly}, f_{tz}} \left(1 - \frac{Var(u_f - u_f^{NM} - \hat{u}_f^{BDFT})}{Var(u_f - u_f^{NM})} \right) \times 100 \quad (9)$$

For both versions of the metric, VAF is used to evaluate the identification performance, i.e., how much of the BDFT signal is accounted for by the model. $VAF = 100\%$ indicates a perfectly modeled signal, with decreasing modeling performance as the VAF decreases. Given the presence of remnant in the $VAF_{G/P}$ used for Gaussian and patchy conditions, this metric is to be interpreted more as an index of identification performance rather than as an explicit quantification of the amount of feedthrough modeled.

- Cancellation Index (CI). This metric is used to evaluate the performance of the SA and OSFA models for the cancellation of BDFT in the evaluation data set. As for the VAF, two versions of this metric are used, one applicable to BDFT with any type of motion disturbance, CI in Eq. (10), and one specific for BDFT due to a multisine motion disturbance, CI_M in Eq. (11).

$$CI[\%] = - \sum_{f \neq f_{ly}, f_{tz}} \left(1 - \frac{Var(u_f - u_f^{NM} - \hat{u}_f^{BDFT})}{Var(u_f - u_f^{NM})} \right) \times 100 \quad (10)$$

$$CI_M[\%] = - \sum_{f_d''} \left(1 - \frac{Var(u_{f_d''}^{BDFT} - \hat{u}_{f_d''}^{BDFT})}{Var(u_{f_d''}^{BDFT})} \right) \times 100 \quad (11)$$

For both, the BDFT component of the input signal is being fully canceled when $CI = -100\%$, with values lower in magnitude indicating a lower cancellation performance. A positive value for CI indicates that the BDFT mitigation applied is actually increasing the amount of input linearly related to the accelerations instead of decreasing it.

To be noted, $CI_M = -VAF_M$ and $CI = -VAF_{G/P}$. While calculated in the same manner as the performance of the identification of the model (VAF), the CI was defined as the negative of the VAF to highlight how much of the BDFT component of the input is being canceled, and to make a clear distinction between identification performance and cancellation performance.

- BDFT modeling error e . Defined as the absolute value of the difference between the BDFT component of the input recorded during the experiment and its modeled counterpart, this metric is used to show whether there is correspondence between a higher modeling error and peaks in the simulated accelerations caused by time-varying turbulence.

$$e = |u^{BDFT} - \hat{u}^{BDFT}| \quad (12)$$

Lower than expected performance in the identification of the BDFT models for the multisine motion disturbance conditions prompted the evaluation of additional variables, which were used to explain the findings. The metrics used are reported below:

- Run variability RV . This metric is used to show the presence of variability in the BDFT component of the TSC input u^{BDFT} across the repeated measurement runs of a specific participant. The variability is calculated using Eq. (13).

$$RV(i, j) [\%] = 100 - \sum \left(1 - \frac{Var(u^{BDFT}(i) - u^{BDFT}(j))}{Var(u^{BDFT}(i))} \right) \times 100 \quad (13)$$

The quantity RV is a three-by-three matrix, for each element of which the indices i and j indicate two of the four experimental runs, therefore $1 < i < 4$, $1 < j < 4$ and $i \neq j$. If the BDFT components in run i and in run j are exactly the same, $RV(i, j) = 0\%$. The metric RV is therefore used such that, when the BDFT components of two runs are consistent, the index is close to zero. On the other hand, when there is a lot of variability in the BDFT, the metric will output a high value. Two elements of the matrix will therefore be calculated for each two experimental runs, $RV(i, j)$ and $RV(j, i)$. The average of these two elements is used as the estimated variability across the two runs.

- Relative remnant ρ_u^2 . This metric is used to quantify the linearity of the BDFT dynamics in the multisine cases, estimating the contribution of the remnant to the power of the TSC input signal at the frequencies of the disturbance signal, $\tilde{S}_{uu,n}(j\omega_d)$, and relating it to the contribution of the BDFT component to the power of the same signal, $S_{uu}(j\omega_d)$.

$$\rho_u^2(j\omega_d) = 1 - \frac{\tilde{S}_{uu,n}(j\omega_d)}{S_{uu}(j\omega_d)} \quad (14)$$

The estimated remnant power at the frequencies of the disturbance signal $\tilde{S}_{uu,n}(j\omega_d)$ was calculated from the assumption of smooth variations in the power of the remnant across adjacent frequencies, as the average of the remnant power at frequencies in the neighbor of the disturbance frequencies. A value of ρ_u^2 close to zero indicates a non-linear response, in which the remnant dominates over the signal. On the other hand, $\rho_u^2 = 1$ indicates a perfectly linear dynamic, on which no remnant is present.

IV. Results

The results presented in this section are divided in five parts, connected to one of the hypotheses formulated before the start of the experiment. These relate to the identification of BDFT using the multisine, high intensity runs (M3 condition, Section IV.A, accompanied by Appendices D and E of Leto [23]), the identification accuracy and mitigation performance of a BDFT model at low and medium intensity (M1 and M2 conditions, Section IV.B, Appendices G and H), identification and mitigation of BDFT occurring with time invariant turbulence (G3 condition, Section IV.C, Appendices G and H) and the effect of variability on model-based BDFT mitigation (P3 condition, Section IV.D, Appendix H). In addition, results for the Gaussian and patchy conditions at lower intensities are discussed in Section IV.E, complemented with plots in Appendix I of Leto [23].

A. Biodynamic Feedthrough Identification at the Baseline High Intensity Multisine Condition

1. Comparison with previously collected data

Figure 8 shows performance of the identification of the BDFT model in the baseline M3 condition for each participant, for the dataset collected in the experiment discussed in this paper (21 participants) and for the dataset collected in

Khoshnewiszadeh and Pool's experiment (18 participants) [13]. In the left panel, the mean performance across runs for each participant is indicated with a thick line, while the shaded area shows the standard deviation. On the right panel, a boxplot condensing the information for the two datasets in a median and in the spread are shown. Identification performance is calculated through the Variance Accounted For (VAF) tailored to multisine signals, Eq. (8). Time domain identification and the personalized SA models are used for this comparison, allowing a later comparison between the M3 condition and the G3 and P3 conditions, for which identification can only be performed fitting the BDFT components of the input in the time domain.

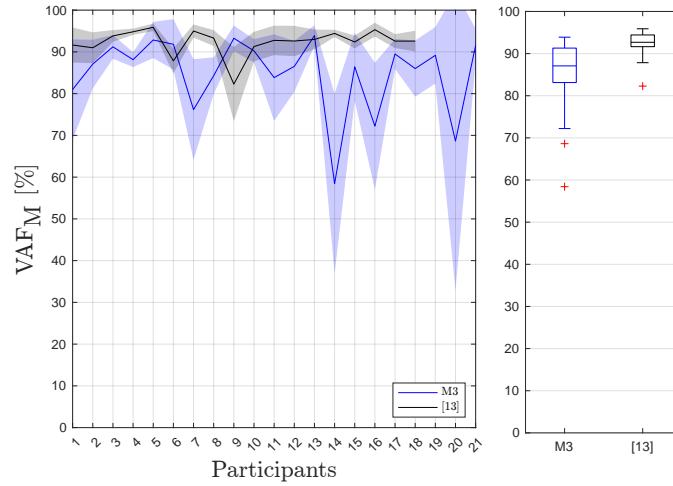


Fig. 8 Performance of the identification of BDFT (time domain approach, SA model).

Using the data of this experiment, 87.1% of the BDFT component of the input was modeled (median VAF across participants), which is 5.6% lower compared to Khoshnewiszadeh and Pool's dataset, for which this performance reaches 92.7%. The difference in identification performance was confirmed to be highly significant using a non-parametric Wilcoxon signed-rank test ($p < 0.01$). To infer the causes of the difference between the two datasets, the variability across the BDFT components of the TSC input recorded during the four identification runs was investigated. Figure 9 and Figure 10 show, for each participant of the M3 dataset of this experiment and of Khoshnewiszadeh and Pool's dataset, respectively, a boxplot of all the values generated with averaging Eq. (13) across each two runs. The higher the median, the less consistent the measurements obtained from the participant.

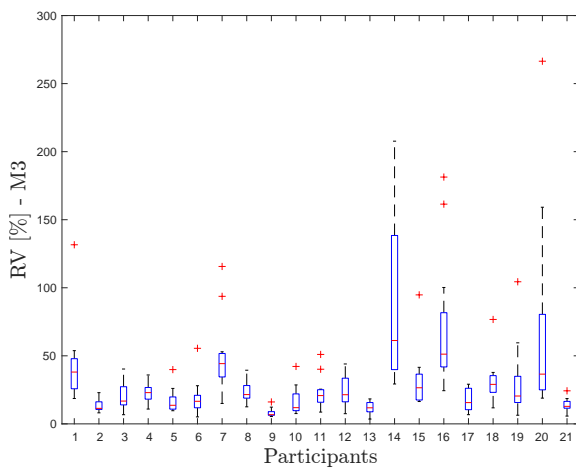


Fig. 9 Variability across measurement runs, M3 condition.

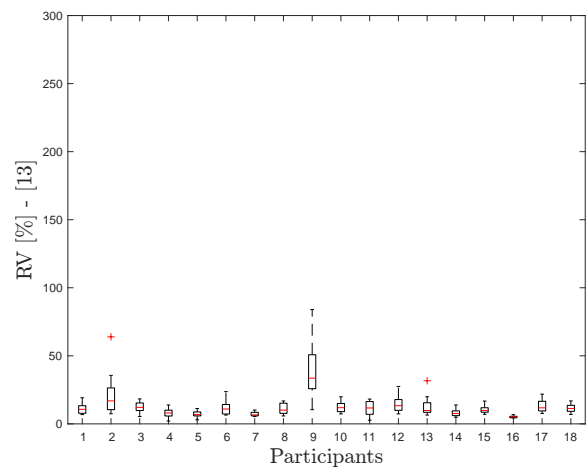


Fig. 10 Variability across measurement runs, Khoshnewiszadeh and Pool's data for M3 condition.

Comparing identification performance and variability for the M3 dataset, respectively, in Figure 8 and Figure 9,

it can be seen that participants with the lowest identification performance (participants 7, 14, 16, and 20, all with a median VAF_M below 80%) show inconsistent BDFT across runs, with a high median and spread. Although scaled in magnitude, this trend is also visible in Khoshnawisadeh and Pool's dataset, see participant 9 in Figure 10.

The increased BDFT variability in the M3 condition can be linked to the longer duration of this experiment compared to Khoshnawisadeh and Pool's. For reference, Khoshnawisadeh and Pool's identification dataset was collected from an experiment session totaling 16 runs (see Khoshnawisadeh and Pool [13]), in comparison to a total of 56 runs in the experiment performed for this research. Despite the multiple breaks outside the simulator, the majority of participants of this research verbally reported the experiment to be tiring and repetitive. Most likely, fatigue and boredom caused participants to be less consistent in performing the tracking task over the time-span of the experiment, for example changing their neuromuscular dynamics to minimize fatigue, therefore increasing the variability in the BDFT dynamics.

Another difference between the procedures of the two experiments is in the amount of different conditions presented to each participant. In Khoshnawisadeh and Pool's experiment, participants were exposed to the same multisine motion disturbance repeatedly along different axes (heave and sway), while participants in the current research were exposed to a total of 10 motion conditions, having different characteristics and different intensities. The exposure to different motion conditions lead participants of both experiment to adapt their neuromuscular dynamics at every new run to minimize the impact of the motion on their tracking performance, therefore affecting BDFT. The additional variability introduced in the motion conditions of this experiment is a likely cause of higher variability of the BDFT component of the TSC input.

2. Comparison of One-Size-Fits-All, Subject-Averaged and Individual-Run models

To some degree, fatigue, boredom and variability are all factor that will be present in turbulent flight conditions. It was therefore decided to investigate whether an identification algorithm tailored to each run (the IR model) can increase the identification performance, decoupling the identification of the model from the variability over time of the dynamics. The performance of the identification of the M3 data with the IR model is shown in Figure 11, in comparison to the one obtained using the SA models, and of that of a model averaging the BDFT dynamics across participants, the OSFA model already proposed by Khoshnawisadeh and Pool [13].

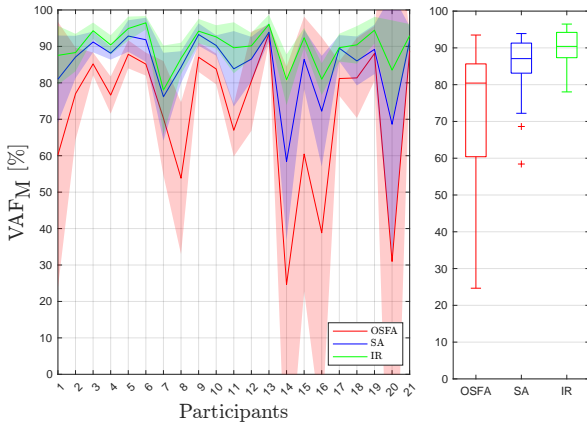


Fig. 11 Performance of the OSFA, SA and IR $H_{BDFT/M3}$ models for the identification of BDFT (time domain approach, VAF evaluated on multisine disturbance frequencies).

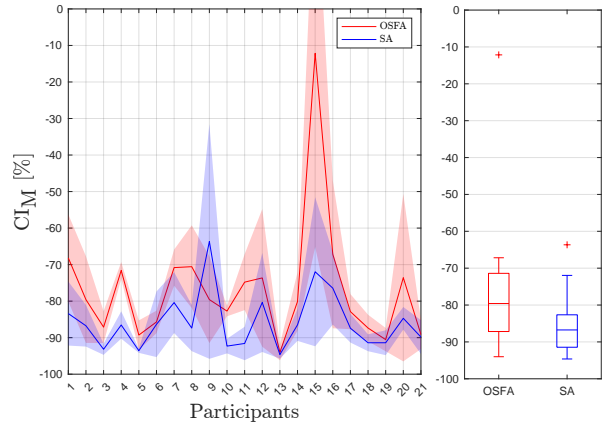


Fig. 12 Cancellation performance of OSFA and SA $H_{BDFT/M3}$ models on BDFT occurring in M3 condition (time domain approach, CI evaluated on multisine disturbance frequencies).

Clearly, the more the BDFT model is tailored to each specific data set, the better the identification performance. The OSFA model gives a median VAF_M of 80.4%, considerably lower when compared to the SA (87.1%) and IR (90.4%) models. A Friedman test confirmed these differences to be highly significant ($p < 0.01$). Post-hoc Wilcoxon signed-rank tests confirmed the significance of the difference across subsets ($p < 0.01$). To be noted, the largest improvement in identification performance with the IR model is visible for participants having low performance for the SA model, such as participants 14, 16 and 20, having the highest variability across runs as visible in Figure 9.

Figure 12 shows the cancellation performance achieved applying the OSFA and SA $H_{BDFT/M3}$ models on the

evaluation dataset, using the CI_M index defined in Eq. (11). Using the OSFA model on this dataset, up to 79.6% of the involuntary input is canceled, only 0.8% less compared to the performance of the model on the identification dataset. Similarly, with the SA model, a performance of (median) $CI_M = -86.8\%$ is achieved, differing from identification performance of only 0.3%, with one outlier. These results prove that the effects of the variability among participants are in general much larger than effects of variability across runs also when using BDFT models identified on separate runs. In fact, only for a single participant (participant 9) the variability in their BDFT dynamics was high enough to cause the OSFA model to perform better than the personalized SA model.

B. Performance of Biodynamic Feedthrough Mitigation at Different Intensities

Figure 13 and Figure 14 show the performance of the identification of the OSFA, SA, IR BDFT models for the M2 condition ($H_{BDFT/M2}(j\omega)$) and for the M1 condition ($H_{BDFT/M1}(j\omega)$), respectively.

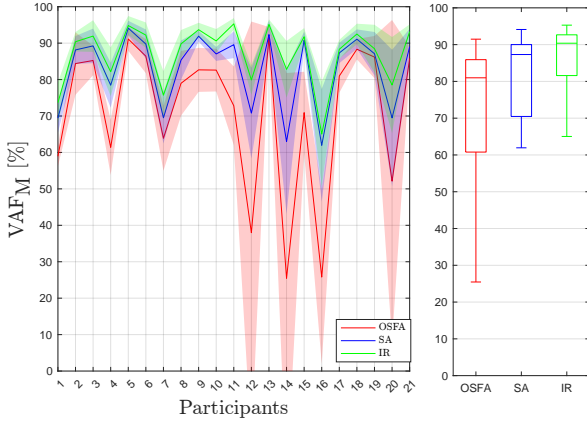


Fig. 13 Performance of the OSFA, SA and IR $H_{BDFT/M2}$ models for the identification of BDFT from the M2 data (time domain approach, VAF evaluated on multisine disturbance frequencies).

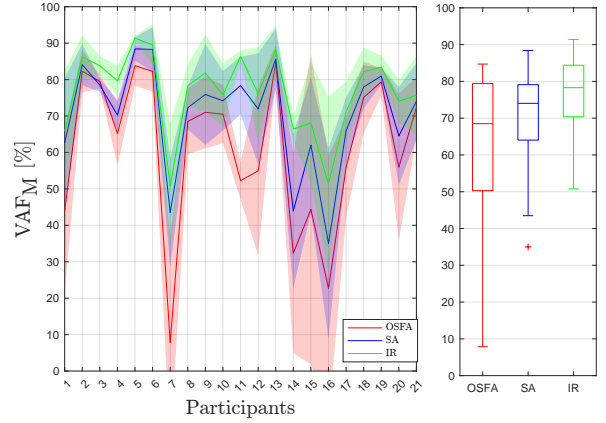


Fig. 14 Performance of the OSFA, SA and IR $H_{BDFT/M1}$ models for the identification of BDFT from the M1 data (time domain approach, VAF evaluated on multisine disturbance frequencies).

For the $H_{BDFT/M2}$ model performance appears to be comparable to the performance of $H_{BDFT/M3}$, presented in Figure 11 for all three model types, with OSFA modeling up to 81.0% of the BDFT component of the input (+0.6% compared to $H_{BDFT/M3}$), with SA 87.3% (+0.2%) and with IR models 90.4% (+0%). Differences in performance of the identification of the OSFA and SA $H_{BDFT/M2}$ and $H_{BDFT/M3}$ models were confirmed statistically insignificant with Wilcoxon signed-rank ($p \geq 0.05$). With the IR model, the Wilcoxon signed-rank reported significant differences ($0.01 \leq p < 0.05$), which are due to the larger spread across participants in the identification performance, see the green boxplots in Figure 11 and Figure 13.

The identification of $H_{BDFT/M1}$ gave considerably lower results compared to the identification of both $H_{BDFT/M2}$ and $H_{BDFT/M3}$: 68.5% with the OSFA model (-11.9% compared to $H_{BDFT/M3}$ and -12.5% compared to $H_{BDFT/M2}$), 74.0% with the SA model (-13.1% compared to $H_{BDFT/M3}$ and -13.3% compared to $H_{BDFT/M2}$) and 78.3% with the IR model (-12.1% compared to both $H_{BDFT/M3}$ and $H_{BDFT/M2}$). For all three OSFA, SA and IR models, differences in performance were shown to be highly significant (Wilcoxon signed-rank test, $p < 0.01$).

To understand the reasons behind the differences in identification performance, the reliability of the identification of the BDFT model at the motion intensities tested during the experiment was quantified as a function of frequency using the relative remnant ρ_u^2 in Eq. (14). Results of the analysis for the three intensity levels are shown in Figure 15, where the thin lines represent individual participants, and the thick lines their averages.

At high frequencies, ρ_u^2 is close to 1 for all three motion intensities, indicating that the contribution of the remnant is negligible, and that the dynamics are approximately linear. The relative remnant, however, decreases with decreasing frequency, more steeply for the progressively lower intensities: the non-linearities in the recorded input are larger at low frequencies and at low motion intensity. Most likely, the increasing non-linearities highlighted at the low frequencies are related to an increasingly lower signal-to-noise ratio (SNR): there is simply not much feedthrough occurring at low intensities, confirming that BDFT is a high-frequency phenomenon. This trend is more visible at the medium and low

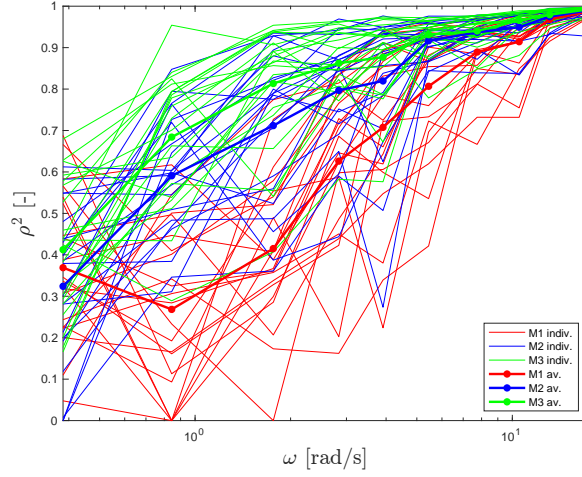


Fig. 15 Relative remnant across intensities, showing contribution of individual participants and their average.

motion intensities, hinting that the magnitude of the feedthrough occurring at those intensities is lower throughout the entire frequency range compared to the high motion intensity case.

To further verify this, the parameters of the BDFT models identified at the different intensities were compared. Figure 16 shows, for the three motion intensities tested, the median and spread of the parameters of the SA BDFT model across participants, as well as their averages (the OSFA model, displayed with diamond markers).

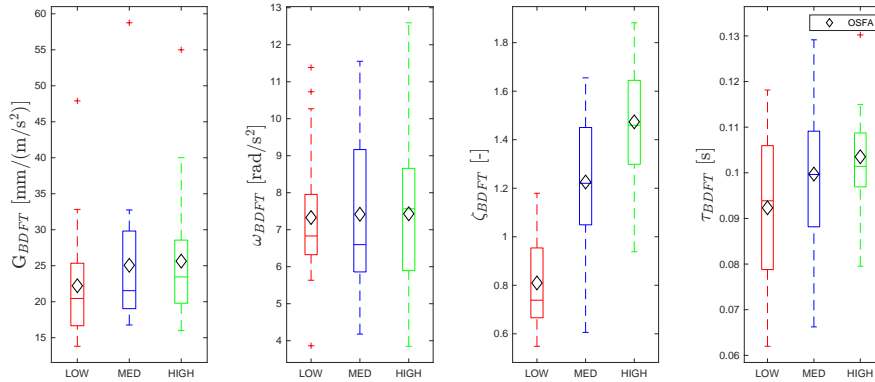


Fig. 16 Median and spread of the parameters of the $H_{BDFT/M}(j\omega)$ models across intensities (time domain approach, SA and OSFA models).

The first panel from the left of Figure 16 shows a small decrease in the median of the gain G_{BDFT} with decreasing intensity (in the M1 condition G_{BDFT} is 13% lower than in the M3 condition, in M2 8% lower than in M3), with the spread remaining roughly constant. Differences in median and spread of the break frequency ω_{BDFT} (second panel) are small and inconsistent (10% lower in M1 compared to M3, 13% lower in M2), hinting that no changes in neuromuscular stiffness occur across the three intensities tested. The damping ratio ζ_{BDFT} shown in the third panel of Figure 16 decreases with decreasing frequencies. The median values of ζ_{BDFT} found for M1 and M2 are, respectively, 49% and 16% lower than in M3. Also the time delay τ_{BDFT} (fourth panel) decreases with decreasing motion intensity, with a 7% and a 2% decrease compared to M3 in M1 and M2 cases, respectively. However, while for ζ_{BDFT} the spread is unchanged across intensities, a very clear decrease in spread is visible for the time delay τ_{BDFT} with increasing intensity. At low intensity the spread of the time delay is larger, likely because the low SNR causes the estimation of this parameter to be inaccurate. To further visualize these results, a Bode plot with the BDFT estimates across intensities is shown in Figure 17 together with the frequency responses of the BDFT models identified for individual participants, grouped per intensity by color.

Figure 17 shows no clear differences in the gain, break frequency and in the time delay constants across intensities,

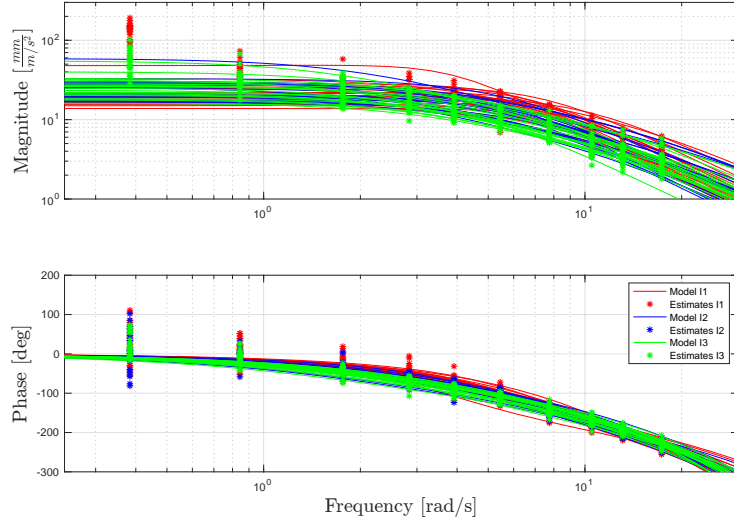


Fig. 17 BDFT estimates and frequency response of the BDFT models (time domain approach, SA model) of individual participants across intensities.

confirming the finding in Figure 16. Differences in the damping ratio are instead very visible, especially in the phase shift. In fact, the phase shift increases with increasing intensity over the frequency range characterizing the damping of the response, suggesting that it will not be possible to use a single model for mitigation of BDFT across intensities. To confirm these findings, the performance of the cancellation of BDFT occurring at the low and medium intensities was evaluated with the model identified from the high intensity accelerations, and compared to the performance of BDFT models identified from low and medium intensity data. Figure 18 shows the cancellation performance (calculated using the multisine specific CI_M in Eq. (11)) of the SA BDFT model identified at the high motion intensity $H_{BDFT/M3}(j\omega)$ and of the SA BDFT model identified at the medium motion intensity $H_{BDFT/M2}(j\omega)$, on the M2 data. Similarly, Figure 19 compares cancellation performance on the M1 data of the high intensity and the low intensity SA models, $H_{BDFT/M3}(j\omega)$ and $H_{BDFT/M1}(j\omega)$ respectively.

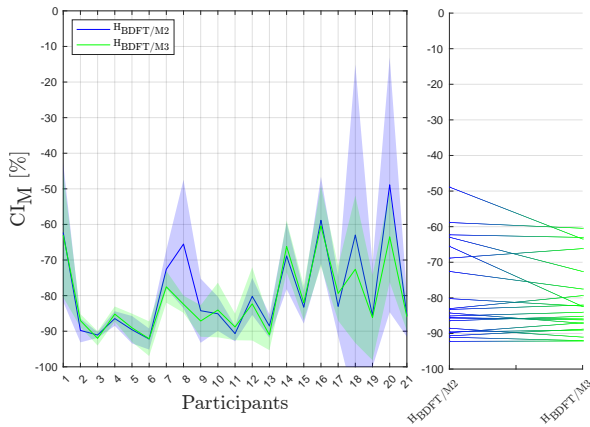


Fig. 18 Cancellation performance of models $H_{BDFT/M3}$ and $H_{BDFT/M2}$ on BDFT occurring in condition M2 (time domain approach, SA model).

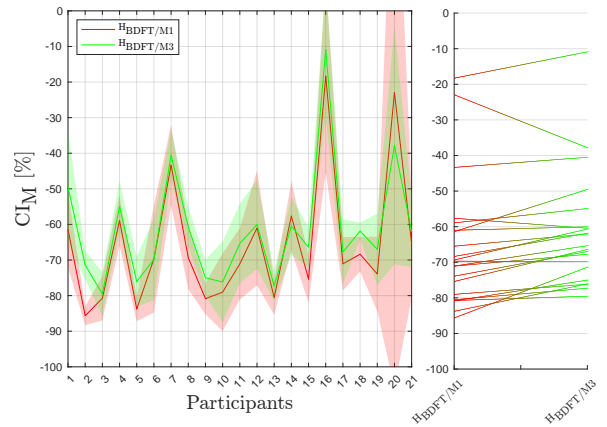


Fig. 19 Cancellation performance of models $H_{BDFT/M3}$ and $H_{BDFT/M1}$ on BDFT occurring in condition M1 (time domain approach, SA model).

From Figure 18 is it immediately visible that the two models have roughly the same performance. For the model $H_{BDFT/M2}(j\omega)$, a median of -84.2% of the BDFT component of the input is canceled across participants, while using the $H_{BDFT/M3}(j\omega)$ model, the median cancellation index is -84.0%. The difference was confirmed to be not significant through a Wilcoxon signed-rank test, $p \geq 0.05$, leading to the conclusion that the model identified at the high intensity

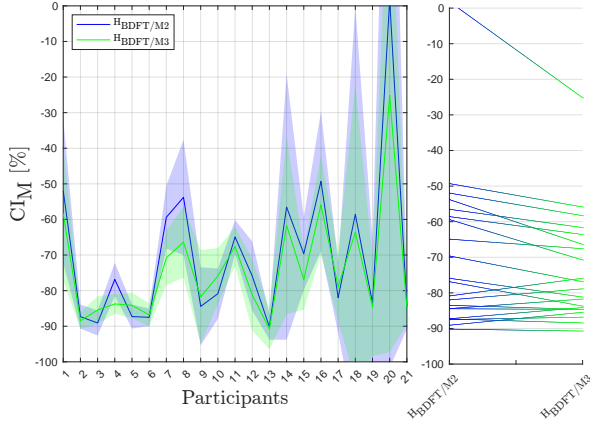


Fig. 20 Cancellation performance of models $H_{BDFT/M2}$ and $H_{BDFT/M3}$ on BDFT occurring in condition M2 (time domain approach, OSFA model).

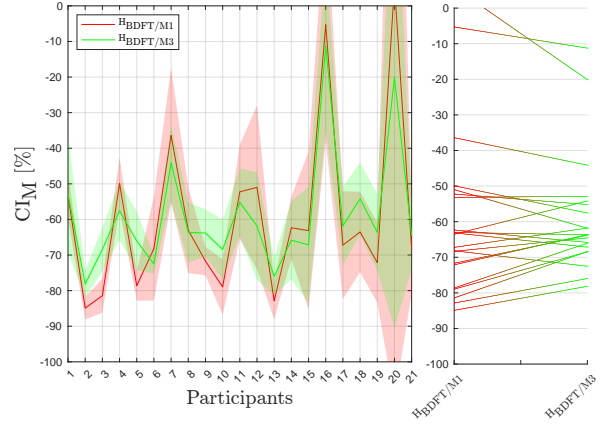


Fig. 21 Cancellation performance of models $H_{BDFT/M3}$ and $H_{BDFT/M1}$ on BDFT occurring in condition M1 (time domain approach, OSFA model).

case can be used for cancellation of BDFT at the medium intensity case. With the low intensity model $H_{BDFT/M1}(j\omega)$ a median CI_M of -69.7% is reached, with $H_{BDFT/M3}(j\omega)$ median CI_M = -65.4%. The difference between the two models is proven highly significant ($p < 0.01$), suggesting that the high intensity model $H_{BDFT/M3}(j\omega)$ is not adequate to be used in BDFT mitigation at the low intensity case. In addition, performance of the $H_{BDFT/M3}(j\omega)$ model on the M3 data (-86.8%, see Figure 12), of $H_{BDFT/M2}(j\omega)$ model on the M2 data (-84.2%) and of $H_{BDFT/M1}(j\omega)$ on the M1 data (-69.7%) were compared using Friedman's test and with post-hoc Wilcoxon signed-rank tests. These proved a statistically significant difference between the first two ($H_{BDFT/M3}(j\omega)$ on M3 data and $H_{BDFT/M2}(j\omega)$ on M2, $0.01 \leq p < 0.05$), and a highly significant difference for all other combinations ($p < 0.01$), confirming that with lower intensities, identification of the BDFT model is less accurate, as already showed by the analysis of the relative remnant.

The same analysis was conducted using the OSFA model, to assess its capabilities with regards to the different intensities. Similarly to the two earlier figures, Figure 20 show the cancellation performance of the OSFA models identified at medium and at high intensities ($H_{BDFT/M2}(j\omega)$ and $H_{BDFT/M3}(j\omega)$) on the M2 data. Figure 21 shows the same for the M1 data, with the OSFA models $H_{BDFT/M1}(j\omega)$ and $H_{BDFT/M3}(j\omega)$.

Compared to the SA models, performance of the cancellation of BDFT occurring at medium intensities with OSFA models decreased, as visible in Figure 20: using $H_{BDFT/M2}(j\omega)$, the median value of CI_M indicates that -76.9% of BDFT is canceled, -78.9% using $H_{BDFT/M3}(j\omega)$. The higher performance of the high intensity model $H_{BDFT/M3}(j\omega)$ is proven significant by statistical tests (Wilcoxon signed-rank test, $0.01 \leq p < 0.05$). For the low intensity case in Figure 21, performance using the $H_{BDFT/M1}(j\omega)$ OSFA achieved -63.5% of BDFT canceled, while using the $H_{BDFT/M3}(j\omega)$ OSFA model -63.7% (difference not significant, Wilcoxon signed-rank test, $p \geq 0.05$). Therefore, for both cases, the OSFA model identified at higher intensity performs better or equally compared to the model tailored to the specific intensity. The fact that the OSFA $H_{BDFT/M3}(j\omega)$ can be used at both lower intensities tested, including in the low intensity case for which the high intensity SA model was significantly outperformed by the low intensity one, is a symptom of the loss of identification power of the OSFA models, which is due to the averaging of the BDFT dynamics across all participants. A few outliers are clearly visible from the right panels of Figure 20 for the M2 case and of Figure 21 for the M1 case, corresponding to participants 16 (only for M1) and 20, showing low performance in terms of the cancellation index. While these outliers likely had very different BDFT dynamics compared to the majority of participants, conclusions drawn from the use of the high intensity OSFA model on BDFT occurring at medium and low intensity disturbance still hold, as performance of BDFT mitigation for these participants considerably increases with the use of the high intensity BDFT model $H_{BDFT/M3}(j\omega)$, as visible from the down-sloping lines in Figure 20 and Figure 21.

Lastly, comparing with Friedman's test and with post-hoc Wilcoxon signed-rank tests the performance of the OSFA model $H_{BDFT/M3}(j\omega)$ on the M3 data (median CI_M = -79.6% from Figure 12), $H_{BDFT/M2}(j\omega)$ on the M2 data (-76.9%) and $H_{BDFT/M1}(j\omega)$ on the M1 data (-63.5%), it was shown that the difference between the first two is not significant ($p \geq 0.05$) while for the rest it is highly significant ($p < 0.01$). This further confirms the impact of the increasing inaccuracies in BDFT identification, as already found using the SA model. In addition, it again shows that

the OSFA model reduces the performance differences between the datasets especially at high mitigation performance.

C. Biodynamic Feedthrough Mitigation in Gaussian Turbulence

To evaluate whether model-based BDFT identification is effective in turbulent flight, the parametric BDFT model was also fitted to an estimate of the BDFT component in the TSC input recorded at the high intensity Gaussian condition (G3). This estimate of BDFT was obtained by removing from the Fourier transform of the vertical TSC input the frequencies belonging to the vertical and horizontal components of the control task, constituting the direct and cross-coupling effects of the voluntary input. The time domain identification algorithm described in Section II.C.2 was used to fit the model, keeping in mind that with motion disturbance other than multisine signals, BDFT cannot be separated from the remnant, as they both contribute to the power of the signal in the entire frequency spectrum. To prevent noise from affecting the estimation of the time delay, τ_{BDFT} was fixed to the values obtained through the identification of the SA BDFT model with the multisine signal for the SA and IR models, and of the OSFA BDFT model for the OSFA case. Parameters found with τ_{BDFT} being a free variable of the $H_{BDFT/G3}$ model can be found in Appendix F of Leto [23]. The performance of the identification of the $H_{BDFT/G3}$ model was evaluated using the equation for the model $VAF_{G/P}$ in Eq. (9), and is shown in Figure 22 for the OSFA, SA and IR models.

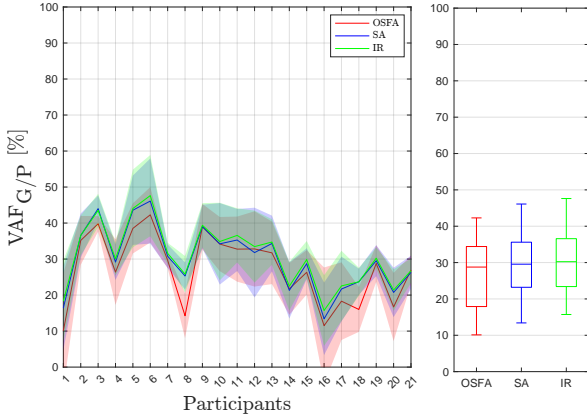


Fig. 22 Performance of the OSFA, SA and IR $H_{BDFT/G3}$ models for the identification of BDFT from the G3 data (time domain approach, VAF evaluated on the full frequency spectrum).

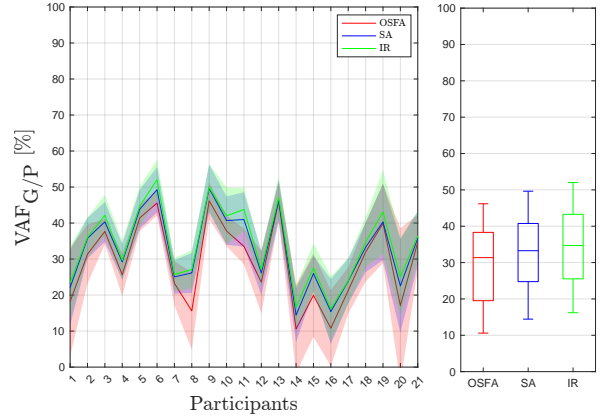


Fig. 23 Performance of the OSFA, SA and IR $H_{BDFT/M3}$ models for the identification of BDFT from the M3 data (time domain approach, VAF evaluated on the full frequency spectrum).

As already seen for the identification of the BDFT occurring with multisine disturbances, the more the model is tailored to the data, the better the performance. With the OSFA model, a performance of 28.8% is reached (median $VAf_{G/P}$), a number which increases to 29.6% for the SA model and to 30.2% for the IR model. The differences in identification performance across the models were proven highly significant with a Friedman's test and with post-hoc Wilcoxon signed-rank tests ($p < 0.01$).

To infer whether the accuracy of the identification of the Gaussian model $H_{BDFT/G3}$ is comparable to the identification of the $H_{BDFT/M3}$ model for the multisine signal, the performance of the $H_{BDFT/M3}$ model is shown in Figure 23 using the generic $VAf_{G/P}$ in Eq. (9), evaluating performance over the entire frequency spectrum instead of only at the disturbance frequencies as done by the multisine tailored VAf_M in Eq. (8), previously shown in Figure 11. With the OSFA model identified for the multisine motion disturbance, the generic $VAf_{G/P}$ index indicates only 31.4% performance, 49% less than indicated by the more accurate multisine specific VAf_M in Eq. (8). Similarly, with the SA model a performance of 33.3% is noted (53.8% less than measured with the multisine specific VAf_M), 34.7% with the IR model (55.7% less). These numbers suggest that there is a -50% bias in the performance measured using the generic $VAf_{G/P}$ index, increasing with increasing accuracy of the models. This bias is caused by the contribution of the remnant over the frequency spectrum. Recalling the definition of the generic $VAf_{G/P}$ in Eq. (9), this contribution was estimated using the TSC inputs recorded in the NM condition. This estimate can never be fully accurate, as the realization of the TSC input signal is never the same across repeated runs. In conclusion, accounting for this bias, BDFT modeling with the G3 conditions achieves a performance comparable to the multisine cases when using the OSFA and SA models (Wilcoxon signed-rank tests, $p \geq 0.05$: differences not significant). Only with the IR model, the model

identification is significantly less accurate for the Gaussian turbulence BDFT (Wilcoxon signed-rank tests, $0.01 \leq p < 0.05$).

The differences in the BDFT dynamics of the M3 and G3 conditions were evaluated using the median and spread across participants of the parameters of the $H_{BDFT/M3}$ and $H_{BDFT/G3}$ models, shown with a boxplot in Figure 24.

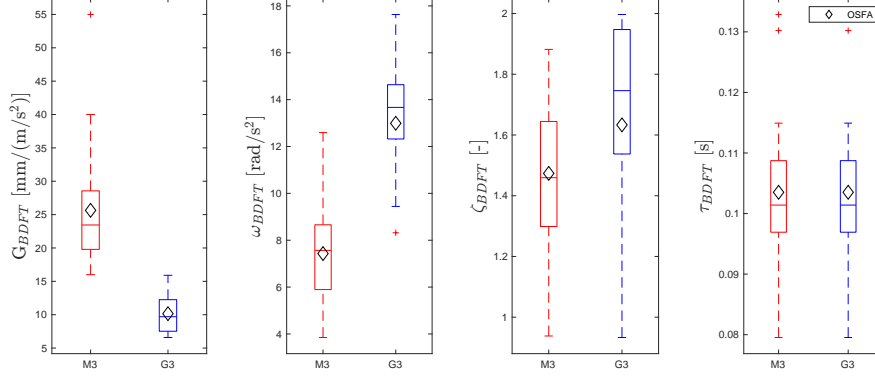


Fig. 24 Median and spread of the parameters of the model identified from high intensity Gaussian BDFT data $H_{BDFT/G3}$ and from high intensity multisine BDFT data $H_{BDFT/M3}$ (time domain approach, SA and OSFA model). The time delay τ_{BDFT} for model $H_{BDFT/G3}$ is fixed to the values found for model $H_{BDFT/M3}$.

Compared to the multisine condition, the Gaussian condition shows 59% lower feedthrough (indicated by the gain G_{BDFT}) with 81% higher damping (ζ_{BDFT}) and a 20% higher neuromuscular stiffness, as clear from the break frequency ω_{BDFT} . It should be recalled that time delay τ_{BDFT} for model $H_{BDFT/G3}$ is assumed to be equal to the values of τ_{BDFT} found for model $H_{BDFT/M3}$, to prevent the remnant from influencing the fit.

Finally, the capability of the SA models for the cancellation of BDFT from the TSC input signal on the G3 condition were evaluated through a comparison of the performance obtained with the model identified from the G3 data $H_{BDFT/G3}(j\omega)$ (Figure 25) and the one obtained with the model identified from the multisine data, $H_{BDFT/M3}(j\omega)$, shown in Figure 26. For comparison, Figure 26 also shows the cancellation performance of model $H_{BDFT/M3}(j\omega)$ for the M3 dataset, calculated using the CI on the entire frequency spectrum, Eq. (10). Both figures report performance of the two models in canceling BDFT with the high intensity patchy condition P3 (the green data), which however will only be discussed in Section IV.D. Unlike previous cancellation performance figures, the axis limits in these plots show both the negative CI (the BDFT component of the input signal being canceled) and the positive CI (disturbance related contributions are increasing rather than being canceled).

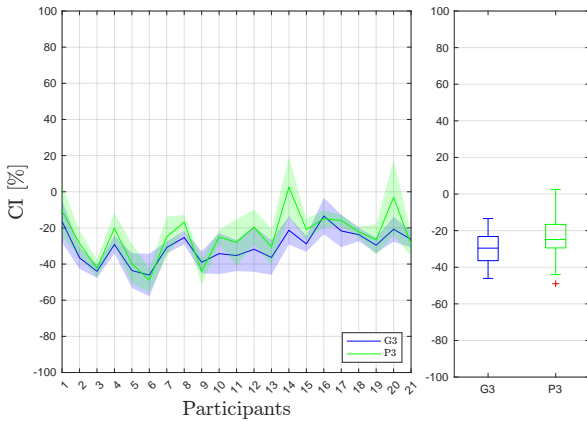


Fig. 25 Cancellation performance of model $H_{BDFT/G3}$ on BDFT occurring in G3 and P3 conditions (time domain approach, SA model, CI evaluated on the full frequency spectrum).

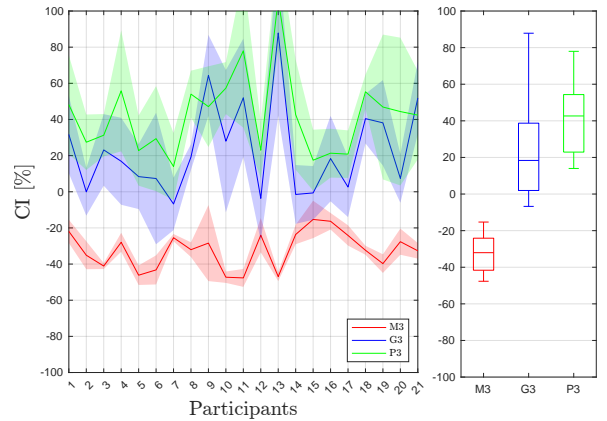


Fig. 26 Cancellation performance of model $H_{BDFT/M3}$ on BDFT occurring in M3, G3 and P3 conditions (time domain approach, SA model, CI evaluated on the full frequency spectrum).

One note should be made on the Gaussian identification. For this experiment, only one dataset of four runs was collected with the G3 condition, to make space for the identification at lower intensities. Therefore, the cancellation performance shown in Figure 25 is biased towards a higher performance (a lower value of CI) when compared to the data shown in Figure 26, where identification and evaluation are performed on separate runs. A decrease in performance can be expected from the use of a dedicated cancellation dataset, comparably to the loss in performance noted from the multisine datasets.

On the G3 data, the $H_{BDFT/G3}(j\omega)$ models have a cancellation performance of -29.6% (median CI), greatly outperforming $H_{BDFT/M3}(j\omega)$ which effectively adds to the TSC input components linearly related to the disturbance rather than canceling them (median $CI = 18.4\%$). As with the model identification performance, these results can only be compared to the multisine performance results when using the same performance index. For the M3 case, the median CI of the BDFT cancellation performance is -32.0%, only 2.5% better than Gaussian cancellation with the $H_{BDFT/G3}(j\omega)$ models, a difference proved to be non significant with a Wilcoxon signed-rank test $p \geq 0.05$. In conclusion, model-based BDFT mitigation works almost as well in stationary turbulence as in experimental conditions such as with a multisine motion disturbance. Since the dynamics of BDFT are different for the two cases, identification of a BDFT model in stationary turbulent conditions is required.

D. Biodynamic Feedthrough Mitigation in Patchy Turbulence

The effect of turbulence variability on performance of model-based BDFT mitigation was researched with the patchy turbulence condition P3. In particular, this research set out to quantify how much the variability in the disturbance input would affect performance of the time-invariant model identified from time-invariant turbulence, the Gaussian turbulence. In order to do so, the cancellation performance of the patchy turbulence is shown in Figures 25 and 26, respectively, for the $H_{BDFT/G3}(j\omega)$ and $H_{BDFT/M3}(j\omega)$ SA models. While the model identified from the multisine motion disturbance data fails to cancel BDFT (median $CI = 42.7\%$, therefore increasing BDFT as already seen with the cancellation in Gaussian turbulence in Figure 26), the model identified from the Gaussian turbulence data effectively cancels BDFT with a performance of $CI = -24.8\%$, which is 4.7% lower compared to the performance of this model in non-varying Gaussian turbulence, and 7.2% lower compared to cancellation of BDFT in the multisine motion disturbance. These differences were shown to be highly significant with Friedman's test and post-hoc Wilcoxon signed-rank tests ($p < 0.01$).

To infer the causes of these differences, the modeling error was calculated for the G3 and P3 cases using Eq. (12). The average of the modeling error, calculated across the experimental runs for the two conditions and across participants, is plotted as a function of time in Figure 27 for a interval of 40 seconds, below the corresponding disturbance signals. The patchy motion disturbance (top panel of Figure 27) shows peaks with high accelerations (for example at 3, 10, 20

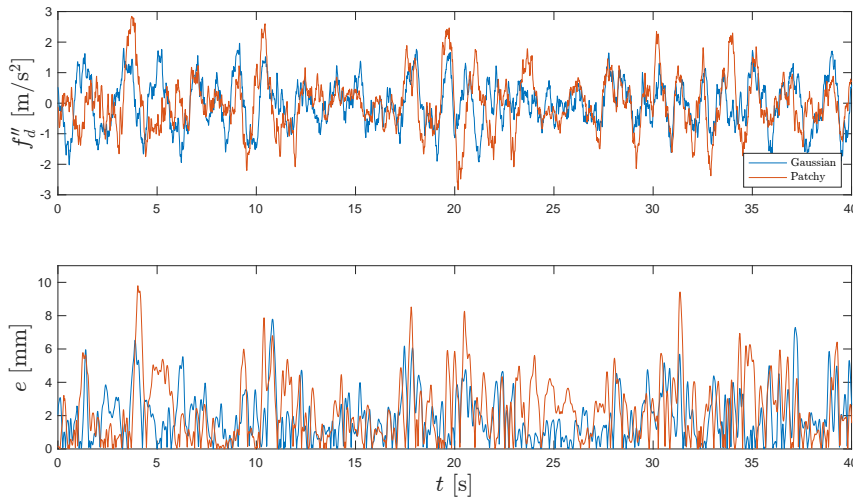


Fig. 27 Comparison between Gaussian and patchy motion disturbances and the absolute value of the error between measured and modeled BDFT component of the TSC input for the two disturbances, averaged across participants (time domain approach, SA model, $H_{BDFT/G3}$).

seconds) with higher magnitude and more frequently than peaks visible in the Gaussian motion disturbance. From the

bottom panel of Figure 27, it can be seen that the modeling error is indeed higher in correspondence to these peaks, especially when accelerations are steep (for example at 3 and 20 seconds). Given these findings, it was concluded that the variability present in the patchy turbulence is a primary cause for the small, yet significant difference in BDFT cancellation performance between the Gaussian and patchy turbulence cases. It should be noted, however, that mitigation performance for the Gaussian case is being evaluated directly on the identification dataset, in contrast to the patchy turbulence being a separate evaluation dataset, and that this could affect the magnitude of the difference in cancellation performance between the two case. In conclusion, models identified from Gaussian turbulence can be used for the mitigation of BDFT in both Gaussian and patchy conditions with minimal loss in performance for the latter, caused by the time-varying characteristics of the patchy turbulence.

E. Biodynamic Feedthrough Mitigation in Gaussian and Patchy Turbulence at Low and Medium Intensities

Analysis of the BDFT component of the input collected at G2, G1, P2, and P1 conditions confirmed the findings discussed in previous sections. The models identified from multisine motion disturbances ($H_{BDFT/M1}(j\omega)$ and $H_{BDFT/M2}(j\omega)$) are outperformed by models identified in Gaussian turbulence for all IR, SA and OSFA models, $H_{BDFT/G1}(j\omega)$ and $H_{BDFT/G2}(j\omega)$, which achieve effective cancellation performance. As found identifying the model at the different intensities for the multisine in Section IV.B, when intensity decreases identification becomes less accurate (on average, in comparison to $H_{BDFT/G3}(j\omega)$, a performance decrease of -5.8% is seen for $H_{BDFT/G2}(j\omega)$, -12.5% for $H_{BDFT/G1}(j\omega)$). Consequently, cancellation performance also decreases with decreasing intensity. In fact, the median value of CI is on average -21.6% for the medium intensity and -14.2% for the low intensity, with cancellation of Gaussian BDFT outperforming cancellation of patchy BDFT by 3.3% and 4.7%, respectively for medium and low intensity, suggesting that variability still plays a role on BDFT mitigation. Figure 28 gives the median and spread of the parameters of the Gaussian BDFT models across intensities. As done for the identification of $H_{BDFT/G3}(j\omega)$, for $H_{BDFT/G2}(j\omega)$ and $H_{BDFT/G1}(j\omega)$ the time delay τ_{BDFT} was fixed to the corresponding multisine identified values.

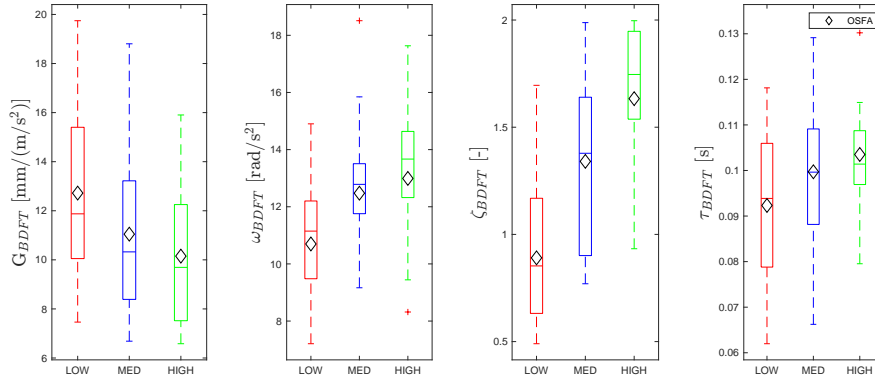


Fig. 28 Median and spread of the parameters of the $H_{BDFT/G}(j\omega)$ models across intensities (time domain approach, SA and OSFA models).

Compared to the trends seen in the parameters of the multisine models $H_{BDFT/M3}(j\omega)$, $H_{BDFT/M2}(j\omega)$ and $H_{BDFT/M1}(j\omega)$ in Figure 16, differences are seen in the gains G_{BDFT} and break frequencies ω_{BDFT} across intensities. In particular, as intensity decreases the values of the gain increase and those of the break frequency decrease. On average, a 51% lower gain and a 79% higher break frequency are seen in Gaussian models $H_{BDFT/G}(j\omega)$ compared to multisine models $H_{BDFT/M}(j\omega)$. These findings confirm that differences between multisine and Gaussian motion disturbance remain not negligible at medium and low intensity for the implementation of BDFT mitigation.

V. Discussion

In this paper, a human-in-the-loop simulator experiment was used to evaluate the effect of turbulence variability and intensity on biodynamic feedthrough (BDFT) occurring with touchscreen (TSC) dragging tasks, with the ultimate objective to enable the use of TSC interfaces for safety critical task in aircraft cockpits. The study, performed on the SIMONA Research Simulator (SRS) of the Faculty of Aerospace Engineering of TU Delft, involved 21 participants performing a tracking task on a TSC placed directly in front of them, in a total of 9 motion conditions along the heave

axis of the simulator, and in a static condition. Three types of motion disturbance were tested: a multisine disturbance resembling aircraft accelerations caused by turbulence, and two simulated realistic turbulent conditions, differing in their variability (invariant perceived Gaussian turbulence and variable patchy turbulence). All these conditions were tested at three levels of motion intensity.

Unlike hypothesized (**H1**), significantly less than 90% of the BDFT component of the input was modeled by participant personalized BDFT models at the high intensity multisine condition. The current experiment achieved a 5.6% lower identification performance compared to the experiment described by Khoshnewisadeh and Pool [13], despite the use of the same forcing function and same experimental set-up. Hence, Hypothesis 1 is rejected. A link was found between identification performance and variability in BDFT measured across experimental runs, with low performance linked to high variability. Three factors were proposed that might have led to the increased variability seen in participants of this research compared to Khoshnewisadeh and Pool's: fatigue and boredom, due to the longer duration of the experiment, as well as the increased amount of conditions to which participants were exposed. In addition, it was shown that models identified from single experiment runs (Individual-Run models, IR) achieve an improved performance in BDFT modeling than models averaging a participant's BDFT dynamics throughout runs (Subject-Averaged models, SA), which in turn outperform models generalizing BDFT dynamics across participants (One-Size-Fits-All models, OSFA). Specifically, the IR model achieves 3.3% higher performance than the SA model and 10% higher performance than the OSFA for the high intensity multisine case. While all models perform sufficiently well to allow for their use in BDFT mitigation (over 70% identification performance, as discussed by Mobertz et al. [14]), these findings confirm what was already hinted in Khoshnewisadeh and Pool's research [13], that highly tailored models are preferable to achieve the most effective BDFT mitigation.

With **H2**, it was hypothesized that high motion intensity BDFT would be larger in magnitude compared to medium and low motion intensity, and that therefore high intensity BDFT models would not be suitable for mitigation at medium and low intensity. This part of the hypothesis was evaluated using only the multisine motion disturbance. A second statement hypothesized that the success of model-based BDFT mitigation would be independent of the motion intensity if applied using a model identified for the same motion intensity at which cancellation is being employed. In relation to the first part of **H2**, the generalizability of a BDFT model across intensities was evaluated on the multisine data using both SA and OSFA models. Using the SA model, it was shown that the M3 and M2 models performs comparably when applied on the M2 data, canceling over 84% of the BDFT component of the input. However, when applied on M1 data, the M3 model gives a 4.3% lower performance compared to the M1 model. This is due to a 49% decrease in damping ratio visible in the identification of the M1 data compared to the M3 data. Using the OSFA models, the model identified from M3 data was shown to perform comparably for cancellation on M2 and M1 data, although achieving on average 6.5% lower performance compared to the SA models. The first statement in **H2** is therefore partially disproven, as no SA models can be generalized across intensities, while OSFA models can be, at the cost of accuracy.

In regards to the second statement of **H2**, it was shown that performance of the model-based BDFT mitigation is influenced by the intensity of the accelerations causing BDFT, disproving this part of the hypothesis. In particular mitigation at lower intensities was shown to achieve a lower performance compared to mitigation at higher intensities (canceling 86.8%, 84.2% and 69.7% of the BDFT component of the input for M3, M2 and M1, respectively). The reason for this was found through an analysis of the non-linearities in the TSC input at the frequencies of the disturbance signal. Increasingly higher non-linearities were found in the signals registered from medium and low motion intensity, especially at low frequencies, symptoms of an increasingly lower signal-to-noise ratio due to a lower amount of feedthrough present in the TSC input. The decrease in mitigation performance with decreasing intensity was further confirmed with the BDFT occurring at Gaussian and patchy turbulence, using models identified from the Gaussian experimental conditions.

The study of the dynamics of BDFT in Gaussian turbulence revealed considerable differences with the dynamics of BDFT occurring in multisine motion disturbances (heave disturbances, at fixed, high intensity). Disproving the first statement of **H3**, which postulated more compliant neuromuscular dynamics in Gaussian turbulence, an increase in stiffness and damping was noted, as well as a decrease in the magnitude of BDFT, also confirmed at medium and low intensities. The first part of **H3** is therefore rejected. It follows that the BDFT model identified from the multisine signal was unable to mitigate BDFT occurring in realistic Gaussian turbulence. Using a time domain estimator to identify the model directly from BDFT recorded from the Gaussian high intensity turbulence, SA models were shown to still effectively cancel BDFT, with comparable performance to mitigation in the multisine motion disturbance case.

Evaluating a cancellation index over the full frequency spectrum, a performance of 29.6% was achieved by SA models in Gaussian conditions in comparison to 32.0% for the multisine case. It should, however, be noted that the evaluation of the performance for the Gaussian case is subject to a bias leading to higher evaluation performance, due to the lack of two separate datasets for identification of the model and evaluation of the BDFT performance. With

this, the second part of **H3**, hypothesizing that model-based BDFT mitigation in realistic turbulence conditions would be effective adapting the model parameters, is accepted. Similar conclusions were drawn from the medium and low turbulence intensity BDFT data.

Finally, **H4** postulated that cancellation with patchy turbulence would have lower performance and that the cause would be the variability of the characteristics of turbulence over time. It was found that the model identified in the high intensity Gaussian turbulence condition is in fact able to effectively cancel BDFT, although with a 4.7% lower performance compared to the Gaussian case. Comparison of the timing of peaks in the BDFT modeling error with the occurrence of steep accelerations in the P3 condition suggested that the time-varying dynamics are indeed a cause for the lower performance. Similarly using the medium and low intensity data, Gaussian models were shown to effectively cancel BDFT in patchy turbulence, although with lower performance compared to the cancellation of BDFT in Gaussian turbulence. **H4** is therefore accepted.

To conclude this discussion, a few comments are left for future work. From the results of this experiment, several factors causing changes in the dynamics of BDFT were highlighted. Among these, fatigue, engagement in control tasks and turbulence intensity. Especially across turbulence intensities, considerable variations in gain, break frequency and damping ratio were observed. As a consequence, no generalized model achieves a consistently high performance in mitigating BDFT in the control inputs. Instead, individual run models were shown to consistently achieve higher performance for all types of motion tested, from the purely experimental multisine condition to realistic turbulence, and at different intensities as long as enough feedthrough is occurring, leading to conclude that real-time adaptation of the parameters of the BDFT model may be needed. This would require time-varying estimation methods and time-varying BDFT models, using techniques such as the dual extended Kalman filter method [29] or recursive autoregressive exogenous model structures identified in real-time [30, 31]. Findings highlighting a connection between turbulence variability and increased BDFT modeling error for the variable turbulence case also suggest that time-varying BDFT models and estimation techniques would outperform the currently used time-invariant methods. Future works should replicate the experiment to explicitly quantify how much can be gained in terms of mitigation performance with time-varying methods.

Concurrently, in view of future use of time-varying estimation methods, the amount of parameters to update in each iteration should be minimized [30]. In this optic, a note can be made from the results on BDFT modeling across acceleration intensities. It was showed that accuracy of the models decreased with decreasing intensity, and that this caused additional spread in the identification of the time delay. As fixing this parameters could greatly benefit the computational time for the real-time estimation of the parameters, the accuracy of BDFT modeling assuming this parameter to be time-invariant should be tested in a dedicated experiment. For example, an experiment in which the intensity of the motion disturbance is varied in time could allow to test real-time estimation of the parameters of the BDFT both fixing time delay, and updating it at each iteration.

In regards to the BDFT model used in this study, an additional note can be made. The selection of an underdamped second-order model instead of an overdamped equivalent was motivated by the fact that, in case of overdamped BDFT dynamics, the accuracy using an overdamped model would mainly increase in the modeling of high frequency components, and that the multisine motion disturbance only had a limited bandwidth. In addition, using the underdamped model would allow for a direct comparison with the results of previous works on BDFT mitigation in multisine motion disturbances (Khoshnewiszadeh and Pool [13], for which underdamped BDFT dynamics where found, see Appendix D of Leto [23]), and for comparison across motion intensities, which show damped BDFT dynamics. When limiting the analysis to the high intensity motion disturbances, however, overdamped BDFT dynamics were found for the majority of the data, with only one participant out of 21 showing underdamped dynamics for the multisine condition, two for Gaussian disturbance. In the turbulence motion disturbance, BDFT occurs at frequencies at which the use of the overdamped model might make a difference on model identification performance, as high-frequency components are present in the disturbance signal. In addition, the disturbance tested in this study was filtered with a low-pass motion filter, used to simulate the aircraft vertical accelerations on a moving-base simulator, leading to the assumption that in real flight these considerations on BDFT at high-frequency would be especially relevant.

Future research aiming to mitigate BDFT in turbulence with a lumped model should explicitly compare identification performance of an second-order overdamped model dynamics with its underdamped counterpart, possibly in real flight. A different approach to lumped BDFT modeling would be the use of physical models, capturing the dynamics of the transmission of accelerations based on the characteristics of the limbs of specific TSC users. This further personalization might shed light on the physical aspects of the BDFT dynamics and possibly improve mitigation performance, as suggested by the fact that BDFT models averaging the dynamics across all participants of the experiment

were considerably outperformed in all tested conditions by models personalized to each participant.

Another factor was shown in previous research to influence BDFT, i.e., the control task performed during the experiment [13, 14]. The control task used to collect BDFT data in this experiment was designed with the purpose of facilitating the identification of BDFT, and as such lacks the realism when compared to possible tasks performed by pilots in aircraft cockpits. In this experiment, the amount of feedthrough in the input across frequencies was implicitly quantified through the analysis of the relative remnant, leading to the conclusion that the low frequency components of the multisine motion disturbance have little impact on the tracking task, especially at low motion intensity. These findings suggest that the measurement time could be considerably reduced without losing accuracy in the modeling of BDFT, ultimately increasing the realism of the control task in regards to its duration. In addition, the shorter measurement time might allow similar experiments to be performed without using anti-static gloves, which are currently needed to reduce fatigue and wear due to friction in the prolonged contact of the participants' finger with the TSC. This would further increase the realism of the experiment in relation to the finger-TSC dynamics, enabling further verification of the applicability of model-based BDFT mitigation in aircraft cockpits. Verification of the performance of the model-based BDFT mitigation in flight could then be a further step to verify the applicability of BDFT models generated from the modified control task.

A final comment should be made on the applicability of the findings of this experiment in real flight. The stationary (Gaussian) turbulence and the variable (patchy) turbulence conditions tested were not a fully accurate simulation of aircraft vertical accelerations caused by turbulence, but rather a filtered version of these, designed to be simulated within the motion space of the SIMONA Research Simulator. The effects of these filters, a low-pass filter and a classical high-pass washout filter, can only be fully taken out of the equation by replicating the experiment in actual aircraft cockpits and real flight. In consideration to this and other points made in this discussion, it was concluded that such experiment is required for the final assessment of the impact of turbulence and turbulence variability on BDFT.

VI. Conclusions

This paper explored the impact of turbulence on model-based biodynamic feedthrough (BDFT) mitigation with touchscreens (TSCs) dragging tasks, canceling on a software level the involuntary inputs consequence of the aircraft accelerations due to turbulence. In particular, the effect of variability and intensity of the motion disturbance signal were explored through a human-in-the-loop moving-base simulator experiment. Several heave motion disturbances were simulated: a multisine motion disturbance, a realistic turbulent flight condition perceived as time invariant in the cockpit (Gaussian condition), and a time-varying turbulent flight condition (patchy condition), each at three different motion intensities.

Using the high intensity multisine motion disturbance it was shown that BDFT models can be used to cancel over 80% of the involuntary components of the input, over 90% with models identified on an individual run basis. It was concluded that variations in time and across participant of the BDFT dynamics have significant impact on BDFT mitigation, and highly personalized models are preferable for achieving the best results. Testing model-based BDFT mitigation at three levels of turbulence intensity, it was shown that with decreasing intensity the amount of BDFT in the TSC input decreases, making the identification of models less accurate. With models identified separately for each user (Subject-Averaged models) and multisine motion disturbances, over 86% of the BDFT can be canceled at the high intensity, percentage which goes down to about 70% for the low intensity case tested. In addition, the damping of the BDFT dynamics was shown to decrease with decreasing intensities. Despite these variations, the high intensity model was shown to mitigate about 84% of the BDFT component of the input both at high and medium motion intensity, while only about 65% for the low motion intensity.

In conclusion, although no BDFT model can be identified to give a consistently high performance across intensities, models identified at a specific intensity will be applicable to a range of intensities for which variations in the BDFT dynamics are sufficiently small. Mitigation with BDFT models identified in a high intensity multisine motion disturbance was tested on BDFT occurring in a simulated stationary (Gaussian) turbulence condition. Results show that such models are unable to cancel BDFT in realistic turbulence, and instead add disturbance related components to the TSC inputs (positive cancellation index $CI = 18.4\%$). It was also shown that time-domain estimation can be used to identify a BDFT model from the Gaussian dataset, achieving performance on average only 3.6% lower than models identified in multisine motion disturbances. With such models, effective BDFT mitigation can be achieved on BDFT occurring in Gaussian turbulence ($CI = -29.6\%$, only 2.4% worse than canceling BDFT occurring in multisine motion disturbance with the multisine model).

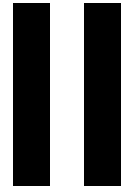
Finally, testing cancellation on turbulence with variable characteristics (patchy case), effective BDFT mitigation

performance was achieved using the model identified in realistic Gaussian turbulence ($CI = -24.8\%$, 4.7% lower when compared to Gaussian turbulence). A clear connection was found between the variability present in patchy turbulence and the BDFT modeling error, suggesting that future work should focus on time-varying BDFT models and real-time identification of parameters to further improve BDFT mitigation performance. A valuable next step would be to evaluate model-based mitigation of BDFT on aircraft, as motion filtering applied to simulate turbulence on the ground will inevitably affect results.

References

- [1] Dodd, S. R., Lancaster, J., Grothe, S., DeMers, B., Rogers, B., and Miranda, A., "Touch on the flight deck: The impact of display location, size, touch technology & turbulence on pilot performance," *2014 IEEE/AIAA 33rd Digital Avionics Systems Conference (DASC)*, IEEE, 2014, pp. 2C3–1. <https://doi.org/10.1109/dasc.2014.6979570>.
- [2] Rouwhorst, W., Verhoeven, R., Suijkerbuijk, M., Bos, T., Maij, A., Vermaat, M., and Arents, R., "Use of touch screen display applications for aircraft flight control," *2017 IEEE/AIAA 36th Digital Avionics Systems Conference (DASC)*, IEEE, 2017, pp. 1–10. <https://doi.org/10.1109/dasc.2017.8102060>.
- [3] Van Zon, N. C. M., Borst, C., Pool, D. M., and Van Paassen, M. M., "Touchscreens for Aircraft Navigation Tasks: Comparing Accuracy and Throughput of Three Flight Deck Interfaces Using Fitts' Law," *Human Factors: The Journal of the Human Factors and Ergonomics Society*, Vol. 62, 2019. <https://doi.org/10.1177/0018720819862146>.
- [4] Degani, A., Palmer, E. A., and Bauersfeld, K. G., "“Soft” controls for hard displays: Still a challenge," *Proceedings of the Human Factors Society Annual Meeting*, Vol. 36, SAGE Publications Sage CA: Los Angeles, CA, 1992, pp. 52–56. <https://doi.org/10.1177/154193129203600114>.
- [5] Hutchins, E. L., Hollan, J. D., and Norman, D. A., "Direct manipulation interfaces," *Human–computer interaction*, Vol. 1, No. 4, 1985, pp. 311–338. <https://doi.org/10.1201/b15703-5>.
- [6] Coutts, L. V., Plant, K. L., Smith, M., Bolton, L., Parnell, K. J., Arnold, J., and Stanton, N. A., "Future technology on the flight deck: assessing the use of touchscreens in vibration environments," *Ergonomics*, Vol. 62, No. 2, 2019, pp. 286–304. <https://doi.org/10.1080/00140139.2018.1552013>.
- [7] Kaminani, S., "Human computer interaction issues with touch screen interfaces in the flight deck," *2011 IEEE/AIAA 30th Digital Avionics Systems Conference*, IEEE, 2011, pp. 6B4–1. <https://doi.org/10.1109/dasc.2011.6096098>.
- [8] Venrooij, J., Mulder, M., Van Paassen, M. M., Mulder, M., and Abbink, D. A., "A review of biodynamic feedthrough mitigation techniques," *IFAC Proceedings Volumes*, Vol. 43, No. 13, 2010, pp. 316–321. <https://doi.org/10.3182/20100831-4-fr-2021.00056>.
- [9] Tao, D., Zeng, J., Liu, K., and Qu, X., "Effects of control-to-display gain and operation precision requirement on touchscreen operations in vibration environments," *Applied Ergonomics*, Vol. 91, 2021, p. 103293. <https://doi.org/10.1016/j.apergo.2020.103293>.
- [10] Cockburn, A., Gutwin, C., Palanque, P., Deleris, Y., Trask, C., Coveney, A., Yung, M., and MacLean, K., "Turbulent touch: Touchscreen input for cockpit flight displays," *International Conference for Human-Computer Interaction (CHI 2017)*, 2017, pp. 6742–6753. <https://doi.org/10.1145/3025453.3025584>.
- [11] Cockburn, A., Masson, D., Gutwin, C., Palanque, P., Goguy, A., Yung, M., Gris, C., and Trask, C., "Design and evaluation of braced touch for touchscreen input stabilisation," *International Journal of Human-Computer Studies*, Vol. 122, 2019, pp. 21–37. <https://doi.org/10.1016/j.ijhcs.2018.08.005>.
- [12] Lancaster, J., De Mers, B., Rogers, B., Smart, A., and Whitlow, S., "57.3: The Effect of Touch Screen Hand Stability Method on Performance & Subjective Preference in Turbulence," *SID Symposium Digest of Technical Papers*, Vol. 42, Wiley Online Library, 2011, pp. 841–844. <https://doi.org/10.1889/1.3621464>.
- [13] Khoshnewisadeh, A., and Pool, D. M., "Mitigation of Biodynamic Feedthrough for Touchscreens on the Flight Deck," *International Journal of Human–Computer Interaction*, 2021, pp. 1–13. <https://doi.org/10.1080/10447318.2021.1890490>.
- [14] Mobertz, X., Pool, D. M., van Paassen, M., and Mulder, M., "A Cybernetic Analysis of Biodynamic Effects in Touchscreen Operation in Turbulence," *2018 AIAA Modeling and Simulation Technologies Conference*, 2018. <https://doi.org/10.2514/6.2018-0115>.

- [15] Alapetite, A., Fogh, R., Zammit-Mangion, D., Zammit, C., Agius, I., Fabbri, M., Pregnotato, M., and Becouarn, L., "Direct tactile manipulation of the flight plan in a modern aircraft cockpit," *Proc. of HCI Aero*, 2012. URL https://www.researchgate.net/profile/Alexandre-Alapetite/publication/260297675_Direct_tactile_manipulation_of_the_flight_plan_in_a_modern_aircraft_cockpit/links/00b7d530b16b6dc72e000000/Direct-tactile-manipulation-of-the-flight-plan-in-a-modern-aircraft-cockpit.pdf.
- [16] Smith, M. A., Plant, K. L., Parnell, K. J., Wynne, R. A., and Stanton, N. A., "P-28: Investigating the Usability of Touchscreen Interfaces in a Turbulent Flight Deck–For Panning and Numeric Data Entry Tasks," *SID Symposium Digest of Technical Papers*, Vol. 51, Wiley Online Library, 2020, pp. 1438–1441. <https://doi.org/10.1002/sdtp.14158>.
- [17] Abrahamsson, H., and Karlsson, L., "Case Study: Digitization of a User Interface: Investigating the use of a touch screen in Helicopter 14," 2020. <https://doi.org/urn:nbn:se:kth:diva-276838>.
- [18] Damveld, H. J., Beerens, G. C., van Paassen, M. M., and Mulder, M., "Design of forcing functions for the identification of human control behavior," *Journal of Guidance, Control, and Dynamics*, Vol. 33, No. 4, 2010, pp. 1064–1081. <https://doi.org/10.2514/1.47730>.
- [19] Zaal, P. M. T., Pool, D. M., Chu, Q. P., Van Paassen, M. M., Mulder, M., and Mulder, J. A., "Modeling human multimodal perception and control using genetic maximum likelihood estimation," *Journal of Guidance, Control, and Dynamics*, Vol. 32, No. 4, 2009, pp. 1089–1099. <https://doi.org/10.2514/1.42843>.
- [20] Vrouwenvelder, S., Postema, F., and Pool, D. M., "Measuring the Drag Latency of Touchscreen Displays for Human-in-the-Loop Simulator Experiments," *AIAA Scitech 2021 Forum*, 2021. <https://doi.org/10.2514/6.2021-0896>.
- [21] Jacobson, B., "A novel Fitts' law: Evaluating touch-based interfaces in atmospheric turbulence," Master's thesis, Unpublished. Delft University of Technology, 2021. URL <http://resolver.tudelft.nl/uuid:2404d466-fbc9-4cca-ba54-097413df9eea>.
- [22] Stewart, E. C., "Evaluation of the Ride Quality of a Light Twin-Engine Airplane by Means of a Ride Quality Meter," Tech. rep., NASA, 1989. URL <https://ntrs.nasa.gov/citations/19890013197>.
- [23] Leto, G., "Effect of Turbulence Intensity and Variability on Model-Based Biodynamic Feedthrough Mitigation with Touchscreen Dragging Tasks. Preliminary Report." Master's thesis, Unpublished. Delft University of Technology, 2023.
- [24] Van de Moesdijk, G. A. J., "The description of patchy atmospheric turbulence, based on a non-Gaussian simulation technique," *Delft University of Technology, Department of Aeronautical Engineering, Report VTH-192*, 1975. URL <http://resolver.tudelft.nl/uuid:d9060267-cef5-4955-982a-1a7b5da25d90>.
- [25] Van de Moesdijk, G. A. J., "Non-Gaussian structure of the simulated turbulent environment in piloted flight simulation," *Technische Hogeschool Delft, Vliegtuigbouwkunde, memorandum m-304*, 1978. URL <http://resolver.tudelft.nl/uuid:b5e66aad-6a6e-44e8-af4d-58d51684c515>.
- [26] Mulder, J. A., van der Vaart, J. C., van Staveren, W. H. J. J., Chu, Q. P., and Mulder, M., *Aircraft Responses to Atmospheric Turbulence: Lecture Notes AE4304*, TU Delft, 2016.
- [27] Van Der Linden, C. A. A. M., "DASMAT-Delft University aircraft simulation model and analysis tool: A Matlab/Simulink environment for flight dynamics and control analysis," *Series 03: Control and Simulation 03*, 1998.
- [28] Gouverneur, B., Mulder, J. A., van Paassen, M. M. R., Stroosma, O., and Field, E., "Optimisation of the SIMONA Research Simulator's Motion Filter Settings for Handling Qualities Experiments," *AIAA Modeling and Simulation Technologies Conference and Exhibit*, American Institute of Aeronautics and Astronautics, 2003, p. 5679. <https://doi.org/10.2514/6.2003-5679>.
- [29] Popovici, A., Zaal, P., and Pool, D. M., "Dual extended Kalman filter for the identification of time-varying human manual control behavior," *AIAA Modeling and Simulation Technologies Conference*, 2017, p. 3666.
- [30] Van Grootheest, A., Pool, D. M., van Paassen, M., and Mulder, M., "Identification of Time-Varying Manual Control Adaptations with Recursive ARX Models," *2018 AIAA Modeling and Simulation Technologies Conference*, 2018, p. 0118.
- [31] Plaetinck, W., Pool, D., van Paassen, M., and Mulder, M., "Online identification of pilot adaptation to sudden degradations in vehicle stability," *IFAC-PapersOnLine*, Vol. 51, No. 34, 2019, pp. 347–352.



Preliminary Report

Note: Part II has already been graded under the course AE4020 - Literature study.

2

Preliminary Research Questions

The following preliminary research question guided the literature review aimed at understanding the status of the research in the field of *biodynamic feedthrough* (BDFT) in aircraft cockpits employing *touchscreens* (TSCs) for control purposes, allowing to define a knowledge gap that will be filled by this thesis project.

What is the state of the research on BDFT mitigation with TSC interfaces in an aircraft cockpit subject to turbulence?

The main keywords that can be identified are *biodynamic feedthrough*, *touchscreens* and *turbulence*. The literature on BDFT and TSCs is grouped together in Chapter 3, and is further guided by the following subquestions:

1. *What is the influence of turbulence on the performance of humans engaged in manual control tasks with TSC interfaces in aircraft cockpits?*
2. *What research has been done in the field of BDFT mitigation for TSCs, and under what assumptions?*

To answer these questions, in Chapter 3 after a general introduction on TSC interfaces and BDFT, manual control in dynamic environments is discussed with particular reference to finger-TSC interaction, moving on to benefits and limitations of the use of TSCs for control, BDFT mitigation and the research performed on BDFT with touchscreens, with focus model-based BDFT mitigation in touchscreens.

As for the last keyword, literature on turbulence is presented in Chapter 4, with the aim to answer the following subquestions:

- 3 *What are the characteristics of the turbulence encountered in phases of flight relevant to the use of TSC interfaces in aircraft cockpits?*
- 4 *How is this turbulence modeled in literature?*

Chapter 4 gives a general theoretical introduction to turbulence, leading to the statistical description of turbulence on which most models are based. Several turbulence models are then described, as well as their use in previous TSC related research. The validity of the models in the atmosphere is then shortly discussed.

Touchscreens and Biodynamic Feedthrough

This chapter provides a literature review on *touchscreens* (TSCs) and their use as manual control interfaces in aircraft cockpits, with particular focus to their use in turbulent atmospheric conditions, Section 3.1. The phenomenon of *biodynamic feedthrough* (BDFT), i.e., the influence of the aircraft accelerations on manual control, is overviewed in Section 3.2 together with possible strategies for its mitigation. Previous work on the topic of mitigation of BDFT in control tasks performed with TSC interfaces is presented in Section 3.3, with particular reference to model-based BDFT mitigation, in Section 3.4. The chapter then concludes with a summary in which knowledge gaps identified are discussed, Section 3.5.

3.1. Touchscreen technologies

A *touchscreen* (TSC) is a display combined with sensors, able to pick up the coordinates at which the screen is being touched. TSC interfaces are sometimes categorized under the name 'soft controls', as alternative to the 'hard', not re-programmable mechanical controls [18].

For control applications, several different TSC technologies are considered in literature:

- *Projected Capacitive TSCs* pick up changes in capacitance thanks to a conductive pattern placed below a protective glass screen. Although very sensitive, only contact with a conductive element is converted into input coordinates. This technology supports multi-touch interaction [5, 8],
- *Resistive TSCs* register a point of contact when two separated electrically resistive layers come in contact with each other, leading to the registration of only one input at a time. For the two layers to touch, a certain force has to be exerted on the surface. This leads to low sensitivity of the TSC to inputs [5],
- *Infrared TSCs* detect the points at which an object interferes with a grid of infrared beams and sensors, placed on top of the display surface. This technology shows a high occurrence of false positives [4, 5],
- *Surface acoustic wave TSCs* work analogously to their infrared counterpart. On top of the screen, transducer generates a grid of ultrasonic waves, which are attenuated when a finger or any other object is positioned on the surface. This technology doesn't require extra layers on top of the display, and as such, is better in terms of image quality. However, the functioning of the TSC is very susceptible to dirt [19],
- *Force sensing TSCs* are capacitive TSCs which include a layer of pressure sensors, able to differentiate between different levels of pressure exerted when giving an input, leading to the availability of additional interaction methods [20].

The *interaction methods* supported by TSC interfaces can be subdivided between single and multi-touch gestures, and between continuous or discrete gestures. The most common gestures are single tap, double tap, hold, scroll or swipe, pinch, zoom, drag, rotate [17]. Depending on the use case, discrete gestures (single tap, double tap, hold) are associated with different *activation methods*, which define how the contact picked up by the TSC is converted into an input for the interface [17]. The most common are registering an input at the point of first contact (the 'land on' method and the 'first contact' method, in which the input is registered at the first point of contact only if this coincides with an interactive element of the interface), or at the point of last contact with the TSC (the 'lift off' method), allowing the user to give an immediate correction in case of erroneous input by dragging the finger to the correct position [17]. In addition, a force threshold can be applied on force sensing TSCs [21]. Other activation methods include combinations of the above mentioned and the 'sequential touch' method, with which a confirmation screen is presented before the input is registered [17].

3.1.1. Touchscreen interfaces in control applications

There are many benefits as well as drawbacks in regards to the use of TSCs in control tasks. Many studies have highlighted these both in static and dynamic environments with various end goals, related to control in aviation and not.

TSC technologies are promising in control applications first and foremost thanks to the flexibility of the interface design. The same panel can display information from any subsystem at command, through the use of different menus and tabs, leading to the *decluttering of the flight deck*, where traditionally a different interface is required for each subsystem and function [22]. To the removal of mechanical parts follows a *reduction in weight* of the aircraft, as well as a *reduction in maintenance costs*, favored especially by the operators [6]. Another cost saving feature is that updates of the cockpit interfaces only require software updates [17]. On the downside of this decluttering is the *unavailability of all subsystems' controls at all times*, as well as the *increased look-down time* required when searching through tabs or menus, which reduces the user's attention to the surrounding environment [12, 23].

Another characteristics that distinguishes TSCs from other interfaces, is that the screen from which the user collects the information is also used for giving control inputs and subsequently receiving feedback. This co-location of input and feedback leads to an overall *reduction in motor movement* required from the users, possibly reducing their physical fatigue during operations [18]. On the downside, this can lead the temporary *occlusion of information* when giving an input, raising safety concerns [5].

Thanks to the flexibilities mentioned, the TSC's software can be designed according to the 'direct manipulation' interface guidelines, bridging the gap between the human's understanding of a control problem and the machine's required inputs, by presenting to the user a representation of the controlled element that behaves like the actual real life object [18, 24]. For this reason, TSCs have the potential to *reduce the cognitive effort* required for control, whilst *increasing situation awareness* of the pilot, and therefore the overall safety of his control actions [18, 25]. This can be especially useful when control of an aircraft is shared between pilot and automation, as the user is more aware of the actions taken by the automation, and their effect [18, 25]. An interface design with these characteristics requires *lower training time* for novices compared to other interface designs [12].

Setting aside the opportunities they offer, TSC interfaces have some inherent characteristics which have limited their use to non safety critical control tasks, especially in dynamic environments such as an aircraft cockpit.

With regards to the display of information, the illuminated surface causes *eye fatigue*, especially in low light conditions [17]. In bright environments, the high reflectivity of the display *compromises the visibility* of the information [17]. Also dirt and finger oils can limit considerably the visibility of the screen, if no specialized coating is applied [26].

In regards to the use of TSCs as control manipulators, several issues have been identified. Firstly, friction between the finger and the display can cause significant *fatigue* to the user, if no coating is applied [1]. Similarly, giving an input without being able to support the arm on the sensitive surface leads to *physical fatigue*, especially in dynamic environments which require the user to steady their arms [4, 12, 27]. In such conditions, *pointing accuracy decreases* leading to an *increase in input error rates and data entry time* [4, 27, 28]. Moreover, the *latency* of the TSC interface (including update rate, processing and response time) can compromise the user's ability to react timely to control issues [1]. Depending on the position and orientation of the touchscreen, the user's ability to control the interface

can be influenced by *parallax errors*: when the screen is not perpendicular to the line of sight of the user, the user's perception of a point on the screen will differ from its actual position [29]. Finally, the high sensitivity to touch of TSCs can easily lead to *accidental touches* being registered as inputs [12, 18].

Above all, the main concern raised with TSC interfaces is that their flat surface *lacks any tactile feedback*, requiring the user to search confirmation of whether the given input are registered as intended [12, 18]. This also implies that the user will not be able to locate a specific control with muscle memory without looking down to confirm the correct positioning, reducing the advantages of mnemonic control, *slowing down the user's actions* and possibly *taking away their attention* from their surroundings and their other control tasks [5, 12].

3.1.2. Requirements for touchscreen interfaces in aviation

With the introduction of TSC interfaces in aircraft cockpits, it became necessary to regulate their use through requirements. An example is provided by the FAA [30], indicating requirements for the maximum error rate, speed and accuracy of the inputs, as well as workload experienced by the TSC users. The requirements are all listed in a qualitative manner, not specifying any strict threshold: performance should be 'acceptable' [30]. On the software level, these requirements translate in suggestions on the use of menus for navigation through the subsystems [30]. On the hardware level, requirements include that TSC interfaces should not be susceptible to wear in the long run, nor to scratching and hazing, and resistant to impacts and exposure to sun radiation, chemicals (including skin oil) and liquids, again to an 'acceptable' level [30]. TSC calibration should maintain an 'acceptable' performance in the long run, or at least be adjustable [30]. Other requirements have been identified by authors performing research on touchscreen technologies. For example, the reflectiveness of the display should be such that content can be visualized under all light conditions [31]. In addition, the visibility of the display shouldn't be hindered excessively by fingerprints residues on the display [31].

3.2. Biodynamic feedthrough

When a human is performing a manual control task in a vehicle in motion, the accelerations of the vehicle propagate through his limbs and joints, involuntarily influencing their control inputs [14]. This phenomenon, called *biodynamic feedthrough* (BDFT) has been studied extensively by Venrooij [14, 32], who also devised a framework for the development of strategies to mitigate the impact of this interference between the vehicle's accelerations and the human's control inputs. This section first introduced the topic of manual control in a dynamic environment, then deals more in specific with the phenomenon of BDFT and its mitigation.

3.2.1. Manual control in dynamic environments

There are several sources of vibrations and accelerations to which a human pilot is exposed in a cockpit environment. Examples are the aircraft's engines, turbulence and landing gear transmitted vibrations when the aircraft is on the ground [13]. Vibrations and accelerations have been shown to affect motor control, sensory ability (especially causing visual impairment) and cognitive ability, each to a different degree depending on the frequencies of the vibrations and the *root-mean-square* (RMS) of the accelerations, in extreme cases leading to disorientation and sickness [13, 33].

The degree to which manual control performance is impaired during exposure to vibrations depends on various factors: the direction of the vibrations, the characteristics of the task to be performed (control element dynamics, manipulator dynamics), the biodynamic characteristics of the person performing the task together with the modality in which the vibrations are transmitted to the body (seat, any seating restrains, the grip on the control interfaces) [33, 34].

Several studies developed estimations for the range of frequencies at which vibrations most affect manual performance. According to Kim and Martin [34], vibrations along the longitudinal and lateral axis affect manual control performance when below 3 Hz. Conway et al. [35] reported the same effects in the range 1-2 Hz. For vibrations along the vertical direction, Lone and Cooke [36] reported as performance impairing frequencies between 2 Hz and 16 Hz, associated with a RMS acceleration above 0.05 g. Similarly, Conway et al. [35] suggested that the degradation in performance occurs between 4 and 8 Hz. Kim and Martin [34] between 3 and 8 Hz. In general, the authors agree that vibrations in the vertical axis disrupt manual control performance in a broader range and higher frequencies when compared to vibrations in the longitudinal and lateral axes [33–35].

Worth noting for its possible application when applied to TSC related research, the performance degradation in control tasks requiring an unsupported stretched arm seems to mostly occur with vibrations in the range between 2-6 Hz [13].

The duration of the exposure to vibrations has also been highlighted as a key factor in manual control performance, a long exposure impacting humans to a greater extent than a short one [35].

In regards to the characteristics of the control tasks, tasks which require an accurate input are compromised to a greater extent, compared to tasks which prioritize speed of execution over accuracy [35]. Apart from the obvious advantage provided by a less accurate requirement, which could reduce the error rates even in static conditions, this is also caused by the different dynamics unconsciously employed by a human pilot when exposed to vibrations [36]. For example, a pilot might loosen the grip on the control manipulator to prevent the control inputs from being affected by vibrations, at the cost of accuracy of the movement. In most cases however, a pilot exposed to vibrations will instinctively strengthen the grip instead. The urgency of the task also influences the performance of a pilot in a vibrating environment. An urgent task often leads the humans to stiffen their grip on the controls, again leading to higher vibration feedthrough [36].

Models of the human dynamics in dynamic environments

In order to quantify the dynamics of the human body in vibrating environments, several models have been studied in literature. Most common are lumped models, which attempt to capture the frequency response of the human body by tuning the parameters of mass-spring-damper systems [36, 37]. These models are usually developed under the assumptions of linearity, absence of friction and uni-axial vibrations [37]. Lone and Cooke [36] provide a well structured review of pilot models.

For the study of human-touchscreen interaction, aside from the general pilot models, models of the contact mechanics between a finger and a flat surface might be of interest. Wiertlewski and Hayward [38] derived the frequency response of the fingertip from measurements of its impedance, performed using a flat probe vibrating tangentially, on which rested an index finger. The fingertip was noted to behave elastically until 100 Hz, while its viscosity dominates at higher frequencies [38]. A second order highly damped system, the Kelvin-Voigt model in Equation 3.1, was found suitable to approximate the fingertip frequency response shown in Figure 3.1.

$$Z_{FTIP}(j\omega) = b_{FTIP} + j \left(m_{FTIP}\omega - \frac{k_{FTIP}}{\omega} \right) \quad (3.1)$$

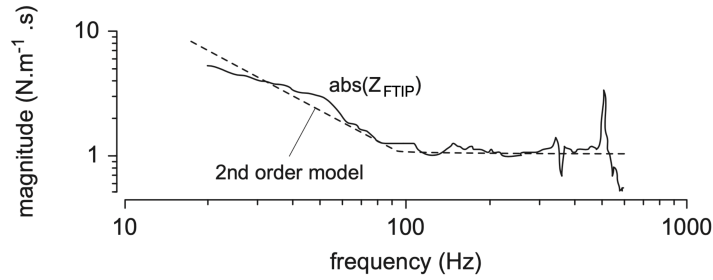


Figure 3.1: Frequency response of the fingertip, with corner frequency at around 100 Hz. Adapted from Wiertlewski and Hayward [38].

The parameters of the model are the mass of the fingertip m_{FTIP} , its viscosity b_{FTIP} and its stiffness k_{FTIP} [38]. Each was found to be dependent on gender, and, except for the stiffness, independent on the direction of the vibration [38]. The parameters are shown in Table 3.1 for two direction of the applied vibrations, proximal-distal and medial-lateral.

The force impinged on the flat probe by the finger was shown to influence the model parameters m_{FTIP} , b_{FTIP} and k_{FTIP} [38]. This influence was modeled with a zero-intercept power law, in the form $m_{FTIP}/b_{FTIP}/k_{FTIP} = \beta(n_{FTIP})^\alpha$, with n_{FTIP} being the normal force in N, and α and β constants, reported in Table 3.2 [38].

Table 3.1: Parameters for the fingertip model when impinging 0.5 N on the probe, averaged from measurements reported by Wiertelowski and Hayward [38].

Direction	k_{FTIP} [N/mm]	b_{FTIP} [Ns/m]	m_{FTIP} [g]
Medial-lateral	0.91 ± 0.35	1.33 ± 0.53	0.13 ± 0.04
Proximal-distal	1.43 ± 0.46	1.49 ± 0.47	0.17 ± 0.06

Table 3.2: Dependency of the fingertip model parameters on the normal force impinged on the surface. Adapted from Wiertelowski and Hayward [38].

Parameters	α	β
m_{FTIP}	0.26 ± 0.19	0.20 ± 0.06
b_{FTIP}	0.35 ± 0.10	1.78 ± 0.60
k_{FTIP}	0.35 ± 0.09	1.48 ± 0.60

3.2.2. Open-loop and closed-loop biodynamic feedthrough

When dealing with the phenomenon of BDFT, an important distinction should be made between its occurrence in open-loop and in closed-loop systems. In closed-loop systems, the human is controlling the state of the vehicle, and therefore any involuntary motion of his body caused by the vehicle's accelerations is fed back to the vehicle, leading to an interference between the control input and the output accelerations [32]. When the interference leads to unstable dynamics, the phenomenon takes the name of 'biodynamic coupling' [32]. In open-loop systems, the vehicle's accelerations are fed to a control system which does not directly influence the state of the vehicle [32].

An example of a control task in which closed-loop BDFT occurs is the manual control of an aircraft through a control stick or column. An example in which open-loop BDFT occurs is a navigation task on an aircraft [1].

3.2.3. Framework for biodynamic feedthrough mitigation

Verrooij et al. [14] built a framework to categorize strategies for the reduction of BDFT based on factors which have an influence on manual control performance, often specific to the task to be performed: the human operator, the controlled element, the manipulator and their interfaces with the human.

The following categories were therefore defined:

- *Mitigation at human level* is based on the ability of the human body to adapt to various control regimes. Neuromuscular adaptation is one of such mitigation strategy. Loosening the grip on a mechanical manipulator for example, will lead to a lower feedthrough of the vehicle motion in control inputs. This mitigation is however not ideal, as it forces the human to implement a control strategy with a loosened grip, sacrificing control bandwidth [14].
- *Mitigation at the controlled element level* can be achieved by minimizing the accelerations of the vehicle, but causes the maneuverability of the vehicle to decrease as well [14].
- *Mitigation at the manipulator level* is achieved by reducing the sensitivity of the manipulator to the frequencies of the motion disturbance. However, this is only possible when there is a clear separation between frequencies used for control of the vehicle and frequencies belonging to the motion disturbance. This assumption is often far from realistic [14].
- *Mitigation at the interfaces* aims to reduce as much as possible the transmission of the motion from the vehicle to the human, and from the human to the manipulator. Examples of this type of mitigation are seat damping or isolation, and arm support. Seat isolation, while effective in reducing involuntary limb motion, also reduces the motion cues that the human would need for his control action, especially when dealing with a closed-loop control task [14]. Arm support allows motion cues to be perceived by the human, but is less effective in mitigating BDFT. In addition, it causes a reduction in mobility of the arm, hindering the human engaged in the control task [14]. Finally, looking at the interface between the manipulator and the vehicle, the frequency range assumed to belong to the motion disturbance can be filtered out before the input is received

by the vehicle [14]. This mitigation strategy however again relies on the frequency separation assumption, often leading to the loss of part of the intended control input [14].

- *Model-based BDFT mitigation* is as a software based mitigation strategy, in which a model approximating the components in the control input caused by the vehicles accelerations is used to cancel the involuntary component from the input signals [14]. The main issue with this approach lies in the fidelity of the model, which depends on the set-up for its identification, the task, the user, the accelerations employed [1, 17]; the more a model is tailored for one combination of task, user and conditions, the less it is valid for the general case [1, 39]. Model-based BDFT mitigation can be done in two ways: using black box identification, which implies fitting the data to estimate both the dynamics of the systems and the parameters, ultimately yielding a lumped model of BDFT, or with insight of the working mechanisms of human interaction with the control interface [32]. This may include arm, wrist and shoulder dynamics, and any other physical aspect involved in the motion feedthrough [32]. For a TSC interface these also include the contact dynamics between fingers and TSC, discussed in Section 3.2.1.

3.3. Biodynamic feedthrough occurring with touchscreens

Several authors expanded the research pertaining the use of TSCs in dynamic environments qualitatively describing observations made during experiments and from a quantitative perspective, developing performance indexes to compare traditional interfaces with TSC ones, as well as proposing solutions to mitigate the effects of BDFT. This section gives an overview of the performance metrics used for comparison of control interfaces, followed by an overview of the effects of motion disturbances on the use of TSCs, and of BDFT mitigation experiments.

3.3.1. Measuring touchscreen interfaces performance

Across different studies, several quantitative metrics have been used to compare the performance observed with TSCs interfaces with respect to conventional interfaces. The most common are measures of the error rates, the average task completion time, the total movement time and gesture counts [1]. In addition, several authors have investigated the applicability to TSC interfaces of Fitts' law, used in manual control to predict the movement time required for completion of a task based on the characteristics of the task [5, 11, 16, 40].

Fitts' law, shown in Equation 3.2, linearly relates the *movement time* (MT) required to complete a task to an *index of difficulty* (ID), dependent on a tolerance range for the input and on the average amplitude of the movement required to give the input [40]. For the case of TSCs, the tolerance range for the input coincides with the size of the target [16]. This relation provides the means to quantify the trade-off between execution speed of a task and accuracy in its completion, which is often seen in human control behavior [40].

$$MT = a_{FL} + b_{FL} \cdot ID \quad (3.2)$$

Bi et al. [40] noted that the MT predictions made with Fitts' law become inaccurate with small targets on a TSC, and implemented a calibration term within the definition of the ID accounting for the variance of the inputs occurring independently of the task characteristics, dependent only on the precision of the finger input. Through this modification, the authors demonstrated improvements in the prediction capability of Fitts' law with TSCs, especially with small targets, effectively compensating the 'fat finger' problem [40]. This version of the Fitts' law is referred to as the Finger-Fitts' law [40].

In parallel, Coutts et al. [11] proposed an extension to dynamic environments of the original Fitts' law, meant to explicitly evaluate interface performance across different magnitudes of motion. As shown in Equation 3.3, a term multiplied by a metric V_{metric} , quantifying the total magnitude of the accelerations of the vehicle, is added [11].

$$MT = (a_{FL/V} + b_{FL/V} \cdot V_{metric}) + (c_{FL/V} + d_{FL/V} \cdot V_{metric}) \cdot ID \quad (3.3)$$

For this extension of the original Fitts' law, the authors did not provide an estimation of the accuracy of the model compared to the original Fitts' law or to the Finger-Fitts' law.

Lastly, Jacobson [16] combined the two works to further investigate this performance metric, using in the formulation of the original Fitts' law implemented by Coutts et al. [11] the ID term derived for the Finger-Fitts' law by Bi et al. [40]. In addition, he used a method defined as 'return to zero', such that

the coefficients $a_{FL/V}$ and $c_{FL/V}$ of his version of Finger-Fitts' law would coincide with the coefficients a_{FL} and b_{FL} obtained using the original Finger-Fitts' formulation, ensuring that the extension would be able to predict MT also in static conditions ($V_{metric} = 0 \text{ m/s}^2$) [16]. Experimental results showed that the V -metric formulation of the original Fitts' law without accounting for the 'fat finger' problem, coupled with the 'return to zero' method, performs best in predicting the MT for different IDs and for different magnitudes of the motion to which the TSC user is exposed [16].

3.3.2. Touchscreens in dynamic environments

Several authors studied the effects of vibrations and accelerations on TSCs. Tao et al. [15] highlighted some effects of vibrations on the performance, perceived workload, task difficulty and discomfort while using TSCs for manual control tasks. The authors showed that during vibrations a decrease in accuracy can be observed compared to performing the same action in static conditions, testing dragging tasks, zoom-in/out tasks, and rotation tasks, leading to lower task completion times [15]. The authors noted however that this could be the result of the participants being instructed to perform the experiment with only one touch, leading to a quicker and less precise movement to prevent loss of contact with the screen while under vibrations [15]. For dragging tasks, Jacobson [16] noted that an increase in path length to reach a target can be correlated to increasing magnitude of the motion, and that a considerable difference exists between tasks requiring to 'push' compared to tasks requiring to 'pull', with the former showing almost twice the increase in path length compared to the latter. Cockburn et al. [27], performing an experiment with increasing levels of vibrations, noted that the error rates with sliding and dial tasks increase as vibrations increases. No significant correlation with increases in vibrations were noted for error rates occurring with keypad tasks, although for all tasks an increase in selection time with increasing vibrations was proven [27]. These results align with the study performed by Rider and Martin [41], that noted through a simulator experiment that increases in movement time and in endpoint variability with a discrete pointing task can be correlated to an increase in vibrations.

In subjective ratings, the participant of the study by Tao et al. [15] recorded an increase of workload, task difficulty and discomfort for all tasks performed under vibrations, though notably less for dragging tasks. The authors attributed this difference to the fact that dragging is a single gesture, while the other tasks tested require the coordination of multiple fingers and therefore have a higher task difficulty rating also in static conditions [15]. Participants of the study from Cockburn et al. [27] also reported increasingly higher workload and frustration when using TSCs in increasingly stronger vibrations.

3.3.3. Mitigation of biodynamic feedthrough in touchscreens

Many studies have looked into ways of minimizing the effects of BDFT when using TSCs as control interfaces, some of which do so indirectly, by attempting to minimize the error rates or providing tactile feedback in static conditions. Directly or indirectly, these studies contribute to the useful knowledge for the reduction of the transmission of the vehicle's accelerations through the TSC controls, so they are included in the review. This section gives an overview of these works, roughly classified following the BDFT mitigation framework discussed in Section 3.2.3.

Mitigation at the touchscreen level

In literature, various TSC configurations have been compared in order to find options which minimize the error rates when a TSC interface is used for control purposes.

Touchscreens with *stencil overlays* are mainly studied as a means to introduce tactile feedback, especially when using gloves, but also to clearly separate the input areas for discrete interaction [27, 42]. Abrahamsson and Karlsson [42] reported the results of interviews conducted on helicopter pilots tasked with menu navigation and input selection on a TSC in a static environment, using stencil overlays. The study concluded that the proposed solution is not optimal, giving tactile feedback but overall limiting the flexibility of the touchscreen interface [42]. Similar conclusions were reached by Cockburn et al. [27] through a simulation on a vibrating platform, with input selection tasks employing keys, dials and sliders, and panning and zooming tasks. Especially with smaller keys, the stencils did not improve the error rate. In this experiment, it was noted that participants were not keen on stabilizing their hand by leaning on the stencil, reducing its efficacy [27].

In the already mentioned study from Abrahamsson and Karlsson [42], discussion with participants suggested the introduction of feedback to reduce the error rates in input selection, *auditory*, *visual* (colour coding or blinking) or *haptic*, in the form of vibrations of the screen. No agreement on a pre-

ferred solutions was noted. Similar suggestions were given by participants in another study, Alapetite et al. [7], testing navigation tasks on TSCs in fixed base simulators.

Another way studied to make sure that TSC inputs would be registered as intended, is the use of different activation methods. In an experiment on a vibrating platform, testing tapping, dragging and sliding tasks on touchscreens, Coutts et al. [11] highlighted the need for a way for the user to confirm their inputs in safety critical tasks, suggesting a *pop up confirmation window* as mandatory, as it has a considerable beneficial effect on the error rate. The authors also suggested the use of *force touch* as an alternative to the confirmation windows, though requiring further experimentation [11].

To be noted, the use of different TSC types (TSC technologies described in Section 3.1) also has an impact on biodynamic feedthrough [4]. When experimenting on a vibrating platform, Dodd et al. [4] showed that TSC with capacitive technologies allow faster interaction when compared to resistive technologies, while the opposite was observed when looking at the task completion times. Especially with smaller screens, the error rate in turbulence caused by the more sensitive capacitive technologies was shown to have a large impact on the manual control task [4].

Mitigation at the touchscreen/human interaction level

These studies include supporting the hand on the TSC or its edges [21, 43] and studies on the position and orientation of the touchscreen with respect to the user [44].

In hand stabilization studies, the user are asked to support their hand by holding the fingers directly on the display (*brace touch*), *gripping its edges*, or by using a *wrist or arm support*, with the objective of reducing the error rates and fatigue while controlling a TSC interface exposed to motion disturbances [21, 43]. Cockburn et al. [21] tested brace touch on a vibrating platform, with different activation methods, such as double tap, hold and force threshold, to allow the participants to rest their fingers on the touchscreen while correctly registering the control inputs, concluding that brace touch indeed reduces the error rates in turbulence, especially when using double tap as an activation method. In a similar study, Lancaster et al. [43] tested panning, data entry and menu navigation with four edge grips configurations: large edges, lateral rails, a supporting bar sliding vertically just above the surface and rough edge with multiple supporting possibilities. Turbulence was simulated by off-road driving. Results showed no difference in performance between the various methods, while the users expressed a significant preference for the lateral rails method, and lower fatigue with the supporting sliding bar [43].

The location of the touchscreen with reference to the sitting user influences the dynamics of the arm, and therefore the control inputs. For aircraft cockpits, several positions have been identified: overhead, frontal, inboard, outboard of the pilot [4, 7, 11, 26]. In a fixed base simulation, Alapetite et al. [7] concluded that between a low inboard configuration and a frontal configuration, the frontal TSC leads to a good time performance, but also to a high error rate when compared to conventional interfaces in an input selection task. The low, inboard configuration showed a considerably slower task completion time [7]. Coutts et al. [11] arrived to similar conclusions performing an experiment with tapping, dragging and sliding tasks on a vibrating platform, showing that between a frontal, side and overhead touchscreen, the frontal one grants both faster movement and lower error rate, but adding that the side position causes minimal fatigue and discomfort, for all tested tasks. Dodd et al. [4] further confirmed these results, by experimenting with menu navigation, input selection and dragging tasks with TSCs located overhead, in front, inboard and outboard of the pilot, in a motion simulator subject to vibrations. An additional result is that the overhead and outboard TSC result in higher fatigue than the other configurations [4].

In this same experiment, Dodd et al. [4] showed that larger TSC are preferable to smaller ones, as they considerably reduce the error rates. Then, in a follow-up experiment again in simulated turbulence, Dodd et al. [44] looked at the influence of the orientation of the TSC interfaces on performance, noting that an inclination between 15 and 85 degrees from the horizon is optimal to support the visualization of the content of a screen, and specifically that the front panel mounted at 75 degrees was preferred over higher orientations, while for the side panel, an orientation between 30 and 45 degrees should be used. The conclusion for the side panel is in line with the work of Lewis [45], which, in a study on the marketing of TSCs, recommended an adjustable angle between 30 and 45 degrees from the horizontal to minimize fatigue.

In order to make sure that the use of touchscreen interface would not be a source of distraction from the outside environment and the other control panels, a shape changing TSC interface mounted

on a side console was developed by Pauchet et al. [46]. When the user is gazing at the side panel, the interface is a flat sensing surface, with an image projected onto it [46]. When the user's gaze is instead focused on the frontal screens, three knobs emerge from the surface through servo actuators connected with an eye gaze detection system, and the touch sensitivity is deactivated [46]. In this experiment, the control task to be executed with these rotary knobs or through the TSC was to bring the needle of a dial to a specific location along its edge, location displayed both on the side panel where the user interacted with the interface and on a display on the central panel [46]. The outcome of the study showed this concept as very promising, reducing the amount of time the user's gaze is focused on the side panel therefore leading to a shorter completion time of the task and to lower perceived workload when compared to a conventional TSC [46]. The technology itself is however too early in its development: participants reported a difficulty in completing the task on the TSC in one continuous gesture, because of the uneven surface at the locations where the knobs emerged when the user's gaze was focused elsewhere [46]. Concerns about the timing and triggers as well as the continuity of the switch between the two interfaces were also raised [46].

Model-based mitigation

Mobertz [17] first showed that it is possible to identify a linear time-invariant model for BDFT occurring when a continuous pursuit task is being performed on a TSC while the TSC operator is subject to a purposely studied one-dimensional multisine motion disturbance, through an identification experiment performed in a moving base simulator. Mobertz [17] exploited the frequency separation principle (separating the longitudinal target signal describing the longitudinal coordinates of the target on the screen, the lateral target signal and the motion disturbance signal) to extract from the input recorded by the TSC the voluntary control action and the feedthrough due to the disturbance signal. Lateral and longitudinal screen inputs showed power at the frequencies corresponding respectively to the lateral and longitudinal target signals, denoting the voluntary part of the input [17]. At the same time, cross-coupling between the arm's motion performed by the human operator in the lateral and longitudinal axis was visible as power present in the lateral and longitudinal TSC inputs respectively at the frequencies of the longitudinal and lateral targets [17]. Finally, power at the frequencies of the disturbance signal was used to study and model BDFT [17]. In particular, Mobertz [17] used the variance of the error between the target signal and the input signal to evaluate tracking performance, as well as the effects of BDFT for different motion conditions (surge, sway, heave, and no motion) and for two different TSC locations: on the side of a sitting human operator, such as where the *Control Display Unit* (CDU) would be in an aircraft cockpit, and directly in front of the operator, in the position of a *Primary Flight Display* (PFD).

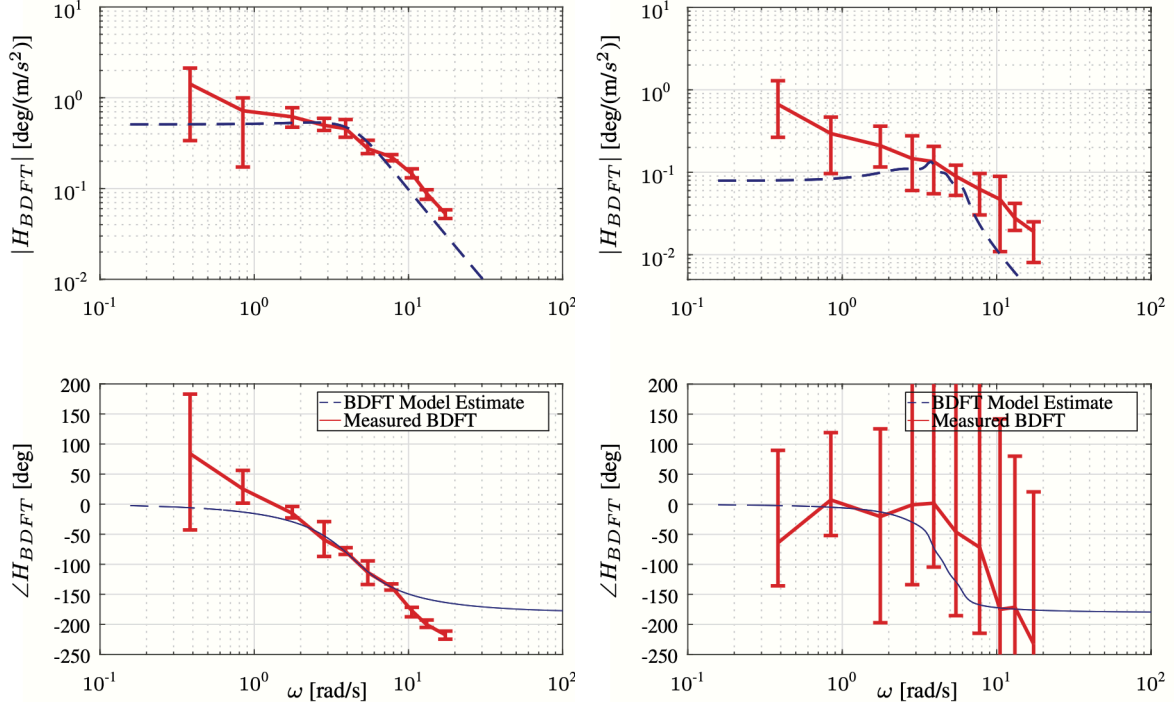
Mobertz [17] showed that the input on a TSC is most affected by the motion disturbance when this acts on the same axis of the input: sway and surge disturbances impacted the TSC input predominantly in the lateral and longitudinal directions respectively for the CDU display, since the lateral touchscreen inputs aligned with the sway axis, and the longitudinal aligned with the surge axis. Similarly for the case of the PFD (inclined at an angle of 18 degrees from the vertical axis), strong coupling was observed between the sway axis and the lateral touchscreen inputs [17]. In addition, a strong coupling was observed not only between the vertical screen input and heave motion, but also with surge, explainable because the inclination of the screen caused the finger to slip upwards in surge motion [17]. Overall, Mobertz [17] concluded that there is no significant difference in the acceleration feedthrough for either TSC location.

The study also highlighted that changing the position of the TSC with respect to the human body affects tracking performance: the error variance at the frequency components of the target signals highlighted that more power due to the target signal is present in the CDU-located display compared to the PFD-located one, noting however that an overall higher input tracking performance is achieved with a PFD-located TSC in comparison to a CDU-located TSC [17]. This was connected to fact that using the CDU-positioned display the participants were able to lean on their arms and therefore experienced less fatigue in tracking compared to the PFD-located TSC (also inferred because the variance of the remnant signal was found to be higher for the PFD-located TSC), while at the same time higher parallax errors on the CDU-located TSC caused an overall lower tracking performance [17].

In relation to BDFT modeling, Mobertz [17] identified a linear model H_{BDFT} , incorporating the neuromuscular dynamics of the human arm and a gain, see Equation 3.4 [17].

$$H_{BDFT}(s) = G_{BDFT} \cdot \frac{1}{m_{BDFT} \cdot s^2 + b_{BDFT} \cdot s + k_{BDFT}} \quad (3.4)$$

To be noted, in this model the parameters of the second order transfer function, the mass m_{BDFT} , the damping b_{BDFT} and the stiffness k_{BDFT} , are uncoupled from the gain G_{BDFT} . Mobertz [17] showed that the fitted model is reliable only when at least 0.5% of the variance of the TSC input signal is caused by the disturbance feedthrough [17]. In such cases, the *Variance Accounted For* (VAF, see Equation 3.13), used to estimate the accuracy of the BDFT model by quantifying how much of the motion disturbance components of the TSC input signal is accounted by the model, lies above a value of 70% [17]. This accuracy requirement is visualized in Figure 3.2 from Mobertz [17]: a lower spread in the estimates leads to an accurate model fitting, see Figure 3.2a, while on the contrary a higher spread leads to the opposite, Figure 3.2b.



(a) BDFT model for longitudinal input and surge motion (PFD), variance of the input > 0.5 . (b) BDFT model for longitudinal input and surge motion (CDU), variance of the input < 0.5 .

Figure 3.2: Accuracy in the BDFT estimate and modeling. Reproduced from Mobertz [17].

Among all combination tested, Mobertz [17] found that accurate BDFT estimation was only achievable with the cases shown in Table 3.3.

Table 3.3: Experimental conditions and input directions for which a BDFT model can be estimated accurately. Adapted from Mobertz [17].

Display	Input Direction	Disturbance
CDU	lateral	sway
CDU	longitudinal/vertical	surge
PFD	lateral	sway
PFD	lateral	surge
PFD	longitudinal/vertical	heave
PFD	longitudinal/vertical	surge

Extending Mobertz's work, Khoshnewiszadeh [1] showed that a BDFT model identified from a continuous tracking task on a TSC and a multisine motion disturbance can be used to cancel the involuntary components of TSC inputs on a software level, again through an experiment performed in a moving base simulator. The experiment was performed in two rounds, a session dedicated to identification and one to evaluate online cancellation [1]. Only one TSC position was used, with the interface placed in front of the participant and fixed to the motion base, corresponding to the PFD-located TSC used

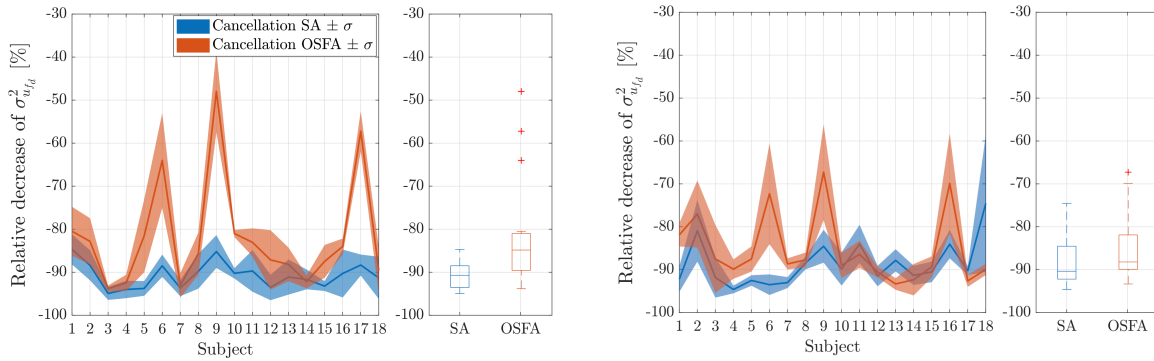
by Mobertz [1]. In the identification round, the participants were tasked with performing the same continuous tracking task used by Mobertz while subjected to the same sinusoidal motion disturbance, separately in heave and sway [1]. The data collected from this round were used for the estimation of BDFT, which was then fitted to the following lumped model.

$$H_{BDFT}(s) = G_{BDFT} \cdot \frac{\omega_{BDFT}^2}{s^2 + 2\zeta_{BDFT}\omega_{BDFT} \cdot s + \omega_{BDFT}^2} e^{-s\tau_{BDFT}} \quad (3.5)$$

Like in Mobertz's model, a second order transfer function was used to account for the neuromuscular dynamics involved in the feedthrough of accelerations. Khoshnawizadeh [1] corrected the model for the extra degree of freedom that was present in Mobertz model, by coupling the model's gain with the second order system and added a time delay component τ_{BDFT} , accounting for the latency of the touchscreen and for the delays in the transfer of the accelerations through the body.

Taking a step further from previous work, Khoshnawizadeh [1] used a *Subject-Averaged* (SA) model with the parameters derived independently for each participant to cancel the involuntary component from the control input. The model was fitted for the case of vertical inputs caused by heave disturbances, and of lateral inputs for sway disturbances [1]. Cancellation was evaluated for these conditions during the second session of the experiment, in which participants were subjected to the same experimental conditions as for the identification round, and tasked with the same continuous tracking task. Without their knowledge and without any feedback, the BDFT canceling signal was applied to their control inputs [1]. Again using the VAF as a performance index, Khoshnawizadeh [1] showed that the described approach is able to cancel above 90% of the involuntary part of the input [1]. To be noted, the simulator's accelerations used for the identification rounds and the cancellation rounds were exactly the same multisine signal.

In addition to the SA model, Khoshnawizadeh [1] also estimated the parameters of the BDFT model from all data collected across the different participants, as if deriving a model for a generalized human controller, the *One-Size-Fits-All* (OSFA) model. The study showed however that the OSFA model performed consistently worse than the SA model (VAF = 85-90%), and that the variability of the parameters of the BDFT model between subjects was not significantly correlated with their physical characteristics, such as height, weight and Body-Mass-Index. Figure 3.3 shows the difference in performance between the SA and OSFA models using the VAF metric for both heave and sway motion disturbances [1].



(a) Vertical screen input caused by heave motion disturbance.

(b) Lateral screen input caused by sway motion disturbance.

Figure 3.3: Performance of BDFT mitigation across all participants for the OSFA and SA models. The vertical scale corresponds to -VAF. Reproduced from Khoshnawizadeh [1].

The considerably worse performance of the OSFA model compared to the SA model for participants 6, 9, 17 for the heave-vertical input (VER) condition and for participants 6, 9, 16 for the sway-lateral input (HOR) condition was explained by noting that the amount of feedthrough occurring in these cases was considerably lower than for other participants, leading to an overall overestimation of BDFT when cancellation was performed using the OSFA model [1]. On the contrary, participant 18 for which the OSFA model performed considerably better than the SA model for the HOR condition, had a considerably different amount of feedthrough in the identification session compared to the cancellation session [1]. The generalized OSFA model averaged out this difference, leading to higher cancellation performance when compared to the SA model [1]. Khoshnawizadeh [1] also looked at the different averages and

spread of each parameter of the fitted BDFT model across participants, for the two motion conditions HOR and VER. These data are shown in Figure 3.4.

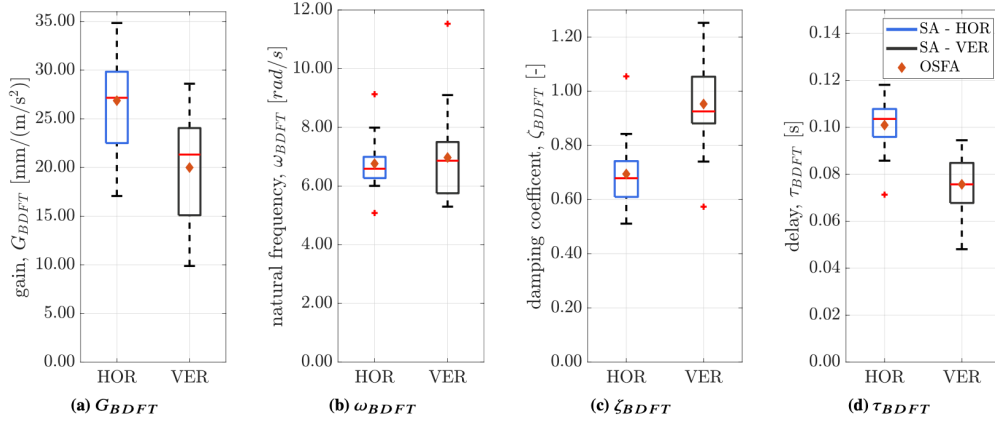


Figure 3.4: Average and spread of the BDFT model parameters across participants, for the two motion conditions. Reproduced from Khoshnawisadeh [1].

The author noted that the gain G_{BDFT} , directly related to the amount of feedthrough caused by the accelerations, had a higher average for the HOR condition than for the VER, though similar spread was observed leading to the conclusion that a higher feedthrough can be experienced in sway compared to heave for the same motion disturbance [1]. The natural frequency ω_{BDFT} had same average value across the conditions, but larger spread for the VER condition, relating to different overall stiffness across participants [1]. The damping ratio ζ_{BDFT} was found to be lower for the HOR condition, while the time delay τ_{BDFT} was found to be lower for the VER [1]. Khoshnawisadeh [1] attributed both of these characteristics to the different dynamics of the human body in the sway and heave axes, since the bending of the spine and the joint at the hip would cause motion in sway to have a lower damping and a higher time delay.

Finally, Khoshnawisadeh [1] also attempted to cancel BDFT in the case of more realistic TSC usage, a discrete tracking task. This time, the target on the screen was a point on one of four possible fixed locations on the screen, and the user was tasked with tracking the location of the target without lifting their fingers from the screen [1]. Cancellation performance was evaluated with the SA and the OSFA models, and the analysis was limited to the steady state of the recorded input, i.e., if the target was stationed at the same location for 3 seconds, cancellation was only evaluated in the last 1.5 seconds. An impression of the step task and the corresponding steady state (the purple area) is given in Figure 3.5.

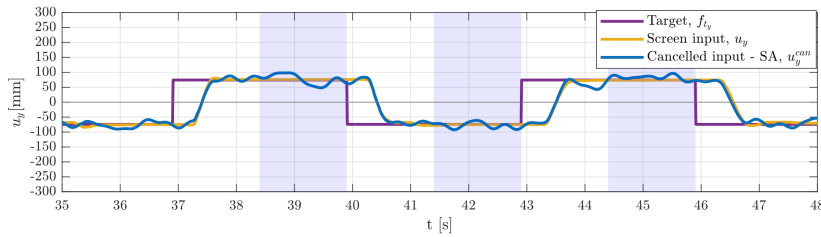


Figure 3.5: Cancellation of the discrete input signal. Reproduced from Khoshnawisadeh [1].

The experiment just described showed that the BDFT model estimated from a continuous tracking task is incapable of mitigating BDFT occurring in discrete tracking tasks [1]. By computing the standard deviation of the canceled input in the last 1.5 seconds after the re-positioning of the finger onto the target, Khoshnawisadeh [1] noted that this standard deviation was considerably higher compared to the original, non canceled input signal. He therefore concluded that the BDFT model overestimates the amount of BDFT in the input, likely because the TSC operators were able to support their hand on the TSC itself when touching for a long time the same location on the screen, consequently reducing

the impact of the motion disturbance on the input in the first place [1].

In addition to the findings related to BDFT modeling, Khoshnawisadeh [1] also showed that the drag latency of TSCs varies with input speed. Figure 3.6 shows the latency profile for the TSC equipped in the *SIMONA Research Simulator* (SRS) of the Control & Simulation Department of TU Delft (Iiyama ProLite TF1534MC-B1X), together with the range of speeds required to perform the tracking task for the BDFT experiment [1].

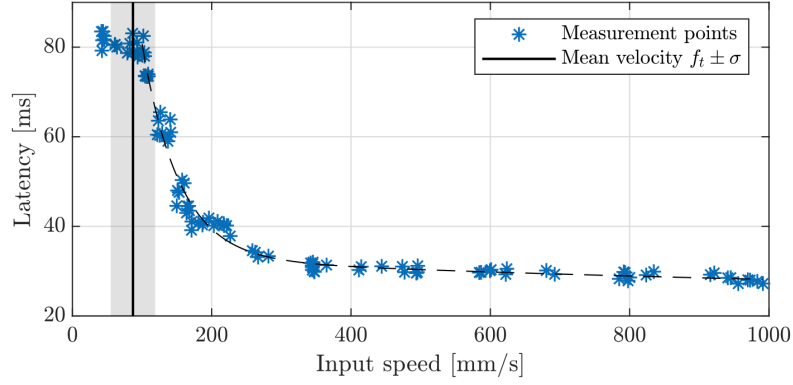


Figure 3.6: Drag latency of Iiyama ProLite TF1534MC-B1X as a function of input speed. Reproduced from Khoshnawisadeh [1].

Given the very promising results obtained by Mobertz [17] and Khoshnawisadeh [1], their identification procedures are reported more in details in the next section.

3.4. Biodynamic feedthrough model identification on touchscreens

Model-based BDFT mitigation studies [1, 17] are based on the quasi-linear model of the dynamics of a human operator employed in a target-following disturbance-rejection task, described schematically in Figure 3.7 [1].

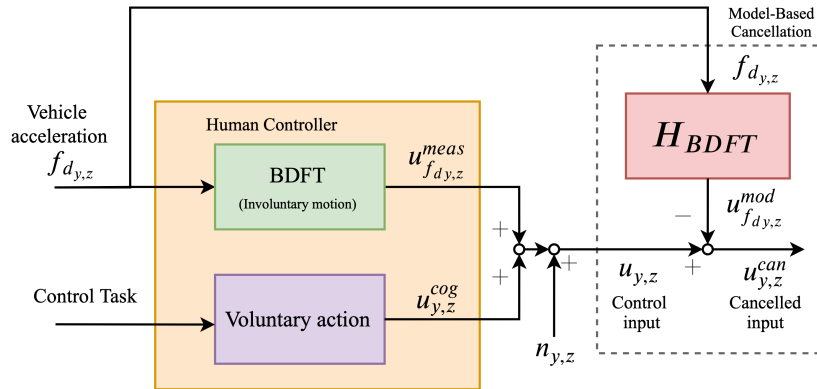


Figure 3.7: Quasi-linear model of the human operator and BDFT model-based mitigation model. Reproduced from Khoshnawisadeh [1].

The control input signal u , i.e., the input given by the human operator on the touchscreen, has two components: the lateral input u_y and the vertical/longitudinal input u_z (depending on the orientation of the TSC) [1]. Each of these components of the control input signal u is the sum of a voluntary component u^{cog} , linearly correlated to the target signal employed, and an involuntary part u^{meas} , linearly correlated to the vehicle's accelerations f_d [1]. A remnant component n accounts for the non-linearities in the

human control dynamics, representing the component not linearly correlated to the target nor to the disturbance signals [1]. Equation 3.6 reports the dynamics just described [1].

$$u = u^{meas} + u^{cog} + n \quad (3.6)$$

Using a BDFT model $H_{BDFT}(s)$, defined as a transfer function between the vehicle's accelerations and the involuntary input to the TSC caused by such accelerations, this involuntary component u^{mod} can be estimated, from which a canceled input signal u^{can} can be calculated and used as estimate of the voluntary component of the input u^{cog} [1], see Equation 3.7 [1].

$$u^{can} = u - u^{mod} \quad (3.7)$$

An estimation of the frequency response of the BDFT model $H_{BDFT}(s)$ can be obtained through the identification experiment designed by Mobertz [17] and subsequently used by Khoshnewiszadeh [1]. The experiment, run on the SRS, required participant to perform an open-loop continuous tracking task on a touchscreen, while exposed to a motion disturbance along one of the axis of the simulator [17]. Both the target that the participants were asked to follow on the TSC (its y and z coordinates) and the motion disturbance were multisine signals, each having different frequency components, therefore enabling the use of systems identification techniques on the experimental data [17]. Figure 3.8 shows the *power spectral density* (PSD) of the target signal and the acceleration signal just mentioned, the details of their construction are reported later in this section [17].

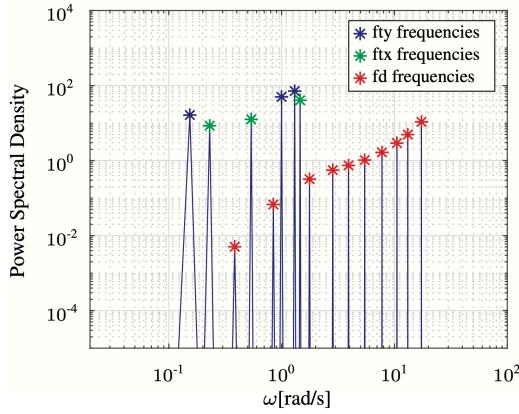


Figure 3.8: PSD of the TSC target and motion disturbance signals. Reproduced from Mobertz [17].

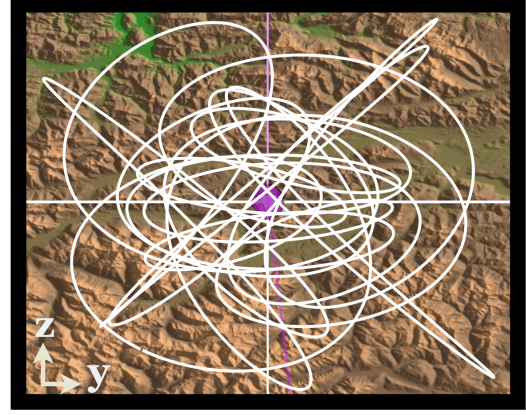


Figure 3.9: Example of the target trajectory in the continuous tracking task on the TSC. Reproduced from Khoshnewiszadeh [1].

The frequency response function of the BDFT model was estimated non-parametrically from the ratio between the PSD of the input recorded by the TSC at the frequencies of the disturbance signal, and the PSD of the disturbance signal itself, as shown in Equation 3.8 [1, 17].

$$\hat{H}_{BDFT}(j\omega_d) = \frac{S_{f_d u}(\omega_d)}{S_{f_d f_d}(\omega_d)} \quad (3.8)$$

This estimate was then fitted to a transfer function, Equation 3.4 in Mobertz's work [17] and Equation 3.5 in Khoshnewiszadeh's work [1]. The cost function $J(\delta)$ is shown in Equation 3.9, minimizing the normalized magnitude of the error between the model H_{BDFT} and the estimate \hat{H}_{BDFT} for each set of model parameters δ with MATLAB's algorithm *fminsearch* [1].

$$J(\delta) = \sum_{k=1}^{Nd} \frac{|\hat{H}_{BDFT}(j\omega_d) - H_{BDFT}(j\omega_d|\delta)|}{|\hat{H}_{BDFT}(j\omega_d)|} \quad (3.9)$$

The initial conditions and constraints for the optimization are given in Table 3.4 [1]. The data collected from a total of four runs was used for each different experimental condition for the identification of the BDFT model [1].

Table 3.4: Initial conditions and constraints for BDFT model fitting. Reproduced from Khoshnewiszadeh [1].

	G_{BDFT} [mm/(m/s ²)]	ω_{BDFT} [rad/s]	ζ_{BDFT} [-]	τ_{BDFT} [s]
Lower limit	0.0	0.0	0.0	0.0
Upper limit	35.0	15.0	2.0	2.0
Initial condition	20.0	6.0	0.6	0.1

The target was shown on the TSC with a pointer, its location highlighted with a vertical and an horizontal line intercepting at the coordinates of the pointer [1, 17]. The position of the pointer followed a predefined trajectory, an example of which is shown in Figure 3.9, with its y and z coordinates generated independently as a sum of three sines with different frequencies [1, 17]. The frequencies of the target signal were chosen among the integer multiples of the base frequency $\omega_m = 2\pi/T_m = 0.0767$ rad/s, derived from the measurement time $T_m = 81.92$ s, therefore preventing leakage [1]. The measurement time T_m was selected because together with a time resolution of 0.01 s it leads to a number of data point which is a power of 2 [47]. This particular characteristic greatly reduces the computational time of the Fast Fourier Transform algorithms, therefore the measurement time of 81.92 s is often employed in cybernetics research [1, 17, 48]. Equation 3.10 describes a multisine signal built from sine components k with amplitude A_k , phase ϕ_k and frequency ω_k . [1, 17].

$$f(t) = \sum_{k=1}^N A_k \sin(\omega_k t + \phi_k) \quad (3.10)$$

Denoting with subscript ty the multisine defining the y coordinates of the target on the TSC and with tz the one defining the z coordinates, the values used for their construction are shown in Table 3.5 together with the integers n_t used for the generation of frequencies ω_t multiples of the base frequency [1].

Table 3.5: Values used for construction of the target signal for the TSC tracking task. Reproduced from Khoshnewiszadeh [1].

k	Target, f_{ty}				Target, f_{tz}			
	n_{ty} [-]	ω_{ty} [rad/s]	A_{ty} [mm]	ϕ_{ty} [rad]	n_{tz} [-]	ω_{tz} [rad/s]	A_{tz} [mm]	ϕ_{tz} [rad]
1	3	0.230	32.767	1.445	2	0.153	22.771	0.308
2	7	0.537	39.777	0.000	13	0.997	39.775	-0.431
3	19	1.457	71.354	-1.825	17	1.304	47.511	-1.591

The use of only three sinusoidal components for each signal was motivated by the need of keeping the task simple for the user to perform [1, 17]. To keep the participants from memorizing the signal, and therefore influencing the results of the experiments, four different configurations were created for the trajectory of the TSC target signal, by mirroring the y and z coordinates of the signal about their axis [1, 17]. The coordinates generated from Equation 3.10 were therefore multiplied by the following arrays: (1, 1), (1, -1), (-1, 1) and (-1, -1) [1, 17]. The amplitude of the sines was chosen to provide enough power for the identification of the BDFT model [17].

For the generation of a motion disturbance signal, a similar approach was used: a multisine with 10 frequency components was used to define the position of the simulator [1, 17]. The frequency components were selected to cover as much as possible in the limited bandwidth of a multisine signal the range of frequencies at which humans are sensible, as well as to ensure that the motion disturbance signal was not recognizable during the repeated simulations [1, 17]. The integers n_d , the frequencies ω_d , the amplitudes A_d and the phases ϕ_d used for each multisine component k are given in Table 3.6 [1, 17].

Since the SRS requires an acceleration signal to be programmed, and it requires a zero starting value for both the position and the acceleration, the position signal $f_d(t)$ constructed from the values in Table 3.6 was multiplied to a fade-in signal $g_d(t)$, with the result differentiated twice using the chain rule, as

Table 3.6: Values for construction of the motion disturbance signal used in place of turbulence. Reproduced from Khoshnewiszadeh [1].

k	Disturbance, f_d			
	n_d [-]	ω_d [rad/s]	A_d [m]	ϕ_d [rad]
1	5	0.383	$1.067 \cdot 10^{-1}$	-0.269
2	11	0.844	$8.069 \cdot 10^{-2}$	4.016
3	23	1.764	$4.019 \cdot 10^{-2}$	-0.806
4	37	2.838	$2.048 \cdot 10^{-2}$	4.938
5	51	3.912	$1.246 \cdot 10^{-2}$	5.442
6	71	5.446	$7.568 \cdot 10^{-3}$	2.274
7	101	7.747	$4.735 \cdot 10^{-3}$	1.636
8	137	10.508	$3.424 \cdot 10^{-3}$	2.973
9	171	13.116	$2.856 \cdot 10^{-3}$	3.429
10	226	17.334	$2.416 \cdot 10^{-3}$	3.486

shown in Equation 3.11 [17, 49]. The fade-in time t_{fade} was set to 8 seconds [1].

$$f''_{d_{faded}}(t) = f_d(t) \cdot g''_d(t) + 2g'_d(t) \cdot f'_d(t) + f''_d(t) \cdot g_d(t), \quad (3.11)$$

with

$$g_d(t) = \begin{cases} 1/2 - 1/2 \cos\left(\frac{\pi t}{t_{fade}}\right) & , \quad 0 \leq t \leq t_{fade} \\ 1 & , \quad t > t_{fade} \end{cases} \quad (3.12)$$

To simplify the notation, Khoshnewiszadeh [1] used $f_d(t)$ to indicate the vehicle's accelerations in Figure 3.7 in place of $f''_{d_{faded}}(t)$.

The accuracy of the modeling of BDFT is evaluated with the VAF, shown in Equation 3.13. This metric quantifies how much of the BDFT component of the input u_{fd} , i.e., of the content of the input signal at the frequencies of the disturbance signal, is accounted for by the identified model [17].

$$VAF[\%] = \sum_{fd} \left(1 - \frac{Var(u_{fd} - u_{fd}^{mod})}{Var(u_{fd})} \right) \times 100 \quad (3.13)$$

Similarly, performance of the cancellation algorithm, i.e., how much of the involuntary component of the input signal u_{fd} can be canceled using the BDFT model, is also quantified through the VAF, in the form shown in Equation 3.14 [1].

$$VAF[\%] = \sum_{fd} \frac{Var(u_{fd}) - Var(u_{fd}^{can})}{Var(u_{fd})} \times 100 \quad (3.14)$$

This VAF describes the relative percentage change in the amount of BDFT present in the control signal before and after cancellation, by evaluation of the reduction occurring in the variance of the canceled input with respect to the variance of the non-canceled input at the frequencies of the motion disturbance [1]. From the schematic in Figure 3.7, it can be noted that the performance metric used for cancellation is identical to the one used for identification. However, to indicate that the cancellation implies a decrease in BDFT, the negative VAF is used to show the cancellation performance, for example in Figure 3.3 [1].

3.5. Summary and research gaps

The literature presented above showed that *touchscreen* (TSC) interfaces are intuitive to use and flexible in their design, providing unprecedented possibilities for direct manipulation interface concepts, potentially reducing the perceived workload and cognitive effort required for the control of complex systems such as the aircraft cockpit, when compared to conventional mechanical interfaces. However

promising, the use of TSCs comes with shortcomings, such as the lack of tactile feedback and a required longer look-down time. Literature expressed concern in regards to the high error rates in the inputs registered by TSCs, mainly due to the high sensitivity of the surface coupled with the involuntary motion of the limbs of a TSC controllers in dynamic conditions, i.e., with *biodynamic feedthrough* (BDFT). Several studies attempted to reduce the impact of BDFT on TSCs, proposing different positions for the interface, different technologies, stencils and other types of hand or arm support. These studies focused on establishing the feasibility of BDFT mitigation strategies on TSCs, but often lack validation with concrete scenarios, as they are limited by the simplified and unrealistic methods used for the simulation of motion: the majority of the studies tested their solutions simulating uni-axial vibration at specific frequencies [1, 4, 11, 17]. Only a few studies worked with realistic scenarios, such as roller-coaster set-ups [28] or cars driving off-road [43]. Only the study conducted by Jacobson [16] on TSC performance with Fitts' Law is validated with a simulation of aircraft responses to turbulence.

In particular, results achieved with model-based mitigation of BDFT [1, 17] proved very promising. For their future use in aircraft cockpits, their effectiveness in simulated turbulence should be researched. Particularly promising would be to bridge Jacobson's experiment [16] regarding the prediction of movement time with TSCs at different turbulence intensities with the model-based BDFT experiments. This would help in filling the gap regarding the validity in simulated turbulence of Khoshnewisazadeh's work.

On model based BDFT mitigation experiments, some considerations can be made: in Mobertz's and in Khoshnewisazadeh's experiments [1, 17], the same forcing functions are used for derivation of a BDFT model on the three simulator axis (heave, sway and surge). In turbulent flight, the magnitude of the accelerations in the horizontal and lateral directions are much smaller than the ones on the vertical axis. The models derived with these experiments are likely to overestimate the involuntary movement occurring in turbulent flight. Future work can be performed to adapt the BDFT model to account for these differences, before attempting to mitigate BDFT occurring in presence of (simulated) turbulence.

Again in regards to the validity of the research, it should be noted that while identification is performed on each axis independently, BDFT in turbulent flight will not occur separately in each axis, nor independently. A further step in the research could be to research whether effective BDFT mitigation can be achieved through the superposition of the models derived separately. This could be eventually addressed in future work, as the model performance has yet to be validated with realistic motion disturbances separately in each axis.

To model more precisely the dynamic of BDFT occurring with TSCs, several knowledge gaps can be identified. Previous works focused on discerning the involuntary component of the user input in target following task, limiting the analysis to the contact point of the fingertip as read by the touchscreen. Using different touch technologies, involuntary input identification could be refined by the integration of the position data with other measurements, for example data from pressure sensors or full contact area data.

Another possible point of improvement of these researches [1, 17] can be identified in the use of lumped BDFT models. Currently accounting only for the neuromuscular system with a time delay component, this model could be refined to encompass the interaction dynamics between the TSC and the fingertip, with the risk of over-fitting the data. Modeling this interaction would require a redesign of the experimental set-up and procedures. In addition, the models that have developed in model-based BDFT mitigation research [1, 17] are identified from data collected using anti-static gloves, which change deeply the contact interaction dynamics between fingertip and TSC. The use of gloves in the experiment is dictated by the experiment plan itself, to prevent the participants from experiencing excessive fatigue. Collecting data from a continuous tracking task on touchscreens requires the TSC user to drag their finger, without losing contact with the surface, for a considerable amount of time. The identification of a fingertip model would only be possible by removing the glove, modifying the experiment set-up to reduce the amount of continuous dragging time, possibly reducing the overall amount of data collected, or splitting the experiment in multiple sessions to further reduce fatigue on the test subject.

In addition, the current approach to model-based identification of BDFT is quite limited by the choice of control task, i.e., by the continuous tracking task. While a continuous tracking task is required to identify the BDFT model, this same task does not fully correspond to any tasks to be performed in the cockpit by a pilot. Khoshnewisazadeh [1] verified that the model derived for continuous tracking fails to mitigate involuntary inputs in discrete dragging tasks. For such tasks, an appropriate choice of activa-

tion method could probably be a more suitable choice to prevent involuntary inputs from effecting the task performance.

Finally, worth mentioning is the fact that BDFT model identification has currently only been performed through a frequency domain approach. The time domain identification approaches can be easily used on the already available data from previous experiments to achieve a better fit of the data.

4

Turbulence

The objective of this part of the literature research is to provide the background for the selection of a turbulence model to be used to study the effects of *biodynamic feedthrough* (BDFT) on *touchscreens* (TSCs) in aircraft cockpits. This chapter provides a literature review on turbulence, starting from a conceptual introduction to the mechanisms behind turbulence in Section 4.1 and introducing the statistical description of turbulence, Section 4.2, leading to a discussion of the available turbulence models and their applicability, Section 4.3. The applicability of the turbulence models is contextualized in Section 4.5, while previous turbulence modeling in BDFT studies is overviewed in Section 4.6. A summary on the use of the described models for BDFT experiments is given in Section 4.7, together with some considerations on the knowledge gaps identified.

4.1. Turbulence mechanisms

In fluid motion theories, a turbulent flow is defined as a flow containing swirls of the fluid of many sizes and in continuous motion [50]. These swirls, called *eddies*, form as a means to reduce the instabilities of the flow, by allowing dissipation of mechanical energy through viscous effects [51]. The process begins with the formation of large eddies, generated when the flow instabilities are too large to be dissipated immediately by the viscosity into heat [50]. From this point, turbulence can evolve uniformly through the fluid or with intermittent patches, in which patches of turbulent flow alternate with patches of laminar flow [50]. During the evolution of the turbulent flow, the largest eddies break up, transferring energy to progressively smaller eddies, until the energy contained in each swirl is small enough to allow viscous dissipation, ultimately stabilizing the flow [50, 51]. The evolution of the eddies is referred to as *energy cascade*, and is conceptually shown in Figure 4.1 [50].

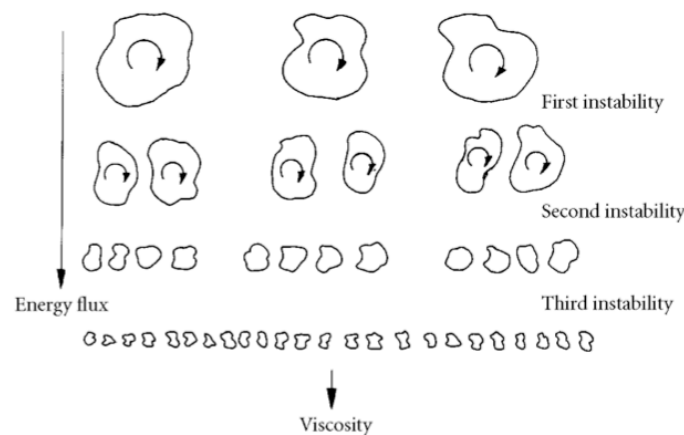


Figure 4.1: Energy cascade leading to the generation of gradually smaller eddies after the occurrence of a first instability. Reproduced from Davidson [50].

The size of the largest eddies, which defines the *integral scale* L of the turbulence, is related to the mechanism through which the eddies are generated [50]. When the eddies are created by instabilities of the mean flow, integral scale length is comparable to length scale of the mean flow [50]. The size of the smallest eddies, the *Kolmogorov microscale* η , is related to the Reynolds number of the integral scales [50]. High Reynolds number of the integral scales will result in a smaller eddy structure at the Kolmogorov microscale, when compared to lower Reynolds number: the eddies will have to break up further for the energy dissipation to occur [50].

In a fully developed turbulent flow, all scales of turbulence are present at the same time [50]. Literature uses energy spectra as a means to show the distribution of the turbulent kinetic energy among the sizes of the eddies in such turbulent flows [50, 52, 53]. Figure 4.2 gives a conceptual illustration of a one dimensional kinetic energy per unit mass $E(\Omega)$ plotted against wavenumber Ω , associated to eddies sizes as follows: each eddy of size l contributes to the energy spectrum across a range of wavenumbers centered at $\Omega = 2\pi/l$ [50, 53]. An example of the spectrum generated by eddies of fixed size l can be found in Figure 4.3 [50].

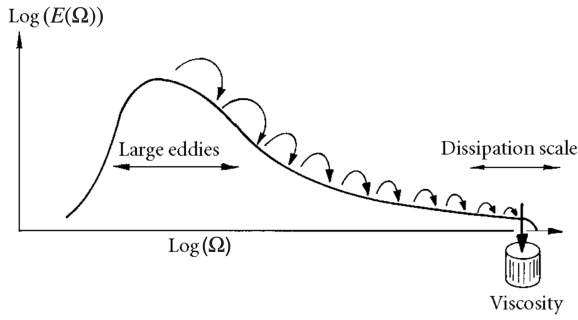


Figure 4.2: Illustration of a one dimensional energy spectrum for fully developed turbulence. Adapted from Davidson [50].

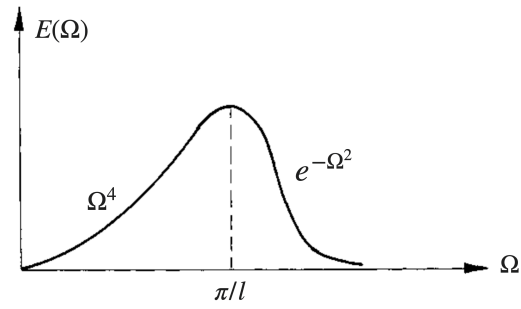


Figure 4.3: Shape of the energy spectrum $E(\Omega)$ for eddies of fixed size l . Adapted from Davidson [50].

In addition, the high wavenumbers in the energy spectrum corresponding to eddies of smaller size are usually observed rotating fast in the flow, while large eddies contribute to the low frequencies of the motion by rotating slowly [50].

4.2. The statistical approach

Theoretically, turbulent flow is deterministic, and is described by Navier-Stokes equations [50]. Resolving the velocity from these equations is however impractical: eddies in a flow are dynamically coupled in the energy cascade process described in Section 4.1. This means that the smallest difference in initial and boundary conditions cause the flow to evolve in completely different ways compared to any other realization, i.e., the flow is chaotic [50].

The study of turbulence from a statistical point of view greatly simplifies the problem at hand, and as such, has been a topic of research developed in parallel with the deterministic theories, see the works of Dryden and von Kármán [54, 55]. In addition, when dealing with turbulence modeling, resolving the exact turbulent velocity field might be unnecessary, depending on the scope of the research. Such is the case when dealing with aircraft responses to atmospheric turbulence for the purposes of manual control studies, where the use of statistical properties of the flow field not only suffices, but is also beneficial, making the simulations easily reproducible [50].

4.2.1. Statistical description of turbulence

The velocity of the turbulent flow at position \mathbf{x} can be seen as the superposition of a mean flow velocity $\bar{\mathbf{u}}(\mathbf{x})$ and a time dependent fluctuating component $\mathbf{u}'(\mathbf{x}, t)$, see Equation 4.1 [50].

$$\mathbf{u}(\mathbf{x}, t) = \bar{\mathbf{u}}(\mathbf{x}) + \mathbf{u}'(\mathbf{x}, t) \quad (4.1)$$

The two components are conceptually shown in Figure 4.4, where Figure 4.4a gives an impression of the mean flow, while Figure 4.4b shows its instantaneous, fluctuating component [50].

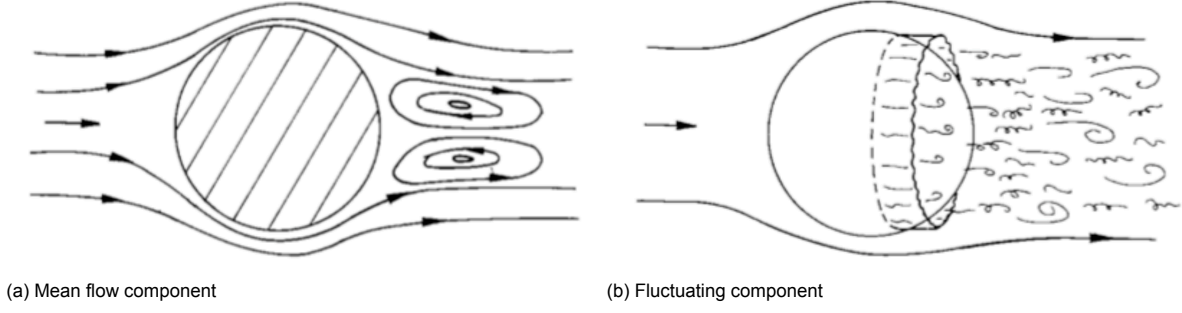


Figure 4.4: Statistical description of the turbulence velocity field. Reproduced from Davidson [50].

In the context of manual control studies, the mean flow has little relevance. A human pilot performing a manual control task will be subject to time variations in the rotational rates and accelerations, affecting their performance. These time variations originate from the fluctuating component of the turbulent velocity field, and are not affected by the mean component of the flow, which is uniform in time [47]. As in literature, a reference frame relative to which the mean motion is null can be used to deal only with the time fluctuating component of the motion [47].

The covariance and the *power spectral density* (PSD) of the fluctuating component $\mathbf{u}'(\mathbf{x}, t)$ of the turbulence velocity are of prime importance, as they are particularly useful to describe at least partially the statistical characteristics of atmospheric turbulence [47]. The auto-covariance function $C_{\mathbf{u}'\mathbf{u}'}$ of the stochastic turbulence velocity is shown in Equation 4.2, $E\{\cdot\}$ being the expectation operator [47].

$$C_{\mathbf{u}'\mathbf{u}'}(\mathbf{x}, t; \mathbf{x} + \boldsymbol{\xi}, t + \tau) = E\{\mathbf{u}'(\mathbf{x}, t) \cdot \mathbf{u}'(\mathbf{x} + \boldsymbol{\xi}, t + \tau)\} \quad (4.2)$$

This function describes the statistical correlation of the zero mean fluctuating velocity component of the flow at adjacent locations in time and space, therefore depends on the position vector \mathbf{x} , on the three dimensional distance $\boldsymbol{\xi}$ separating the two locations, on the time t and on the time separation τ [47].

Taking the Fourier transform of the auto-covariance function, the PSD is obtained, see Equation 4.3 [47]. The PSD is useful to determine the distribution of energy between eddies of various scales [47]. As can be seen from the equation, this function is now dependent both on the angular frequency ω as well as on the three dimensional wavenumber $\boldsymbol{\Omega}$, relating to the eddy sizes as shown in Section 4.1. The auto-PSD of the stochastic turbulence velocity $S_{\mathbf{u}'\mathbf{u}'}$ is also function of the position and time [47].

$$S_{\mathbf{u}'\mathbf{u}'}(\mathbf{x}, t; \boldsymbol{\Omega}, \omega) = \int_{-\infty}^{+\infty} \int_{-\infty}^{+\infty} \int_{-\infty}^{+\infty} \int_{-\infty}^{+\infty} C_{\mathbf{u}'\mathbf{u}'}(\mathbf{x}, t; \mathbf{x} + \boldsymbol{\xi}, t + \tau) e^{-j(\boldsymbol{\Omega} \cdot \boldsymbol{\xi} + \omega \tau)} d\xi_1 d\xi_2 d\xi_3 d\tau \quad (4.3)$$

Integrating over the auto-PSD of the fluctuating component of the turbulence velocity provides a measure of the variance of the velocity, i.e., of the turbulence intensity [47, 56].

4.2.2. Energy spectral density and power spectral density

Section 4.1 introduced the *energy spectral density* (ESD) of the turbulence velocity as a way to determine the distribution of the energy across eddy sizes. Subsequently, when dealing with the statistical description of turbulence in Section 4.2, the PSD was introduced, providing the same information.

In general, both PSD and ESD can be obtained from the Fourier transform of the auto-covariance function C_{yy} of a variable $y = f(t)$ [47, 52]. In the introduction given in Section 4.1, as in the majority of literature, turbulence is approached as a deterministic quantity. For a deterministic zero mean energy signal y , the energy spectrum is defined as the Fourier transform of the auto-covariance function given by Equation 4.4, coinciding with the definition in Equation 4.2 from Section 4.2.1 [57].

$$C_{yy}(\tau) = \int_{-\infty}^{\infty} y(t)y(t + \tau)dt \quad (4.4)$$

However, when dealing with turbulence as a stochastic process, only a sample limited in time of the signal will be available for analysis [57]. In these cases, the assumption of ergodicity allows to estimate

the ensemble's characteristics from the characteristics of the process measured over such limited time interval T [57]. With this assumption, the auto-covariance function can be estimated with Equation 4.5 [57].

$$C_{yy}(\tau) = \lim_{T \rightarrow \infty} \frac{1}{2T} \int_{-T}^T y(t)y(t+\tau)dt \quad (4.5)$$

This equation describes the auto-covariance function of a zero mean power signal, its Fourier transform is defined as the PSD [57]. Consequently, in stochastic turbulence modeling, the PSD is used.

4.3. Introduction to turbulence modeling

In order to simulate the aircraft motion in turbulence, a model for the turbulent velocity field has to be selected, which is then going to be used as input to the aircraft model, outputting the aircraft responses, i.e., the accelerations and rotational rates that a pilot would experience in those turbulence conditions. The aircraft model commonly used on the SIMONA Research Simulator at TU Delft for human machine interfaces and simulator studies is a Cessna Citation 500 model, based on the DASMAT architecture [16, 49, 58–60]. A detailed description of the inputs and outputs to such model can be found in van der Linden [61]. Here, it suffices to say that the aircraft equations of motion are derived separately for symmetric and asymmetric responses of the aircraft.

This section provides the description of the turbulence inputs required by the aircraft model, together with a collection of methods used in literature to simulate such turbulence, starting from the description of the coordinate system used for turbulence modeling.

4.3.1. Coordinate system

The coordinate system used for the definition of turbulence velocity components in the DASMAT aircraft model is the aircraft fixed stability reference frame, with origin on the aircraft's center of gravity (c.g.), x_s axis positive into the undisturbed velocity, y_s axis positive towards the right and z_s axis positive downwards [47, 61]. The stochastic turbulence velocities u_g , v_g and w_g are defined positive along the negative axis of the stability reference frame, as showed in Figure 4.5 [47].

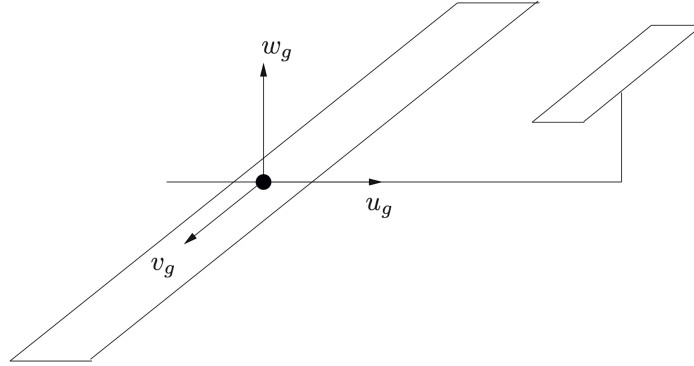


Figure 4.5: Definition of turbulence velocities. Adapted from Mulder et al. [47].

4.3.2. General assumptions for turbulence modeling

Most methods used to simulate turbulence velocities are based on simplifying assumptions that limit the validity of the simulation to specific turbulence conditions [47, 54, 62]. The assumptions used in the models described in this chapter are listed here.

- *Homogeneity* implies that the statistical properties of turbulence are independent of any translation in space of the coordinate system [47]. To explain the validity of this assumption, it should be noted that atmospheric turbulence can be seen as a collection of different patches of turbulence, homogeneous within each patch, but inhomogeneous across the different patches [56]. At high altitudes, the patches are large enough to allow the assumption of fully homogeneous turbulence [56]. At lower altitudes, the assumption only holds when the aircraft is flying at a constant altitude,

since there is a large variation in the vertical structure of turbulence [47]. Applying this assumption, the covariance and PSD functions in Equation 4.3 lose their dependency from the position \mathbf{x} at which the velocities are measured, and only depend on the distance ξ separating the two points at which the velocities are being correlated [47].

- *Stationarity*, otherwise called *Taylor's hypothesis*, implies that the statistical properties of turbulence are independent of time shifts [47]. This assumption is in general valid, as an aircraft crosses the turbulence velocity field at high enough airspeed to allow neglecting the velocity gradients of the turbulent air [47]. Thanks to this assumption, the covariance and PSD functions can be considered independent of time t [47]. Moreover, considering two points along the flight path of the aircraft, and therefore with the separation distance vector ξ becoming one dimensional, the wavenumber Ω can be related to the angular frequency ω through the aircraft velocity V : $\Omega = \omega/V$ [47].
- *Isotropy* implies the independence of the statistical characteristics of the turbulent velocity field from rotations in space of the coordinate system [47]. This assumption restricts the validity of turbulence models to outside the Earth's boundary layer, since the geometry of the Earth's surface makes low altitude turbulence highly anisotropic [56]. Isotropic turbulence implies that the variance of the turbulence velocity is independent of the orientation of the axes [47].

A flow that is both homogeneous and stationary is also ergodic, meaning that time averages can be used in place of expected values to study the statistical properties of the flow, allowing the use of the PSD as described in Section 4.2.2 [56].

4.3.3. Turbulence inputs required from the aircraft model

As mentioned in the introduction, a non-linear aircraft model of the Cessna Citation 500 will be used for the simulation of aircraft responses to turbulence. The equations describing the dynamics of a generic aircraft in zero mean turbulence are developed by Gerlach and Baarspul, for symmetric responses [63] and for asymmetric responses [64].

When dealing with the symmetric aircraft responses, only the variations in a symmetric turbulence field are considered. In particular, this turbulence field can be described by its longitudinal and vertical components u_g and w_g , assumed invariant in the spanwise direction and in the vertical direction [63]. The aircraft model requires as inputs [61]:

- the dimensionless longitudinal gust velocity $\hat{u}_g = \frac{u_g}{V}$,
- the gust angle of attack $\alpha_g \approx \sin(\alpha_g) = \frac{w_g}{V}$ (in radians),
- the dimensionless derivative of the longitudinal gust velocity $\dot{\hat{u}}_g = \frac{\dot{u}_g}{V} \frac{c}{V}$,
- the rate of the gust angle of attack $\dot{\alpha}_g = \frac{\dot{w}_g}{V} \frac{c}{V}$ (in radians).

In order to also simulate the asymmetric aircraft responses to turbulence, an antisymmetric component of the turbulence is superimposed to the velocity field just described [64]. This antisymmetric component can be attributed to the fluctuations in the lateral velocity v_g , together with the components of the longitudinal and vertical u_g and w_g fluctuating in the spanwise direction. In particular, the aircraft model requires as input the time traces of the following variables [61]:

- the gust sideslip angle $\beta_g \approx \sin(\beta_g) = \frac{v_g}{V}$ (in radians),
- the rate of the gust sideslip angle $\dot{\beta}_g = \frac{\dot{v}_g}{V} \frac{b}{V}$ (in radians),
- the dimensionless component of the longitudinal gust velocity varying along the wingspan \hat{u}_{gasy} ,
- the component of the gust angle of attack varying along the wingspan α_{gasy} (in radians).

In the equations given above, c and b are the chord and span of the aircraft and, as such, are constants. On the other hand, the airspeed V is variable, but assuming small deviations from the trim conditions, it can be considered constant. Furthermore, the description of the angle of attack α_g and the sideslip angle β_g are based on a small angle assumption, i.e., that w_g and v_g are small in comparison to the aircraft's airspeed V .

It becomes apparent that the inputs needed from the turbulence model are the time traces of u_g and w_g for symmetrical motion, and v_g , \hat{u}_{gasy} and α_{gasy} for asymmetric responses. In literature, these variables have been simulated using different turbulence models, all based on the approximation of the shape of their PSD functions [56, 63–65]. The following section will give an overview of the modeling of the PSDs required for simulations through linear filtering.

4.3.4. Power spectral density models

Knowledge of the shape of the PSD function is essential for the correct simulation of the frequency content of turbulence. Several authors derived analytical equations describing the auto-correlation functions of the turbulence velocities, relating to their covariance and therefore defining their power spectrum [54, 62]. These derivations are based on the distinction between longitudinal and lateral correlation functions: when correlating the gust velocities at two points in space, the longitudinal correlation refers to the correlation between the velocities parallel to the line connecting them (Figure 4.6a), while lateral refers to the correlation of the velocities perpendicular to such line (Figure 4.6b) [47, 54].

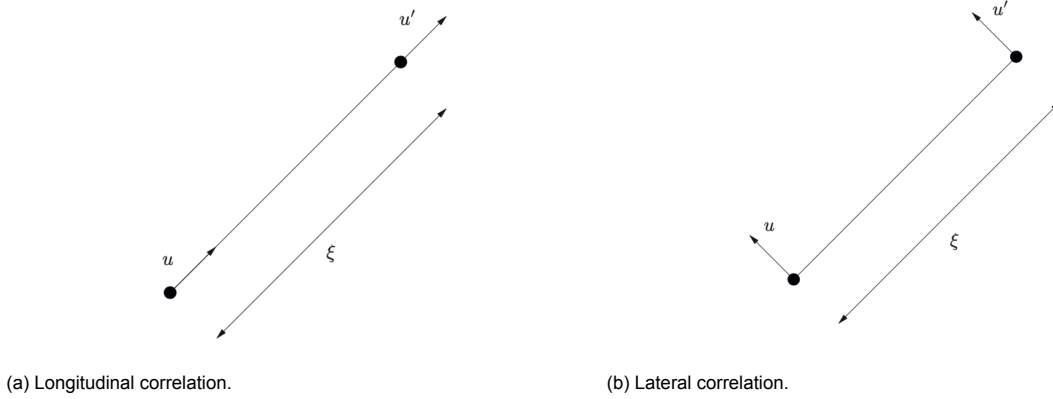


Figure 4.6: Definition of longitudinal and lateral correlations between velocities u and u' , at distance ξ from one another. Reproduced from Mulder et al. [47].

Dryden derived equations for the longitudinal and lateral correlation functions under the assumptions of isotropic, homogeneous and stationary turbulence [66]. The Fourier transform of these correlations, i.e., the PSDs of the turbulence velocities are given in Equations 4.6 and 4.7 [47].

$$S_{u_g u_g}(\omega) = 2\sigma_g^2 \frac{L_{u_g}}{V} \frac{1}{1 + \left(L_{u_g} \frac{\omega}{V}\right)^2} \quad (4.6)$$

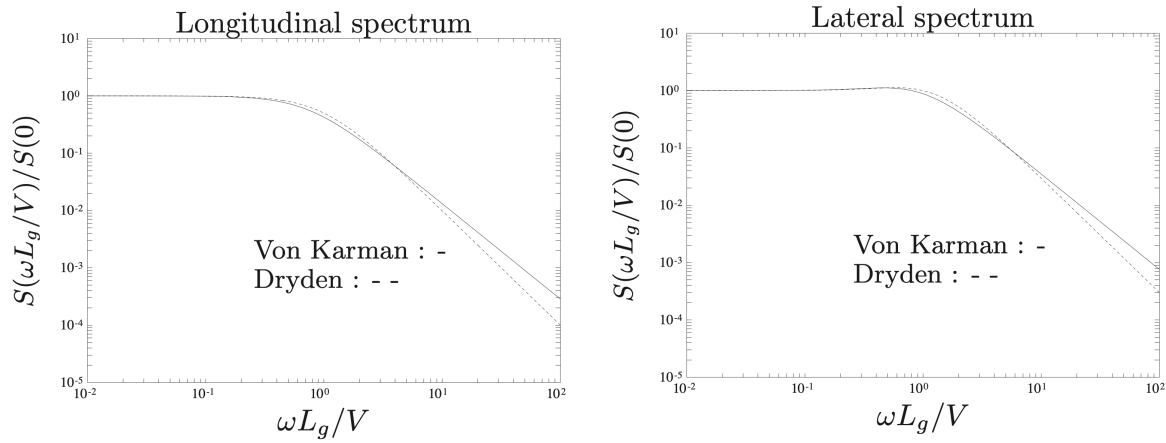
$$S_{v_g v_g}(\omega) = \sigma_g^2 \frac{L_{u_g}}{V} \frac{1 + 3\left(L_{u_g} \frac{\omega}{V}\right)^2}{\left[1 + \left(L_{u_g} \frac{\omega}{V}\right)^2\right]^2} \quad (4.7)$$

These analytical expressions are derived as a function of the integral length scale of turbulence L_{u_g} for the longitudinal direction and the variance σ_g^2 of the turbulence velocity [47]. The variance σ_g^2 is otherwise known as the turbulence intensity, and can be calculated equivalently either in the time domain from the time traces of each turbulence velocity component, or in the frequency domain from the integration of their PSDs [47, 67]. For isotropic turbulence, the intensity σ_g^2 is the same in all directions: $\sigma_{u_g}^2 = \sigma_{v_g}^2 = \sigma_{w_g}^2 = \sigma_g^2$ [47, 67]. The longitudinal and lateral integral length scales of turbulence L_{u_g} and L_{v_g} are shown to be related as follows: $2L_{v_g} = L_{u_g}$ [47].

The two analytical functions in Equations 4.6 and 4.7 can be used to simulate the longitudinal u_g and lateral v_g components of the turbulence velocity field, as well as the vertical w_g component. In fact, because of the isotropic turbulence assumption, Equation 4.7 for the lateral spectrum holds also for the vertical spectrum:

$$S_{w_g w_g}(\omega) = \sigma_g^2 \frac{L_{u_g}}{V} \frac{1 + 3 \left(L_{u_g} \frac{\omega}{V} \right)^2}{\left[1 + \left(L_{u_g} \frac{\omega}{V} \right)^2 \right]^2}. \quad (4.8)$$

These Dryden equations for the PSDs are the most used in literature for turbulence modeling with linear filtering [56, 63]. However, Dryden spectra lead to the generation of turbulence velocities with high frequency components not representative of actual turbulence, because the analytical functions diverge at high frequencies from the PSDs measured in actual turbulence [47, 68]. To give a better idea of this divergence, the Dryden spectra can be compared to the von Kármán spectra, which have been shown through experimental measures to closely match the PSDs of turbulence [47]. As visible in Figure 4.7, the main difference between the von Kármán spectra and the Dryden spectra is observed in the high frequencies asymptote of the functions [47, 56].



(a) Longitudinal PSDs.

(b) Lateral PSDs.

Figure 4.7: Difference between the von Kármán and Dryden spectra. Reproduced from Mulder et al. [47].

Although providing a better approximation of the PSD of actual turbulence, the von Kármán spectra cannot be used for linear filtering due to their mathematical description as rational functions [47, 56]. When dealing with aircraft responses, the difference is in general negligible, especially when simulating turbulence on a motion simulator, where the high frequency components of the motion will be filtered out to prevent damages to the sensible hardware. Moreover, previous research on BDFT with TSCs noted that such frequencies are of little relevance for BDFT studies, supporting the use of the simpler Dryden spectra for the ease of their implementation [16].

Two additional power spectra were derived by Gerlach and Baarspul [64] to model the spanwise varying longitudinal and vertical components of the antisymmetric turbulence velocity field, again under the assumptions of homogeneous, stationary and isotropic turbulence. An approximation for the power spectrum of the two quantities \hat{u}_{gasymp} and α_{gasymp} is given in Equations 4.9 and 4.10 as function of the span b and the longitudinal integral scale length of turbulence L_{u_g} , through the span loading $B = \frac{b}{2L_{u_g}}$ [64].

$$I_{\hat{u}_g}(\omega, B) = I_{\hat{u}_g}(0, B) \frac{L_{u_g}}{V} \frac{1 + \tau_3^2 \left(\omega \frac{L_{u_g}}{V} \right)^2}{\left(1 + \tau_1^2 \left(\omega \frac{L_{u_g}}{V} \right)^2 \right) \left(1 + \tau_2^2 \left(\omega \frac{L_{u_g}}{V} \right)^2 \right)} \quad (4.9)$$

$$I_{\alpha_g}(\omega, B) = I_{\alpha_g}(0, B) \frac{L_{u_g}}{V} \frac{1 + \tau_6^2 \left(\omega \frac{L_{u_g}}{V} \right)^2}{\left(1 + \tau_4^2 \left(\omega \frac{L_{u_g}}{V} \right)^2 \right) \left(1 + \tau_5^2 \left(\omega \frac{L_{u_g}}{V} \right)^2 \right)} \quad (4.10)$$

The constants $I_{\hat{u}_g}(0, B)$ and $I_{\alpha_g}(0, B)$ are tabulated in Gerlach [64] as function of B and of the quantities $\sigma_{\hat{u}_g}^2 = \sigma_{\alpha_g}^2 = \sigma_g^2/V^2$. Similarly, constants τ_1 to τ_6 are tabulated as a function of B [64]. To be noted, the variables \hat{u}_{gasymp} and α_{gasymp} should not be interpreted as turbulence velocities, but just as signals constructed with the purpose of modeling asymmetric aircraft responses [69].

4.4. Turbulence models

Simulation of the turbulence velocities is generally performed by recreating their spectrum through linear filtering, and adjusting the properties of the resulting signals to match as closely as possible the ones observed in flight. In this perspective, this section gives an overview of three models used for turbulence modeling, starting from a simpler model for the generation of turbulence velocities having Gaussian distribution, leading to more complex models for non-Gaussian velocity fields.

4.4.1. Gaussian turbulence models

Turbulence velocities having Gaussian distribution and Dryden spectrum can be generated by linear filtering of white noise signals, as shown in Figure 4.8 [47].

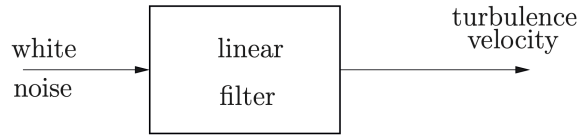


Figure 4.8: Schematic of linear filtering of white noise. Adapted from Mulder et al. [47].

Using the linear filtering method, the turbulence velocity $w(t)$ with PSD $S_{ww}(\omega)$ is obtained from white noise with constant power spectrum $S_{kk}(\omega) = 1$, using Equation 4.11 [47].

$$S_{ww}(\omega) = |H_w(j\omega)|^2 \cdot S_{kk}(\omega) \quad (4.11)$$

The equations for the linear filters $H_w(j\omega)$ of the symmetric and antisymmetric turbulence velocity components, based on the Dryden spectra in Section 4.3.4, can be found in Appendix A. As mentioned, the resulting turbulence velocities are Gaussian distributed: white noise signal, by definition having Gaussian *probability density function* (PDF), will maintain the Gaussian characteristics when filtered with a linear filter [56]. With that in mind, it should be noted that the velocity field in atmospheric turbulence is governed by the Navier-Stokes equations, implying the time and space coupling of the velocity field of the air: there is no randomness in the evolution of turbulence [56]. For the turbulent velocity field to have Gaussian distribution, randomness should be a factor in its evolution [56]. Models able to generate non-Gaussian turbulence velocities are presented in the following section.

4.4.2. Non-Gaussian turbulence models

As mentioned, more complex models compared to linear filtering are required to generate turbulence velocities with non-Gaussian characteristics. Van de Moesdijk [56, 65] gave a substantial contribution in this field, by developing two models from statistical observations on turbulence data.

In order to generate non-Gaussian turbulence, van de Moesdijk [56, 65] introduced the two concepts of patchiness and intermittency. *Patchiness* indicates that, in the flow field, areas of high and low energy alternate randomly [65]. Compared to a Gaussian process, the PDF of the velocity of patchy turbulence has the tails and the peak of the distribution shifted up, corresponding to a higher occurrence of turbulence with higher and lower velocity when compared to intermediate one [65]. This patchy characteristic is quantified through the Kurtosis K of the PDF of the turbulence velocity, indeed describing

the shape of its tails [65]. The PDF of real turbulence can be seen, compared to the PDF of Gaussian turbulence, in Figure 4.9 [65].

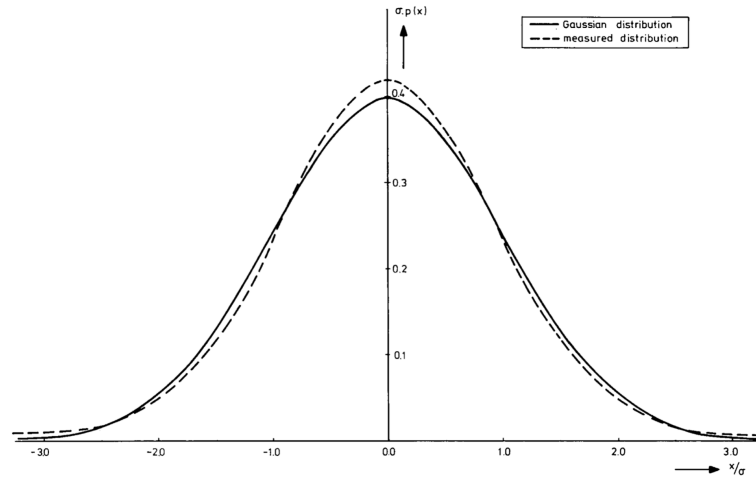


Figure 4.9: Comparison between the PDF measured from real turbulence and the PDF of Gaussian turbulence. Reproduced from van de Moesdijk [56].

The concept of patchiness therefore introduces a spatial variation in the models: turbulence can now be seen as subsequent patches inhomogeneous from patch to patch, while still maintaining Gaussian characteristics within each patch [56].

On the other hand, the concept of *intermittency* indicates a non-uniform temporal distribution of the turbulence velocity, quantified through the PDF of the time gradients of the velocity [65]. The non-Gaussian characteristics just described are independent from the turbulence's PSDs and as such patchy turbulence and intermittent turbulence are modeled from the Dryden spectra [56, 65]. A short description of these different models follows.

Patchy turbulence model

The non-Gaussian turbulence velocities based on the concept of *patchiness* are constructed from the filtering, amplitude modulation and sum of three independent Gaussian filter, as shown in Figure 4.10 and now briefly described.

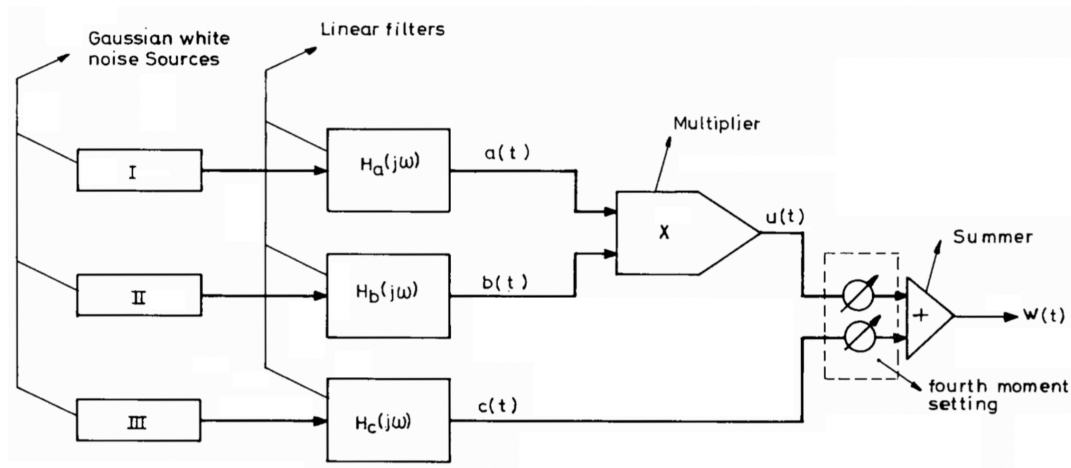


Figure 4.10: Schematic for the *patchy turbulence model*. Reproduced from van de Moesdijk [56].

The independent white noise signals with constant power, indicated in the figure as *I*, *II* and *III*, are passed each through a linear filter, represented in the figure with their transfer functions $H_a(j\omega)$, $H_b(j\omega)$, $H_c(j\omega)$, resulting in the Gaussian distributed signals $a(t)$, $b(t)$, and $c(t)$, respectively [56]. The linear

filters are constructed in such a way that the resulting turbulence velocity $w(t) = a(t) \cdot b(t) + c(t)$ has a Dryden spectrum, equivalently to a signal constructed with the linear filtering technique [56]. Non-Gaussian distribution is achieved in this model through the multiplication of the two independent signals $a(t)$ and $b(t)$, shaping the PDF of the signal $u(t) = a(t) \cdot b(t)$, and consequently of $w(t)$ [56]. After this multiplication, the PDF of signal $u(t)$ has the shape of a modified Bessel function, with Kurtosis $K = 9$ [56]. Figure 4.11 shows a Gaussian PDF ($K = 3$) together with a modified Bessel PDF ($K = 9$), with same mean and same variance σ^2 [56].

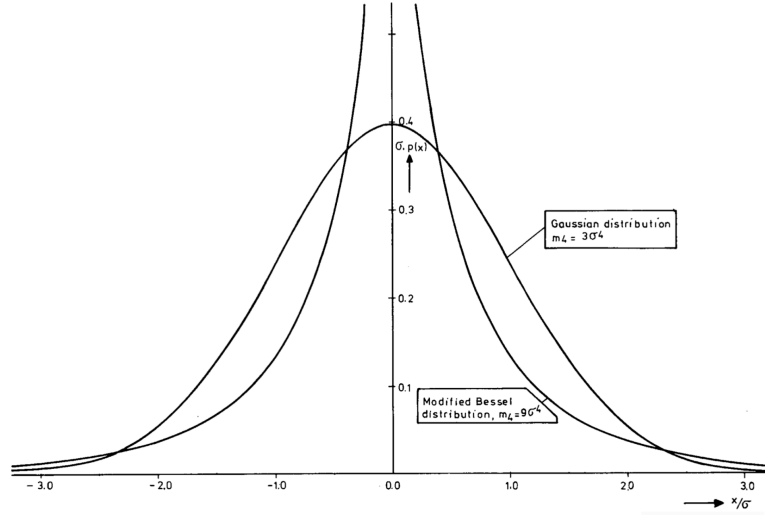


Figure 4.11: Gaussian and modified Bessel PDF, differing by their Kurtosis K (fourth central moment $m_4 = K \cdot m_2^2$, with m_2 being the variance σ^2). Reproduced from van de Moesdijk [56].

For atmospheric turbulence, measurement campaigns have shown that the PDF of turbulence velocities can have Kurtosis up to $K = 6$, leading to the PDF shown in Figure 4.9 [65]. Achieving such values for the Kurtosis of the PDF of $w(t)$ is only possible through the addition of signals $u(t)$ and $c(t)$, lowering the value of the Kurtosis depending on the ratio between the standard deviations σ_u and σ_c of signals $u(t)$ and $c(t)$, respectively [56]. The Kurtosis of the resulting turbulence velocities $w(t)$ is now parameterized as follows:

$$K = \frac{9Q^4 + 6Q^2 + 3}{(1 + Q^2)^2}, \quad (4.12)$$

with $Q = \sigma_u/\sigma_c$ [56]. Parameter Q varies from 0 to $+\infty$: if Q is set to 0, the PDF of the simulated patchy turbulence equals the Gaussian distribution, while when Q tends to ∞ the PDF is a modified Bessel function of the order zero, as shown in Figure 4.11 [56].

The functions of the filters to be used with the *patchy turbulence model* to generate the five signals required as input to the aircraft model can be found in Appendix A. These functions depend on the general characteristics of the turbulent flow, such as the scale length L_{u_g} and the variance of the turbulence velocities σ_g^2 , but also on parameter R , varying between 0 and 1, specifying the ratio of the cutoff frequencies of the linear filters $H_a(j\omega)$ and $H_b(j\omega)$ [56]. The choice of this parameter affects the frequency distribution of the energy of $w(t)^2$, the square of the turbulence velocity [56]. The spectrum of $w(t)^2$ is used by van de Moesdijk [56] as a means to quantify the way that pilots perceive patches of turbulence. Parameter R can be interpreted as a way to specify the scale of a patch of turbulence in comparison to the integral scale of turbulence indicating the size of the largest eddies in the flow [65]. In particular, $R = 1$ indicates short patches, which increase in length as R decreases [65]. The difference between long and short patches can be seen in Figure 4.12: in Figure 4.12a a long patch with higher turbulence intensity can be seen between around 90 to 140 seconds into the simulation, while in Figure 4.12b short patches are shown, an example at around 40 seconds into the simulation [65].

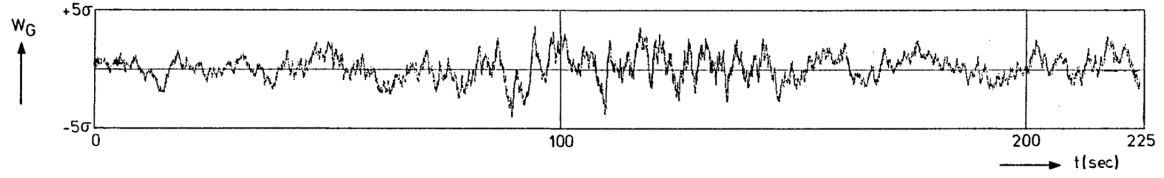
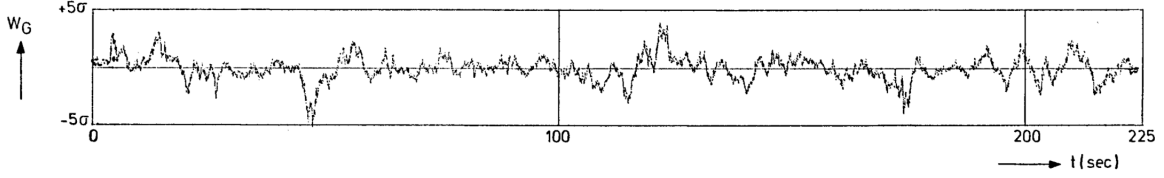
(a) Long patches, R small.(b) Short patches, R large.

Figure 4.12: Graphical interpretation of R , showing the turbulence velocity for short patches and long patches. Reproduced from van de Moesdijk [65].

Intermittent turbulence model

The model just discussed captures the variability of the turbulence velocities across patches of turbulence, but fails to fully replicate their variability in time, otherwise called the *intermittency* of turbulence [65]. In his work from 1978, van de Moesdijk [65] showed intermittency can be quantified through the Kurtosis of the PDF of the velocity gradients, i.e., of the changes in velocity of the flow field in a short time interval. Van de Moesdijk [65] showed that the *patchy model* underestimates the time variability of turbulence, and subsequently presented an adaptation to the schematic in Figure 4.10 to correct the PDF of the velocity gradient; this adaptation replaces the inputs to the filters $H_a(j\omega)$ and $H_b(j\omega)$ with a white noise signal and its Hilbert transform, implying that the input to filter $H_b(j\omega)$ will have the same magnitude as the input of filter $H_a(j\omega)$, but its phase will be shifted 90 degrees [65]. The schematic for *intermittent turbulence model* is shown in Figure 4.13 [65]. It should be noted that the mathematical

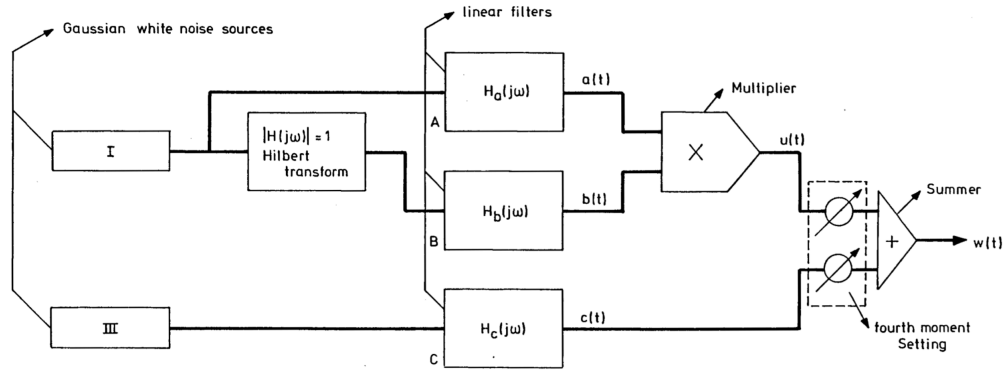


Figure 4.13: Schematic for the *intermittent turbulence model*. Reproduced from van de Moesdijk [65].

description of the filters is not entirely the same as for the simpler *patchy turbulence model*, as intermittency and patchiness are two interdependent features [65]. The methods for the derivation of the new filter equations are reported in [65], but the equations themselves were published in a subsequent work not currently available in digital repositories. Nevertheless, the *intermittent turbulence model* was shown to achieve its goal in correctly simulating the PDF of the gradient of the turbulence velocities, as can be seen from the values of Kurtosis of such PDF shown in Figure 4.14.

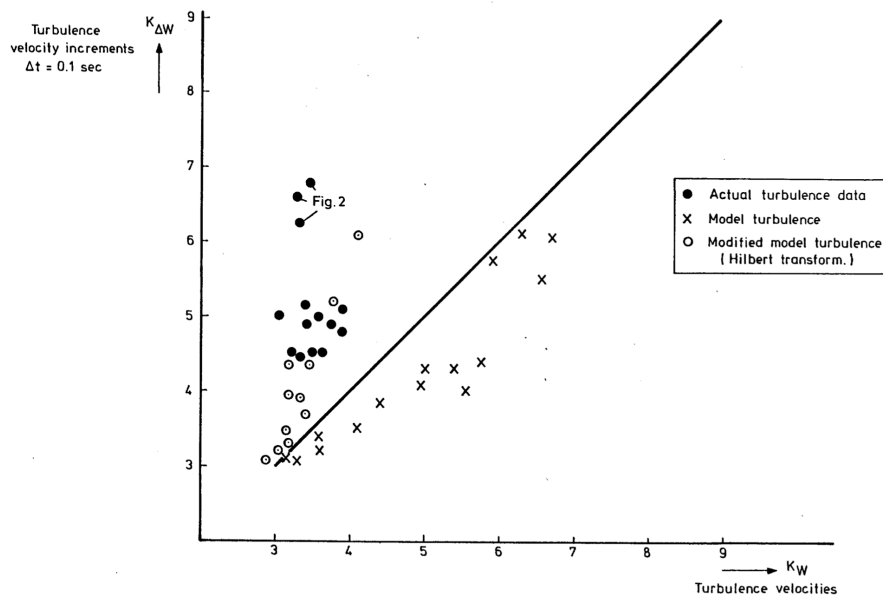


Figure 4.14: The Kurtosis of the PDF of the turbulence velocity gradient $K_{\Delta W}$ plotted against the Kurtosis of the PDF of the turbulence velocity K_W , for the *patchy turbulence model*, the *intermittent turbulence model* and for data measured in turbulence. Reproduced from van de Moesdijk [65].

4.5. Validity of the models in the Earth's atmosphere

In general, the altitudes considered for aviation go from the Earth's surface, up to 13 km above the surface for commercial aviation, and even higher around 16 km for business jets¹. The turbulence occurring at these altitudes falls in general into 2 categories, turbulence occurring in the Atmospheric Boundary Layer (ABL) and large scale turbulence [52]. To understand the validity of the turbulence models in different flight regimes and turbulence types, this section contextualizes the assumptions on which the models are based, provides an estimation for the height of the Earth's boundary layer and gives an overview of the most common conditions generating atmospheric turbulence.

The ABL is the region immediately above the surface where the flow is affected by surface effects such as moisture, heat and momentum exchanges [52]. The height of the atmospheric boundary layer is variable depending on various factors like the topography of the surface, the time of the day, the ground temperature and the presence of winds [52]. During the day, the turbulent boundary layer is estimated to reach 1-2 km above solid ground [52]. This height reduces considerably during night time, going down to 100-200 m above the surface [52]. Above oceans, the height of the boundary layer normally reaches a few hundreds of meters [52]. As mentioned in the assumptions in Section 4.3.2, turbulence at low altitude is highly anisotropic, and inhomogeneous in the vertical direction to the surface [47]. The models discussed are all based on the assumption of isotropic flow, and are therefore not suitable to reliably simulate atmospheric turbulence in the ABL: its structure will not be discussed further. Instead, a short description of the mechanisms of large scale turbulence, to which the models are applicable, follows.

There are three main mechanisms that generate turbulence above the ABL:

- *Clear air turbulence* is turbulence generated in areas with strong vertical wind shear, especially near the Jet Streams (the air currents generated in the Tropopause of the atmosphere, around 12 km above the surface, by the heating of the air through solar radiation) [51]. Instabilities between the layers of wind tend to disrupt the flow at the boundary of subsequent layers, generating small scale turbulence [51]. This turbulence is generally referred to as mechanical turbulence.
- *Turbulence in and above clouds* occurs when parcels of air at the top of the cloud are cooled by radiation with the surrounding atmosphere [51]. This generates an internal circulation within the cloud, with the cooled air parcels descending and losing their identity by mixing with the

¹[https://en.wikipedia.org/wiki/Ceiling_\(aeronautics\)](https://en.wikipedia.org/wiki/Ceiling_(aeronautics)), retrieved 10th October 2021

surrounding air [51]. Turbulence in clouds can be severe, especially at their top where cooling takes place and when rain downdrafts meet the updrafts of warmer air particles [47].

- *Wake air turbulence* is caused by other aircraft, generating a pair of counter-rotating vortices behind and below them [70].

4.6. Turbulence in touchscreen biodynamic feedthrough research

In BDFT research with TSCs performed by Jacobson [16], turbulence simulations were made using a turbulence model. In particular, an extension of the Finger-Fitts' law was tested for use in turbulent environments employing the *patchy turbulence model* described in Section 4.4.2. For his experiment, a turbulence intensity of $\sigma_g^2 = 1 \text{ m}^2/\text{s}^2$ with $Q = 0.5$ and $R = 0.7$ were used, simulating the aircraft's responses with a reference velocity of $V = 165 \text{ m/s}$ [16]. The motion profile generated with the *patchy turbulence model* with these characteristics was then passed through a motion filter, and used to simulate the aircraft responses to such turbulence in the limited motion space of the SIMONA Research Simulator (SRS) [16]. The experiment was performed by simulating the aircraft responses to turbulence in all degrees of freedom of the simulator: surge, sway, heave, pitch, roll and yaw [16]. To experiment across different intensities of the motion without changing the characteristics of the simulated turbulence, Jacobson [16] employed a set of three gains in the motion filtering: 0.3, 0.6 and 0.9 were implemented on all the components of the motion, in order to simulate the aircraft responses to respectively low, medium and high turbulence intensities. The root-mean-square (RMS) accelerations of the aircraft cockpit simulated for the experimental conditions selected by Jacobson are reported in Table 4.1 [16].

Table 4.1: Jacobson's turbulence conditions, defined by the RMS accelerations. Adapted from Jacobson [16].

Turbulence level	Filter [Hz]	\ddot{x}_{RMS} [m/s ²]	\ddot{y}_{RMS} [m/s ²]	\ddot{z}_{RMS} [m/s ²]	\dot{q}_{RMS} [rad/s ²]	\dot{p}_{RMS} [rad/s ²]	\dot{r}_{RMS} [rad/s ²]	V_{metric} [m/s ²]
Low turbulence	2 – 10	0.038	0.082	0.243	0.050	0.021	0.010	0.26
Medium turbulence	2 – 10	0.076	0.164	0.486	0.100	0.043	0.021	0.52
High turbulence	2 – 10	0.113	0.246	0.729	0.150	0.064	0.031	0.78

The last column of the table shows the V -metric, defining the total magnitude of the RMS linear accelerations, used by Jacobson [16] to quantify the motion to which the participants were exposed for his Finger-Fitts' law study, as explained in Section 3.3.1. Mathematically, V_{metric} is defined as follows [16]:

$$V_{metric} = \sqrt{\ddot{x}_{RMS}^2 + \ddot{y}_{RMS}^2 + \ddot{z}_{RMS}^2} \quad (4.13)$$

The same V -metric, although including the RMS of the rotational accelerations in its definition, was used by Coutts et al. [11] in his study in which Fitts' law is expanded to be applicable in turbulence, as mentioned in Section 3.3.1. Also in this work three turbulence setting were used, motion was simulated for a combination of vertical accelerations, roll and pitch accelerations [11]. The work however, simulated turbulence through vibration with set RMS values, instead of using a more accurate aircraft response to turbulence [11]. Like for Coutts et al. [11], other works including Dodd et al. [4] and Cockburn et al. [27] evaluated TSC usage in pure vibrations, without accounting for the characteristics of turbulence. The RMS of the vibrations can be found in each work, but will not be further reported here.

As a final remark, the turbulence models discussed in Section 4.3 are parameterized with respect to the intensity σ_g^2 and the longitudinal length scale L_{u_g} of turbulence. A few examples of typical values of these quantities have been found in literature. Gerlach and Schuring [67] proposed analytical equations valid for low altitudes up to 500 m relating these two parameters with the height above the ground and the lapse rate of the atmosphere. It should be reminded that these altitudes fall within the ABL, where turbulence is not isotropic, and therefore also the relations between each longitudinal, lateral and vertical components of the length scale and of the turbulence intensity vary with altitude as well. Estimations for these relations are also provided by Gerlach and Schuring [67], but not reported here as not suitable for the high altitude turbulence models discussed. In more recent works, the European

Union Aviation Safety Agency (EASA) provided the values of standard deviation of turbulence σ_g (the square root of the turbulence intensity σ_g^2) used in their simulator for low altitude pilot training [71]. These can be found in Table 4.2 [71].

Table 4.2: Standard deviation of low altitude turbulence of different intensity for horizontal σ_{u_g} , vertical σ_{w_g} and lateral σ_{v_g} turbulence velocities. Adapted from EASA [71].

Standard deviations [m/s]	Light	Moderate	Heavy
σ_{u_g}	0.4	0.8	1.3
$\sigma_{v_g} = \sigma_{w_g}$	0.8	1.5	2.5

For high altitude turbulence, $\sigma_g^2 = 1 \text{ m}^2/\text{s}^2$ and $L_{u_g} = 300 \text{ m}$ are described as typical values used in simulation, see [47]. In a more specific report from the US Department of Defense, an estimation is given of RMS turbulence amplitude as a function of altitude, valid for altitudes above 2000 ft (609.6 m), see Figure 4.15 [72]. The RMS turbulence amplitude coincides with the standard deviation σ_g , as we are dealing with zero mean fluctuating turbulence components².

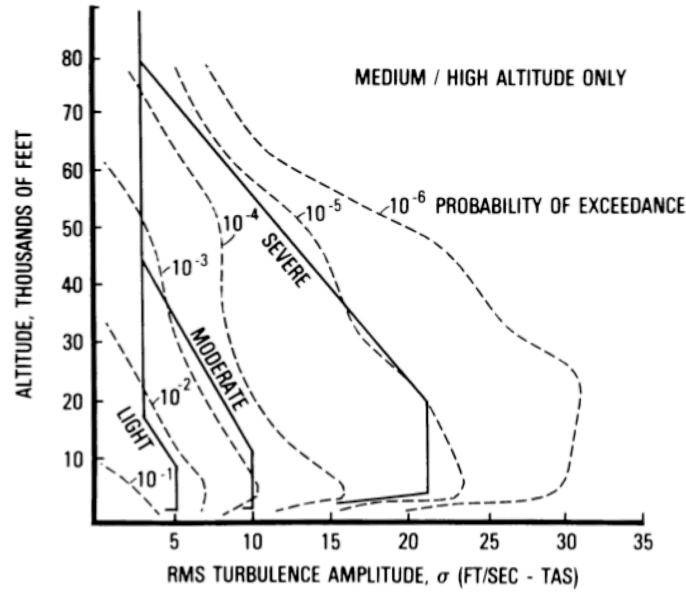


Figure 4.15: RMS of the turbulence velocity as a function of the altitude, for altitudes above 2000 ft. Reproduced from US Department of Defense report [72].

In addition, it is reported that the length scale to be used in simulations varies depending on the model employed for the spectrum of turbulence [72]. For von Kàrmàn spectra $L_{u_g} = 2500 \text{ ft}$ (762 m) should be used, for Dryden spectra $L_{u_g} = 1500 \text{ ft}$ (457.2 m) is a more correct estimation [72].

4.7. Summary and research gaps

This chapter provided a general overview on turbulence, its physical and statistical description, leading to the introduction of models for its simulation. The validity of the models in the atmosphere was then discussed from the assumptions on which they are based. Three models commonly used for the simulation of turbulence were identified, based on characteristics of turbulence such as its intensity, the size of the eddies present in the flow, the *probability density function* (PDF) of the turbulence velocity, and the PDF of the time gradient of this velocity.

In the *Gaussian turbulence model*, turbulence velocities have *power spectral density* (PSD) based on the Dryden spectra and normally distributed PDF [47]. Studies performed with pilots have confirmed

²https://en.wikipedia.org/wiki/Root_mean_square, retrieved 17th November 2022

that this model lacks the ability to simulate the variations perceived when flying through turbulent regions [56, 65]. The assumption of normally distributed velocity therefore makes the resulting aircraft motion excessively uniform in time. The *patchy turbulence model* was developed to compensate for this lack of variability, by modeling turbulence as a structure composed of patches, non-homogeneous from one another. Again based on Dryden turbulence spectra, the patchy model simulates the spatial variability of turbulence, which can be tuned to exhibit different characteristics (more or less homogeneous turbulence, shorter or longer patches) [56]. The final model presented is an *intermittent turbulence model*. This model is an adaptation of the *patchy turbulence model*, which ensures an higher variability of the time gradient of the turbulence velocity, matching more closely experimental measures performed in flight [65].

Some considerations are required for the selection, among these three models, of a suitable one for *biodynamic feedthrough* (BDFT) studies with *touchscreens* (TSCs). While as a first step research could be limited to understanding the effect of homogeneous turbulence on BDFT mitigation performed with model-based approaches, further analysis should also account for the variability of turbulence. The *patchy turbulence model*, being an extension of the *Gaussian turbulence model*, can be used both to simulate homogeneous Gaussian turbulence, as well as more variable, non-Gaussian turbulence. As such, the *patchy turbulence model* is preferred over the *Gaussian turbulence model* for use in BDFT studies. Conversely, the *intermittent turbulence model* is created as an extension to the *patchy turbulence model* ensuring that the variability of the turbulence velocity field both in time and space matches experimental data. To be noted, in a BDFT study where the variability in the control behavior of the pilot is relevant during the time span of the experiment, the exact modeling of the time and space behavior of turbulence would be superfluous. The space variability is already perceived as a time variability of turbulence in the simulator, and therefore the *patchy turbulence model* suffices for the purposes of this BDFT study. Moreover, using the *patchy turbulence model* will link this thesis work with other research performed to model human-TSC interaction in turbulence, see Jacobson [16].

Using the *patchy model* to simulate turbulence, several opportunities for research on BDFT mitigation can be identified. Firstly, it should be noted that a total of four parameters can be varied in the *patchy turbulence model*. These are the length scale of turbulence, its intensity, the probability of occurrence of extreme (high and low) turbulence velocities and the length of patches of different intensity within the overall turbulence length scale. In particular, the last two parameters define the variability of turbulence, while length scale and intensity are characteristics that can vary both in Gaussian and in patchy turbulence. As mentioned in the conclusion to the literature review regarding BDFT and TSCs, a promising gap to research pertains the performance, in (simulated) turbulence, of model-based BDFT mitigation with continuous tracking tasks on TSCs. An interesting first step in this evaluation would be to compare the performance of the model-based mitigation achieved with the multisine motion disturbance used in previous studies [1, 17], with performance achievable with turbulence causing accelerations of intensity comparable to the ones caused by the multisine. This can already be a metric in understanding whether the model-based approach is suitable for BDFT mitigation in aircraft cockpits, or whether the two disturbance signals have characteristics too different from each other, for example in their frequency content.

A second interesting step for this research is understanding whether one model identified with multisine motion disturbances can be used to mitigate BDFT across different turbulence intensities. On this issue, it can be expected that the human operator would adapt their dynamics depending on the intensity of the accelerations perceived to mitigate the impact of BDFT on their control action. For example, a human operator exposed to turbulence with high intensity, and therefore with large accelerations, could be prone to relax his arm, in an attempt to more accurately perform his control action. In essence, depending on the intensity, it is likely that the dynamics of the arm of the human operator would change, and that mitigation, performed with a model identified from one specific condition, would fail to give good results.

Additional research could be done in regards to the effects of the variability of turbulence on the model-based BDFT mitigation approach. The currently used BDFT model is a linear time-invariant model, which is by construction unable to account for variability. It can be expected that, unless the variability is small, the performance of the model as derived by Khoshnewiszadeh [1] would be greatly compromised by the changes in the turbulence velocity field. It is likely that the human operator would adapt his muscle dynamics to compensate for the variations in turbulence dynamically, and if this were

the case an adaptive model and different identification methods would be required to mitigate BDFT.

Introduction to the Preliminary Research

With the literature review presented in the previous chapters, interesting research gaps were identified in regards to model-based mitigation of *biodynamic feedthrough* (BDFT) occurring with *touchscreen* (TSC) interfaces, specifically for the context of aircraft cockpits. In particular, the model used in literature [1] lacks validation with realistic motion disturbances, such as (simulated) turbulence.

Expanding the research in this direction was the main goal of the remainder of the thesis' work. This work was split in a preliminary phase, in which research was performed through computer simulations, and in an experimental phase, in which the SIMONA Research Simulator (SRS) of TU Delft will be used to verify the hypothesis formulated from the initial simulations.

In the first part of the preliminary research, the data from the experiment conducted by Khoshnewisazadeh [1], available in the repositories of the research group at TU Delft, were used to test different methods to fit the BDFT model to the data, in an attempt to achieve higher performance of BDFT mitigation. This includes the evaluation of a time domain identification approach and of different cost functions for the frequency domain approach already used in literature, both discussed in Chapter 6.

In the second phase, BDFT occurring in turbulence was simulated using the model derived in Khoshnewisazadeh's research [1]. This simulation required a sequence of steps, described by the schematic in Figure 5.1.

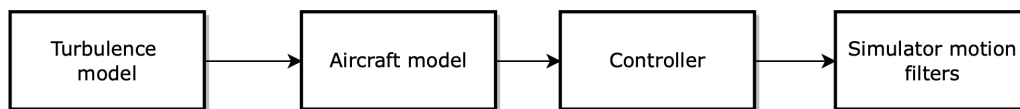


Figure 5.1: Schematic of the steps required for the simulation of experimental conditions.

At first, the *patchy turbulence model* was used to generate a turbulence velocity field. The characteristics of this velocity field dependent on the selection of the parameters used as input to the turbulence model. Once generated, the turbulence was fed as input to an aircraft model, which simulates how the aircraft, in a certain trim configuration, responds to such disturbances. The aircraft model used in this work is a non-linear MATLAB Simulink model for the Cessna Citation 500, frequently employed for human machine interface studies, including in previous work modeling human-TSC interaction in turbulence [16, 49, 58–60]. The coupling of the output of the patchy turbulence model with the aircraft model is straightforward, as both models have been developed within the same department at TU Delft. The specifics have already been mentioned in Section 4.3.3 for the Literature Review part of this report, and are not discussed further.

For the cases in which turbulence leads to instability of the aircraft, a controller was developed to stabilize the aircraft, removing the low frequency components in the aircraft motion, while maintaining intact the high frequency components to which human-TSC interaction is susceptible.

If one were to directly perform the BDFT experiment on an aircraft, the accelerations output of this

aircraft model (coupled with the controller) would suffice for the preliminary analysis. For a first iteration however, testing on the ground with a moving base simulator is sufficient and cost effective. An extra step was therefore required: the aircraft responses were filtered with algorithms which restrict the aircraft's motion to the available motion space of the simulator, and optimize the filter settings to keep the fidelity of the simulations high. The in-depth study of the patchy turbulence modeling, the development of a controller and the selection of experimental conditions through parameters and filter setting optimization is discussed in Chapter 7.

Only after all the steps mentioned can BDFT be simulated giving the simulator's accelerations as input to the BDFT model. From various considerations made throughout the preliminary study, the plan of the experiment to be performed in the SRS was drawn, and from the outcome of the simulations, hypothesis were made, and presented in Chapter 8.

Biodynamic Feedthrough Identification

The data of Khoshnewisadeh's [1] experiment, available in the TU Delft repositories, were used to gain more insight on the *biodynamic feedthrough* (BDFT) model and its identification. While replicating the model identification proposed in literature, the use of cost functions tailored to the optimization algorithms was explored to increase identification performance. The cost function tested and the results obtained are discussed in Section 6.1. In addition a time domain identification approach was used to fit the BDFT data directly to the parametric BDFT model, in an attempt to obtain a more accurate and versatile method for the specific problem of the identification of a BDFT model for interactions between a human operator and a *touchscreen* (TSC) interface. Methods and results are shown in Section 6.2. The chapter concludes with a summary, Section 6.3.

6.1. Effect of different cost functions

In literature, in order to model BDFT occurring with TSCs in continuous tracking tasks, BDFT estimates derived from experimental data were fitted to a parametric model, as explained in Section 3.4. The accuracy of this fit depends on the optimization algorithm used, on the cost functions minimized, and of course on the accuracy of the non-parametric estimates themselves. The optimization algorithm used by Mobertz [17] and subsequently Khoshnewisadeh [1] was MATLAB's *fminsearch*, iterating over sets δ of model parameters with the objective to minimize the normalized magnitude of the error between the non-parametric estimate of BDFT $\hat{H}_{BDFT}(j\omega_d)$ and the BDFT model $H_{BDFT}(j\omega_d|\delta)$, Equation 3.9 from Section 3.4, reported here for clarity.

$$J(\delta) = \sum_{k=1}^{Nd} \frac{|\hat{H}_{BDFT}(j\omega_d) - H_{BDFT}(j\omega_d|\delta)|}{|\hat{H}_{BDFT}(j\omega_d)|} \quad (6.1)$$

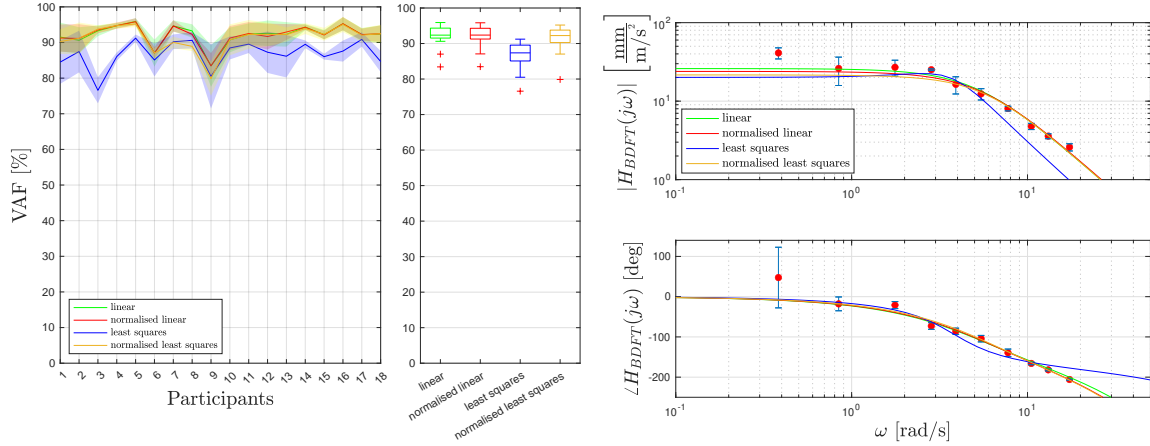
As mentioned, performance of the optimization is dependent on how suited the cost function is for the algorithm used. Many optimization algorithms are designed to use the second derivative of the cost function to search for the global minimum: cost functions having a second derivative, like ones based on the square of the error, lead to faster and more accurate optimizations. For this reason, identification of the BDFT model is replicated here using the data from Khoshnewisadeh's experiment [1] with the following cost functions: a linear cost function (Equation 6.2), the normalized linear cost function used in literature (Equation 6.1), a least squares cost function (Equation 6.3) and a normalized least squares cost functions (Equation 6.4).

$$J(\delta) = \sum_{k=1}^{Nd} |\hat{H}_{BDFT}(j\omega_d) - H_{BDFT}(j\omega_d|\delta)| \quad (6.2)$$

$$J(\delta) = \sum_{k=1}^{Nd} |\hat{H}_{BDFT}(j\omega_d) - H_{BDFT}(j\omega_d|\delta)|^2 \quad (6.3)$$

$$J(\delta) = \sum_{k=1}^{Nd} \frac{|\hat{H}_{BDFT}(j\omega_d) - H_{BDFT}(j\omega_d|\delta)|^2}{|\hat{H}_{BDFT}(j\omega_d)|^2} \quad (6.4)$$

To quantify how much of the BDFT component of the TSC input is modeled by each different fit, therefore giving a metric for identification performance, the *Variance Accounted For* (VAF) in Equation 3.13 is used. The cost function yielding the highest performance will be one having a high VAF averaged over the data of all participants, with a small spread. Figure 6.1a shows the identification performance of the cost functions for the case of heave motion disturbances causing BDFT on the vertical screen input (the VER condition in literature), using the *Subject-Averaged* (SA) model.



(a) Identification performance across all participants.

(b) BDFT estimates for participant 1 and Bode plot of the fitted models.

Figure 6.1: Performance of different cost functions with the SA model, VER case.

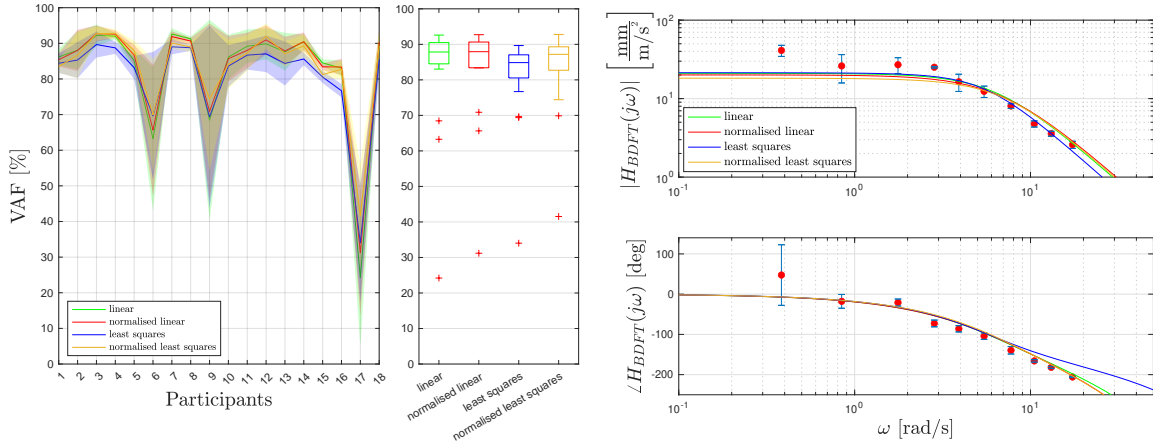
The highest average performance is achieved using the normalized least squares cost function, closely followed by the normalized linear and linear cost functions. The normalized linear and normalized least squares cost functions have a slightly larger spread, the linear has more outliers. To have a closer look at how the fitted models differ, the BDFT estimates and the frequency response of the model fitted with the different cost functions are shown in Figure 6.1b. It can be seen that the least squares cost function and, to a lower extent, the linear cost function, fail to model the high frequency content of BDFT. This is to be expected, as the value of the cost function will depend on the magnitude of the estimates at each point, which is clearly lower at high frequencies compared to the value at low frequencies. The low-middle frequencies will therefore be overfitted at the expenses of the high frequencies. The normalized error cost functions solve this problem, giving equivalent weight to the value of the cost function at all point, low and high frequencies alike, and in general a better fit.

Similar considerations can be made when looking at the identification performance and model fit for the *One-Size-Fits-All* (OSFA) case, in Figure 6.2. Again, performance is roughly equivalent for the normalized least squares, normalized linear and linear cost functions, and similarly the spread. The three outliers were already identified by Khoshnawisadeh [1] as showing considerably lower feedthrough compared to the other participants, and therefore not being well modeled with the OSFA model.

In conclusion, contrary to expectations there is no clearly better performing cost function between the normalized least squares, the normalized linear and the linear cost function. The normalized least squares cost function will lead in most cases to a negligibly higher performance, while the use of the normalized linear will be preferable if the need arises to make a direct comparison between the results of the experiment proposed in this work and the data reported in Khoshnawisadeh's work [1].

6.2. Time domain identification of biodynamic feedthrough

As mentioned in Section 3.4, a frequency domain approach was used by Mobertz [17] and Khoshnawisadeh [1] to derive a BDFT model from the data collected in their respective experiments. This frequency domain identification approach requires a non-parametric estimation of BDFT before the



(a) Identification performance across all participants.

(b) BDFT estimates for participant 1 and Bode plot of the fitted models.

Figure 6.2: Performance of different cost functions with the OSFA model, VER case.

data can be fitted to a transfer function. In the cases where the dynamics of the system are not known in advance, this extra step can be useful to derive a lumped model to fit to the data. However, since a parametric BDFT model has been already tested in literature, this step becomes superfluous, and only contributes to add estimation errors to the final BDFT model fitting, especially when considering the large errors associated to the low frequencies estimates, see Figure 3.2a. Time domain identification directly fits the model on the time domain data, avoiding the extra step just mentioned, possibly increasing accuracy.

A time domain identification algorithm is therefore tested on the data collected by Khoshnawiszadeh [1] during his experiment, evaluating the performance through the VAF in Equation 3.13, and comparing it to the VAF resulting from the frequency domain identified models. For a valid comparison with the frequency domain approach used in literature, the cost function originally employed by Khoshnawiszadeh [1] is used. The notation used in this section follows the one used in Figure 3.7.

6.2.1. Implementation

A time domain identification algorithm is used here to fit the parametric BDFT model described by Equation 3.5 directly to the time traces of the involuntary component of the TSC input signal u^{meas} , that is obtained by Fourier transforming the TSC input signal u , removing all the components at frequencies not belonging to the disturbance signal and bringing the signal back to the time domain with the inverse Fourier transform. This BDFT component of the input u^{meas} is then fed to the optimization algorithm, which outputs a optimal set of parameters for the parametric model, corresponding to a minimum error between the time domain signal u^{meas} and the BDFT model output.

For this study, a Maximum Likelihood Estimation method is used, in particular the Gauss-Newton algorithm described by Zaal et al. [48]. Since the BDFT model is linear, a gradient based estimation is sufficient to consistently find a solution for the set of parameters corresponding to the global minimum. The upper and lower limits used by Khoshnawiszadeh [1] for the frequency domain identification, reported here in Table 3.4, are used as constraints for the time domain optimization. Similarly, the initial guess in Table 3.4 is used.

6.2.2. Performance comparison of the time and frequency domain identification

Figure 6.3 shows the BDFT identification performance for the case of heave motion affecting the vertical inputs on the TSC, the VER case. Figure 6.3a and Figure 6.3b respectively show the SA and the OSFA models.

Using either model, the two identification methods give comparable results in terms of identification performance. A slightly higher performance is achieved with the SA model for the time domain identification. This difference causes a slightly lower performance of the time domain identification using the OSFA model. This is because the closer the fit gets to the actual BDFT dynamics of each participant, which is of course positive for the evaluation of the SA model, the less generalized the parameters of

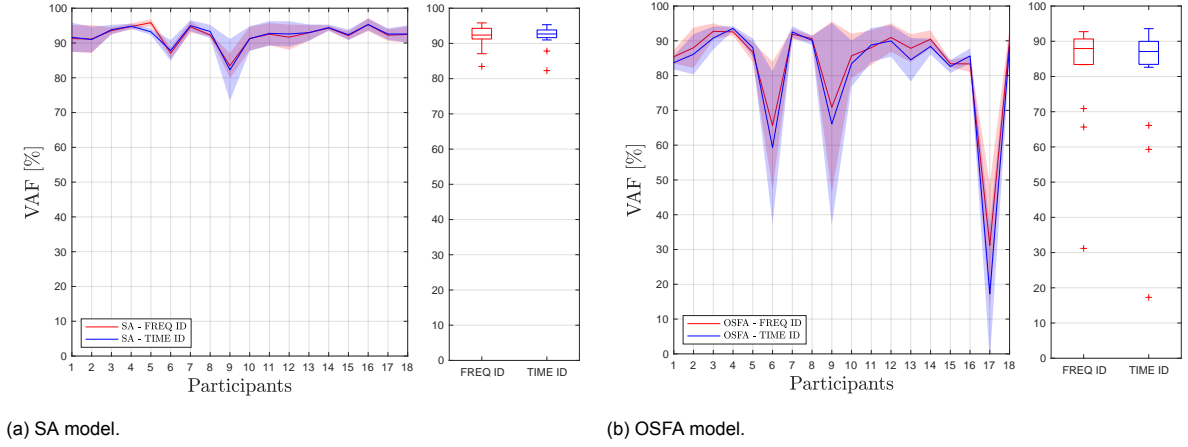


Figure 6.3: Performance of the time domain and the frequency domain identification, VER case.

the OSFA model are for the participants with outlier behaviors.

Figure 6.4a shows the frequency response of the models identified with the time domain and the frequency domain approaches. Figure 6.4b shows the time traces of the measured BDFT component of the inputs signal u^{meas} , as well as the BDFT component simulated using the time domain and the frequency domain models, u^{mod} , all for the VER case and the SA model, for participant 1.

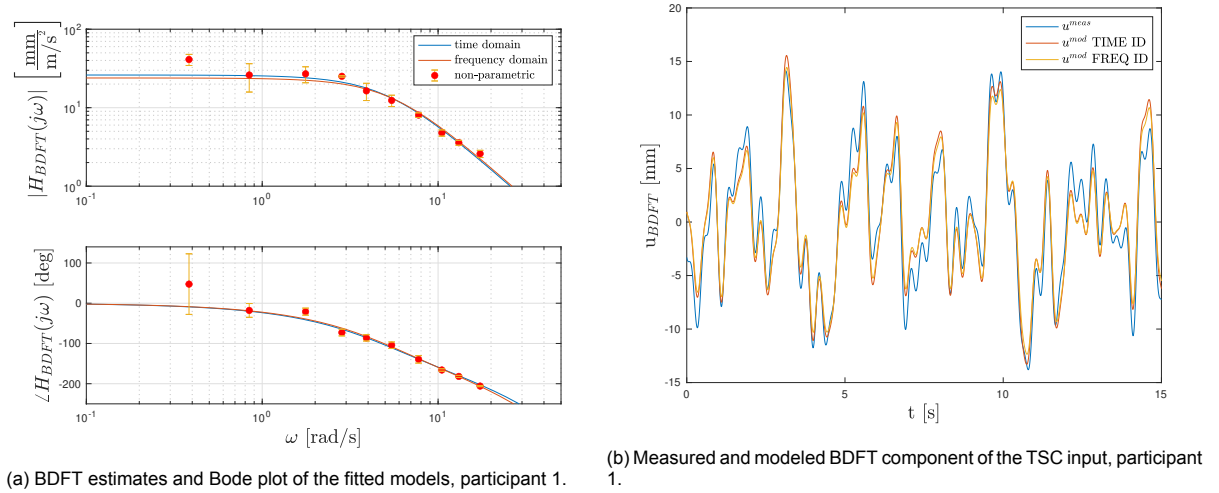


Figure 6.4: Comparison between the SA models obtained with the frequency domain approach and the time domain approach, VER case.

These figures show that the main differences between the two models for participant 1 lie in the gain, which is clearly higher in the time domain identified model, and in the time constant, which is lower in the time domain model. These findings can be generalized through boxplots showing the distribution of the parameters for the time and the frequency domain data across all participants, for both the heave-vertical input case (VER) and the sway-horizontal input case (HOR), see Figure 6.5. As mentioned however, the higher gain and lower time constant in the time domain identified models do not lead to a considerably higher VAF, their effect is averaged out throughout the measurement with points at which the feedthrough occurring is actually lower, such as around 14 seconds in Figure 6.4b.

A final comment can be made from the boxplots showing the values of the parameters for the SA model in Figure 6.5. For almost all cases, the time domain approach leads to a larger spread of the values of the parameters across the participants. This can again be connected to fact that most time domain SA fits slightly outperform the frequency domain fits. The larger spread of the parameters is linked to the variability of the dynamics across participants, which are somewhat averaged out by the

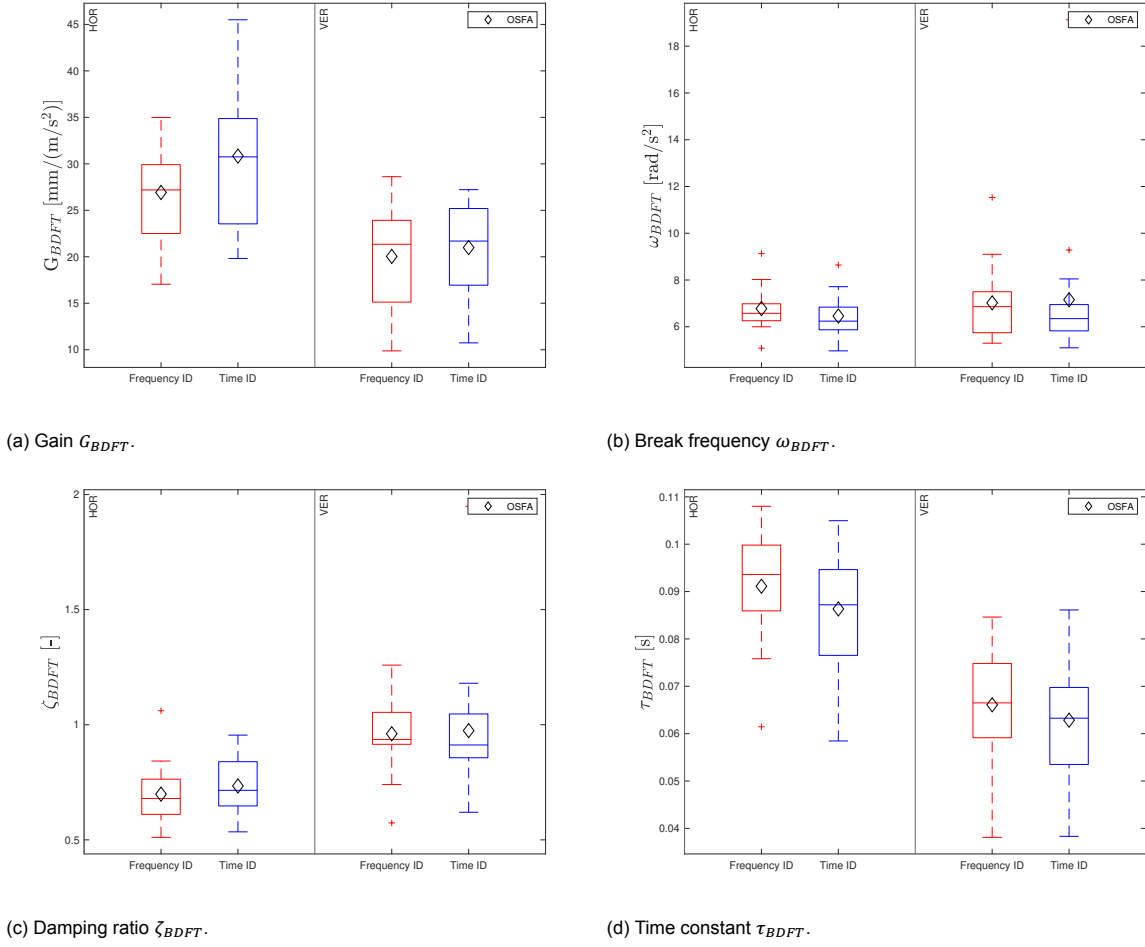


Figure 6.5: Comparison between the model parameters of the SA and OSFA models, identified from a time and frequency domain approach, for the heave-vertical TSC input (VER) case and the sway-lateral TSC input (HOR) case.

slightly less precise frequency domain fit. Causing also the OSFA model to perform better when the frequency domain approach is used.

6.3. Summary

Using the data from Khoshnewisadeh's experiment [1], different methods for the identification of the parameters of the *biodynamic feedthrough* (BDFT) model from literature were tested, with the objective to increase the amount of the BDFT component of the input accounted by the model.

Research on different cost functions to be used for a frequency domain identification approach showed that a slightly higher performance is achieved using a normalized least squares cost function compared to linear, least squares and normalized linear cost functions. The difference in performance between the normalized least squares and the normalized linear cost function is very small, therefore to maintain the ability to compare subsequent works with Khoshnewisadeh's [1], the normalized linear cost function can be used without a great compromise.

Research on the use of time domain approach in place of frequency domain approach for the identification of BDFT highlighted that time domain approach gives a slightly better performance when applied to the Subject-Averaged models. On the contrary frequency domain identification outperforms its time domain alternative for the One-Size-Fit-All model, as the time domain identification overfits the data of each participant, leading to a lower generalizability of the parameters especially in the presence of outliers. It is however stressed that the differences found are on average very small, and that either method is suitable for effective BDFT mitigation.

Design of the Experimental Conditions

The *patchy turbulence model* has been identified as the preferred model to simulate the turbulence velocity field to be used in a simulator experiment on the *SIMONA Research Simulator* (SRS). Not only it can generate turbulence homogeneous in time, it also can be used to simulate non-Gaussian turbulence, presenting variability in the form of patchiness. Moreover, use of this model allows to connect the current study with the Finger-Fitts' law study performed by Jacobson [16]. This chapter describes the preliminary research performed on *biodynamic feedthrough* (BDFT) occurring in patchy turbulence. The baseline conditions used for the study of the turbulence model are described in Section 7.1, followed by the verification of the *patchy turbulence model* in Section 7.2. The design of a controller to be used to maintain the aircraft at trim conditions while going through patches of turbulence is dealt with in Section 7.3. The study of the parameters and filter settings for the design of the experimental conditions for the simulator experiment are discussed in Section 7.4, followed by an overview of the experimental conditions chosen, and the expected effects on BDFT modeling and mitigation in Section 7.5. Lastly, the content of this chapter is summarized in Section 7.6.

7.1. Baseline turbulent flight conditions

In Jacobson's work [16], the turbulent velocity field was generated using a MATLAB Simulink script of the *patchy turbulence model*, available in the repository of the research group at TU Delft. Older versions of these files were used in other thesis works, see [58, 73]. These scripts were used as a starting point for the verification of the model and subsequently for research on *biodynamic feedthrough* (BDFT) with *touchscreens* (TSCs). To relate the new research with Jacobson's work [16], the turbulence conditions selected by Jacobson were investigated as a possible experimental condition for this study. These were replicated from the information provided in the thesis and in the files accompanying it, for example the original MATLAB files and the configuration files for the *SIMONA Research Simulator* (SRS). The parameters used for the generation of patchy turbulence are the following:

- Altitude, $h = 28000$ ft,
- Velocity, $V = 165$ m/s,
- Length scale, $L_{u_g} = 300$ m,
- Intensity, $\sigma_g^2 = 1$ m²/s²,
- Kurtosis related, $Q = 0.5$,
- Patch length related, $R = 0.7$.

In addition, a trim file for the Simulink aircraft model was generated for straight, level flight at an altitude of 28000 ft (8534.4 m), simulating the trim conditions used in Jacobson's study [16]. These are suitable values for the current study, as tasks that are likely to be performed on a TSC in future interfaces, for example waypoint changing, can be assumed to be performed mostly at cruise altitudes and velocities.

Moreover the conditions implemented are indeed valid for the *patchy turbulence model*, which is based on the assumption of isotropy. The selected altitude is well above the 2 km atmospheric boundary layer, which is where the turbulent flow is anisotropic [52]. The initial aircraft mass used by Jacobson could not be established with certainty, so a mass of 4000 kg was used, within the normal range described in the trimming routine files.

While each run in Jacobson's experiment [16] lasted about 10 minutes, only 90 seconds of simulation are needed for the BDFT mitigation experiment developed by Mobertz and Khoshnewisadeh [1, 17]. Since the experiment for this work will be a modification of the latter, the simulations that are conducted for the preliminary study all have a duration of 90 seconds.

7.2. Verification of the patchy turbulence model

As mentioned, the MATLAB Simulink implementation of the *patchy turbulence model* was a pre-existing file, consequently a first step taken was the verification of such implementation by comparison with the description of the model in the original works implementing it [56, 65]. The output of the model was further processed with the objective of verifying that the statistical properties of the resulting turbulence velocity field would match the desired ones, in accordance with the theoretical description of the model from van de Moesdijk [56, 65]. This verification ended up highlighting issues both in the implementation of the model used by Jacobson [16], and in the model itself.

The following sections discuss the verification of the *patchy turbulence model*, both in its implementation and in its description, and propose a correction to the model. Since the issues found caused overlapping effects, influencing the final results in a variety of ways, in order to clearly show the effect of each issue in the original description of the model, a baseline 'corrected' model is used, with the parameters reported in Section 7.1, varying each concerned variable one at a time. As for the issues contained in the turbulence employed by Jacobson in his study [16], a short list of these is given as reference for future studies together with a quick evaluation of the outcome of the simulation with the original implementation and with the corrected turbulence model.

Finally a note on the notation. This section often borrows the notation of the *patchy turbulence model* schematic in Figure 4.10, to refer to the signals that construct the patchy velocities. The reader should keep in mind that figure to understand the discussion.

7.2.1. Verification of the original description of the model

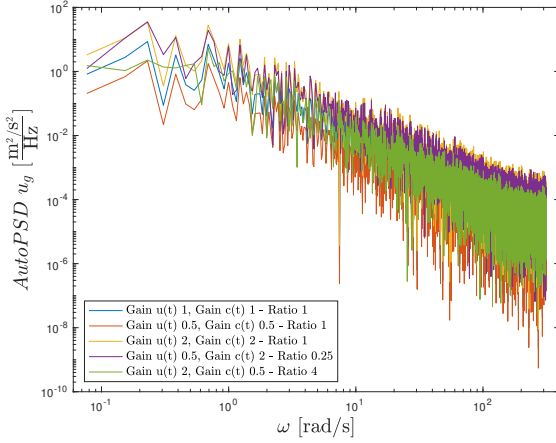
As mentioned in Section 4.4.2, the objective of the *patchy turbulence model* is to simulate a turbulence velocity field having Dryden spectrum with selected intensity and length scale, and presenting variability through the manipulation of parameters dictating the Kurtosis of the *probability density function* (PDF) of the turbulence velocities and the length of inhomogeneous patches within the length scale [56]. From the description of the model it is apparent that, regarding the characteristics mentioned, the generated turbulence is meant to be fully characterized by the parameters of the model, σ_g^2 , L_{ug} , Q and R . In this regards, a first issue arises by noting the presence in Figure 4.10 of gains, labeled in the schematic itself as a means to set the fourth moment of inertia of the distribution of turbulence velocities. These gains multiply the signals $u(t)$ and $c(t)$, and therefore affect both the intensity and the PDF of the resulting turbulence velocity $w(t)$: multiplying a signal with a gain equals to changing the intensity of the signal, therefore the gains on the two signals $u(t)$ and $c(t)$, later multiplied, have an effect on the overall gain of $w(t)$, their product; moreover, recalling that parameter Q is defined as the ratio of the intensities of the two signals, σ_u/σ_c , a set of gains with ratio different from 1 has an effect on the PDF comparable to parameter Q , effectively overwriting the Kurtosis set as input through Q .

The effect of the gains is shown graphically and numerically taking as an example the longitudinal and vertical velocities output of the patchy turbulence model, using the equations in Appendix A. The baseline settings for the parameters used are the ones selected by Jacobson [16], as reported in Section 7.1. For the sake of clarity, the most relevant for the considerations on the effect of the gains are repeated here: turbulence intensity $\sigma_g^2 = 1 \text{ m}^2/\text{s}^2$, and $Q = 0.5$, setting a Kurtosis $K = 3.24$. The simulation is performed with an arbitrary simulation time of 9000 s, sufficient to extract a meaningful (convergent) estimation of the Kurtosis and of the turbulence intensities from the data. In the first columns of Table 7.1, the values of the gain selected for testing are reported, followed by their ratio. The PSDs of the longitudinal and vertical turbulence velocities for each couple of gains reported in the table are shown in Figure 7.1a and Figure 7.1b respectively. To distinguish the input parameters σ_g^2 and

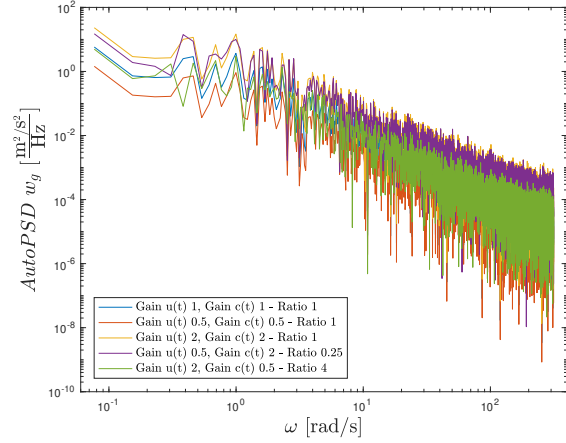
K from the corresponding values calculated from the resulting turbulence velocity $w(t)$, subscript w is used. Therefore σ_w^2 and K_w denote respectively the turbulence intensity and the Kurtosis calculated from the turbulence velocity $w(t)$.

Table 7.1: Influence of the gains and their ratio on Kurtosis K_w and on intensity σ_w^2 of the longitudinal and vertical turbulence velocities.

Turbulence	Gain $u(t)$ [-]	Gain $c(t)$ [-]	Ratio [-]	K_w [-]	σ_w^2 [m ² /s ²]
Longitudinal	1	1	1	3.18	1.02
Vertical	1	1	1	3.24	1.03
Longitudinal	0.5	0.5	1	3.18	0.26
Vertical	0.5	0.5	1	3.24	0.26
Longitudinal	2	2	1	3.18	4.08
Vertical	2	2	1	3.24	4.15
Longitudinal	0.5	2	0.25	3.01	3.27
Vertical	0.5	2	0.25	2.99	3.39
Longitudinal	2	0.5	4	6.99	1.05
Vertical	2	0.5	4	6.93	1.02



(a) Longitudinal PSDs.



(b) Vertical PSDs.

Figure 7.1: Influence of the patchy turbulence model gains and their ratio on the PSD of the longitudinal and vertical turbulence velocities.

Already by looking at the first two rows of the table, it is visible that for both the longitudinal and vertical cases a gain of one leads to Kurtosis K_w and intensity σ_w^2 of the resulting turbulence velocity $w(t)$ which are very close to the input Kurtosis K and the input intensity σ_g^2 . On the other hand, keeping the ratio of the two gains constant while changing their magnitude (Gain $u(t)$ = Gain $c(t)$ = 0.5, and Gain $u(t)$ = Gain $c(t)$ = 2), the resulting Kurtosis K_w remains unchanged, while the intensity decreases and increases, respectively for the two cases. The last four rows of Table 7.1 show cases in which the ratio of the gains is not a unity. In this case, both intensity σ_w^2 and Kurtosis K_w vary greatly from the input ones. These considerations are also visible in Figure 7.1a and Figure 7.1b, where the PSDs of the resulting turbulence velocities have the same shape only as long as the ratio of the gains is kept to 1, while each curve abiding to such condition is displaced above of below the baseline blue curve (with gains equal to 1), depending on whether the turbulence intensity is increasing or decreasing. The results shown in Table 7.1 and in Figure 7.1 demonstrate that the use of gains nullifies the input parameters that are meant to define a precise patchy turbulence velocity field.

For reference, an estimation of the error on the calculation of K_w is made from Equation 7.1¹, which

¹<https://www.ibm.com/support/pages/standard-errors-skewness-and-kurtosis-are-all-same-set-variables>, [cited on 15 June 2022]

gives the standard deviation σ_K of the Kurtosis, as a function of the number of points over which it is calculated, N , and the variance σ_{skew}^2 of the Skewness of the PDF.

$$\sigma_K = \sqrt{\frac{4(N^2 - 1)\sigma_{skew}^2}{(N - 3)(N + 5)}}, \text{ with} \quad (7.1)$$

$$\sigma_{skew}^2 = \frac{6N(N - 1)}{(N - 2)(N + 1)(N + 3)}$$

With measurement points $N = 9001^2$, corresponding to the 9000 seconds of simulation performed, the Kurtosis of the PDF of the turbulence velocity is accurate within an interval of ± 0.05 . The order of magnitude of the error is a further confirmation that the error caused by the presence of gains with ratio different from a unity is not negligible for the modeling of the Kurtosis.

Another criticism to these gains can be made in regards to the assumption of isotropy under which the patchy turbulence model is derived. Following this assumption, the model should take as an input the same turbulence intensity for the longitudinal, lateral and vertical turbulence velocity field. On the other hand, if the gains are set independently for each of the turbulence velocity components, as happens in several works in literature [16, 58, 73], the resulting velocity field will have non-isotropic characteristics, with arbitrary turbulence intensity in each direction and therefore go against the assumptions.

A possible explanation for the use of the gains in the original works [56, 65], comes from the fact that the schematic described by van de Moesdijk actually represents the schematic for the components of an analogue computer, used at the time to make simulation of the turbulence velocities. The gains might have been placed there to be used as signal amplifiers, needed to boost the voltage of the $u(t)$ and $c(t)$ signals, whose initial voltage is limited by the need to keep an high signal-to-noise ratio. This hypothesis however, collides with the writing on the schematic itself, which explicitly states that the gains are used to set the fourth central moment, i.e., the product of the Kurtosis and the square of the variance. To be noted, works subsequent to the original have used the *patchy turbulence model* reporting values for the gains, without giving an explanation of why they were selected as such, and for what purpose, see Veldhuijzen [73], but also the files accompanying the thesis works of Lam [58] and Jacobson [16].

As a correction to the patchy turbulence model, it is proposed to remove the gains from its schematic.

Another issue in the original model is found in the linear filters shaping the spectrum of the antisymmetric components of the turbulence velocity field, i.e., Equation A.10 and Equation A.11 of Appendix A. The issue was first seen in the mismatch between the intensities calculated from the antisymmetric components \hat{u}_{gasymp} and α_{gasymp} simulated through the *patchy turbulence model*, and the same intensities calculated using the *Gaussian turbulence model*.

As a premise, for the antisymmetric case the variables $\sigma_{\hat{u}_g}^2$ and $\sigma_{\alpha_g}^2$, defined as σ_g^2/V^2 , cannot be used as a measure of the intensity of the simulate turbulence component, in contrary to what is done with σ_g^2 in the symmetric case; when looking at the equation describing the power spectrum for symmetric turbulence velocities, for example the longitudinal spectrum in Equation 4.6, the variable σ_g^2 represents the intensity of turbulence and can be directly compared with the intensity calculated from the time traces, or alternatively from the spectrum of the turbulence velocity. Conversely, when looking at the power spectrum in Equation 4.9 and in Equation 4.10, these present a different structure, moreover they are an approximation of the analytical equations for the power spectrum of the turbulence components. Following this considerations, it was decided to compare directly the area under the curve of the PSDs of the Gaussian and patchy turbulence velocities as a way to verify the patchy turbulence model. The outcome of this comparison, again performed using the parameters in Section 7.1 as baseline conditions and with a 9000 seconds simulation can be found in Table 7.2, together with the values found applying a correction to the model, which will be discussed shortly.

As mentioned, it can be immediately noted that there is a mismatch between the intensity obtained with the *Gaussian turbulence model* and the one obtained with the *patchy turbulence model*. Additionally, the value of the Kurtosis of the signal \hat{u}_{gasymp} output of the model, $K_w = 3.66 \pm 0.05$, is off compared

²Erratum: N = 90000.

Table 7.2: Intensity σ_w^2 and Kurtosis K_w of the antisymmetric turbulence components, depending on the model used.

Model used	$\hat{u}_{gasy m}$		$\alpha_{gasy m}$	
	σ_w^2 [-]	K_w [-]	σ_w^2 [rad ²]	K_w [-]
Gaussian	1.44E-06	3.01	1.49E-06	2.99
Patchy (original)	9.56E-07	3.66	9.72E-07	3.24
Patchy (corrected)	1.48E-06	3.26	1.51E-06	3.24

to the input that had been given, $K = 3.24$.

The source of this issue was found when studying the equations of the shaping filter for signal $c(t)$. To show the issue and the correction applied a few equations already discussed are repeated in this paragraph: Equation 7.2 is the shaping filter for signal $c(t)$ for the construction of the symmetric, longitudinal turbulence velocity; Equation 7.3 is the equation of the shaping filter for the longitudinal turbulence velocity in the Gaussian model, directly derived from the Dryden spectrum as mentioned in Section 4.4.1; Equation 7.4 is the shaping filter for signal $c(t)$ for the construction of the antisymmetric component $\hat{u}_{gasy m}$; finally Equation 7.5 is the equation of the shaping filter for the antisymmetric component $\hat{u}_{gasy m}$ in the Gaussian model. The issues and correction are shown here for the longitudinal component $\hat{u}_{gasy m}$. However, the same considerations are valid also for the vertical component $\alpha_{gasy m}$.

$$H_{c_{ug}}(j\omega) = \frac{1}{W_c} \sigma_c \sqrt{2 \frac{L_{ug}}{V}} \frac{1}{1 + \frac{L_{ug}}{V} j\omega} \quad (7.2)$$

$$H_{u_g}(j\omega) = \frac{1}{W_k} \sigma_g \sqrt{2 \frac{L_{ug}}{V}} \frac{1}{1 + \frac{L_{ug}}{V} j\omega} \quad (7.3)$$

$$H_{c_{\hat{u}_{gasy m}}}(j\omega) = \frac{1}{W_c} \sqrt{\frac{1}{1 + Q^2}} I_{\hat{u}_g}(0, B) \frac{1 + \tau_3 \frac{L_{ug}}{V} j\omega}{(1 + \tau_1 \frac{L_{ug}}{V} j\omega)(1 + \tau_2 \frac{L_{ug}}{V} j\omega)} \quad (7.4)$$

$$H_{\hat{u}_{gasy m}}(j\omega) = \frac{1}{W_k} \sqrt{\frac{L_{ug}}{V}} I_{\hat{u}_g}(0, B) \frac{1 + \tau_3 \frac{L_{ug}}{V} j\omega}{\left(1 + \tau_1 \frac{L_{ug}}{V} j\omega\right) \left(1 + \tau_2 \frac{L_{ug}}{V} j\omega\right)} \quad (7.5)$$

Recalling that $\sigma_c = \sigma_g / \sqrt{1 + Q^2}$, as shown in Equation A.7 of Appendix A, Equation 7.2 becomes Equation 7.6.

$$H_{c_{ug}}(j\omega) = \frac{1}{W_c} \frac{\sigma_g}{\sqrt{1 + Q^2}} \sqrt{2 \frac{L_{ug}}{V}} \frac{1}{1 + \frac{L_{ug}}{V} j\omega} \quad (7.6)$$

A quick comparison of Equation 7.6 and Equation 7.3 for the symmetric case shows that, when $Q = 0$, i.e., when the patchy model is set to simulate Gaussian turbulence, the shaping filter for signal $c(t)$ coincides with the shaping filter of the Gaussian turbulence velocity. In fact, looking more closely at the Equation A.6 and Equation A.7, describing the shaping filters for the construction signals $a(t)$ and $b(t)$, it can be clearly seen that the signals $a(t)$ and $b(t)$ are both multiplied by Q , becoming 0 when simulating Gaussian turbulence. In essence, signal $c(t)$ alone simulates Gaussian turbulence when $Q = 0$.

Moving back to the shaping filter $c(t)$ for the antisymmetric component $\hat{u}_{gasy m}$ in Equation 7.4, similar characteristics can be observed when comparing the equation with the Gaussian shaping filter in Equation 7.5, except for a $\sqrt{L_{ug}/V}$ factor. Moreover, looking at the filters for $a(t)$ and $b(t)$ in Equation A.10, exactly the same considerations on the modeling of Gaussian turbulence with the patchy model

can be made. Signal $c(t)$ should coincide with the Equation for the corresponding Gaussian turbulence component (Equation 7.5) when Q is set to 0.

The correction to the patchy turbulence model proposed is therefore the use of the following shaping filters for the signal $c(t)$, used for the construction of the antisymmetric components \hat{u}_{gasymp} and α_{gasymp} .

$$H_{c\hat{u}_{gasymp}}(j\omega) = \frac{1}{W_c} \sqrt{\frac{1}{1+Q^2} \frac{L_{u_g}}{V} I_{\hat{u}_g}(0, B)} \frac{1 + \tau_3 \frac{L_{u_g}}{V} j\omega}{(1 + \tau_1 \frac{L_{u_g}}{V} j\omega)(1 + \tau_2 \frac{L_{u_g}}{V} j\omega)} \quad (7.7)$$

$$H_{c\alpha_{gasymp}}(j\omega) = \frac{1}{W_c} \sqrt{\frac{1}{1+Q^2} \frac{L_{u_g}}{V} I_{\alpha_g}(0, B)} \frac{1 + \tau_6 \frac{L_{u_g}}{V} j\omega}{(1 + \tau_4 \frac{L_{u_g}}{V} j\omega)(1 + \tau_5 \frac{L_{u_g}}{V} j\omega)} \quad (7.8)$$

The reasoning based on the equations discussed above can be further confirmed when looking at Figure 7.2, Figure 7.3 and Figure 7.4. Figure 7.2 shows the PSD of the symmetric turbulence velocity $u_g(t)$, in comparison to the analytical equation for its spectrum as given in Equation 4.6, and the PSD of the construction signal $c(t)$.

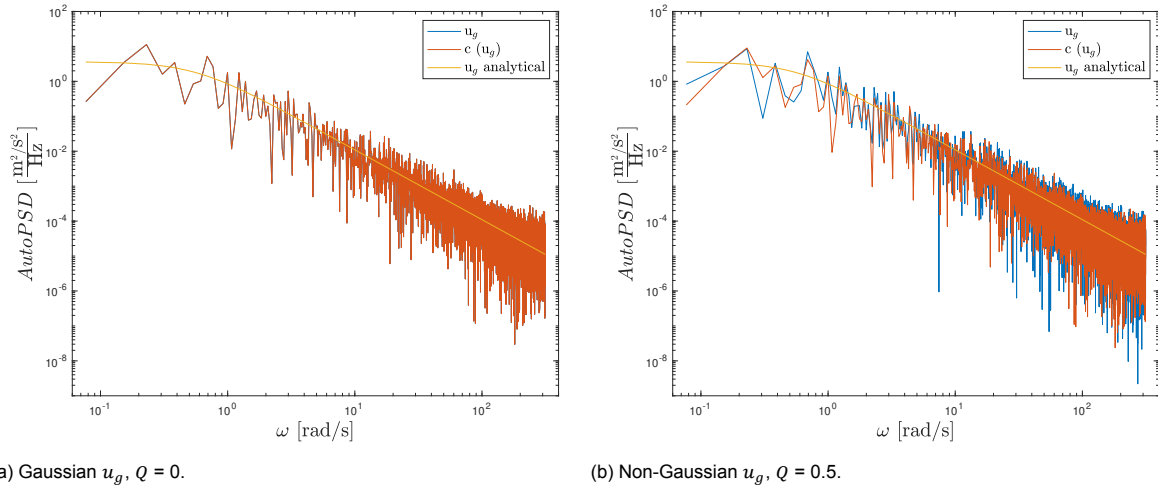


Figure 7.2: PSDs of the turbulence velocity u_g and the construction signal $c(t)$, and the analytical spectrum of u_g , for Gaussian and non-Gaussian turbulence.

For Gaussian turbulence (generated with the *patchy turbulence model*), shown in Figure 7.2a, the PSD of signal $c(t)$ perfectly coincides with the PSD of the turbulence velocity u_g , and is shown to be modeling well the analytical function of the power spectrum. For non-Gaussian turbulence, shown in Figure 7.2b, $c(t)$ does not coincide perfectly with u_g , as the simulated turbulence velocity also depends on a non-zero $u(t) = a(t) \cdot b(t)$ signal. The simulated non-Gaussian turbulence velocity u_g is again accurate in modeling the analytical power spectrum given by Dryden's equations.

Looking at the same plots for the antisymmetric component of turbulence \hat{u}_{gasymp} generated with the *original patchy turbulence model* in Figure 7.3, it can be noted that although the same behavior with regards to the value of Q can be seen, the patchy turbulence model seems to simulate the antisymmetric component of turbulence \hat{u}_{gasymp} with a slightly lower intensity compared to the analytical function, given by Equation 4.9. Figure 7.4 shows the same plots as Figure 7.3, but outcome of a simulation performed with the *proposed correction to the patchy turbulence model*. It can be seen that, whether simulating Gaussian turbulence (Figure 7.4a) or non-Gaussian turbulence (Figure 7.4b), the PSD of the antisymmetric turbulence signal \hat{u}_{gasymp} matches more closely the analytical spectrum of \hat{u}_{gasymp} , in comparison to spectra shown in Figure 7.3 from the *original patchy turbulence model*.

Finally, checking the turbulence intensity from the antisymmetric turbulence components simulated with the proposed corrected patchy turbulence model and the conditions in Section 7.1, results coherent with the turbulence intensity calculated from the Gaussian turbulence model are found, and correct Kurtosis is observed. These values can be seen in Table 7.2, together with the values found with the

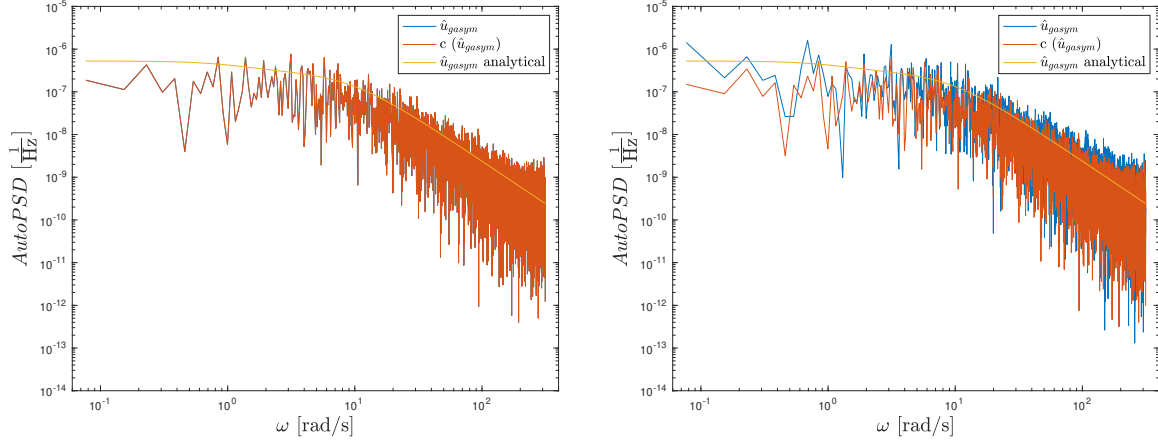
(a) Gaussian $\hat{u}_{g\text{asym}}$, $Q = 0$, from the original patchy model.(b) Non-Gaussian $\hat{u}_{g\text{asym}}$, $Q = 0.5$, from the original patchy model.

Figure 7.3: PSDs of the turbulence velocity $\hat{u}_{g\text{asym}}$ and the construction signal $c(t)$ from the *original patchy turbulence model*, and the analytical spectrum of $\hat{u}_{g\text{asym}}$, for Gaussian and non-Gaussian turbulence.

Gaussian model and with the original patchy turbulence model.

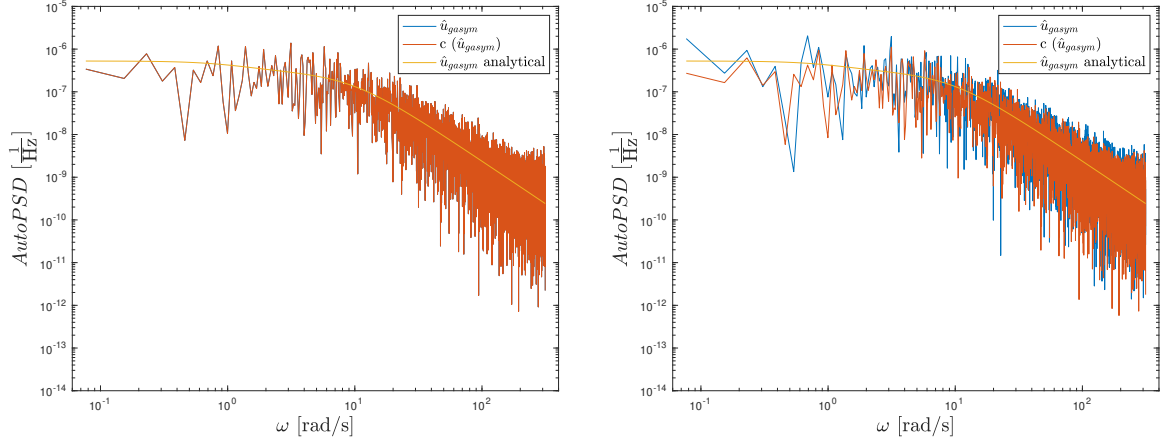
It should be added that a dimensional analysis on the shaping filters further confirms that the factor $\sqrt{L_{u_g}/V}$ is needed in $H_{c\hat{u}_{g\text{asym}}}(j\omega)$ and $H_{c\alpha_{g\text{asym}}}(j\omega)$, otherwise the sum $u(t) + c(t)$, generating signal $w(t)$, would be mathematically incorrect. To solidify the proposed corrections the equations for the shaping filters of the patchy turbulence antisymmetric components should be derived analytically, following the derivation of the symmetric patchy turbulence filter presented by van de Moesdijk in his 1975 report [56]. This is however out of the scope of the study, and is left aside for future research.

7.2.2. Verification of the previous implementations of the model

In addition to the issues that have been identified directly from the original description of the patchy turbulence model, some errors have been found in the implementation of the patchy turbulence model used by Jacobson in his work [16]. Since this research will fit between Jacobson's research [16] on human-TSC interaction and the model-based BDFT mitigation in Khoshnawizadeh's work [1], a few comments are left here on Jacobson's implementation and on its effects on the simulated turbulence used in his experiments.

In Jacobson's work [16], two additional errors were found in the generation of the antisymmetric components of the turbulence velocity field, $\hat{u}_{g\text{asym}}$ and $\alpha_{g\text{asym}}$. Both errors can be traced to the implementation of the constants $I_{\hat{u}_g}(0, B)$ and $I_{\alpha_g}(0, B)$, appearing in the equations of the antisymmetric components of the turbulence velocities, Equation A.10 and Equation A.11. These constants were originally calculated by Gerlach and Baarspul [64] using a definition of PSD which differs from the one used in later works, for example by Mulder et al. [47]. The original work includes a factor $1/\pi$ in the general definition of the PSD of a signal, therefore affecting the PSD of turbulence velocities discussed in this report in Equation 4.3. It is not uncommon for PSDs to have different definitions in literature, the difficulty in keeping track of the conventions used by each work is often a source of mistakes, like in this case. This $1/\pi$ factor was in fact removed in subsequent works using the antisymmetric turbulence components. Mulder et al. [69] reports both the new definition of the equations for the spectrum of $\hat{u}_{g\text{asym}}$ and $\alpha_{g\text{asym}}$ and updated tables containing the new values of the constants $I_{\hat{u}_g}(0, B)$ and $I_{\alpha_g}(0, B)$, differing from the original work of a factor π . The models used in Jacobson's work [16] use the equations for the filters derived from the definition of PSD including the $1/\pi$ factor, while the values of the constants $I_{\hat{u}_g}(0, B)$ and $I_{\alpha_g}(0, B)$ from tables in Mulder et al. [47], corrected for the new definition of PSD.

Again in regards to the constants $I_{\hat{u}_g}(0, B)$ and $I_{\alpha_g}(0, B)$, another error was found in the implementation used by Jacobson [16]. The tables found both in Gerlach [64] and in Mulder et al. [47] provide



(a) Gaussian $\hat{u}_{g\text{asym}}$, $Q = 0$, from the model with the proposed corrections. (b) Non-Gaussian $\hat{u}_{g\text{asym}}$, $Q = 0.5$, from the model with the proposed corrections.

Figure 7.4: PSDs of the turbulence velocity $\hat{u}_{g\text{asym}}$ and the construction signal $c(t)$ from the *patchy turbulence model with the proposed corrections*, and the analytical spectrum of $\hat{u}_{g\text{asym}}$, for Gaussian and non-Gaussian turbulence.

the values of $I_{\hat{u}_g}(0, B)$ and $I_{\alpha_g}(0, B)$ as a function of, respectively, $\sigma_{\hat{u}_g}^2$ and $\sigma_{\alpha_g}^2$, see Table A.1 in Appendix A. In Jacobson's work [16], the constants were used assuming $\sigma_{\hat{u}_g}^2 = \sigma_{\alpha_g}^2 = 1$. However, by construction the values of these constants are related to the turbulence intensity of the symmetric turbulence components σ_g^2 through the equations $\sigma_{\hat{u}_g}^2 = \sigma_{\alpha_g}^2 = \sigma_g^2/V^2$, as described in Section 4.3.4. To keep the resulting turbulence velocities non-dimensional as required by the model, the factor $1/V$ was instead multiplied with the output of the model, the resulting turbulence velocities. This is however not equivalent to the original description, and instead leads to the overestimation of the influence of the antisymmetric component for a given symmetric behavior, as can be seen in Figure 7.5. While the differences in the antisymmetric component are mainly due to the implementation errors, the differences visible in the symmetric components are caused by the use of gains multiplying signals $u(t)$ and $c(t)$ in the schematic in Figure 4.10, which have been discussed earlier in Section 7.2.1.

Following these discoveries, an attempt was made to understand the influence of the erroneous use of the *patchy turbulence model* on the experimental conditions. Figure 7.6 shows the effects on the aircraft responses of Jacobson's [16] turbulence in comparison to the effects of the corrected version of the turbulence model, for the same patchy turbulence parameters. As a disclaimer, it should be mentioned that while Jacobson simulated the patchy turbulence velocity field from the exact files used to generate the turbulence shown in Figure 7.5, the effect on the aircraft responses shown in Figure 7.6 is created from the coupling of the turbulence model with a MATLAB Simulink version of the same aircraft model used by Jacobson [16]. The simulation was not performed using the same files for the aircraft model, as Jacobson [16] worked directly on the DUECA environment (see [74]) of the SRS for the simulation of the aircraft responses, feeding as input to the model the output of the *patchy turbulence model* files that were discussed here. It can be noted immediately both from the specific forces and the rotational rates of the simulated aircraft, that the overestimation of the antisymmetric component of the turbulence velocity field has a major impact on the asymmetric motion of the aircraft. The specific force in the lateral direction, the roll rate and the yaw rate have much greater magnitude compared to the ones simulated with the corrected model. Through the non-linearities in the model, this leads with a small delay to instabilities also in the symmetric aircraft responses.

Indeed in the work performed by Jacobson [16], a (human) controller was needed to stabilize the simulated aircraft, which would not have been needed with a correct implementation of the model with the parameters specified. In any case, due to the influence of the controller on the final simulation used by Jacobson in the human-TSC interaction experiment, the impact of the implementation errors on the validity of Jacobson's [16] results cannot be evaluated further.

From the outcome of the simulations and from the considerations made, it was concluded that the use of Jacobson's [16] baseline conditions as a linking point between his work and the upcoming BDFT

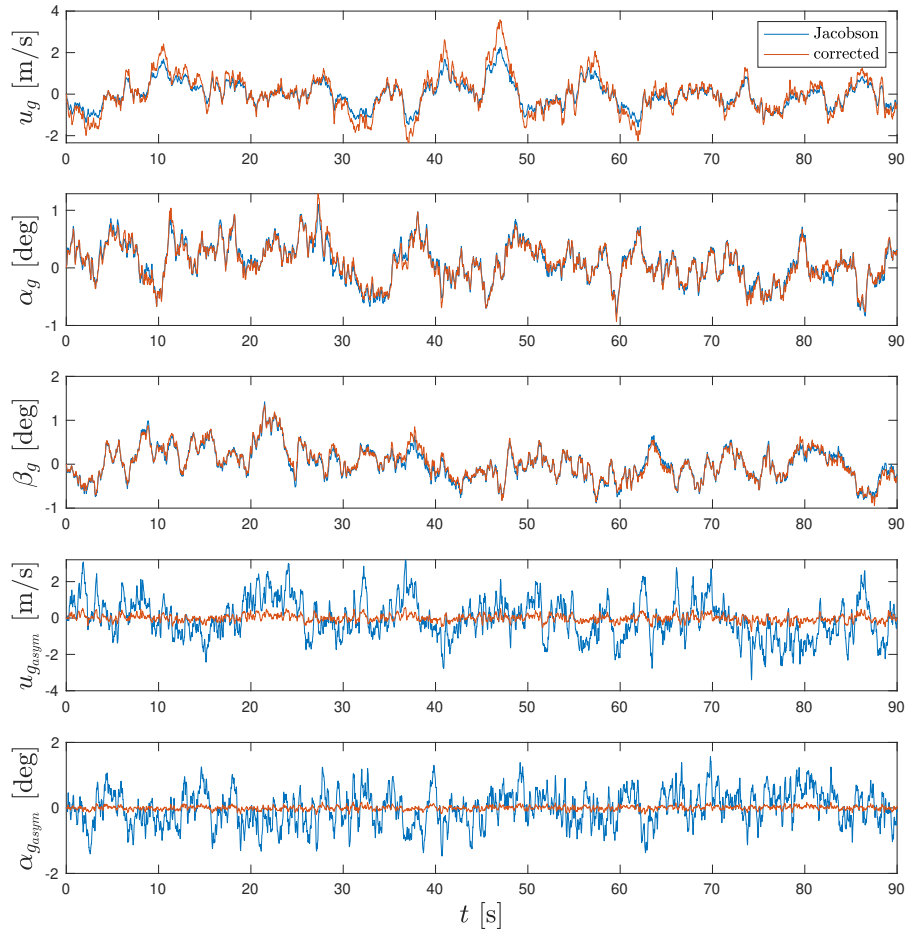
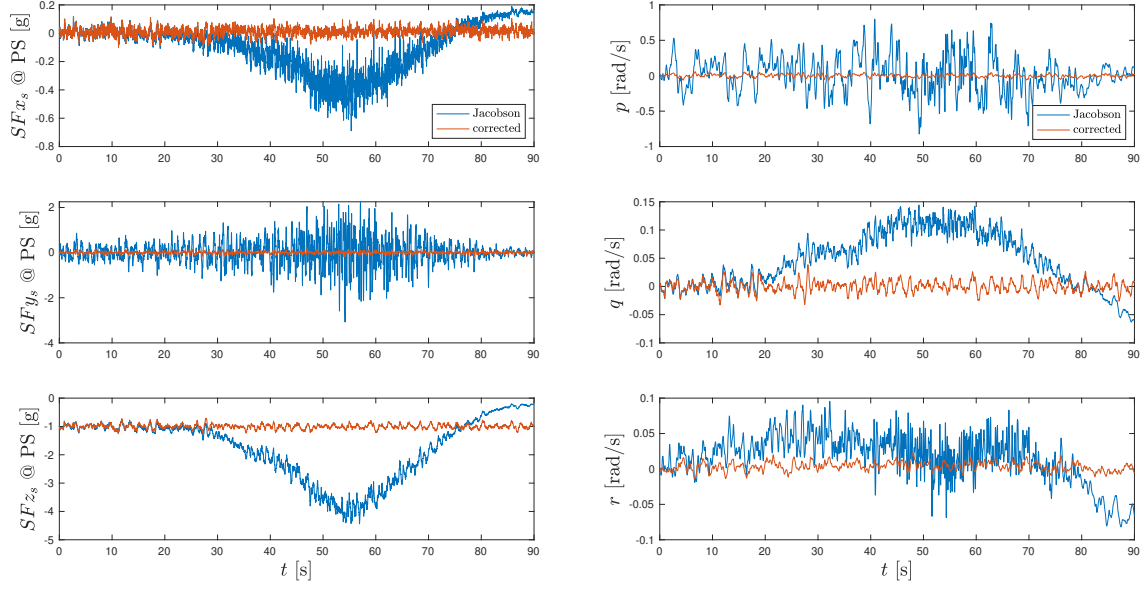


Figure 7.5: Comparison between Jacobson's patchy turbulence model implementation and the proposed corrected model, showing quantities made dimensional.

experiment is superfluous, as the aircraft responses used are not comparable. This section shall remain as a reference for future work aiming to further research Finger-Fitts' Law and connect to Jacobson's results.

7.3. Controller development

Depending on the desired characteristics of the turbulence velocity field, the simulated aircraft responses show low frequency dynamics that cause considerable deviations in the position and attitude of the simulated aircraft, in the worse cases leading it to become unstable. There are a multitude of reasons why these low frequency dynamics, visible in the accelerations and in the rotational rates of the aircraft, should be taken out of the equation for this BDFT study with TSCs. First of all, the study is going to evaluate the performance of a steady state BDFT model for the case of humans operating TSCs in turbulence. This dictates that the aircraft should be kept as much as possible at the trim conditions. With this being the case, the assumption of constant airspeed is formalized in the implementation of the *patchy turbulence model*, considerably reducing the complexity of the simulation. Moreover, the typical scenario in which a pilot would perform control actions for navigation or other open-loop purposes on a TSC (similar to the control action that is performed by participants in the experiment envisioned by Moberitz [17] and Khoshnewiszadeh [1]) is a cruise flight regime, where velocity, attitude and altitude are kept constant. In any case, the low frequency dynamics of the aircraft have little impact on the

(a) Specific forces SF at the pilot station (PS).

(b) Rotational rates.

Figure 7.6: Aircraft responses to Jacobson's patchy turbulence in comparison with responses to the proposed corrected patchy turbulence.

BDFT experienced by the human operating a TSC: as reported in Section 3.2.1, human operators perceive and are affected by a rather limited bandwidth of motion disturbances [13, 34–36].

It follows from this statement that not only low frequency, but also high frequency dynamics can be taken out of the equation when modeling human-TSC interaction. The removal of the high frequencies from the motion to be simulated with the SRS was taken care of in Jacobson by implementation of a second order low pass filter applied directly on the turbulence signals, with cut-off frequency at 10 Hz [16]. The application of the filter directly on the turbulence signal is justified by the fact that the patchy model simulates turbulence with Dryden spectra. As mentioned in Section 4.3.4, Dryden spectra fail to capture the spectrum of real turbulence at high frequencies. Moreover, the use of the filter ensures that the structure of the simulator is not pointlessly subjected to high frequency motion, which can potentially damage it, without affecting the BDFT study. This 'removal' of the high frequencies can therefore be done directly through filtering without affecting the validity of the simulation of the aircraft motion.

On the other hand, filtering out the low frequency components of the turbulence would effect a portion of the aircraft dynamics decisive in the propagation of the aircraft state, compromising the fidelity of the simulation of the aircraft responses. Instead, as in an actual aircraft, a controller is used to give control inputs to adjust the aircraft responses and keep the aircraft at the selected trim conditions, automatically reducing the low frequency components of accelerations and rotational rates that are causing deviations from those conditions. The following sections explain the reasoning behind the structure of the controller, the tuning criteria and show a simulation in which the controller was used.

7.3.1. Controller structure

As mentioned, the controller is designed to keep the aircraft at the trim conditions, and consequently remove the low frequency motion from the acceleration and the rotational rates of the aircraft. The controller designed is showed in Figure 7.7. It is comprised of a pitch rate feedback controller and a roll damper. Initially, a pitch damper was implemented in place of the pitch rate feedback controller, however through simulation it became apparent that faster damping of the pitch rate was needed, which lead to the implementation of a pitch rate inner loop. A yaw damper was not implemented, as the simulated turbulence conditions, and therefore the BDFT affecting the human operator, are independent of the heading of the simulated aircraft.

To be noted, the dynamics of the elevator and aileron's servos and their saturation limits have not

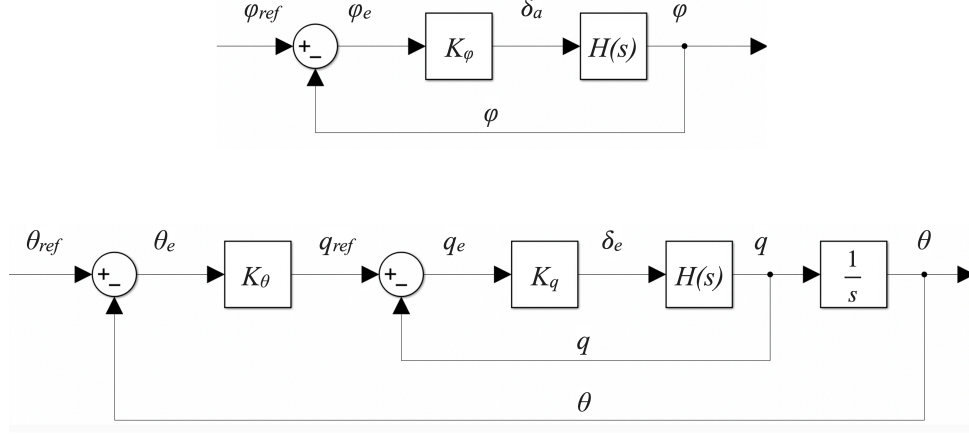


Figure 7.7: Pitch rate feedback controller and roll damper.

been explicitly added in the schematic of the controller, as they are already included in a preexisting block of the DASMAT aircraft model, appearing in the schematic under the general notation $H(s)$. In addition the output state is directly fed back into the controllers, assuming that sensors have unity gain. All controller blocks K_ϕ , K_θ and K_q have a purely proportional architecture, allowing to track the trim input with a short rise time and, through K_q , a faster damping of the pitch rate. The strategy employed to tune this controller is explained in the next section, and an example is given.

7.3.2. Controller tuning

Following from the assumptions employed for turbulence modeling, and considering that the BDFT model that will be investigated is a steady state model, it is important to keep the aircraft at the trim conditions. The objective of the controller is therefore to reduce the low frequency motion of the aircraft causing deviations from trim conditions, without influencing the high frequency motion caused by turbulence which will be used to research model-based mitigation of BDFT in open-loop tracking tasks on TSCs. In addition, to investigate the influence of different profiles of turbulence, the set of gains of the controller should be tuned to achieve this goal for all turbulence conditions used in the experiment at the same time. Tuning separately the gains for each experimental condition would in fact allow to optimize the parameters for the condition studied, but would create a confound in the experimental data meant to understand the BDFT dynamics at different turbulence conditions.

For the case discussed, two tuning steps were designed to achieve the designed performance. A first round of tuning is achieved by simulating the aircraft responses while looping over a broadly spaced set of values for the gains. Among these sets of gain, one set is selected based on its performance, which is established through numerical criteria looking at the aircraft's specific forces at the center of gravity and at its rotational rates. A second step to optimize the parameters is performed by looping separately each gain in the neighborhood of the established initial set, with more closely spaced values and starting from the inner loop, with the goal of reducing as much as possible the values of the gains, and therefore reducing the impact of the controller on the turbulence perceived, while staying within the required performance as established by the criteria.

The criteria that have been mentioned are applied on the variables most relevant for keeping the altitude h and velocity V of the simulated aircraft constant for the duration of the simulation. These are the specific force along the z_s body axis at the location of the center of gravity, the pitch rate and the roll rate. The criteria evaluate if the controller is able to keep the mean, the maximum and the minimum values of these variable, for the entire duration of the simulation, within 1 standard deviation of the corresponding values calculated from the transient response of the uncontrolled case. The standard deviation used is also calculated from the transient behavior of the aircraft in the uncontrolled case. For this simulations, the first 8.09 seconds were considered as the transient part of the response. This value was chosen to coincide with the run-in time used by Mobertz [17] and Khoshnewisazadeh [1]. The criteria are shown in Equation 7.9.

$$\mu_{transient} - \sigma_{transient} < \mu_{controlled} < \mu_{transient} + \sigma_{transient}$$

$$\begin{aligned} \max_{transient} - \sigma_{transient} &< \max_{controlled} < \max_{transient} + \sigma_{transient} \\ \min_{transient} - \sigma_{transient} &< \min_{controlled} < \min_{transient} + \sigma_{transient} \end{aligned} \quad (7.9)$$

Since these criteria are applied on all of the three variables mentioned above, a total of nine criteria evaluate the overall performance of the controller. In addition to these criteria, the sets of gains leading to unreasonable control surfaces' deflection rates, are discarded. The maximum allowed deflection rate for both elevator and aileron is taken to be 50 deg/s [75, 76]. Saturation limits for the control surfaces are already included in the aircraft model. Finally, given the architecture described in Figure 7.7, the sign of the gains are determined beforehand: K_ϕ , being a gain directly transducing an error on the pitch angle to an aileron deflection, is negative, since a positive aileron deflection leads to a negative increase in the roll attitude; conversely, the error in pitch angle is trasduced into an elevator input only through a command in the pitch rate. As such K_θ , describing the relation between the pitch angle and rate, is positive, while K_q takes a negative value, relating a positive change in the pitch rate into a negative deflection of the elevator.

7.3.3. Controlled aircraft responses to turbulence

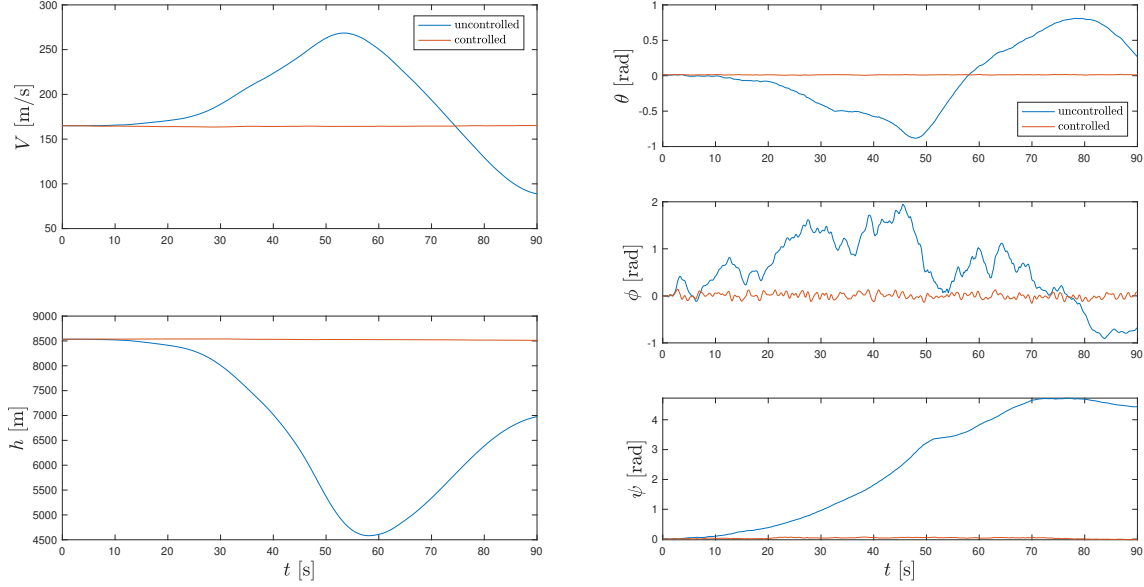
To show in practice the tuning process and a case with controlled aircraft dynamics, Jacobson's [16] version of the model is used, with input turbulence conditions as described in Section 7.1. The reason why Jacobson's [16] model is used despite having been shown to incorrectly model turbulence, as discussed in Section 7.2.2, is that during the preliminary research phase of this thesis the controller structure and tuning methods were developed in an earlier phase, while the verification of the *patchy turbulence model* was only performed afterwards. Correcting the model, the instabilities of the aircraft are negligible during the 90 seconds of simulation required for the BDFT experiment, which is why the controller is not needed nor used for the experimental conditions, as will be shown in the remainder of the report. To discuss in this report the controller which was developed as part of the preliminary research despite not being needed with the corrected turbulence model, all plots in this section are discussed in comparison with Jacobson's aircraft responses, as it would have been difficult to show the effect of the controller with the corrected turbulence simulations for the 90 seconds relevant to this work.

For the first iteration of the tuning process, gains are varied with a step size of 0.5 in the following intervals: $0.5 \leq K_\theta \leq 2.5$, $-2 \leq K_q \leq -0.5$, $-2.5 \leq K_\phi \leq -0.5$. For the case of Jacobson's experimental conditions, the first iteration already leads to a set of gains matching all criteria: $K_\theta = 0.5$, $K_q = -0.5$, $K_\phi = -0.5$. The uncontrolled aircraft responses and the controlled ones with this set of gains are overplotted in Figure 7.8 and Figure 7.9. Figure 7.8 shows that, other than complying to the criteria used for tuning, the controller meets all objectives in terms of maintaining the attitude at trim conditions and keeping both the altitude and the velocity of the aircraft sufficiently constant for the entire duration of the simulation. Figure 7.9 also gives a visual prospective on the compliance to the criteria, both for the specific forces and for the rotational rates: the areas highlighted in the plot show the transient response of the variables which drive the numerical evaluation of the controlled aircraft responses, the specific force in z_s , the pitch rate q and the roll rate p .

From the figures, it can be noted that all low frequency components both in the symmetric and asymmetric aircraft responses have been successfully removed, while in most of the cases the original high frequency vibrations seems to be well represented. In specific, while the specific force in z_s seem to be behaving fully as the corresponding transient of the uncontrolled case, it can be noted that the magnitude of the high frequency components of the pitch rate q seems to be attenuated, and that the roll rate p has lost a portion of its variability in its magnitude.

The second tuning iteration described above was implemented to find more suitable values for the gains. K_q was selected as the first parameter to optimize, as belonging to the inner loop of the controller. Figure 7.10 shows the number of criteria the aircraft responses comply to, for different values of gains in the neighborhood of the initial value $K_q = -0.5$. As can be seen from the plot, values of K_q between -0.5 and -0.1 all lead to full compliance with the criteria. Figure 7.11 shows a comparison between the aircraft responses obtained with $K_q = -0.5$ and $K_q = -0.1$. As expected, the only noticeable change in the aircraft responses is visible in the pitch rate of the controlled aircraft. A lower value of the gain indeed leads to a better performance in letting through the magnitude of the high frequency component of the motion. K_q is therefore set to -0.1.

Following the same reasoning, the remaining two gains can be optimized, leading to a choice of



(a) Velocity and altitude.

(b) Euler angles.

Figure 7.8: Comparison between velocity, altitude and Euler angles of the uncontrolled and the controlled simulated aircraft.

optimal gains for this specific case. For this case, the following set of gains was selected: $K_\theta = 0.1$, $K_q = -0.1$, $K_\phi = -0.2$. A comparison between the results of the initial tuning and the final controlled aircraft responses can be seen in Figure 7.12.

As it can be seen from Figure 7.12, the second round of tuning made a few improvements to the controlled pitch rate, while still filtering out all low frequency components. However, it should be noted that with the controller as currently implemented even the second optimization of the gain drastically reduced the variability of the magnitude of the motion, while correctly limiting the presence of low frequency motion. This is visible in the roll rate p . As a reminder, if the turbulence generated with the corrected turbulence model had required the use of the controller, a further iteration would have been needed, in order to comply with the requirement of having common settings for the gains across all the turbulence conditions used for the experiment, with the objective to minimize the confounds on the data. This step is not performed for the case described, as not meaningful.

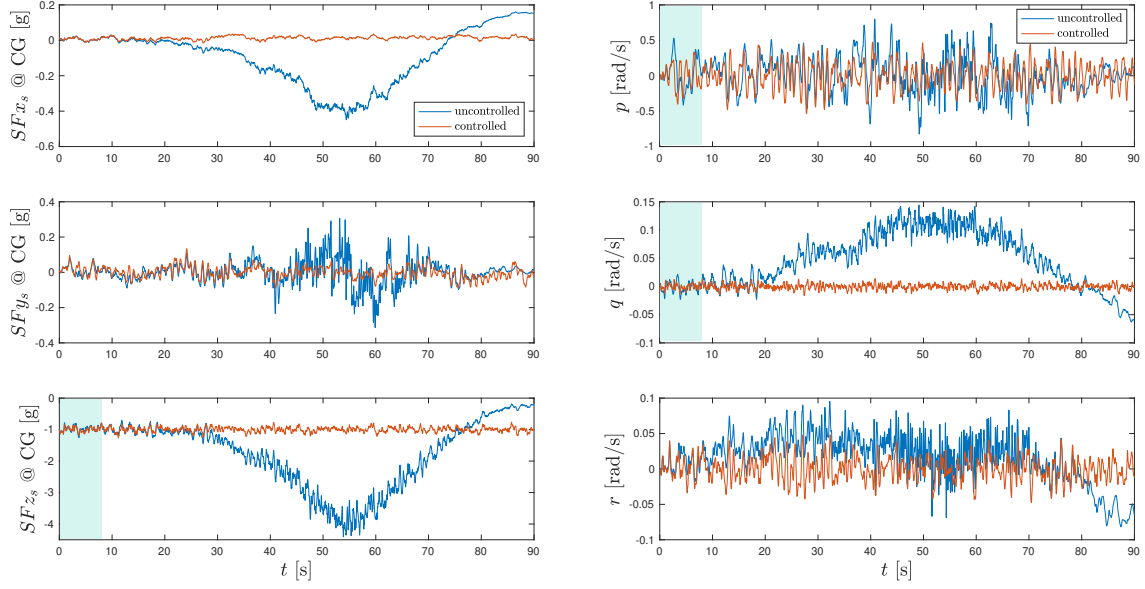
7.4. Design of experimental conditions

In order to assess whether model-based BDFT mitigation can be used effectively in realistic flight conditions, it becomes interesting to study the factors distinguishing the multisine motion disturbance signals from real turbulence. Turbulence intensity and variability have been identified as two factors whose influence on the model-based BDFT mitigation is widely unknown. Considering that the sinusoidal motion disturbance in sway is believed to not accurately model turbulence compared to heave it was decided to limit the current study to the effects of turbulence intensity and variability on the vertical motion of aircraft, and later on the vertical motion of the simulator.

7.4.1. Influence of the turbulence parameters on the aircraft motion

In order to better understand what turbulence conditions can be tested with the use of the *patchy turbulence model*, the influence on the aircraft motion of the parameters that define each realization of patchy turbulence is studied. In particular, the effect of each parameter is explored on the specific forces perceived in the cabin, which are relevant to the pilot's perception.

Through this analysis, the expected behavior of the turbulence time traces while varying each parameter is verified on the symmetric components of turbulence. No particular analysis is performed on the anti-symmetric components, since these are not to be interpreted as components of the turbulence

(a) Specific forces SF at the center of gravity (CG).

(b) Rotational rates.

Figure 7.9: Comparison between the uncontrolled and the controlled aircraft responses, with first iteration tuning. The highlighted parts show the transient response taken as reference for the tuning criteria.

velocities but rather as signals that, coupled with the DASMAT aircraft model, allow to simulate the asymmetric aircraft responses [47]. Variables like the turbulence length scale and the patch length therefore have no physical meaning when dealing with these construction signals.

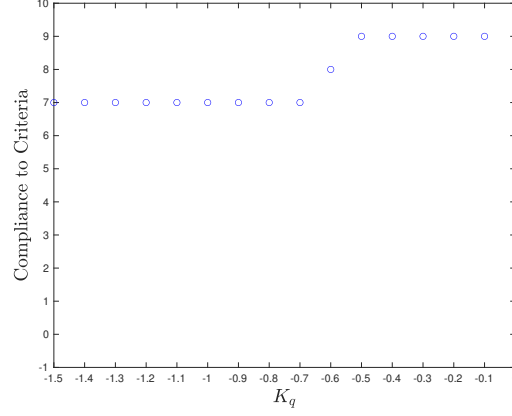
Turbulence intensity

The influence of the turbulence intensity σ_g^2 is straight forward. Recalling that the turbulence intensity σ_g^2 increases the power equally at all frequencies of the spectrum of the turbulence velocity components, an increase in intensity is expected to occur also in the aircraft's responses. This can be seen both on the time traces and on the spectrum of the vertical specific forces at the pilot station in Figure 7.13 for Gaussian turbulence, obtained from the *patchy turbulence model* by setting the parameter defining the Kurtosis of the PDF of the turbulence velocity $Q = 0$, and therefore Kurtosis $K = 3$. For reference, $L = 300$ m, a typical value for high altitude turbulence length scale, and $R = 0.01$ [47]. The choice of this last parameter is however not relevant, as R always appear in the equations for the shaping filters of the patchy turbulence velocities multiplied by Q , see the patchy model equations in Appendix A.

Finally, it should be recalled that a low pass filter with break frequency of 10 Hz is implemented in the generation of the turbulence time traces. The influence of the filter is visible at the high frequencies in Figure 7.13b.

Turbulence length scale

Parameter L_{ug} represents the length scale of the modeled turbulence. Turbulence with higher length scale should have a predominance of low frequency components when compared to lower length scales, which instead should have a predominance of high frequency components. This behavior is visible in the frequency spectrum of the components of turbulence, in Figure 7.14a. The effect on the vertical specific force perceived by the pilot is mainly on the frequency distribution of power as well. In Figure 7.14b it can be seen that the low frequency components of the motion have higher power when the turbulence length scale is higher (setting apart very low frequencies disturbances which are not picked up by the aircraft dynamics), while turbulence with lower length scale causes higher power in the high frequency motion in the aircraft. For reference, the influence of L_{ug} is shown again using a Gaussian turbulence, by setting $Q = 0$ and $R = 0.01$. The intensity σ_g^2 is set to a typical value of $1 \text{ m}^2/\text{s}^2$ [47].

Figure 7.10: Second tuning step, varying K_q .

It should be reminded that while the low pass filter applied on the turbulence velocities reduces their high frequency components, it does not influence the frequency distribution shown for the various values of L_{ug} .

Turbulence variability: Kurtosis

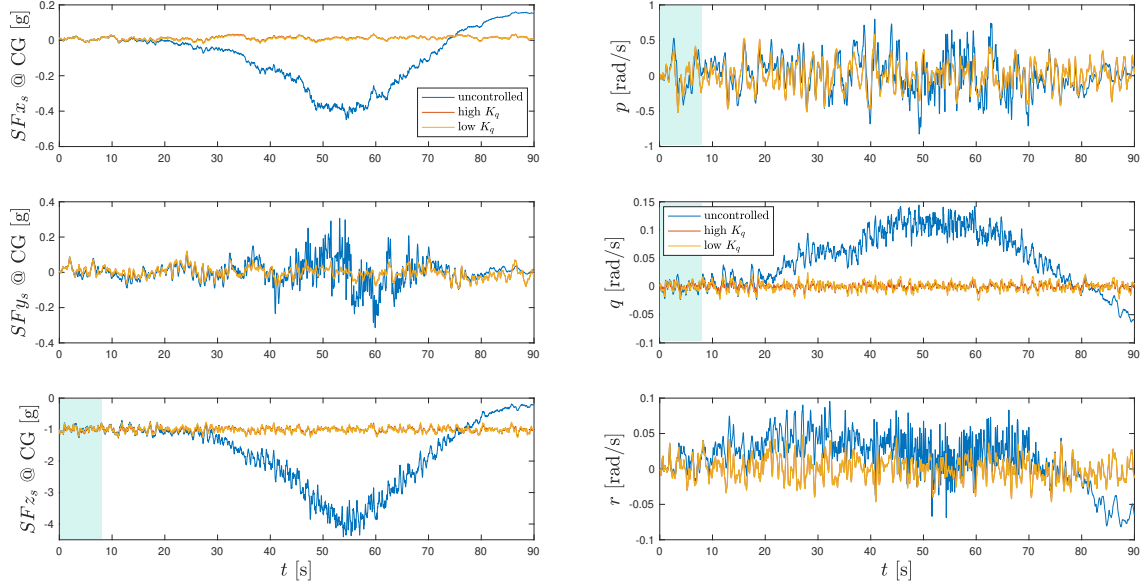
The value of parameter Q changes the Kurtosis of the PDF of the simulated turbulence velocity component, through the relation in Equation 4.12 [56, 65]. Increasing Q from zero, variability is therefore introduced in the simulated turbulence, through a non-Gaussian distribution of high and low turbulence intensities. However, since the Kurtosis is a statistical characteristic, this effect is only visible when considering long simulation times, with large datasets of the turbulence velocities. In such cases, it is verified that the Kurtosis of the generated time traces approaches the values specified by parameter Q , see the second and third column of Table 7.3, where the value of the Kurtosis K is reported as function of Q and from the data of the turbulence velocities simulated for 9000 seconds respectively. However, for a measurement time of 90 second, which is the simulation length used in previous experiments to prevent fatigue from influencing the identification of BDFT, the Kurtosis is no longer a meaningful parameter. This can be seen in the resulting Kurtosis calculated from the time traces of the simulated turbulence for 90 seconds, the fourth column of Table 7.3. Moreover, the actual values of K reported in the table are also influenced by the presence of the low pass filter, although not necessarily impacting the Kurtosis directly.

Table 7.3: Values of the Kurtosis associated to parameter Q , $K(Q)$ calculated with Equation 4.12, K_w measured from a 9000 seconds simulation and K_w measured from a 90 seconds simulation of the vertical component of the turbulence velocity. Error $\sigma_K = \pm 0.05^3$.

Q [-]	$K(Q)$ [-]	K_w (9000 s) [-]	K_w (90 s) [-]
0	3.00	2.97	2.62
0.2	3.01	3.03	2.60
0.4	3.11	3.20	2.59
0.6	3.42	3.57	2.66
0.8	3.91	4.06	2.76
1.0	4.50	4.60	2.88
1.2	5.09	5.09	2.97
1.4	5.63	5.51	3.05

Setting $Q > 0$ is needed regardless of its effect on the Kurtosis of the turbulence velocities, as it allows to use parameter R to vary the patch length. Fixing the value of Q , the influence of R can be explored.

³Erratum: Error σ_K should be ± 0.05 for 9000 seconds simulations, $\sigma_K = \pm 0.5$ for 90 seconds simulations.

(a) Specific forces SF at the center of gravity (CG).

(b) Rotational rates.

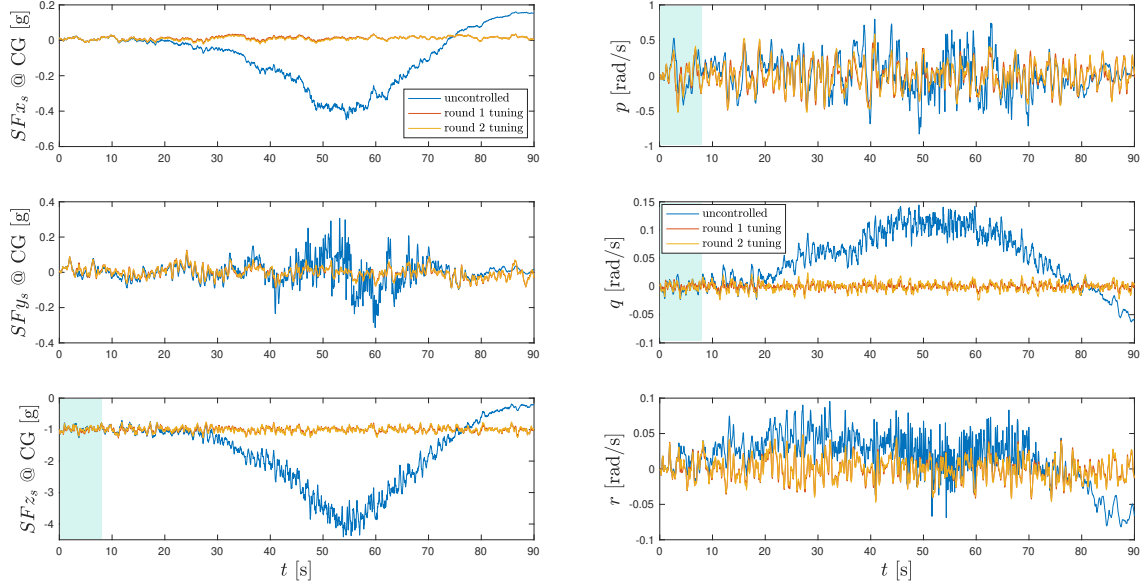
Figure 7.11: Comparison between the controlled aircraft responses with the highest and lowest possible values for gain K_q .

Turbulence variability: patch length

As mentioned in literature, a low value of R corresponds to large sub-patches of turbulence within the length scale L_{u_g} [65]. It is expected that low R will therefore lead to more homogeneous turbulence compared to higher R , where patches will be shorter in length, and therefore the time traces more variable. In order to visualize the homogeneity of the turbulence velocities for different values of R for a fixed combination of the other parameters ($\sigma_g^2 = 1 \text{ m}^2/\text{s}^2$, $L_{u_g} = 300 \text{ m}$, $Q = 1.55$), the standard deviation of the turbulence velocities is calculated in short time intervals across the simulated time traces of the turbulence velocities. The number of data points for the intervals, i.e., the length of the time bin over which the standard deviation is calculated, is chosen by iteration over interval lengths integer factors of the measurement time, and visual evaluation of the meaningfulness of the plot. Figure 7.15a shows this standard deviation in time bins of 32 seconds for the symmetric components of the turbulence velocities across a Gaussian turbulence case and different values of R . Figure 7.15b shows this standard deviation calculated for the vertical specific force perceived at the pilot station.

From Figure 7.15a it is clear that not all turbulence velocity components present patches, and therefore the influence of R cannot be observed on all components. Indeed not much difference can be perceived in the longitudinal and in the lateral components of turbulence, u_g and v_g respectively, between the Gaussian turbulence and the patchy turbulence with different values of R . Instead, for the vertical component of the turbulence velocity w_g , a large patch of higher intensity can be seen with $R = 0.1$, its uniformity decreasing with increasing R .

Recalling that in isotropic turbulence the vertical and lateral components of the turbulence velocities v_g and w_g are modeled by the same spectrum (see Section 4.3.4), and therefore by the same equations (see Appendix A), it is concluded that the white noise used and in particular the seeds used for its generation have a large impact on the presence of patches in the simulated turbulence. For the current study, variability in the vertical component of the turbulence velocity w_g is needed, as the vertical motion of an aircraft in turbulence is mostly dictated by the vertical component of turbulence. No particular requirement is provided for the other components. It is therefore chosen to maintain the seeds currently used for this evaluation, keeping in mind that a further study dealing with the aircraft responses on more than a single axis should take into account whether or not there should be correlation between the patches occurring in the different turbulence components, and whether it is required or acceptable to use the same realization of white noise (i.e., the same seed) for all turbulence components.

(a) Specific forces SF at the center of gravity (CG).

(b) Rotational rates.

Figure 7.12: Comparison between the controlled aircraft responses obtained with the first and second round of tuning.

7.4.2. Selection of the turbulence parameters and filter settings

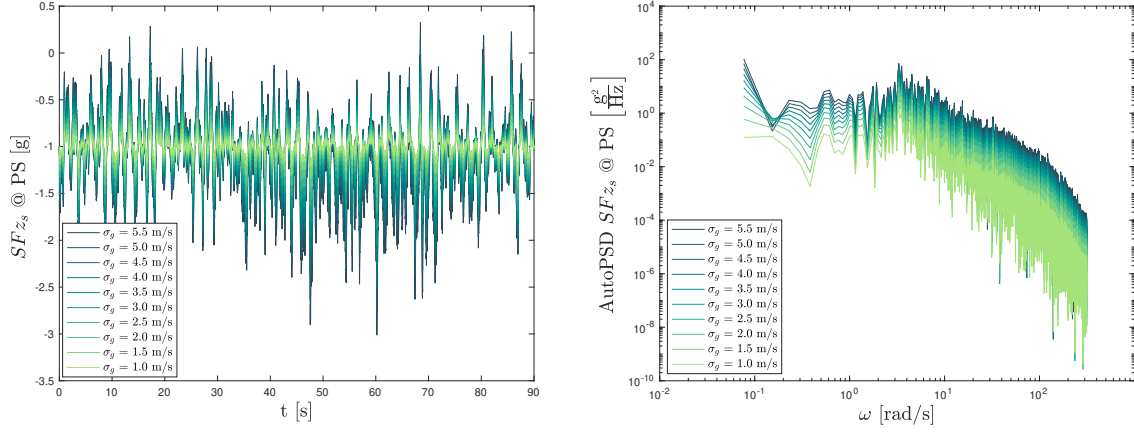
Through the considerations above, it becomes clear that in order to investigate the effects of turbulence intensity and variability on the dynamics of BDFT occurring with TSCs, the turbulence intensity σ_g^2 and the patchy parameter R are the most relevant. It is therefore chosen to fix the value of the turbulence length scale L_{u_g} to a typical high altitude turbulence value: $L_{u_g} = 300$ m as reported in literature [47]. Similarly, the value of Q is fixed. For the simulation of Gaussian turbulence, it is chosen to use a value of $Q = 0$ despite the actual Kurtosis being slightly lower than 3. This is because $Q = 0$ nullifies the influence of R . For patchy turbulence $Q = 1.55$ is chosen, corresponding in the limit to a Kurtosis of 6, the maximum observed in measurement campaigns [65]. For the selection of the value of R for a patchy turbulence experimental condition and the values of σ_g^2 for both a Gaussian and a patchy turbulence condition, some further analysis is presented here.

Selection of R

As it was concluded with the analysis reported in Section 7.4.1, any value of R leading to a visible patchy behavior in the vertical component of the turbulence velocity w_g , and therefore in the vertical specific force experienced in the aircraft at the pilot station shown in Figure 7.15b, can be selected for the study.

Ultimately, the selection of a specific value for R is driven by the need to simulate the accelerations of the aircraft with the SRS, in a frequency band as broad as possible. A heave Gouverneur analysis is performed on different values of R , calculating the required actuator extension and extension velocity for each case on a grid of filter settings (gain in the interval $0.1 \leq K_{heave} \leq 1$, break frequency $0.1 \text{ rad/s} \leq \omega_{heave} \leq 4 \text{ rad/s}$) for the classical washout filter (CW16) currently used on the SRS with the Cessna Citation 500 aircraft model. The enabling gains for the motion on all axis except for heave are set to 0, damping ratio is fixed to 0.7 and the third order pole of the high pass filter to 0.2 rad/s, following the specification in Gouverneur et al. [77].

As mentioned, for each value of R the algorithm tests combinations of gain and break frequency of the heave high pass filter, calculating the extensions of the actuators and their velocity. These values are then compared to the actuator's maximum extension and velocity, giving as output a list of filter setting that can be used to simulate the flight condition without incurring into the actuator's limits of the SRS. For the details of the algorithm, see Gouverneur et al. [77]. Figure 7.16 shows the results of a heave Gouverneur analysis performed for three values of R : 0.1, 0.2, 0.3 (for different values of σ_g^2 , as

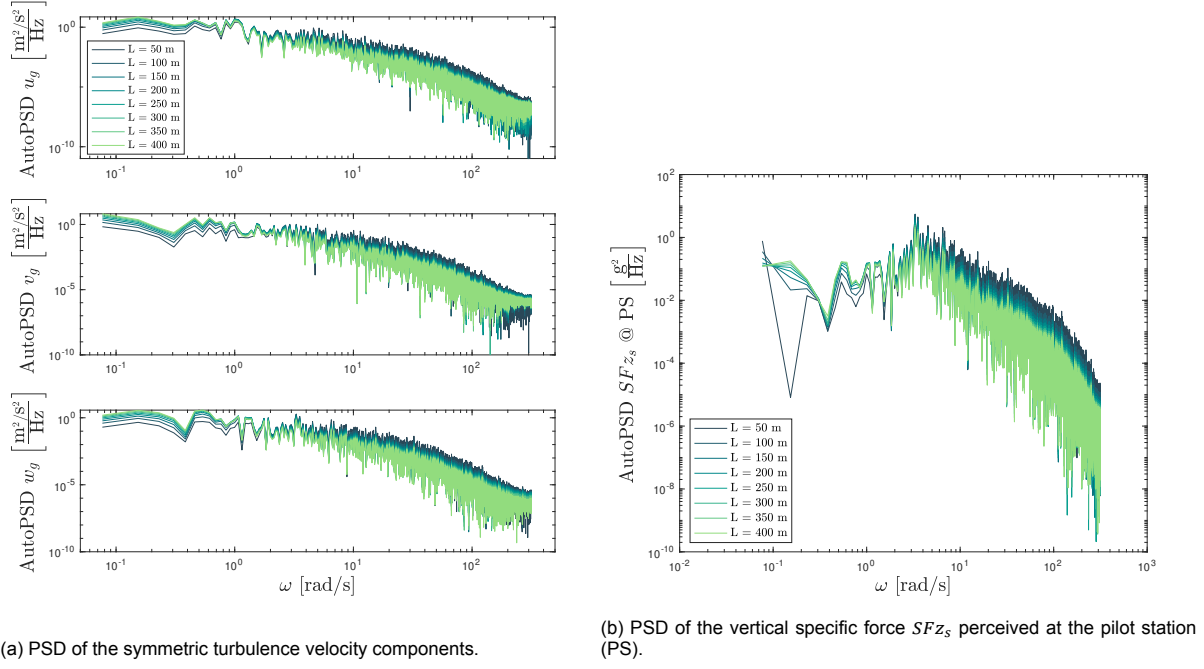
(a) Vertical specific force SF_{z_s} perceived at the pilot station (PS).(b) PSD of vertical specific force SF_{z_s} perceived at the pilot station (PS).Figure 7.13: Effect on the aircraft specific forces of variations in σ_g (Gaussian turbulence: $L_{u_g} = 300$ m, $Q = 0$ and $R = 0.01$).

will be briefly explained). For each tested case, feasible solutions are found above the corresponding line in the plot. In general, a high fidelity simulation would require break frequency as low as possible, and a high gain to prevent losing frequency content or magnitude of the motion [77]. Since only the heave component of the motion will be simulated, there is not need to account for lags caused by the filter.

A few notes should be made on this figure before discussing the selection of parameter R . When decreasing the gain or increasing the break frequency of the high pass filter, the magnitude of the acceleration experienced in the simulator will decrease compared to the one of the simulated aircraft. The intensity of the accelerations experienced by the pilots, measured through the V-metric in Equation 4.13, have been used in literature to compare experimental data on human control behavior [11, 16]. It is therefore chosen to use the V-metric as the primary means to compare the intensity of the motion experienced across different experimental conditions and to connect to the results of previous literature. The intensity of motion experienced with the multisine motion disturbance used in the BDFT-TSC studies by Moberitz [17] and by Khoshnewisazadeh [1] is taken as a baseline: $V_{metric} = 0.75$ m/s². Parameter V_{metric} is then calculated for each combination of filter settings, of parameter R and of the turbulence intensity σ_g^2 . The selection of the above parameters and settings is therefore dictated by the need to have an experimental condition with intensity $V_{metric} = 0.75$ m/s² or above, to be able to make a direct comparison of the results of the upcoming simulator experiment with the previous BDFT studies.

Getting back to Figure 7.16, the colored lines represent the boundaries between feasible and unfeasible filter setting for each turbulence condition tested. The currently selected filter settings, gain of 1 and break frequency of 0.9 rad/s, are feasible only for the case of $R = 0.1$. For these filter settings and values of R , the turbulence intensity σ_g^2 required to have $V_{metric} = 0.75$ m/s² are shown in the legend of Figure 7.16. It can be noted that with increasing R , to keep the same overall intensity of the motion experienced by the pilots, the values of the turbulence intensity σ_g^2 has to be increased. This is because, as visible already in Figure 7.15b, the high intensity patch becomes less homogeneous for increasing R , therefore the V_{metric} experienced on average by the pilots is lower. However, in increasing V_{metric} through an increase in turbulence intensity, the peaks of the higher intensity patches become more extreme and require more aggressive filtering to be simulated with the SRS: this is the main reason why the Gouverneur analysis for $R = 0.2$ and $R = 0.3$ results in a lot more unfeasible combinations of settings compared to $R = 0.1$.

It should be added that, as mentioned, the current combination of turbulence intensity with $R = 0.2$ and $R = 0.3$ leads to $V_{metric} = 0.75$ m/s² with unfeasible filter settings. A feasible configurations of the filter settings requires to either increase the break frequency or decrease the gain, or both. These actions however, further decrease the intensity of the motion perceived by the pilot V_{metric} , and will need to be compensated by using an even higher value of the turbulence intensity σ_g^2 , leading to a snowball effect for which even more combinations of the filter settings will be unfeasible. Even though a combination of filter settings and turbulence intensity can be found that simulates the motion with the required



(a) PSD of the symmetric turbulence velocity components.

(b) PSD of the vertical specific force SF_{z_s} perceived at the pilot station (PS).

Figure 7.14: Effect on the turbulence velocity components and on the vertical specific force of variations in L_{ug} (Gaussian turbulence: $\sigma_g^2 = 1 \text{ m}^2/\text{s}^2$, $Q = 0$ and $R = 0.01$).

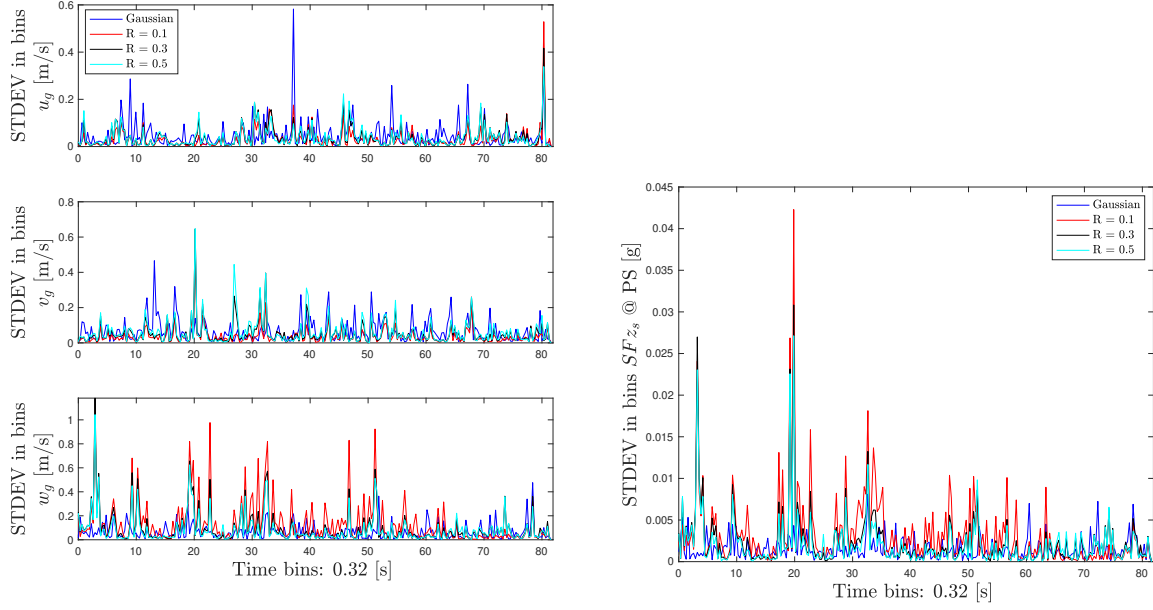
V_{metric} , this will come at a great compromise in terms of the frequency band of the motion simulated, discarding a considerable portion of the frequency content of the turbulence motion disturbance. This is undesirable, especially considering that any comparison with the multisine motion disturbance should as much as possible span its frequency band: 0.38-17.33 rad/s. Following these considerations, a value of $R = 0.1$ is chosen, discarding the frequency content only below 0.9 rad/s. With $R = 0.1$ it is already visible in Figure 7.15b that a considerable patchy behavior can be perceived in comparison to the Gaussian case.

Selection of σ_g^2

For the selection of the turbulence intensity to be used for the Gaussian and the patchy turbulence conditions, very similar consideration to the ones discussed for the selection of R need to be made: as mentioned, the intensity of the motion experience during the experimental conditions has more relevance for human-in-the-loop experiments than the value of the turbulence intensity itself. Having fixed all other parameters ($L_{ug} = 300 \text{ m}$, $Q = 0$ for Gaussian turbulence and $L_{ug} = 300 \text{ m}$, $Q = 1.55$, $R = 0.01$ for patchy turbulence), to get a condition with a certain V_{metric} a feasible combination of the filter setting for the heave high pass filter and of the intensity has to be found. An additional consideration can be made: in order to evaluate BDFT occurring at different intensities, the gain of the heave motion filter of the simulator can be used to reduce the magnitude of the accelerations, giving a straightforward way to do so equivalent to lowering the intensities of turbulence. By doing this, only the highest motion intensity condition has to be designed for each turbulence type. It is also important to note that the settings chosen for the motion filter should be equal for the Gaussian and patchy turbulence, as to avoid confounds.

As already mentioned, $V_{metric} = 0.75 \text{ m/s}^2$ should be a baseline condition to bridge Mobertz's [17] and Khoshnewisadeh's [1] studies with the current. Figure 7.17a and 7.17b show an heave Gouverneur analysis for different values of the turbulence intensity σ_g^2 respectively for the Gaussian and patchy cases, aimed at understanding whether a higher intensity of the motion can be simulated without losing too much of the frequency content of the motion.

While for the Gaussian case, different intensities σ_g^2 lead to a contained increase of unfeasible filter settings compared to the baseline V_{metric} , it is immediately visible in Figure 7.17b that for patchy turbulence already a 0.1 m/s^2 higher intensity would require a much larger compromise in fidelity of the



(a) Bin averaged standard deviation of the symmetric turbulence velocity components. (b) Bin averaged standard deviation of the vertical specific force perceived at the pilot station.

Figure 7.15: Effect on the turbulence velocity components and on the aircraft specific forces of variations in R .

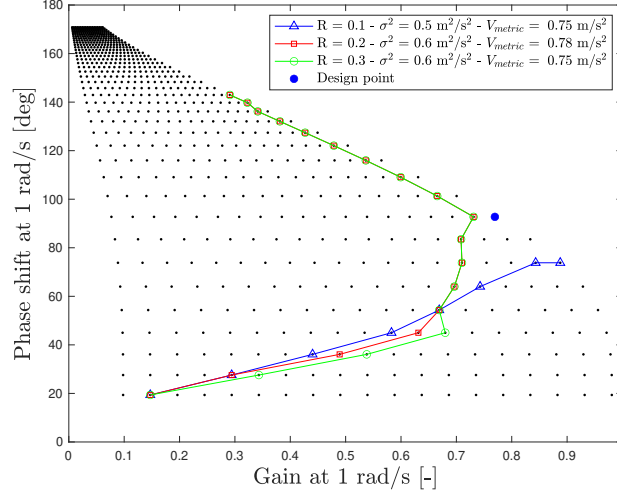
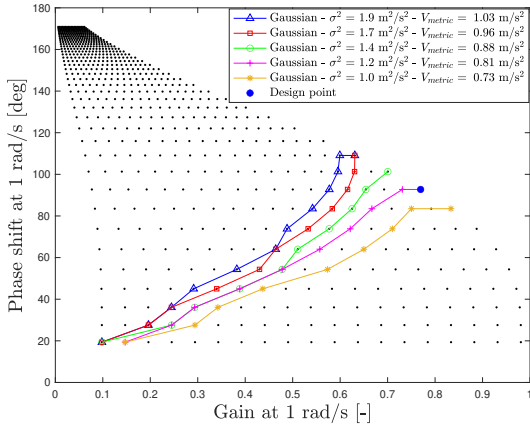
simulation. This is because with higher intensities, the peaks of the patchy turbulence are even more extreme, hitting the actuator's rates limits in their simulation. Compromising on the gain is not a solution, as a higher intensity would need to be used to maintain the same V_{metric} , leading again to even more unfeasible settings. To have a meaningful variation in intensity, such as 0.25 m/s^2 , a compromise in terms of frequency content would need to be made, with frequencies up to 2.9 rad/s removed from the motion.

In conclusion, following the same reasoning as for the selection of R , a maximum intensity of $V_{metric} = 0.75 \text{ m/s}^2$ is designed for, to maintain a large overlap between the frequency content of the simulated turbulence motion disturbance and the multisine motion disturbance: using a gain of 1 and break frequency of 0.9 rad/s , as shown in Figure 7.17, for the Gaussian turbulence condition an intensity of $\sigma_g^2 = 1 \text{ m}^2/\text{s}^2$ is selected, and for the patchy turbulence an intensity of $\sigma_g^2 = 0.5 \text{ m}^2/\text{s}^2$ will be used.

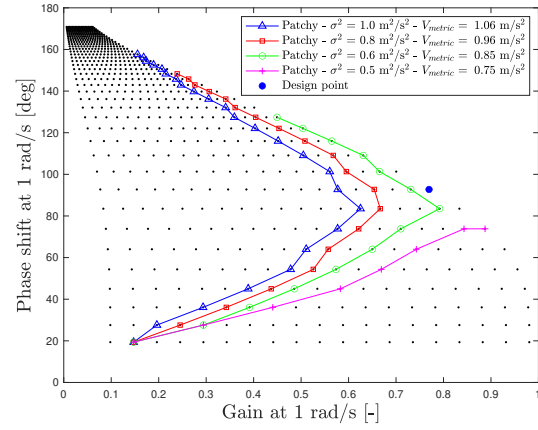
7.5. Overview of the experimental conditions

Performance of the model-based mitigation of BDFT will be evaluated in two realistic motion conditions, a Gaussian condition (G) in which a more uniform turbulence is experienced, and a patchy turbulence condition (P), through which the effect of variability will be investigated. Variability of turbulence is introduced through the implementation of inhomogeneous patches within the turbulence length scale. As this will be the first experiment evaluating the performance of model-based BDFT mitigation for the case of turbulence with variable characteristics, only one setting for variability will be introduced: the effect of variations in the characteristics of the variability will not be explicitly considered at this point. In addition, to evaluate the influence of intensity on the model-based BDFT mitigation, and on the BDFT model itself, the existing BDFT model will be identified at three different levels of motion intensity, defined through the V -metric reported in Equation 4.13, already used in previous studies to quantify the motion to which TSCs operators were subjected while performing control tasks [16].

Table 7.4 gives an overview of the conditions that will be used for these purposes. The baseline case will be the multisine motion disturbance already implemented by Moberitz [17] and by Khoshnewisadeh [1], with $V_{metric} = 0.75 \text{ m/s}^2$, called condition M3. Two scaled versions of the same signal will be used to evaluate the influence of intensity on the BDFT mitigation achieved in literature. These conditions, named M2 and M3, will have respectively 2/3 and 1/3 of the original intensity. A similar set up will be used to evaluate BDFT mitigation performance with turbulence, uniform and variable, at the same

Figure 7.16: Heave Gouverneur analysis for different values of R .

(a) Gaussian turbulence.



(b) Patchy turbulence.

Figure 7.17: Heave Gouverneur analysis, design point $K_{heave} = 1$, $\omega_{heave} = 0.9$ rad/s.

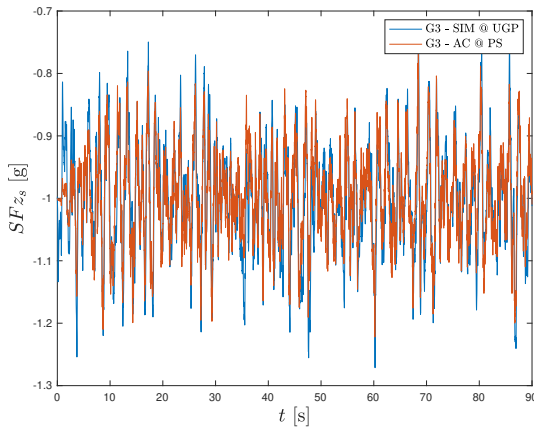
levels of V_{metric} already mentioned for the multisine case. The parameters and filter settings used for Gaussian turbulence G3, G2 and G1 (highest to lowest intensity) are reported in Table 7.4. Similarly for the patchy turbulence conditions P3, P2, P1.

For reference, in Figure 7.18 the time traces of the vertical specific force of the simulator at the *upper gimbal point* (UGP) are shown in comparison to the one of the aircraft at the *pilot station* (PS), for condition G3 and P3. The two reference positions are defined each at the same coordinates with respect to the *design eye reference point* (DERP), and are therefore comparable, and useful to understand the effect of the motion filter on the specific force simulated. Figure 7.18a shows the effect of the filtering on the vertical motion caused by Gaussian turbulence, Figure 7.18b the one caused by patchy turbulence. From the time traces, it is clear that the filter does not effect the overall uniformity and variability of the two different cases. The magnitude of the perceived specific forces is roughly unchanged, apart from the initial fade-in that allows the simulation of the motion. To be noted, the fade-in time will not be considered for BDFT identification and for the evaluation of BDFT mitigation performance.

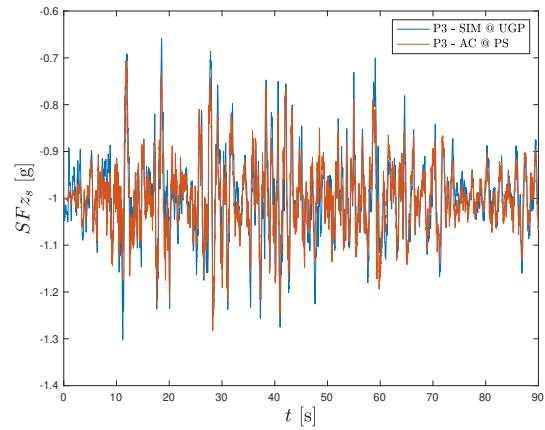
To evaluate the effect of the motion filter on the frequency content of this motion, Figure 7.19a and Figure 7.19b show an average estimation of the power spectral density of the vertical simulator and aircraft accelerations per frequency bin, where each frequency bin contains one of the components of the multisine motion disturbance. This bin averaged power is showed in place of the power spectral density to provide a clear means of comparison between the continuous spectrum turbulence of the

Table 7.4: Experimental conditions to be used in the upcoming experiment.

Condition	Description	σ_g^2 [m ² /s ²]	L_{ug} [m]	Q [-]	R [-]	K_{heave} [-]	ω_{heave} [rad/s]	V_{metric} [m/s ²]
M1	Multisine low intensity	-	-	-	-	1/3	0	0.25
M2	Multisine medium intensity	-	-	-	-	2/3	0	0.50
M3	Multisine high intensity	-	-	-	-	1	0	0.75
G1	Gaussian low intensity	1	300	0	0.01	1/3	0.9	0.24
G2	Gaussian medium intensity	1	300	0	0.01	2/3	0.9	0.48
G3	Gaussian high intensity	1	300	0	0.01	1	0.9	0.73
P1	Patchy low intensity	0.5	300	1.55	0.1	1/3	0.9	0.25
P2	Patchy medium intensity	0.5	300	1.55	0.1	2/3	0.9	0.50
P3	Patchy high intensity	0.5	300	1.55	0.1	1	0.9	0.75



(a) Gaussian case.



(b) Patchy case.

Figure 7.18: Vertical specific force of the aircraft at the pilot station (PS) and vertical acceleration of the simulator at the upper gimbal point (UGP).

Gaussian and patchy conditions and the multisine condition, which is made up of discrete frequency components.

As visible in the figures, the low frequency components of the motion are inevitably attenuated in order to simulate the motion in the constrained motion space of the SRS. This is especially true for the Gaussian condition, which has high power at the low frequencies. Low frequency motion is however of marginal interest for the problem of BDFT, since it has been shown that the amount of power that feeds through from the vehicle's acceleration to the TSCs input increases for increasing frequencies, confirming the intuitive understanding that the involuntary motion of the limbs of the human controller is negligible at low frequency motion [1].

In order to better understand how the multisine signal differs from the turbulence motion disturbances, Figure 7.20 shows a comparison between the time traces of the acceleration for the M3 condition, and the filtered accelerations for the G3 and P3 conditions ($V_{metric} = 0.75 \text{ m/s}^2$), in a zoomed in time interval. The variability of the patchy condition with respect to the Gaussian is somewhat visible in the sudden lower intensity of the turbulence at the end of the time frame, however for a better visual comparison between the two Figure 7.18 should be referred to, as the focus here is on a zoomed portion of the time interval, which allows to see the details of the difference between the multisine and the turbulence conditions. From Figure 7.20 it can be noticed that both patchy and Gaussian turbulence show more high frequency content, albeit with a small amplitude, compared to the multisine motion disturbance. This is also visible in the power spectrum of the accelerations of the patchy, Gaussian and multisine conditions, showed again averaged in the frequency bin in Figure 7.21. The frequency response of

⁴Erratum: the legend corresponding to the blue line should state 'M3 - $V_{metric} = 0.75 \text{ m/s}^2$ '.

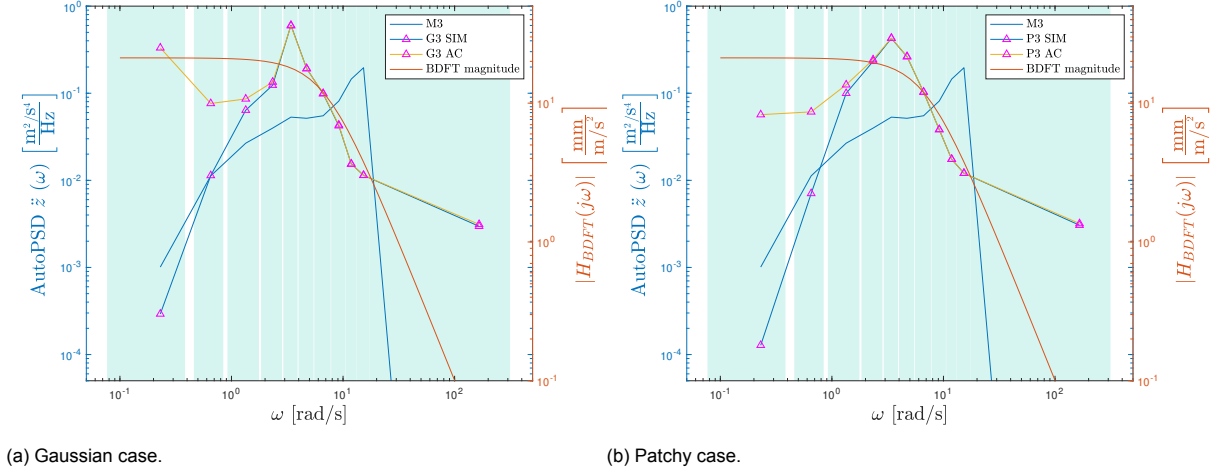


Figure 7.19: Frequency bin averaged PSD of the vertical acceleration of the aircraft at the Pilot Station (PS) and of the vertical acceleration of the simulator at the Upper Gimbal Point (UGP).

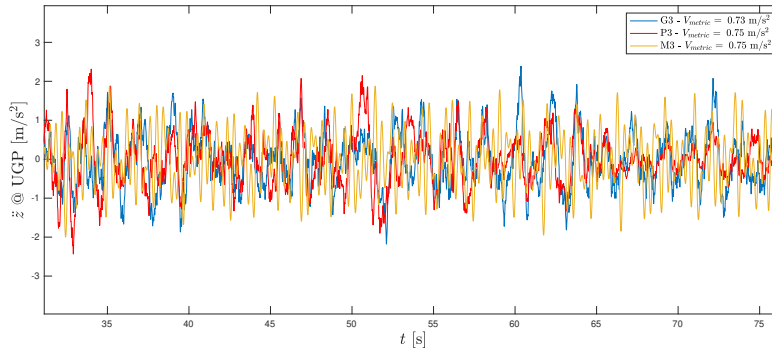


Figure 7.20: Detail of the time traces of the Multisine, Patchy and Gaussian motion disturbances, $V = 0.75 \text{ m/s}^2$.

the BDFT model identified for the heave-vertical input case (VER) in Khoshnawisadeh's work [1] is shown in Figure 7.21 to give a context to the differences between the three motion types. Provided that the plot is given in logarithmic scale, the biggest difference visible in the frequency content of the signals occurs at frequencies above the break frequency identified for the BDFT model. It can be therefore hypothesized that the BDFT model identified from the multisine signal will be able to somewhat still effectively mitigate BDFT for the other two cases. Further analysis however contradicts this first conclusion.

The BDFT model for the heave-vertical input case identified by Khoshnawisadeh [1] using multisine motion disturbance, and with the parameters of the OSFA model describing the BDFT dynamics of a generalized human being, is used to simulate the involuntary component of the input signal caused by BDFT, here called u^{mod} , for all three motion conditions having $V_{metric} = 0.75 \text{ m/s}^2$, that is with intensity corresponding to the one used for the identification of the model. Figure 7.22 shows the simulated involuntary component of the vertical input on the touchscreen, for the multisine, the Gaussian and the patchy cases. It is immediately visible that the simulated involuntary component of the input is considerably larger for the Gaussian and patchy motion disturbance cases compared to the multisine case. Especially in the patchy condition, the simulated BDFT is not constant throughout the simulation. To evaluate whether the human operators are likely to adapt their dynamics in an attempt to reduce the feedthrough, the standard deviation of the simulated involuntary component for each motion disturbance is calculated, and plotted in Figure 7.23 together with the average standard deviation in the involuntary component of the input recorded across participants in Khoshnawisadeh's experiment [1]. To give a range for this measure, the minimum and maximum values of the standard deviation of u^{mod} across the participants is also included, as well as a standard deviation of this measure.

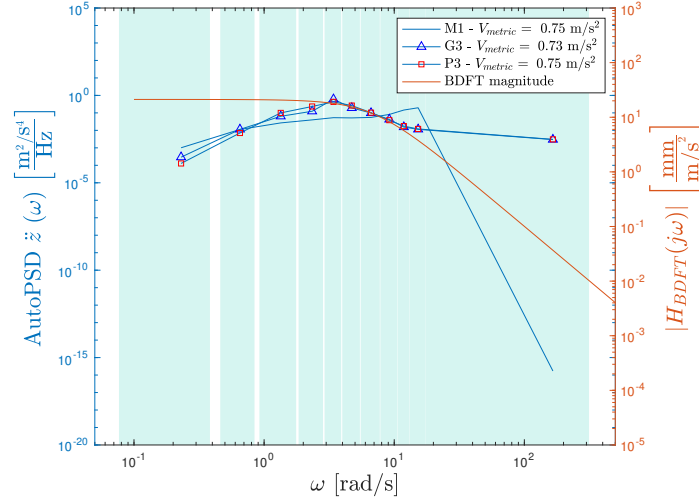


Figure 7.21: Frequency bin averaged PSD of the multisine, patchy and Gaussian motion disturbances, $V_{metric} = 0.75 \text{ m/s}^2$.⁴

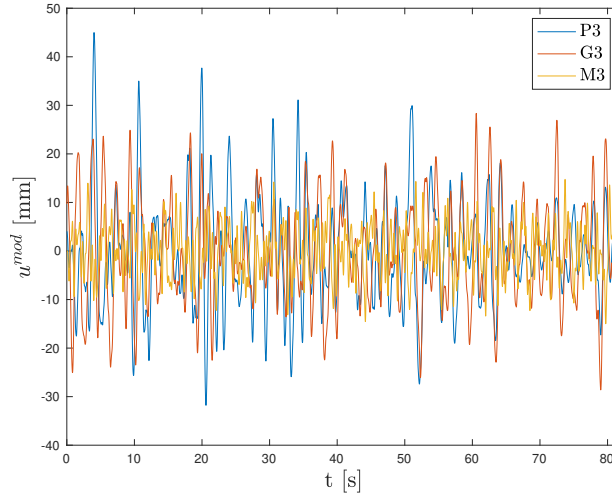


Figure 7.22: Simulated BDFT component of the vertical input for the multisine, Gaussian and patchy turbulence conditions.

While the standard deviation of the simulated BDFT component of the input with a multisine motion disturbance falls within the range from experimental observations, for both the Gaussian and the patchy case the calculated standard deviation is twice as large as the averaged observed one. It is therefore most likely that the human operators will not tolerate such a high feedthrough, and will adapt their dynamics. It can be hypothesized that the current BDFT model identified from the multisine disturbance will not be effective in canceling neither the involuntary input caused by the Gaussian turbulence, nor the one caused by the patchy. As seen in Figure 7.22 however, Gaussian turbulence is likely to causes an involuntary component of the input homogeneous in time, so it can be hypothesized that effective in mitigation can be achieved adapting the parameters of the BDFT model described in literature to the observed feedthrough. On the other hand for patchy turbulence, recalling that the BDFT model currently used is a time-invariant system, it can be hypothesized that mitigation with the current model will not be effective, as the human operators will change their dynamics across the non-homogeneous patches of turbulence since the amount of BDFT they will experience will also change.

Finally, some consideration can be made on the experimental conditions having different intensities. Figure 7.24 shows the bin averaged PSD of the accelerations of the simulator with the multisine, Gaussian and patchy conditions, at their three different intensities, $V_{metric} = 0.75, 0.5, 0.25 \text{ m/s}^2$.

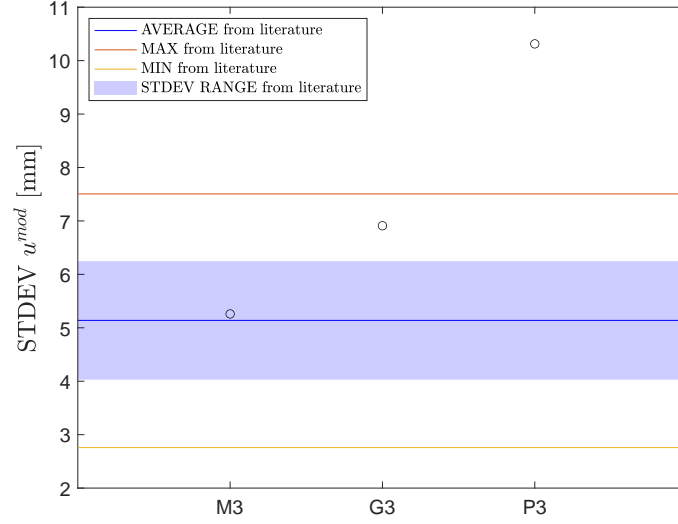


Figure 7.23: Average standard deviation of the involuntary component of the vertical input signal occurring with heave multisine motion disturbance, observed in Khoshnawizadeh's experiment [1], together with the one simulated for each experimental condition.

As expected, for each motion disturbance type, the shape of the frequency spectrum is the same across different intensities. The only difference is in the magnitude of the acceleration at which the participants of the upcoming experiment will be exposed. It can be therefore z that this will have a direct effect on the magnitude of the BDFT experienced by the participants, which is quantified by the gain of the BDFT model. The other characteristics of the BDFT model should however remain the same compared to the ones found for the baseline intensity of $V_{metric} = 0.75 \text{ m/s}^2$. It is therefore hypothesized that the model identified with multisine motion disturbances at $V_{metric} = 0.75 \text{ m/s}^2$, and applied to mitigate BDFT occurring on lower intensities will overestimate the amount of feedthrough at those intensities. However, identifying the dynamics of BDFT at for example $V_{metric} = 0.5 \text{ m/s}^2$, and using these models to mitigate BDFT occurring at the same intensity, performance will be comparable to when mitigation is performed on the baseline intensity case with a model identified at the baseline intensity. It also can be hypothesized that the same will hold for all motion disturbance types. Working on the identification and mitigation at one intensity will not give different mitigation performance than working at a different intensity also for the Gaussian and patchy cases.

7.6. Summary

This chapter discussed the preliminary work that was done on the modeling of turbulence for the purpose of developing an experiment to evaluate the effect of turbulence on model-based mitigation of *bio-dynamic feedthrough* (BDFT) in *touchscreens* (TSCs), while performing open-loop continuous tracking tasks.

The *patchy turbulence model* used in literature was first verified by comparison of the original documentation of the model, the implementation used in literature, and the data output of a MATLAB Simulink implementation. A corrected patchy turbulence model was proposed and verified, adjusting the equations of the filters used for the generation of the antisymmetric component of turbulence and removing a set of gains from the original schematic of the model.

Research then focused on the development of a controller, to be used to keep the simulated aircraft experiencing turbulence at the trim conditions, removing the low frequency components of the motion in pitch and roll and in the vertical acceleration of the aircraft. This was achieved through the implementation of a pitch rate feedback controller and a roll damper, and through a two steps tuning. First a good initial solution for the gains of the controller was found by iteration over a coarsely spaced interval, subsequently tuning was optimized for each gain starting from the innermost loops. While the performance of the controller was verified to be within requirements, the controller is not used in the generation of the experimental conditions, as it turned out not needed when using the corrected

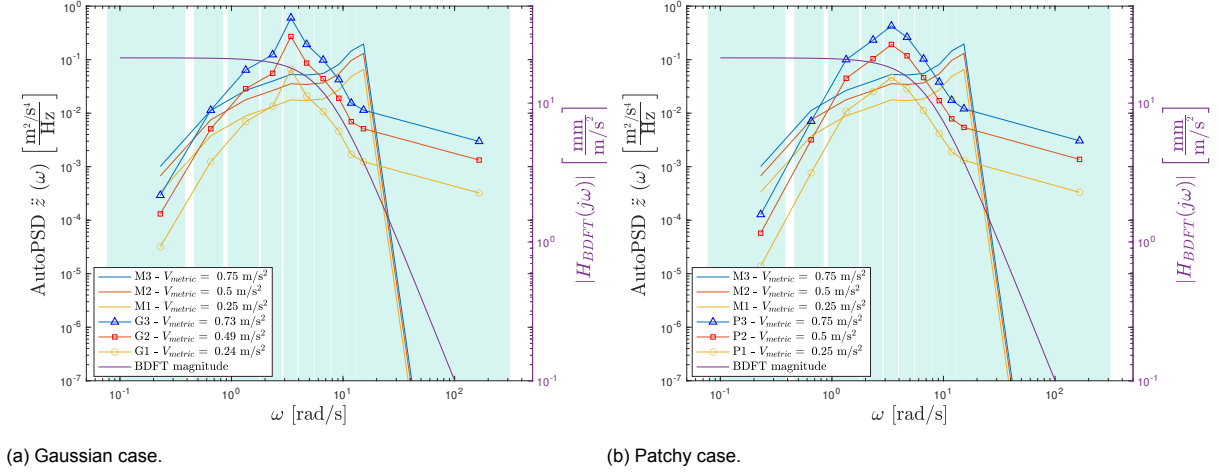
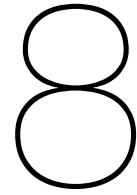


Figure 7.24: Frequency bin averaged PSD of the multisine, patchy and Gaussian motion disturbances, at the three levels of intensity: $V_{metric} = 0.75, 0.5, 0.25 \text{ m/s}^2$.

turbulence model described in this study.

Finally, the turbulence and the aircraft model were used to generate experimental conditions suitable for the upcoming BDFT experiment. Through an analysis of the effect of the parameters of the turbulence model on the aircraft responses, and later on the filter settings for the simulator, three different motion disturbances were defined together with three different intensities of motion, for a total of nine experimental conditions. These are a Gaussian homogeneous motion disturbance, a patchy motion disturbance presenting variability, and the baseline multisine already used in literature, for BDFT identification and performance comparison [1, 17]. Each of these conditions will be tested at a baseline intensity of the accelerations at which the participants are exposed of $V_{metric} = 0.75 \text{ m/s}^2$. Through the use of gains, this intensity will be lowered to create six more experimental conditions, a set with $V_{metric} = 0.5 \text{ m/s}^2$ and a set with $V_{metric} = 0.25 \text{ m/s}^2$. The experiment proposed will have a similar set up to BDFT model-based identification experiments in literature, but will attempt to use BDFT model identified with the multisine motion disturbance to mitigate BDFT occurring with Gaussian and patchy turbulence, at three levels of motion intensity.

Through the conditions mentioned, the effect on BDFT mitigation of realistic motion disturbances such as homogeneous and variable turbulence will be explored, together with the effect of different intensities of the motion to which participants are exposed. For the homogeneous Gaussian turbulence, it is expected based on BDFT simulations that the magnitude of the involuntary component of the motion will be considerably higher than the one observed in literature when participants were exposed to multisine motion disturbances. Given however the homogeneous nature of the turbulence, it is hypothesized that, albeit with a lower performance compared to the multisine case, BDFT mitigation can be performed using the current BDFT model. Using different methods to tune its parameters, a higher mitigation performance should be attained. For the patchy turbulence condition, a considerably higher variability of feedthrough was seen through simulations compared to the multisine case. It can therefore be expected that the current time-invariant BDFT model will be unable to effectively mitigate BDFT with variable patchy turbulence, as the human operator will have to adapt their dynamics when encountering inhomogeneous patches. Finally, it is expected that the main difference across BDFT models identified at different intensities will be in the magnitude of the feedthrough, i.e., in their gains.



Research Plan

The research discussed throughout this report aimed to follow the experiments of Mobertz [17] and Khoshnewiszadeh [1], which proved that a high performance can be achieved when mitigating *bio-dynamic feedthrough* (BDFT) occurring while performing open-loop continuous tracking tasks on a *touchscreen* (TSC), while being exposed to a multisine motion disturbance. As a conclusion to the preliminary study, the proposed set-up for an experiment to be performed in the *SIMONA Research Simulator* (SRS) is summarized here, its aim to further research the applicability of model-based mitigation of BDFT for realistic cases occurring in the aviation environments, such as in turbulence.

8.1. Research questions

Using turbulence modes identified from literature, the variability of turbulence as well as the intensity of turbulence were identified as important factors, whose impact on BDFT modeling and mitigation with TSCs is unknown. The following research question is therefore proposed.

How do turbulence intensity and variability influence the performance of model-based BDFT mitigation whilst performing a continuous tracking tasks on a touchscreen positioned at the Primary Flight Display location?

8.2. Experimental set-up

The proposed experimental set-up is discussed in the following sections, listing control variables, independent variables and dependent variables, and finally touching the experiment procedure.

8.2.1. Control variables

The experiment will be performed in the SRS, a six-degrees-of-freedom moving base simulator, driven by hydraulic pumps, located at the Faculty of Aerospace Engineering at TU Delft. The TSC equipped in the simulator in the *Primary Flight Display* (PFD) location is a 15-inch Iiyama Pro-Lite TF1534MC-B1X, tilted from the vertical plan with an angle of 18 degrees upwards. Participants will be tasked with following a target on the TSC without lifting their hand from the surface of the screen, while exposed to a heave motion disturbance. The continuous pursuit tracking task will be the same that has been used in the experiments from Mobertz [17] and Khoshnewiszadeh [1]. An example of the trajectory of the tracking task can be found in Figure 3.9. To prevent recognition of the signal, the lateral and vertical coordinates of the target will be flipped across the repeated runs. To prevent the participants from experiencing excessive fatigue, anti-static gloves will be used to reduce friction between their skin and the TSC surface.

Summarizing, the control variables are the following:

- motion disturbance axis: heave,

- touchscreen position: PFD location,
- target forcing functions: continuous pursuit tracking task,
- motion system apparatus: SRS,
- use of anti-static gloves.

8.2.2. Independent variables

In order to assess the effect of turbulence and its variability on model-based BDFT mitigation, four different motion disturbance types will be used, including a condition with no motion for calibration. These are a multisine motion disturbance, the simulation of the vertical acceleration of an aircraft in Gaussian turbulence, and the simulation of the vertical acceleration of the same aircraft in patchy turbulence. Each of the three motion conditions will be assessed at three different levels of intensity, quantified as the *root-mean-square* (RMS) vertical acceleration using the V -metric in Equation 4.13. The three intensity levels will be $V_{metric} = 0.75, 0.5, 0.25 \text{ m/s}^2$, corresponding to the intensities used by Jacobson [16] in his experiment evaluating the performance of an extension of the Finger-Fitts' Law for use with TSCs in aviation turbulence.

The independent variables are summarized as follows:

- RMS of the acceleration: $V_{metric} = 0.75, 0.5, 0.25 \text{ m/s}^2$,
- motion disturbance type: no motion (NM), multisine disturbance (M), Gaussian turbulence (G), patchy turbulence (P).

8.2.3. Dependent variables

Given that the experiment will be limited to the heave axis of the SRS, and with PFD-located TSC, the time traces of the vertical touchscreen input will be recorded. From these, BDFT dynamics can be estimated, and the parameters of the BDFT model derived. The differences between the parameters of the BDFT model across different types of motion disturbances will aid in understanding the effect of turbulence variability as well as turbulence intensity on the BDFT dynamics. The *Variance Accounted For* (VAF) calculated from Equation 3.13 for identification and Equation 3.14 for cancellation will be used to evaluate the performance of model-based BDFT mitigation for the different cases.

Summarizing, the dependent variables are:

- BDFT model parameters: $G_{BDFT}, \omega_{BDFT}, \zeta_{BDFT}, \tau_{BDFT}$,
- Variance Accounted For (VAF).

8.2.4. Procedure

Table 8.1 shows gives a summary of all experimental conditions that will be tested.

Table 8.1: Experimental conditions matrix.

Condition	Description	V_{metric} [m/s ²]
NM	No motion	-
M1	Multisine low intensity	0.25
M2	Multisine medium intensity	0.50
M3	Multisine high intensity	0.75
G1	Gaussian low intensity	0.24
G2	Gaussian medium intensity	0.48
G3	Gaussian high intensity	0.73
P1	Patchy low intensity	0.25
P2	Patchy medium intensity	0.50
P3	Patchy high intensity	0.75

About 20 participants will do four training rounds with no motion and with multisine motion conditions at the three intensity levels, (NM, M1, M2, M3). Subsequently, 16 identification and 36 cancellation trials

will be performed, in mixed order. In the 16 identification trials, conditions M1, M2, M3 and NM will be repeated four times each, flipping for each repetition one or both of the coordinates of the target signal on the TSC. These trials will be used for the identification of the BDFT model. The 36 cancellation trials comprise all motion conditions (M1, M2, M3, G1, G2, G3, P1, P2, P3). Each condition repeated four times with flipped target signals, these will be used to evaluate model-based mitigation of BDFT across intensities and across the different motion disturbance types. With two breaks, the experiment is expected to last about 2.5 hours.

8.3. Hypothesis

The hypotheses, already discussed in Section 7.5, are here formulated explicitly.

Regarding the usability and performance of model-based BDFT mitigation in realistic scenarios such as aircraft turbulence, two hypothesis are formulated, separating the case of Gaussian turbulence and patchy turbulence. For Gaussian turbulence, it was noted that both the time traces of the accelerations that the human operators will experience and the simulated involuntary vertical component of the TSC input u^{mod} are quite homogeneous in time. However, the standard deviation of the simulated u^{mod} is significantly higher than the standard deviation of the involuntary input recorded in previous experiments. It is likely that the human operator will adapt their dynamics to reduce the amount of feedthrough, requiring some adaptations to be made in the values of the parametric model for effective mitigation. For this reason, the following hypothesis is formulated:

H1: A more compliant control behavior of the TSC operators, i.e., a lower natural frequency, will be observed with disturbances caused by Gaussian turbulence, when compared to the multisine disturbance. Effective model-based BDFT mitigation will be obtained by adapting the model's parameters.

On the other hand, for the patchy motion disturbance case variations in the intensity of the disturbance as well as the intensity of the simulated involuntary component of the input are seen throughout the measurement time. Also in this case, the amount of feedthrough occurring is noted to exceed the one that human will most likely tolerate, as the standard deviation of the simulated u^{mod} is again higher than even the maximum standard deviation of the BDFT component of the input recorded in the previous study. As such, the following hypothesis is formulated for the patchy turbulence condition:

H2: A time-varying control behavior will be observed with disturbances caused by patchy turbulence. Low performance will be observed with model-based BDFT mitigation using the current time-invariant model.

Finally, in regards to the different intensities of the accelerations that the participants will experience, it is noted that the most likely consequence of a change in intensity will affect the intensity of the feedthrough in terms of the gain of the BDFT model identified. The following hypothesis is therefore proposed:

H3: The BDFT model identified for a higher motion intensity (V_{metric}) will overestimate BDFT when employed for mitigation at lower V_{metric} . Mitigating BDFT on data collected at a specific V_{metric} using a BDFT model identified at the same V_{metric} will lead to comparable performance independently of the magnitude of V_{metric} .

Conclusions

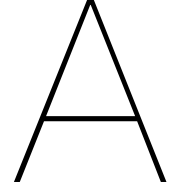
The use of *touchscreen* (TSC) interfaces in aviation has become more and more common in recent years. Originally used only for on ground checklists and manuals, they are today seen as the future for more intuitive human-avionics interaction, increasing situation awareness even with complex scenarios, such as shared control between human and automation. However, the use of TSCs for safety critical tasks is still uncommon. Main challenges are the lack of tactile feedback, requiring the TSC operator to look down to both make selections and confirm their actions, as well as *biodynamic feedthrough* (BDFT). BDFT refers to the transfer of the accelerations of the vehicle through the human body, to the manipulator, and therefore to the control inputs.

This preliminary report provided an overview of literature related to the use of TSCs in dynamic environments, with particular reference to studies related to aviation and to the problem of BDFT, giving at the same time the require context on both topics, TSCs and BDFT. The literature review helped to identify a promising method to mitigate BDFT with TSCs: a model-based approach. A research gap was therefore identified in the applicability of this method, tested in literature only with unrealistic motion disturbances, in realistic scenarios such as in aircraft turbulence. A literature review was therefore conducted on turbulence, and in particular on turbulence modeling, which lead to the selection of a *patchy turbulence model* as a means to simulate realistic motion disturbances in a simulator experiment.

Following this study, preliminary research was conducted first to understand whether the performance of the existing model-based BDFT mitigation could be improved through the use of different cost functions for the frequency domain identification approach proposed in literature, as well as through the use of a time domain identification approach. These studies led to the conclusion that either method can be used, without providing substantial differences in performance.

Further research was also conducted on the simulation of the aircraft responses to turbulence with the *patchy turbulence model*, in order to design the best possible experiment within the given scope and time frame of the research. The research lead to the proposal of corrections to the original turbulence model, to the development of a controller to maintain the aircraft stable at the specified trim conditions, and to the selection of the experimental conditions for the experiment to follow. These experimental conditions were selected to evaluate the impact of variability as well as intensity of turbulence on model-based BDFT mitigation. Each condition was selected by careful study of the influence of the parameters input to the turbulence model on the aircraft responses, as well as on the filtered simulator motion. In conclusion, an experiment plan was developed and hypothesis derived on how the dynamics of BDFT change across different turbulence conditions (uniform, variable) and across different intensity of the accelerations causing BDFT, with particular attention on how these will affect BDFT mitigation.

Appendices to Preliminary Report



Equations of the Linear Filters of the Turbulence Models

This Appendix provides the equations for the shaping filters of the *Gaussian turbulence model* in Section A.1 and of the *patchy turbulence model* in Section A.2.

A.1. Gaussian turbulence model

The equations used for the generation of u_g , v_g , w_g , \hat{u}_{gasymp} and α_{gasymp} through linear filtering with the *Gaussian turbulence model*, as discussed in Section 4.4.1, are given here.

For the generation of symmetric aircraft responses, $H_{u_g}(j\omega)$ and $H_{w_g}(j\omega)$ are given as a function of the integral scale of turbulence L_{u_g} and the square root of the turbulence intensity σ_g , as well as the airspeed V and the constant power spectrum of the white noise $S_{kk}(\omega) = W_k = 1$ [47, 61, 73].

$$H_{u_g}(j\omega) = \frac{1}{W_k} \sigma_g \sqrt{2 \frac{L_{u_g}}{V}} \frac{1}{1 + \frac{L_{u_g}}{V} j\omega} \quad (\text{A.1})$$

$$H_{w_g}(j\omega) = \frac{1}{W_k} \sigma_g \sqrt{\frac{L_{u_g}}{V}} \frac{1 + \sqrt{3} \frac{L_{u_g}}{V} j\omega}{\left(1 + \frac{L_{u_g}}{V} j\omega\right)^2} \quad (\text{A.2})$$

The transfer functions of the linear filters generating the antisymmetric component of the turbulence field from white noise signals are $H_{v_g}(j\omega)$, $H_{\hat{u}_{gasymp}}(j\omega)$ and $H_{\alpha_{gasymp}}(j\omega)$ [47, 61, 73]. The constants appearing in the Equations are listed in Table A.1 as a function of parameter $B = \frac{b}{2L_{u_g}}$, where b is the span [47].

$$H_{v_g}(j\omega) = \frac{1}{W_k} \sigma_g \sqrt{\frac{L_{u_g}}{V}} \frac{1 + \sqrt{3} \frac{L_{u_g}}{V} j\omega}{\left(1 + \frac{L_{u_g}}{V} j\omega\right)^2} \quad (\text{A.3})$$

$$H_{\hat{u}_{gasymp}}(j\omega) = \frac{1}{W_k} \sqrt{\frac{L_{u_g}}{V}} I_{\hat{u}_g}(0, B) \frac{1 + \tau_3 \frac{L_{u_g}}{V} j\omega}{\left(1 + \tau_1 \frac{L_{u_g}}{V} j\omega\right) \left(1 + \tau_2 \frac{L_{u_g}}{V} j\omega\right)} \quad (\text{A.4})$$

$$H_{\alpha_{gasymp}}(j\omega) = \frac{1}{W_k} \sqrt{\frac{L_{u_g}}{V}} I_{\alpha_g}(0, B) \frac{1 + \tau_6 \frac{L_{u_g}}{V} j\omega}{\left(1 + \tau_4 \frac{L_{u_g}}{V} j\omega\right) \left(1 + \tau_5 \frac{L_{u_g}}{V} j\omega\right)} \quad (\text{A.5})$$

Table A.1: Constants used for modeling the antisymmetric turbulence components, as a function of $B = \frac{b}{2L_{ug}}$. Adapted from Mulder et al. [47].

B	$I_{\hat{u}_g}(0, B)/\sigma_{\hat{u}_g}^2$	$I_{\alpha_g}(0, B)/\sigma_{\alpha_g}^2$	τ_1	τ_2	τ_3	τ_4	τ_5	τ_6
[-]	[-]	[rad ²]	[-]	[-]	[-]	[-]	[-]	[-]
0.50	0.79	0.54	0.66	2.31	2.30	0.48	1.49	1.53
0.45	0.70	0.48	0.61	1.24	1.20	0.46	1.33	1.36
0.40	0.62	0.43	0.54	1.02	0.95	0.43	1.12	1.14
0.35	0.53	0.37	0.47	0.90	0.79	0.39	0.79	0.77
0.30	0.43	0.31	0.41	0.83	0.70	0.34	0.59	0.55
0.25	0.34	0.24	0.35	0.79	0.64	0.28	0.55	0.48
0.20	0.25	0.18	0.29	0.75	0.59	0.22	0.49	0.39
0.15	0.17	0.12	0.23	0.71	0.55	0.16	0.44	0.32
0.13	0.13	0.09	0.20	0.68	0.52	0.14	0.42	0.30
0.10	0.09	0.06	0.17	0.65	0.50	0.11	0.39	0.27
0.08	0.06	0.04	0.14	0.62	0.47	0.09	0.37	0.25
0.06	0.04	0.03	0.12	0.60	0.45	0.08	0.35	0.24
0.05	0.03	0.02	0.11	0.57	0.43	0.06	0.34	0.23
0.03	0.01	0.01	0.08	0.51	0.38	0.05	0.31	0.21
0.02	0.00	0.00	0.05	0.42	0.31	0.03	0.28	0.20

A.2. Patchy turbulence model

For the simulation of non-Gaussian turbulence velocities using the *patchy turbulence model*, the equations for each of the three filters appearing for each component of the turbulence velocity is here provided.

For the symmetric turbulence velocity field, the equations of the shaping filters of white noise signals with constant power spectrum $W_a = W_b = W_c = 1$ are given by the following equations [56, 73]. For the longitudinal component of the turbulence velocity, the equations are the following:

$$\begin{aligned}
 H_{a_{ug}}(j\omega) &= \frac{1}{W_a} \sqrt{2\sigma_u \frac{L_{ug}}{V} (R+1)} \frac{1}{1 + \frac{L_{ug}}{V} (R+1)j\omega} \\
 H_{b_{ug}}(j\omega) &= \frac{1}{W_b} \sqrt{2\sigma_u \frac{L_{ug}}{V} \frac{(R+1)}{R}} \frac{1}{1 + \frac{L_{ug}}{V} \frac{R+1}{R} j\omega} \\
 H_{c_{ug}}(j\omega) &= \frac{1}{W_c} \sigma_c \sqrt{2 \frac{L_{ug}}{V}} \frac{1}{1 + \frac{L_{ug}}{V} j\omega}
 \end{aligned} \tag{A.6}$$

The two variables σ_u and σ_c are given as a function of the square root of the turbulence intensity σ_g [47].

$$\sigma_u = \frac{Q\sigma_g}{\sqrt{1+Q^2}} \quad \sigma_c = \frac{\sigma_g}{\sqrt{1+Q^2}} \tag{A.7}$$

As can be seen from the above equations, the ratio $Q = \sigma_u/\sigma_c$ is independent from the intensity of turbulence.

Similarly, for the vertical turbulence velocity, the following transfer functions should be used for the signal filtering [56, 73]:

$$\begin{aligned}
H_{a_{wg}}(j\omega) &= \frac{1}{W_a} \sqrt{2\sigma_u \frac{L_{ug}}{V} \frac{(R+1)}{R}} \frac{1}{1 + \frac{(R+1)}{R} \frac{L_{ug}}{V} j\omega} \\
H_{b_{wg}}(j\omega) &= \frac{1}{W_b} \sqrt{\sigma_u \frac{L_{ug}}{V} (R+1)} \frac{\sqrt{1-R} + (R+1)\sqrt{3+R} \frac{L_{ug}}{V} j\omega}{\left(1 + (R+1) \frac{L_{ug}}{V} j\omega\right)^2} \\
H_{c_{wg}}(j\omega) &= \frac{1}{W_c} \sigma_c \sqrt{\frac{L_{ug}}{V}} \frac{1 + \sqrt{3} \frac{L_{ug}}{V} j\omega}{\left(1 + \frac{L_{ug}}{V} j\omega\right)^2}
\end{aligned} \tag{A.8}$$

Again σ_u and σ_c given by Equation A.7.

When considering the antisymmetric component of the turbulence velocity fields, for the lateral turbulence velocity v_g the following equations should be used (σ_u and σ_c given by Equation A.7) [56, 73]:

$$\begin{aligned}
H_{a_{vg}}(j\omega) &= \frac{1}{W_a} \sqrt{2\sigma_u \frac{L_{ug}}{V} \frac{(R+1)}{R}} \frac{1}{1 + \frac{(R+1)}{R} \frac{L_{ug}}{V} j\omega} \\
H_{b_{vg}}(j\omega) &= \frac{1}{W_b} \sqrt{\sigma_u \frac{L_{ug}}{V} (R+1)} \frac{\sqrt{1-R} + (R+1)\sqrt{3+R} \frac{L_{ug}}{V} j\omega}{\left(1 + (R+1) \frac{L_{ug}}{V} j\omega\right)^2} \\
H_{c_{vg}}(j\omega) &= \frac{1}{W_c} \sigma_c \sqrt{\frac{L_{ug}}{V}} \frac{1 + \sqrt{3} \frac{L_{ug}}{V} j\omega}{\left(1 + \frac{L_{ug}}{V} j\omega\right)^2}
\end{aligned} \tag{A.9}$$

For the normalized antisymmetric component of longitudinal turbulence velocity $\hat{u}_{g_{asym}}$ [65, 73],

$$\begin{aligned}
H_{a_{\hat{u}_{g_{asym}}}}(j\omega) &= \frac{1}{W_a} \sqrt{C} \frac{1}{1 + Aj\omega} \\
H_{b_{\hat{u}_{g_{asym}}}}(j\omega) &= \frac{1}{W_b} \sqrt{F} \frac{B + Ej\omega}{(1 + Dj\omega)(1 + Gj\omega)} \\
H_{c_{\hat{u}_{g_{asym}}}}(j\omega) &= \frac{1}{W_c} \sqrt{H} \frac{1 + Lj\omega}{(1 + Mj\omega)(1 + Nj\omega)}
\end{aligned} \tag{A.10}$$

with

$$\begin{aligned}
A &= \frac{L_{ug}}{V} \frac{R+1}{R} \tau_2 \\
B &= \sqrt{\tau_2(R+1) - \tau_1 R} \sqrt{1 + \frac{(\tau_2^2 - \tau_3^2)R}{\tau_2(\tau_2 + \tau_1)}} \\
C &= \frac{Q}{\sqrt{1+Q^2}} \sqrt{2I_{\hat{u}_g}(0, B) \left(\frac{\tau_2^2 - \tau_3^2}{\tau_2(\tau_2^2 - \tau_3^2)} + \frac{\tau_1^2 - \tau_3^2}{\tau_1(\tau_1^2 - \tau_2^2)} \right) \frac{L_{ug}}{V} \tau_2 \frac{R+1}{R}} \\
D &= \frac{L_{ug}}{V} (R+1) \tau_2 \\
E &= \frac{L_{ug}}{V} (R+1) \sqrt{\tau_2 \tau_3^2 - \frac{R\tau_2^2(\tau_1^2 - \tau_3^2)}{(\tau_2 + \tau_1)}}
\end{aligned}$$

$$\begin{aligned}
F &= \frac{Q}{\sqrt{1+Q^2}} \sqrt{2I_{\dot{u}_g}(0,B) \frac{\tau_2 \tau_1 (\tau_2^2 - \tau_1^2)}{\tau_1 \tau_2^2 - \tau_1 \tau_3^2 - \tau_2 \tau_1^2 + \tau_2 \tau_3^2} \frac{\frac{L_{ug}}{V} \tau_2 (R+1)}{(\tau_2 (R+1) - \tau_1 R)^2}} \\
G &= \frac{L_{ug}}{V} \frac{\tau_2 \tau_1 (R+1)}{\tau_2 (R+1) - \tau_1 R} \\
H &= \frac{1}{1+Q^2} I_{\dot{u}_g}(0,B) \\
L &= \frac{L_{ug}}{V} \tau_3 \\
M &= \frac{L_{ug}}{V} \tau_1 \\
N &= \frac{L_{ug}}{V} \tau_2
\end{aligned}$$

Equivalent expressions hold for the antisymmetric vertical component α_{gasyim} [65, 73]:

$$\begin{aligned}
H_{a\alpha_{gasyim}}(j\omega) &= \frac{1}{W_a} \sqrt{C} \frac{1}{1 + Aj\omega} \\
H_{b\alpha_{gasyim}}(j\omega) &= \frac{1}{W_b} \sqrt{F} \frac{B + Ej\omega}{(1 + Dj\omega)(1 + Gj\omega)} \\
H_{c\alpha_{gasyim}}(j\omega) &= \frac{1}{W_c} \sqrt{H} \frac{1 + Lj\omega}{(1 + Mj\omega)(1 + Nj\omega)}
\end{aligned} \tag{A.11}$$

with

$$\begin{aligned}
A &= \frac{L_{ug}}{V} \frac{R+1}{R} \tau_5 \\
B &= \sqrt{\tau_5(R+1) - \tau_4 R} \sqrt{1 + \frac{(\tau_5^2 - \tau_6^2)R}{\tau_5(\tau_5 + \tau_4)}} \\
C &= \frac{Q}{\sqrt{1+Q^2}} \sqrt{2I_{\alpha_g}(0,B) \left(\frac{\tau_5^2 - \tau_6^2}{\tau_5(\tau_5^2 - \tau_6^2)} + \frac{\tau_4^2 - \tau_6^2}{\tau_4(\tau_4^2 - \tau_5^2)} \right) \frac{L_{ug}}{V} \tau_5 \frac{R+1}{R}} \\
D &= \frac{L_{ug}}{V} (R+1) \tau_5 \\
E &= \frac{L_{ug}}{V} (R+1) \sqrt{\tau_5 \tau_6^2 - \frac{R \tau_5^2 (\tau_4^2 - \tau_6^2)}{(\tau_5 + \tau_4)}} \\
F &= \frac{Q}{\sqrt{1+Q^2}} \sqrt{2I_{\alpha_g}(0,B) \frac{\tau_5 \tau_4 (\tau_5^2 - \tau_4^2)}{\tau_4 \tau_5^2 - \tau_4 \tau_6^2 - \tau_5 \tau_4^2 + \tau_5 \tau_6^2} \frac{\frac{L_{ug}}{V} \tau_5 (R+1)}{(\tau_5 (R+1) - \tau_4 R)^2}} \\
G &= \frac{L_{ug}}{V} \frac{\tau_5 \tau_4 (R+1)}{\tau_5 (R+1) - \tau_4 R} \\
H &= \frac{1}{1+Q^2} I_{\alpha_g}(0,B) \\
L &= \frac{L_{ug}}{V} \tau_6 \\
M &= \frac{L_{ug}}{V} \tau_4 \\
N &= \frac{L_{ug}}{V} \tau_5
\end{aligned}$$

B

Equations of the Proposed Corrected Patchy Turbulence Model

The proposed corrections to the *patchy turbulence model* discussed in Section 7.2.1 are given in this appendix for clarity's sake.

Figure B.1 shows the updated schematic for the *patchy turbulence model*.

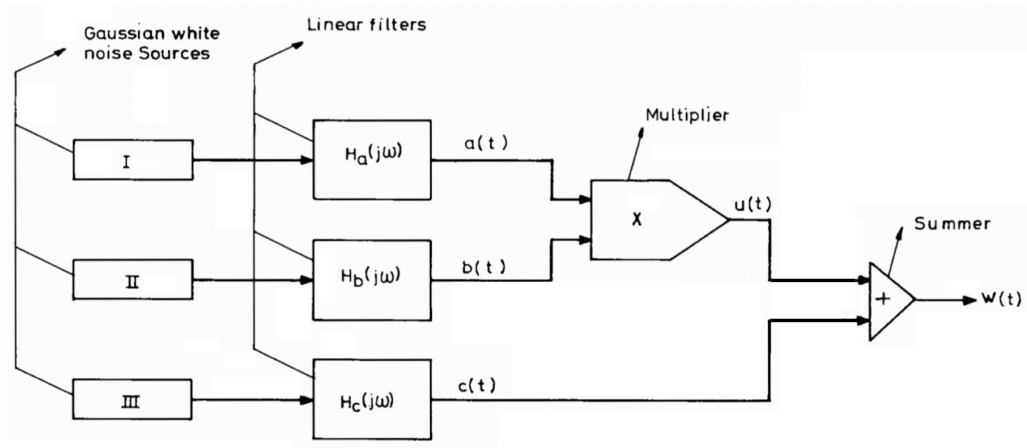


Figure B.1: Schematic for the proposed corrected *patchy turbulence model*.

The equations for the linear filters for the symmetric turbulence velocities are unchanged, refer to Equation A.6, Equation A.7, Equation A.8 and Equation A.9 of Appendix A.

The new equations describing the shaping filters for the normalized antisymmetric component of longitudinal turbulence velocity $\hat{u}_{g_{asym}}$ are the following:

$$\begin{aligned} H_{a_{\hat{u}_{g_{asym}}}}(j\omega) &= \frac{1}{W_a} \sqrt{C} \frac{1}{1 + Aj\omega} \\ H_{b_{\hat{u}_{g_{asym}}}}(j\omega) &= \frac{1}{W_b} \sqrt{F} \frac{B + Ej\omega}{(1 + Dj\omega)(1 + Gj\omega)} \\ H_{c_{\hat{u}_{g_{asym}}}}(j\omega) &= \frac{1}{W_c} \sqrt{H} \frac{1 + Lj\omega}{(1 + Mj\omega)(1 + Nj\omega)} \end{aligned} \quad (B.1)$$

with

$$\begin{aligned}
A &= \frac{L_{ug}}{V} \frac{R+1}{R} \tau_2 \\
B &= \sqrt{\tau_2(R+1) - \tau_1 R} \sqrt{1 + \frac{(\tau_2^2 - \tau_3^2)R}{\tau_2(\tau_2 + \tau_1)}} \\
C &= \frac{Q}{\sqrt{1+Q^2}} \sqrt{2I_{\hat{u}_g}(0, B) \left(\frac{\tau_2^2 - \tau_3^2}{\tau_2(\tau_2^2 - \tau_3^2)} + \frac{\tau_1^2 - \tau_3^2}{\tau_1(\tau_1^2 - \tau_2^2)} \right) \frac{L_{ug}}{V} \tau_2 \frac{R+1}{R}} \\
D &= \frac{L_{ug}}{V} (R+1) \tau_2 \\
E &= \frac{L_{ug}}{V} (R+1) \sqrt{\tau_2 \tau_3^2 - \frac{R \tau_2^2 (\tau_1^2 - \tau_3^2)}{(\tau_2 + \tau_1)}} \\
F &= \frac{Q}{\sqrt{1+Q^2}} \sqrt{2I_{\hat{u}_g}(0, B) \frac{\tau_2 \tau_1 (\tau_2^2 - \tau_1^2)}{\tau_1 \tau_2^2 - \tau_1 \tau_3^2 - \tau_2 \tau_1^2 + \tau_2 \tau_3^2} \frac{\frac{L_{ug}}{V} \tau_2 (R+1)}{(\tau_2(R+1) - \tau_1 R)^2}} \\
G &= \frac{L_{ug}}{V} \frac{\tau_2 \tau_1 (R+1)}{\tau_2(R+1) - \tau_1 R} \\
H &= \frac{1}{1+Q^2} I_{\hat{u}_g}(0, B) \frac{L_{ug}}{V} \\
L &= \frac{L_{ug}}{V} \tau_3 \\
M &= \frac{L_{ug}}{V} \tau_1 \\
N &= \frac{L_{ug}}{V} \tau_2.
\end{aligned}$$

Similarly, the new equations describing the shaping filters for the normalized antisymmetric component of vertical turbulence velocity $\alpha_{g_{asym}}$ are the following:

$$\begin{aligned}
H_{a\alpha_{g_{asym}}}(j\omega) &= \frac{1}{W_a} \sqrt{C} \frac{1}{1 + Aj\omega} \\
H_{b\alpha_{g_{asym}}}(j\omega) &= \frac{1}{W_b} \sqrt{F} \frac{B + Ej\omega}{(1 + Dj\omega)(1 + Gj\omega)} \\
H_{c\alpha_{g_{asym}}}(j\omega) &= \frac{1}{W_c} \sqrt{H} \frac{1 + Lj\omega}{(1 + Mj\omega)(1 + Nj\omega)}
\end{aligned} \tag{B.2}$$

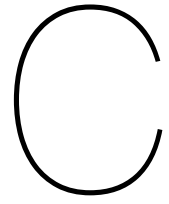
with

$$\begin{aligned}
A &= \frac{L_{ug}}{V} \frac{R+1}{R} \tau_5 \\
B &= \sqrt{\tau_5(R+1) - \tau_4 R} \sqrt{1 + \frac{(\tau_5^2 - \tau_6^2)R}{\tau_5(\tau_5 + \tau_4)}} \\
C &= \frac{Q}{\sqrt{1+Q^2}} \sqrt{2I_{\alpha_g}(0, B) \left(\frac{\tau_5^2 - \tau_6^2}{\tau_5(\tau_5^2 - \tau_6^2)} + \frac{\tau_4^2 - \tau_6^2}{\tau_4(\tau_4^2 - \tau_5^2)} \right) \frac{L_{ug}}{V} \tau_5 \frac{R+1}{R}} \\
D &= \frac{L_{ug}}{V} (R+1) \tau_5 \\
E &= \frac{L_{ug}}{V} (R+1) \sqrt{\tau_5 \tau_6^2 - \frac{R \tau_5^2 (\tau_4^2 - \tau_6^2)}{(\tau_5 + \tau_4)}}
\end{aligned}$$

$$\begin{aligned}
F &= \frac{Q}{\sqrt{1+Q^2}} \sqrt{2I_{\alpha_g}(0,B) \frac{\tau_5 \tau_4 (\tau_5^2 - \tau_4^2)}{\tau_4 \tau_5^2 - \tau_4 \tau_6^2 - \tau_5 \tau_4^2 + \tau_5 \tau_6^2} \frac{\frac{L_{ug}}{V} \tau_5 (R+1)}{(\tau_5 (R+1) - \tau_4 R)^2}} \\
G &= \frac{\frac{L_{ug}}{V} \tau_5 \tau_4 (R+1)}{\tau_5 (R+1) - \tau_4 R} \\
H &= \frac{1}{1+Q^2} I_{\alpha_g}(0,B) \frac{L_{ug}}{V} \\
L &= \frac{L_{ug}}{V} \tau_6 \\
M &= \frac{L_{ug}}{V} \tau_4 \\
N &= \frac{L_{ug}}{V} \tau_5
\end{aligned}$$



Appendices to Paper



Experiment Briefing and Consent Form

The experiment briefing and informed consent form, describing experimental procedures, were sent to participants in advance of the experiment session. Contact information in the informed consent form shown here was redacted for privacy concerns.

Effect of turbulence on touchscreen dragging tasks

Experiment briefing

Thank you for taking the time to participate in this research. This briefing will explain the purpose and procedures of the experiment. Please read the procedure, the informed consent form and watch the SIMONA safety information video carefully. We will further discuss them before starting the experiment, and you will have time to ask any questions you might have.

Purpose

Touchscreens have already been introduced in aircraft cockpits (Airbus A350, Boeing 777X, Thales FlytX, Garmin G5000 amongst others) for consultation of checklists, manuals and maps. This single interface enables control of (potentially) all systems of the aircraft, saving weight compared to conventional interfaces, and introducing interaction methods which increase situational awareness, for example through the interactive consultation with land and weather maps.

Despite these advantages, touchscreen interfaces are generally not used for safety critical tasks in aviation. Especially in dynamic environments such as a cockpit exposed to turbulence, control tasks performed with touchscreens are prone to errors. Causes are the inability of the users to precisely touch a location on the screen without stabilizing their hand on the display, as well as to confirm the location of their touch before giving inputs. This experiment explores the effect of aircraft turbulence on dragging tasks performed on touchscreens.

Procedure

The experiment will be performed in the SIMONA Research Simulator (SRS) at the faculty of Aerospace Engineering at TU Delft. For this experiment, you will use the right seat of the simulator, and give inputs on the touchscreen placed directly in front of you (primary flight display). All other input devices and displays will be disabled. The task you will perform will be detailed in the next section.

In the different condition tested in the experiment, the motion system of the SRS may be turned on to simulate turbulence or turned off to get data in static conditions. Individual tracking runs last 90 seconds each, and the experiment consists of a minimum of 56 runs. In total it is expected that the experiment will be completed in 2.5 hours.

Communication will be handled through speakers and microphones in the cabin. The speakers will be disabled during the 90 seconds of each run. After each run, the experimenter will confirm with you if you are ready to continue or if you need some time to rest. A total of three 15-minute breaks are scheduled, for which the simulator will be stopped and you can exit the simulator. The start of each run will be announced with a countdown.

Task

You will be asked to perform a continuous tracking task on the touchscreen in front of you. Figure 1 shows the visual display that is used in the experiment. Using this display, your task is to closely follow a target marker that continuously moves on the touchscreen, the white triangle in Fig. 1, with your (index) finger. The target's location is also indicated by a vertical and a horizontal line that pass through its center, so that you can also see where the target moves when your hand may block the view of the triangle marker. For reference, the position

of your finger as registered by the touchscreen is indicated with a purple marker. Note that there is some lag between your current finger position and the purple marker, due to the touch processing hard- and software.

Important!

- Please pay attention to never losing contact with the touchscreen. If you do, please notify the experimenter.
- Please sit straight, leaning your back on the backrest for the duration of the measurements.
- Please pay attention to never rest your other arm on your legs during the measurements.
- Please only touch the screen with your index finger, without supporting your hand on the screen.

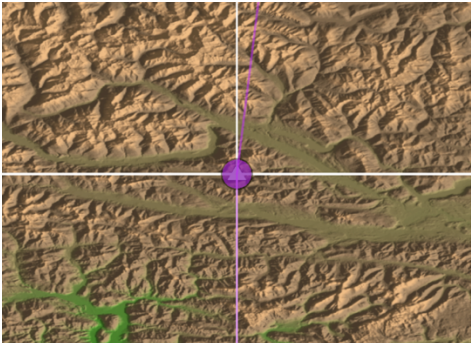
	Symptoms		MISC
	No problems		0
	Some discomfort, but no specific symptoms		1
	Dizziness, cold/warm, headache, stomach / throat awareness, sweating, blurred vision, yawning, burping, tiredness, salivation, ... but no nausea	vague	2
		little	3
		rather	4
		severe	5
	Nausea	little	6
		rather	7
		severe	8
	Vomiting		10

Figure 1: Visual display used in the experiment.

Figure 2: Misery Scale (MISC).

General information

At the scheduled time, we will meet at the coffee area of the SIMONA building, and you will be given time to read this briefing, to sign the informed consent form, to watch the safety video for SIMONA if you haven't already done so, and to ask questions.

Participation in this experiment is voluntary. Although highly unlikely, the motions experienced in the experiment may induce motion sickness in some individuals. To help you quantify your symptoms, the Misery Scale shown in Fig. 2 will be provided to you in the simulator cabin. If your symptoms exceed MISC 3, please let the experimenter know so that the experiment can be paused or stopped.

At any given moment you can request for a break to be taken, or to stop the experiment and withdraw your participation to the study.

The data collected during the experiment is considered confidential and only the experimenter is able to link results to a particular participant. By participating, you agree that your anonymized (pseudonymized) data may be published.

Finally, please do not discuss any detail of your experiment with other participants before their participation, to prevent biased results. By signing the consent form you agree that you have understood these terms and conditions.

Thank you for participating in this study!

Informed Consent Form for the study: Effect of Turbulence on Touchscreen Dragging Tasks

Please tick the appropriate boxes

Yes No

Taking part in the study

I have read and understood the study's briefing document, or it has been read to me. I have been able to ask questions about the study and my questions have been answered to my satisfaction.

☐ ☐

I consent voluntarily to be a participant in this study and understand that I can refuse to answer questions and can withdraw from the study at any time, without having to give a reason.

☐ ☐

I understand that taking part in the study involves the recording of my manual control inputs on a touchscreen while exposed to aircraft turbulence in the SIMONA Research Simulator. I am aware that some demographic information (age, handedness, etc.) will be collected before the experiment, but will not be shared in identifiable form beyond the research team.

☐ ☐

Risks associated with participating in the study

I understand that taking part in the study involves the risk of physical discomfort such as mild motion sickness and that I should always report such discomfort to the experimenter.

☐ ☐

I confirm that the researcher has provided me with detailed safety and operational instructions for the hardware (simulator setup, fire escape ladder) used in the experiment.

☐ ☐

I confirm that the researcher has provided me with detailed safety instructions to ensure my experiment session can be performed in line with current RIVM COVID-19 regulations at all times and that these instructions are fully clear to me.

☐ ☐

I confirm that I currently do not have any COVID-19 symptoms.

☐ ☐

Use of the information in the study

I understand that information collected (excluding information that can identify me) will be used for scientific reports and publications.

☐ ☐

I understand that personal information collected about me that can identify me, such as name and email address, will not be shared beyond the study team, and that my confidentiality as a participant in this study will remain secure.

☐ ☐

Future use and reuse of the information by others

I give permission for the anonymised manual control and questionnaire data that I provide to be archived on the 4TU.ResearchData repository so it can be used for future research and learning.

☐ ☐

Signatures

Name of participant [printed]

Signature

Date

I have accurately read out the information sheet to the potential participant and, to the best of my ability, ensured that the participant understands to what they are freely consenting.

Giulia Leto

Researcher name

Signature

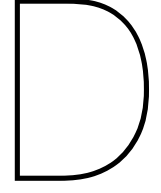
Date

Contact information
researcher:

Giulia Leto

Contact information research
supervisor:

dr. ir. Daan Pool



Baseline Conditions Compared to Khoshnewiszadeh and Pool

Comparison between the performance of the identification of the baseline condition M3 and of the same condition in the study of Khoshnewiszadeh and Pool [78] (reference [13] in the paper) was discussed in Section IV.A.1 of the paper. As a complement, this appendix shows the parameters of the OSFA and of the SA models identified in the two cases, Figure D.1. The BDFT estimates for the participants of both experiments are shown together with the frequency response of the identified models in Figure D.2.

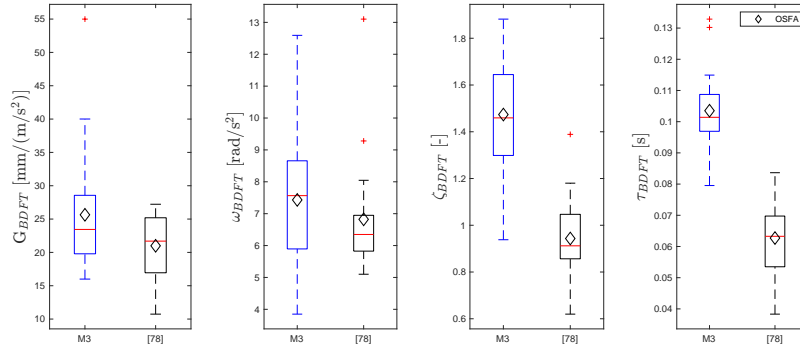


Figure D.1: Median and spread of the parameters of the $H_{BDFT/M}(j\omega)$ models of this study and of Khoshnewiszadeh and Pool [78] (time domain approach, SA and OSFA models).

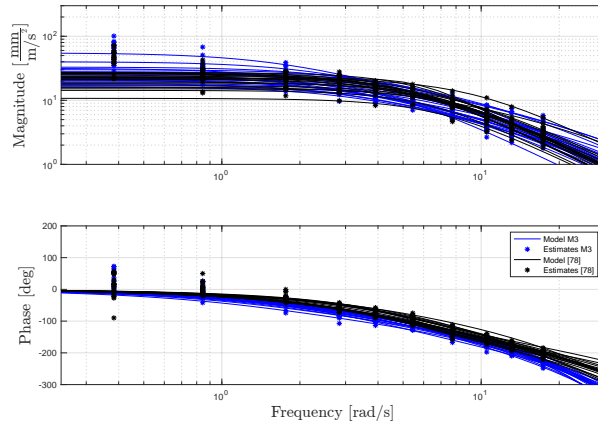
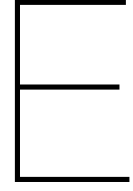
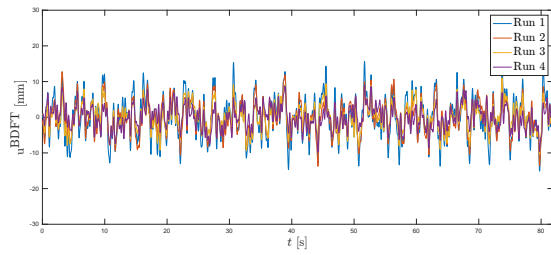


Figure D.2: BDFE estimates and BDFE models frequency response (time domain approach, SA model) of individual participants of this study and of Khoshnewiszadeh and Pool [78].

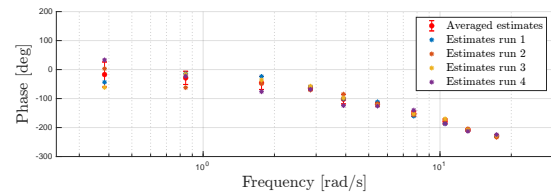
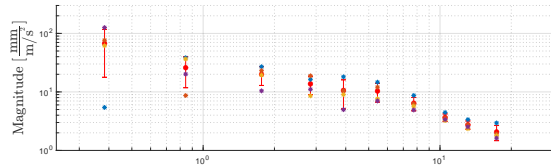


Variability in Biodynamic Feedthrough Across Participants

Section IV.A.1 of the paper discussed the variability in the BDFT input recorded across repeated experimental runs of the same motion disturbance condition, the high intensity multisine condition M3. For each participant this appendix shows the time traces of the BDFT component of the TSC input measured across the four repeated runs of the M3 condition in the identification dataset. Similarly, for each participant the estimates of BDFT, obtained using Eq. (5) of the paper, are plotted for these runs.

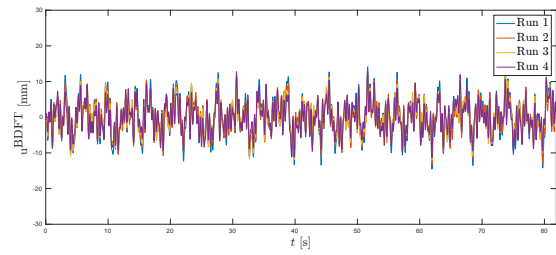


(a) Time traces of the measured BDFT, all runs.

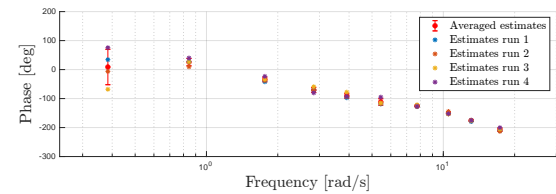
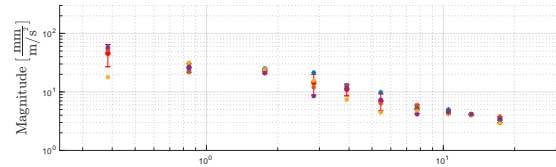


(b) BDFT frequency response function estimates and average, all runs.

Figure E.1: Participant 1, variability in measured BDFT for the identification M3 dataset.

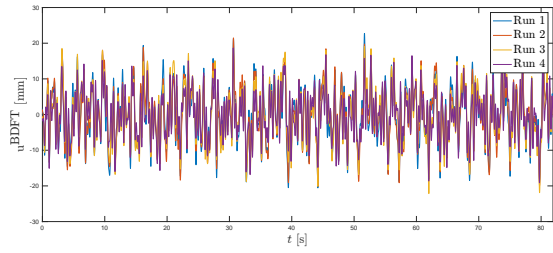


(a) Time traces of the measured BDFT, all runs.

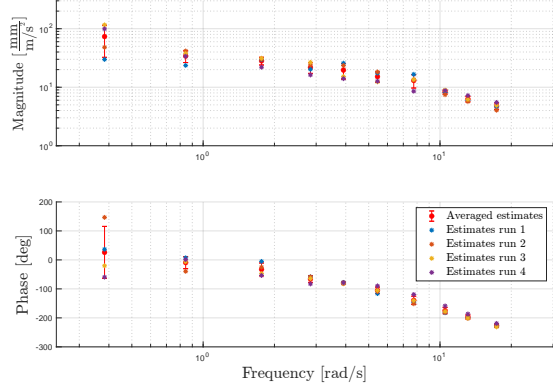


(b) BDFT frequency response function estimates and average, all runs.

Figure E.2: Participant 2, variability in measured BDFT for the identification M3 dataset.

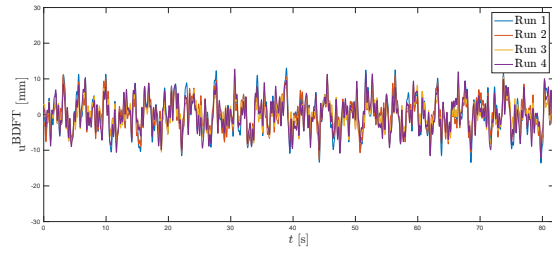


(a) Time traces of the measured BDFT, all runs.

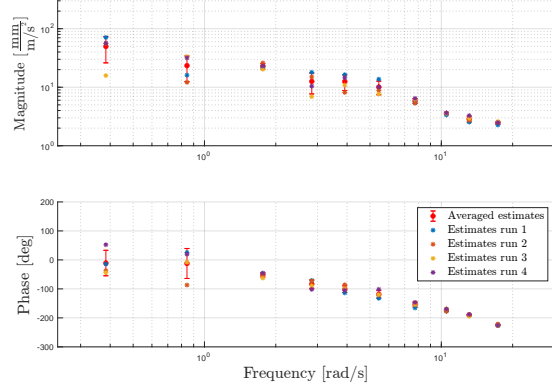


(b) BDFT frequency response function estimates and average, all runs.

Figure E.3: Participant 3, variability in measured BDFT for the identification M3 dataset.

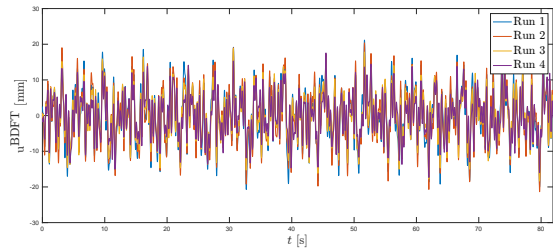


(a) Time traces of the measured BDFT, all runs.

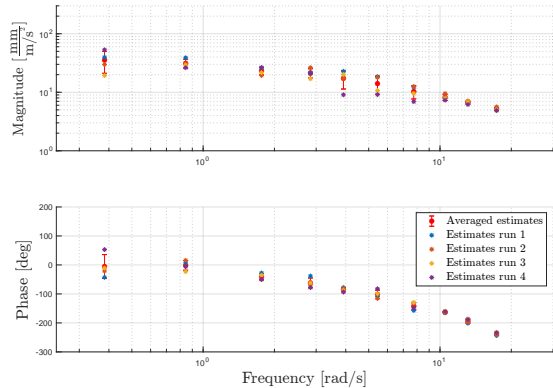


(b) BDFT frequency response function estimates and average, all runs.

Figure E.4: Participant 4, variability in measured BDFT for the identification M3 dataset.

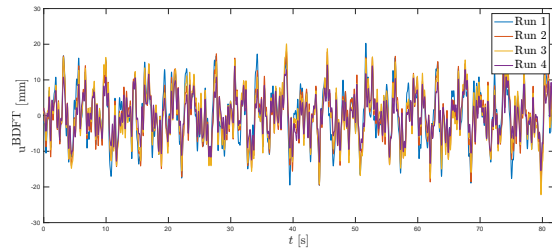


(a) Time traces of the measured BDFT, all runs.

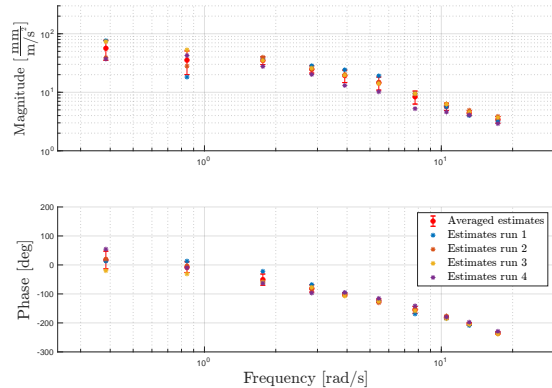


(b) BDFT frequency response function estimates and average, all runs.

Figure E.5: Participant 5, variability in measured BDFT for the identification M3 dataset.

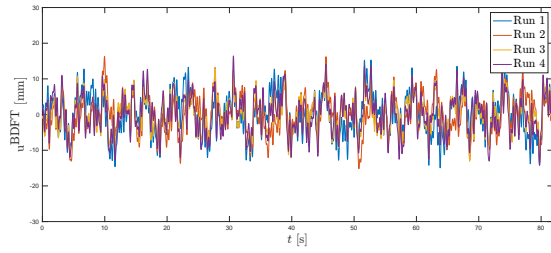


(a) Time traces of the measured BDFT, all runs.

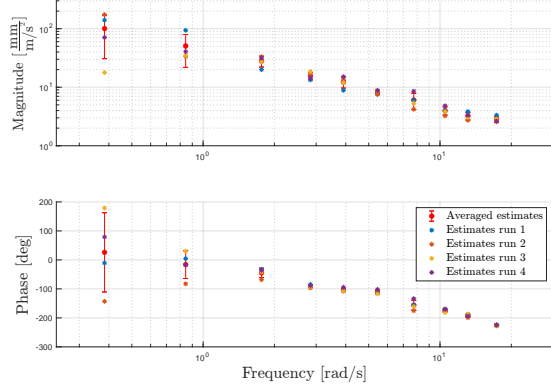


(b) BDFT frequency response function estimates and average, all runs.

Figure E.6: Participant 6, variability in measured BDFT for the identification M3 dataset.

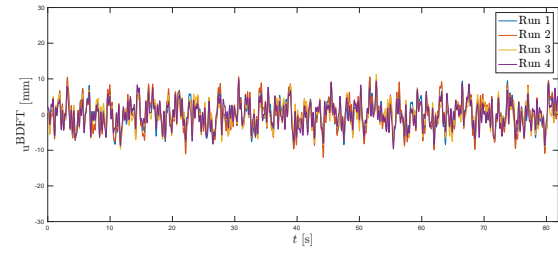


(a) Time traces of the measured BDFT, all runs.

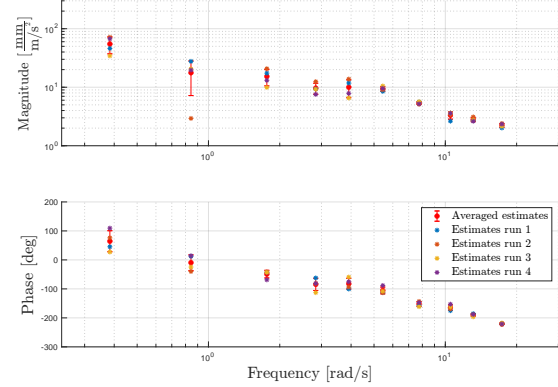


(b) BDFT frequency response function estimates and average, all runs.

Figure E.7: Participant 7, variability in measured BDFT for the identification M3 dataset.

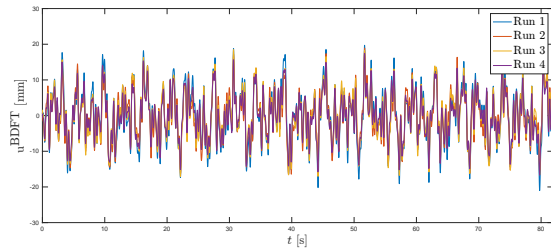


(a) Time traces of the measured BDFT, all runs.

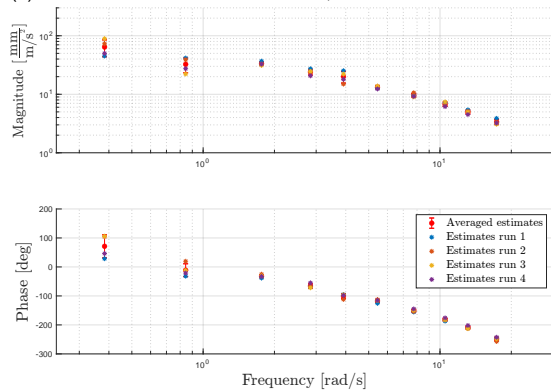


(b) BDFT frequency response function estimates and average, all runs.

Figure E.8: Participant 8, variability in measured BDFT for the identification M3 dataset.

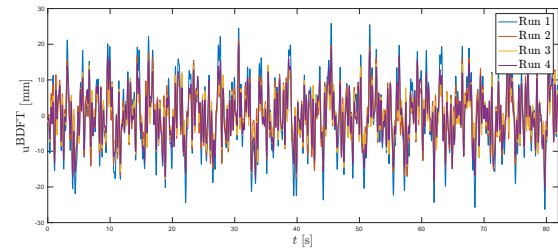


(a) Time traces of the measured BDFT, all runs.

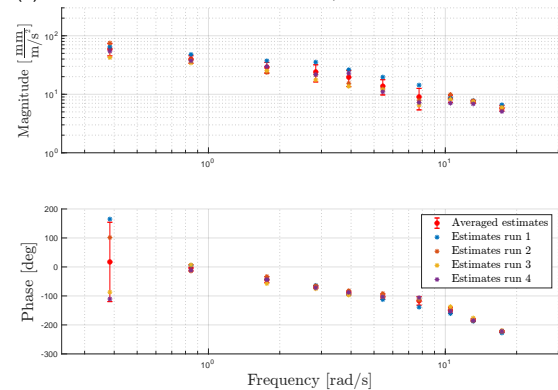


(b) BDFT frequency response function estimates and average, all runs.

Figure E.9: Participant 9, variability in measured BDFT for the identification M3 dataset.

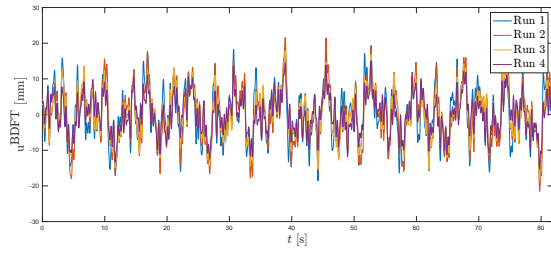


(a) Time traces of the measured BDFT, all runs.

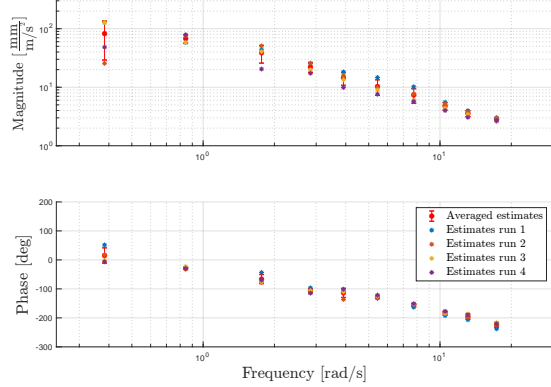


(b) BDFT frequency response function estimates and average, all runs.

Figure E.10: Participant 10, variability in measured BDFT for the identification M3 dataset.

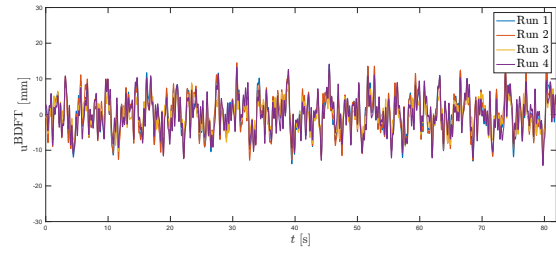


(a) Time traces of the measured BDFT, all runs.

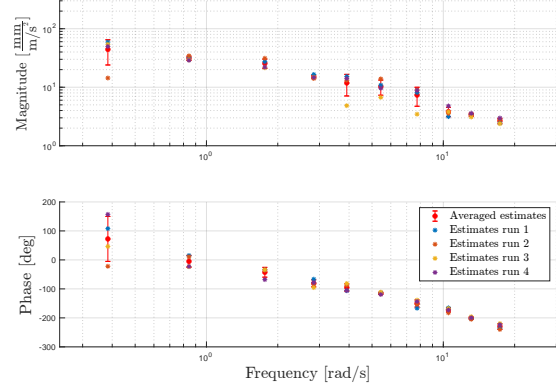


(b) BDFT frequency response function estimates and average, all runs.

Figure E.11: Participant 11, variability in measured BDFT for the identification M3 dataset.

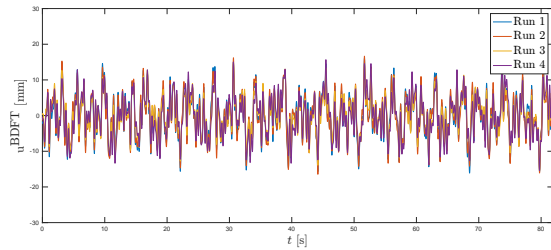


(a) Time traces of the measured BDFT, all runs.

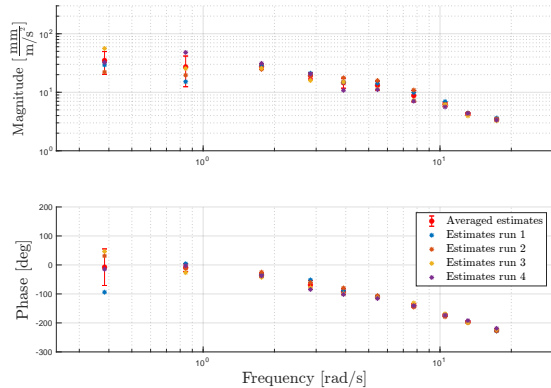


(b) BDFT frequency response function estimates and average, all runs.

Figure E.12: Participant 12, variability in measured BDFT for the identification M3 dataset.

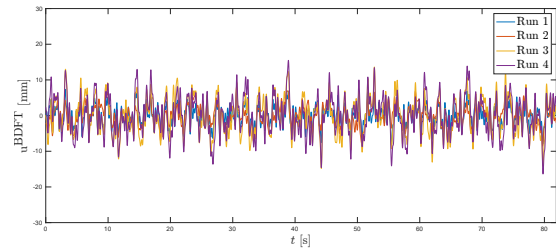


(a) Time traces of the measured BDFT, all runs.

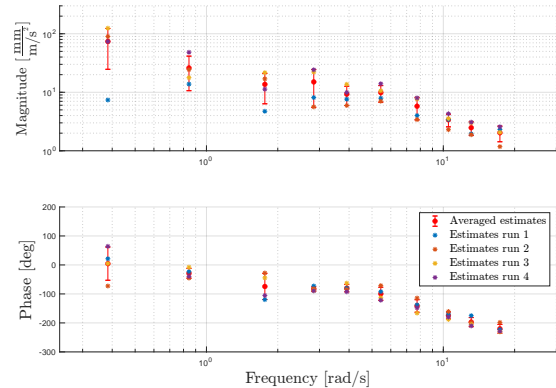


(b) BDFT frequency response function estimates and average, all runs.

Figure E.13: Participant 13, variability in measured BDFT for the identification M3 dataset.

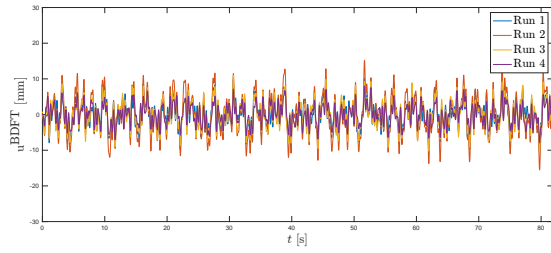


(a) Time traces of the measured BDFT, all runs.

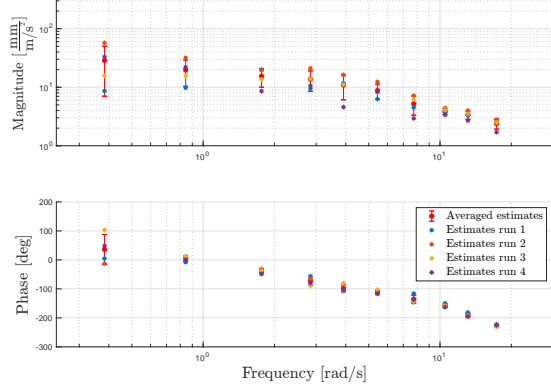


(b) BDFT frequency response function estimates and average, all runs.

Figure E.14: Participant 14, variability in measured BDFT for the identification M3 dataset.

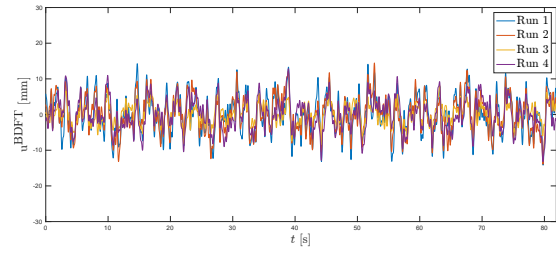


(a) Time traces of the measured BDFT, all runs.

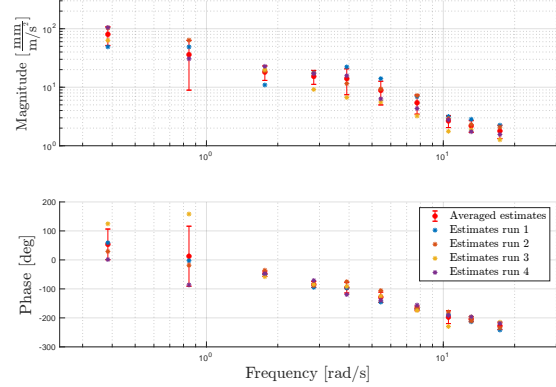


(b) BDFT frequency response function estimates and average, all runs.

Figure E.15: Participant 15, variability in measured BDFT for the identification M3 dataset.

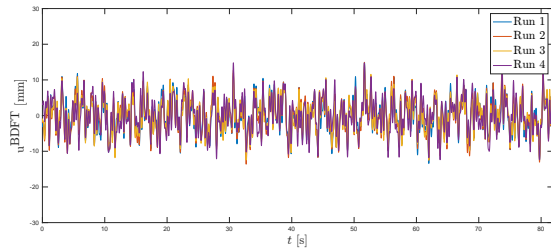


(a) Time traces of the measured BDFT, all runs.

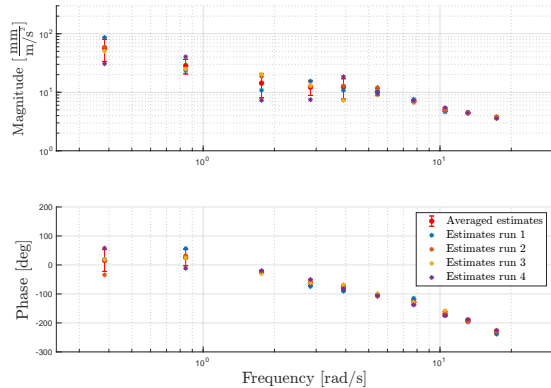


(b) BDFT frequency response function estimates and average, all runs.

Figure E.16: Participant 16, variability in measured BDFT for the identification M3 dataset.

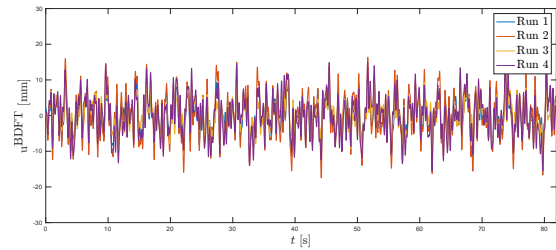


(a) Time traces of the measured BDFT, all runs.

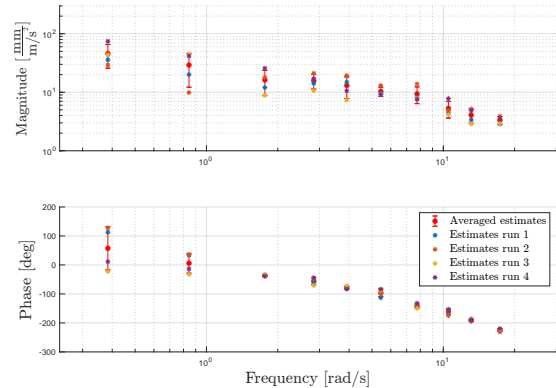


(b) BDFT frequency response function estimates and average, all runs.

Figure E.17: Participant 17, variability in measured BDFT for the identification M3 dataset.

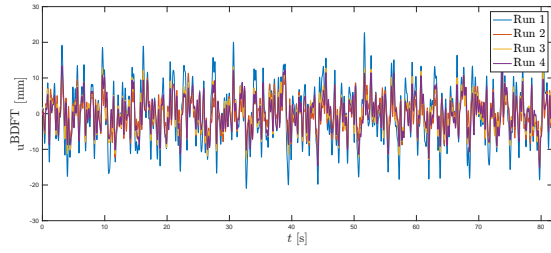


(a) Time traces of the measured BDFT, all runs.

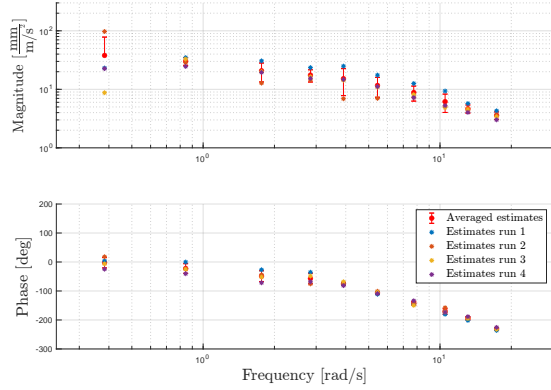


(b) BDFT frequency response function estimates and average, all runs.

Figure E.18: Participant 18, variability in measured BDFT for the identification M3 dataset.

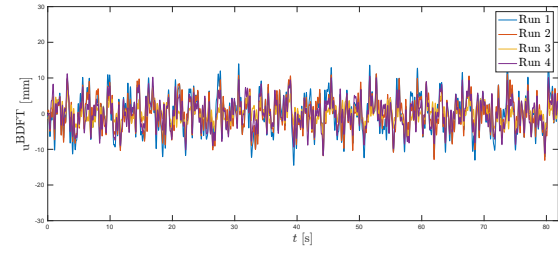


(a) Time traces of the measured BDFT, all runs.

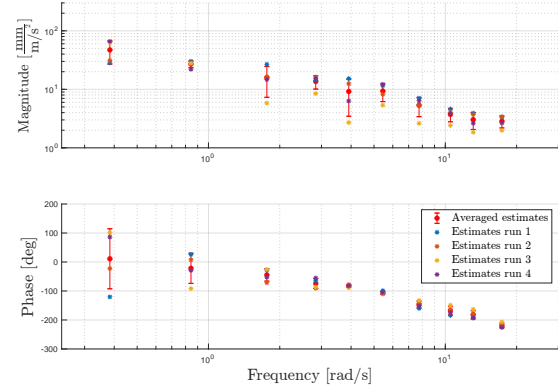


(b) BDFT frequency response function estimates and average, all runs.

Figure E.19: Participant 19, variability in measured BDFT for the identification M3 dataset.

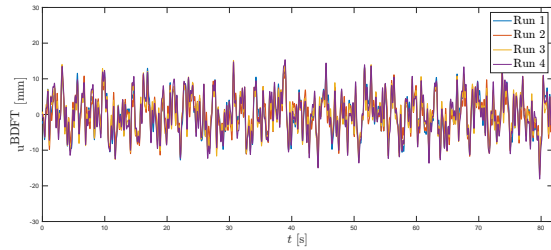


(a) Time traces of the measured BDFT, all runs.

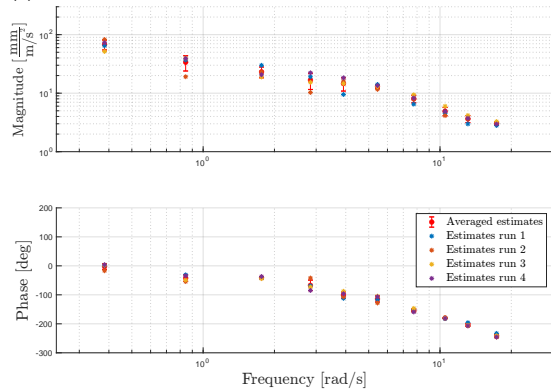


(b) BDFT frequency response function estimates and average, all runs.

Figure E.20: Participant 20, variability in measured BDFT for the identification M3 dataset.



(a) Time traces of the measured BDFT, all runs.



(b) BDFT frequency response function estimates and average, all runs.

Figure E.21: Participant 21, variability in measured BDFT for the identification M3 dataset.

Model Identification of G3 Condition with Fixed and Variable Time Delay

Section IV.C of the paper discussed the performance of model-based mitigation of BDFT in case the motion disturbance is caused by Gaussian turbulence, using a model identified with fixed values for the time delay τ_{BDFT} of the model, corresponding to values found performing identification in the Multisine motion disturbance condition at the same intensity. As a complement, Figure F.1 shows the parameters of the OSFA and of the SA models identified from the G3 data with the time delay fixed, together with those identified with time delay being a variable in the identification algorithm. Despite a large variation in τ_{BDFT} , effects in identification performance are minimal, as shown by Figure F.2 for the SA model and by Figure F.3 for the OSFA model.

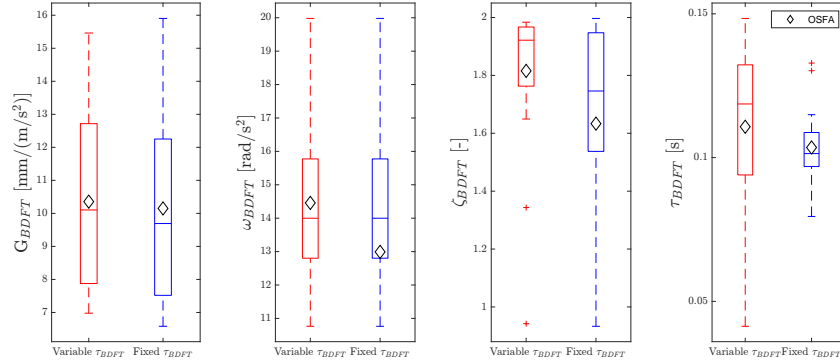


Figure F.1: Median and spread of the parameters of the $H_{BDFT/G3}(j\omega)$ models with fixed and variable time delay τ_{BDFT} (time domain approach, SA and OSFA models).

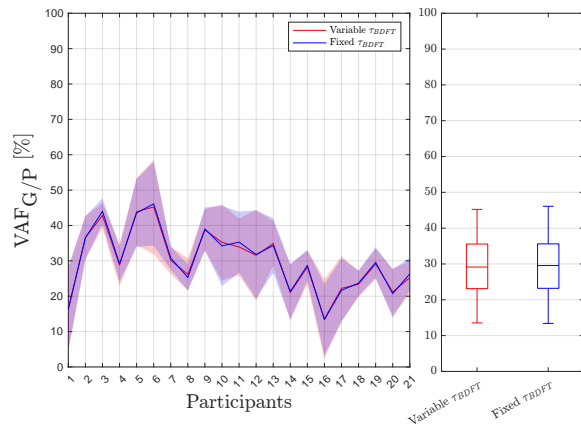


Figure F.2: Performance of the SA $H_{BDFT/G3}$ models with fixed and variable time delay τ_{BDFT} (time domain approach, VAF evaluated on the full frequency spectrum).

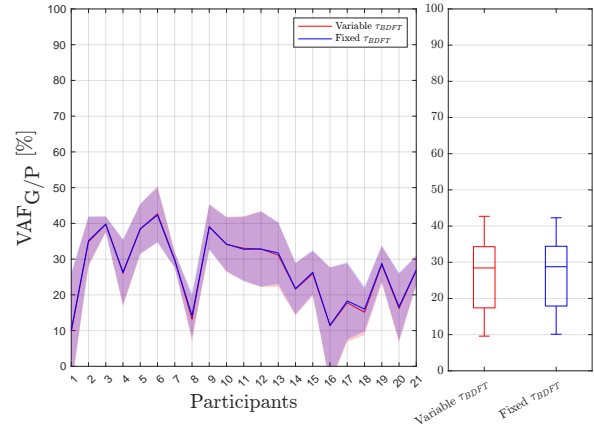


Figure F.3: Performance of the OSFA $H_{BDFT/G3}$ models with fixed and variable time delay τ_{BDFT} (time domain approach, VAF evaluated on the full frequency spectrum).



Biodynamic Feedthrough Model Parameters

This appendix shows for each participant and for each case used for identification of the BDFT models (M1, M2, M3 data from the identification dataset and G3 data) the parameters of the OSFA, SA and IR models, in tables. Parameters for the G3 case are reported for the fixed time delay τ_{BDFT} model as explained in Section IV.C of the paper and Appendix F. Performance of the identification of the models is reported in tables for each run, calculated using VAF_M (Eq. (8) of the paper) for the multisine cases and using $VAF_{G/P}$ (Eq. (9) of the paper) for Gaussian condition. In addition, an example of the time traces of the modeled BDFT and of the frequency response of the three models to the motion disturbance, plotted to the measured BDFT and BDFT estimates respectively, is shown using the data of participant 1 in Figures G.1, G.2, G.3 and G.4.

Table G.1: Participant 1, parameters identification in time domain.

Param.	G_{BDFT} [mm/(m/s ²)]				ω_{BDFT} [rad/s]				ζ_{BDFT} [-]				τ_{BDFT} [s]			
	M1	M2	M3	G3	M1	M2	M3	G3	M1	M2	M3	G3	M1	M2	M3	G3
IR R1	14.1	16.7	23.4	7.5	6.8	5.5	5.3	16.2	0.52	0.56	0.82	1.25	0.09	0.08	0.08	0.10
IR R2	15.6	17.7	21.6	7.6	6.1	5.4	5.1	15.2	0.66	0.70	0.99	1.98	0.08	0.08	0.08	0.10
IR R3	9.9	17.2	18.5	4.4	6.8	6.0	5.6	11.5	0.51	0.94	1.24	1.19	0.09	0.08	0.09	0.10
IR R4	22.3	28.5	17.6	10.0	7.2	4.2	7.2	11.3	1.22	0.95	2.00	1.98	0.10	0.09	0.13	0.10
SA	15.5	20.0	20.3	7.4	6.7	5.3	5.8	13.6	0.73	0.79	1.26	1.60	0.09	0.08	0.10	0.10
OSFA	22.2	25.1	25.6	10.2	7.3	7.4	7.4	13.0	0.81	1.23	1.47	1.63	0.09	0.10	0.10	0.10

Table G.2: Participant 1, identification performance in %, time domain.

Model Case	IR				SA				OSFA			
	R1	R2	R3	R4	R1	R2	R3	R4	R1	R2	R3	R4
M1, VAF_M	47.6	86.2	58.3	71.2	45.4	85.5	52.3	67.4	39.9	63.1	13.9	58.7
M2, VAF_M	68.2	72.6	72.5	81.4	64.9	72.2	67.2	73.3	58.6	62.6	56.2	58.4
M3, VAF_M	93.7	93.1	87.1	76.2	83.3	91.1	85.9	63.7	88.9	84.3	58.4	9.3
G3, $VAF_{G/P}$	34.8	16.4	11.1	10.1	32.8	16.5	6.4	9.9	31.7	12.2	-5.0	1.5

Table G.3: Participant 2, parameters identification in time domain.

Param.	G_{BDFT} [mm/(m/s ²)]				ω_{BDFT} [rad/s]				ζ_{BDFT} [-]				τ_{BDFT} [s]			
	M1	M2	M3	G3	M1	M2	M3	G3	M1	M2	M3	G3	M1	M2	M3	G3
IR R1	22.2	19.9	26.7	8.8	7.4	7.4	6.8	16.9	0.80	0.95	1.55	2.00	0.08	0.08	0.09	0.10
IR R2	22.2	22.2	22.6	10.1	5.4	6.4	8.8	13.4	0.50	0.90	1.99	1.99	0.05	0.07	0.11	0.10
IR R3	17.5	24.1	18.7	8.9	7.0	11.7	10.0	14.2	0.73	1.97	2.00	2.00	0.08	0.11	0.10	0.10
IR R4	23.1	16.9	17.3	10.3	5.7	13.1	10.7	15.8	0.63	1.99	1.99	2.00	0.06	0.13	0.11	0.10
SA	21.2	20.8	21.3	9.5	6.4	9.7	9.1	15.0	0.67	1.45	1.88	2.00	0.07	0.10	0.10	0.10
OSFA	22.2	25.1	25.6	10.2	7.3	7.4	7.4	13.0	0.81	1.23	1.47	1.63	0.09	0.10	0.10	0.10

Table G.4: Participant 2, identification performance in %, time domain.

Model Case	IR				SA				OSFA			
	R1	R2	R3	R4	R1	R2	R3	R4	R1	R2	R3	R4
M1, VAF _M	91.7	85.3	89.6	78.2	90.8	82.6	85.8	77.2	89.7	80.1	83.5	75.8
M2, VAF _M	90.9	93.4	90.3	86.9	89.7	91.2	89.0	82.6	86.4	90.9	88.4	71.8
M3, VAF _M	92.9	92.5	84.9	83.0	90.7	93.2	83.7	80.7	91.0	84.0	69.2	63.7
G3, VAF _{G/P}	32.0	37.9	32.8	44.5	31.4	37.8	32.3	44.7	29.5	37.0	30.2	44.0

Table G.5: Participant 3, parameters identification in time domain.

Param.	G_{BDFT} [mm/(m/s ²)]				ω_{BDFT} [rad/s]				ζ_{BDFT} [-]				τ_{BDFT} [s]			
	M1	M2	M3	G3	M1	M2	M3	G3	M1	M2	M3	G3	M1	M2	M3	G3
IR R1	26.2	33.1	25.6	10.0	7.4	6.1	6.4	14.6	0.77	0.77	0.74	1.07	0.10	0.09	0.09	0.11
IR R2	32.0	33.3	28.3	10.8	6.8	8.9	6.1	14.9	0.79	1.54	0.82	0.94	0.10	0.12	0.09	0.11
IR R3	20.6	29.5	32.8	10.2	18.8	9.6	9.0	13.0	2.00	1.50	1.66	0.96	0.14	0.11	0.12	0.11
IR R4	22.4	24.9	25.4	8.1	10.0	14.5	11.6	13.9	1.16	2.00	1.98	0.77	0.12	0.14	0.13	0.11
SA	25.3	30.2	28.1	9.8	10.7	9.8	8.3	14.1	1.18	1.45	1.30	0.93	0.11	0.12	0.11	0.11
OSFA	22.2	25.1	25.6	10.2	7.3	7.4	7.4	13.0	0.81	1.23	1.47	1.63	0.09	0.10	0.10	0.10

Table G.6: Participant 3, identification performance in %, time domain.

Model Case	IR				SA				OSFA			
	R1	R2	R3	R4	R1	R2	R3	R4	R1	R2	R3	R4
M1, VAF _M	80.6	87.0	84.1	83.4	76.0	78.5	79.6	79.9	77.3	79.9	78.9	81.8
M2, VAF _M	95.3	93.5	93.3	85.6	88.7	92.6	92.9	82.7	81.1	88.2	89.2	82.4
M3, VAF _M	94.1	96.5	95.3	91.3	89.9	93.1	94.0	87.9	80.7	85.7	87.9	86.5
G3, VAF _{G/P}	44.9	49.1	42.7	40.1	45.2	48.4	42.5	39.9	40.3	42.6	38.9	37.5

Table G.7: Participant 4, parameters identification in time domain.

Param.	G_{BDFT} [mm/(m/s ²)]				ω_{BDFT} [rad/s]				ζ_{BDFT} [-]				τ_{BDFT} [s]			
	M1	M2	M3	G3	M1	M2	M3	G3	M1	M2	M3	G3	M1	M2	M3	G3
IR R1	31.0	19.0	22.8	6.1	4.3	4.8	4.2	10.9	0.62	0.62	0.74	0.74	0.09	0.08	0.07	0.10
IR R2	15.4	27.3	23.5	8.5	6.5	4.5	6.0	11.1	0.42	1.27	1.54	2.00	0.05	0.09	0.10	0.10
IR R3	23.1	15.7	23.4	5.2	6.4	6.2	7.2	12.4	1.18	0.86	2.00	1.15	0.10	0.08	0.12	0.10
IR R4	17.6	21.2	24.1	10.4	6.9	6.6	6.3	13.3	0.69	1.45	1.55	1.99	0.08	0.10	0.10	0.10
SA	21.8	20.8	23.4	7.6	6.0	5.5	5.9	11.9	0.73	1.05	1.46	1.47	0.08	0.09	0.10	0.10
OSFA	22.2	25.1	25.6	10.2	7.3	7.4	7.4	13.0	0.81	1.23	1.47	1.63	0.09	0.10	0.10	0.10

Table G.8: Participant 4, identification performance in %, time domain.

Model Case	IR				SA				OSFA			
	R1	R2	R3	R4	R1	R2	R3	R4	R1	R2	R3	R4
M1, VAF _M	86.0	77.0	76.8	78.9	69.5	66.9	68.4	76.2	59.0	69.3	56.9	75.5
M2, VAF _M	87.2	87.4	73.2	80.8	81.9	83.0	69.4	79.5	72.2	55.3	57.1	61.0
M3, VAF _M	93.1	90.3	91.4	86.8	86.6	90.2	89.1	86.7	80.6	77.5	69.2	79.2
G3, VAF _{G/P}	32.5	24.1	27.5	34.8	31.3	21.9	30.2	33.2	29.5	13.3	28.2	34.4

Table G.9: Participant 5, parameters identification in time domain.

Param. Model	G_{BDFT} [mm/(m/s ²)]				ω_{BDFT} [rad/s]				ζ_{BDFT} [-]				τ_{BDFT} [s]			
	M1	M2	M3	G3	M1	M2	M3	G3	M1	M2	M3	G3	M1	M2	M3	G3
IR R1	23.2	28.0	25.5	9.1	9.5	10.3	7.4	14.6	0.82	1.47	0.91	0.51	0.12	0.13	0.11	0.13
IR R2	14.3	25.1	28.2	10.5	13.6	13.2	13.8	14.1	0.86	1.99	2.00	0.63	0.13	0.13	0.15	0.13
IR R3	24.8	22.3	24.9	9.8	8.3	14.1	12.7	13.9	0.81	2.00	2.00	0.66	0.10	0.14	0.13	0.13
IR R4	19.5	24.0	26.2	11.9	9.6	8.6	10.2	15.5	0.83	1.16	2.00	1.98	0.12	0.11	0.13	0.13
SA	20.5	24.9	26.2	10.3	10.3	11.6	11.0	14.5	0.83	1.65	1.73	0.94	0.12	0.13	0.13	0.13
OSFA	22.2	25.1	25.6	10.2	7.3	7.4	7.4	13.0	0.81	1.23	1.47	1.63	0.09	0.10	0.10	0.10

Table G.10: Participant 5, identification performance in %, time domain.

Model Case	IR				SA				OSFA			
	R1	R2	R3	R4	R1	R2	R3	R4	R1	R2	R3	R4
M1, VAF _M	92.6	91.1	90.7	91.1	91.4	83.9	88.5	89.8	85.5	75.6	86.7	87.4
M2, VAF _M	96.6	91.9	97.5	93.3	94.7	92.2	96.7	92.9	90.9	87.2	95.1	91.3
M3, VAF _M	94.9	96.9	97.5	90.3	91.6	95.2	97.2	87.4	83.3	86.7	92.5	88.7
G3, VAF _{G/P}	41.3	55.8	48.4	30.5	38.7	54.5	48.2	32.9	32.6	46.3	42.5	32.7

Table G.11: Participant 6, parameters identification in time domain.

Param. Model	G_{BDFT} [mm/(m/s ²)]				ω_{BDFT} [rad/s]				ζ_{BDFT} [-]				τ_{BDFT} [s]			
	M1	M2	M3	G3	M1	M2	M3	G3	M1	M2	M3	G3	M1	M2	M3	G3
IR R1	26.6	27.1	30.0	17.3	7.6	4.9	4.6	8.1	1.14	0.63	0.66	1.26	0.12	0.07	0.07	0.10
IR R2	32.0	36.4	43.6	16.8	6.4	5.9	5.3	9.9	0.89	1.45	1.43	1.55	0.10	0.11	0.10	0.10
IR R3	35.3	28.5	48.3	16.7	7.2	7.2	5.0	10.5	1.38	1.34	1.53	2.00	0.12	0.11	0.11	0.10
IR R4	37.4	29.3	38.1	12.8	5.6	6.0	5.7	9.4	1.03	1.31	1.90	1.82	0.10	0.10	0.11	0.10
SA	32.8	30.3	40.0	15.9	6.7	6.0	5.2	9.4	1.11	1.18	1.38	1.66	0.11	0.10	0.10	0.10
OSFA	22.2	25.1	25.6	10.2	7.3	7.4	7.4	13.0	0.81	1.23	1.47	1.63	0.09	0.10	0.10	0.10

Table G.12: Participant 6, identification performance in %, time domain.

Model Case	IR				SA				OSFA			
	R1	R2	R3	R4	R1	R2	R3	R4	R1	R2	R3	R4
M1, VAF _M	81.9	95.4	91.2	89.5	79.8	94.1	90.8	88.4	77.2	88.8	84.9	78.1
M2, VAF _M	93.8	92.5	95.2	87.3	87.1	91.2	94.7	86.0	83.1	86.0	93.1	83.4
M3, VAF _M	95.2	97.2	98.7	94.8	85.5	96.5	97.5	87.8	80.5	86.9	86.0	87.2
G3, VAF _{G/P}	56.3	57.3	43.4	33.7	55.0	55.7	43.1	30.7	47.1	49.0	41.1	31.9

Table G.13: Participant 7, parameters identification in time domain.

Param. Model	G_{BDFT} [mm/(m/s ²)]				ω_{BDFT} [rad/s]				ζ_{BDFT} [-]				τ_{BDFT} [s]			
	M1	M2	M3	G3	M1	M2	M3	G3	M1	M2	M3	G3	M1	M2	M3	G3
IR R1	12.5	27.8	29.6	19.1	10.5	8.2	7.0	10.9	1.33	2.00	2.00	2.00	0.13	0.12	0.11	0.09
IR R2	27.0	48.8	41.5	10.7	4.4	4.4	4.3	10.8	0.95	1.94	2.00	1.89	0.10	0.09	0.10	0.09
IR R3	11.6	28.3	26.3	13.9	6.4	5.8	4.7	10.1	0.44	1.15	1.15	1.99	0.07	0.10	0.08	0.09
IR R4	14.5	15.9	29.1	14.9	10.5	8.4	5.8	9.5	1.98	1.30	1.40	1.99	0.15	0.11	0.09	0.09
SA	16.4	30.2	31.6	14.7	8.0	6.7	5.5	10.3	1.18	1.60	1.64	1.97	0.11	0.11	0.09	0.09
OSFA	22.2	25.1	25.6	10.2	7.3	7.4	7.4	13.0	0.81	1.23	1.47	1.63	0.09	0.10	0.10	0.10

Table G.14: Participant 7, identification performance in %, time domain.

Model Case	IR				SA				OSFA			
	R1	R2	R3	R4	R1	R2	R3	R4	R1	R2	R3	R4
M1, VAF _M	53.0	74.3	37.6	38.1	50.9	60.9	31.9	30.2	8.5	32.0	24.0	-33.0
M2, VAF _M	66.0	76.9	80.4	79.5	64.8	70.3	79.2	63.8	59.2	58.4	77.2	60.7
M3, VAF _M	63.3	72.8	86.4	89.6	62.9	69.2	84.9	87.8	59.4	55.0	78.8	88.0
G3, VAF _{G/P}	36.3	29.5	30.3	30.5	35.5	28.1	29.5	30.0	32.8	28.3	28.0	29.6

Table G.15: Participant 8, parameters identification in time domain.

Param. Model	G_{BDFT} [mm/(m/s ²)]				ω_{BDFT} [rad/s]				ζ_{BDFT} [-]				τ_{BDFT} [s]			
	M1	M2	M3	G3	M1	M2	M3	G3	M1	M2	M3	G3	M1	M2	M3	G3
IR R1	23.4	16.0	17.4	6.7	6.0	6.4	5.4	16.7	0.48	0.58	1.06	2.00	0.06	0.07	0.08	0.11
IR R2	13.4	12.9	19.7	7.2	6.6	6.3	6.1	14.3	0.44	0.43	1.25	1.99	0.07	0.05	0.09	0.11
IR R3	13.8	19.3	14.6	6.9	7.5	4.9	10.0	12.8	0.69	0.52	2.00	1.97	0.08	0.06	0.13	0.11
IR R4	20.2	20.2	13.0	6.5	5.4	5.7	12.0	16.7	0.59	0.89	2.00	1.99	0.08	0.08	0.12	0.11
SA	17.7	17.1	16.2	6.8	6.4	5.8	8.4	15.1	0.55	0.61	1.58	1.99	0.07	0.07	0.11	0.11
OSFA	22.2	25.1	25.6	10.2	7.3	7.4	7.4	13.0	0.81	1.23	1.47	1.63	0.09	0.10	0.10	0.10

Table G.16: Participant 8, identification performance in %, time domain.

Model Case	IR				SA				OSFA			
	R1	R2	R3	R4	R1	R2	R3	R4	R1	R2	R3	R4
M1, VAF _M	82.9	74.5	72.2	83.6	76.8	71.6	64.1	76.5	77.3	66.4	56.8	73.5
M2, VAF _M	93.2	84.4	91.3	90.4	91.3	78.5	87.1	84.6	83.8	65.6	83.4	83.1
M3, VAF _M	90.6	90.2	82.4	83.6	88.0	88.0	79.6	81.6	64.9	77.7	34.6	38.1
G3, VAF _{G/P}	30.9	24.0	20.7	26.5	29.9	24.5	20.8	26.0	19.9	16.6	5.4	15.1

Table G.17: Participant 1, parameters identification in time domain.

Param. Model	G_{BDFT} [mm/(m/s ²)]				ω_{BDFT} [rad/s]				ζ_{BDFT} [-]				τ_{BDFT} [s]			
	M1	M2	M3	G3	M1	M2	M3	G3	M1	M2	M3	G3	M1	M2	M3	G3
IR R1	34.5	39.1	36.8	11.5	5.0	5.4	5.5	13.1	0.59	0.89	1.08	2.00	0.08	0.10	0.10	0.11
IR R2	24.7	31.3	27.2	10.5	7.3	5.5	6.4	14.0	0.78	0.73	1.09	1.38	0.11	0.10	0.12	0.11
IR R3	33.5	28.5	29.2	13.1	4.6	5.5	5.8	11.5	0.57	0.83	0.98	1.99	0.09	0.10	0.10	0.11
IR R4	21.8	32.1	27.1	13.8	7.8	7.1	6.1	11.4	1.01	1.13	1.06	1.98	0.12	0.11	0.10	0.11
SA	28.6	32.7	30.1	12.2	6.2	5.9	5.9	12.5	0.74	0.89	1.05	1.84	0.10	0.10	0.11	0.11
OSFA	22.2	25.1	25.6	10.2	7.3	7.4	7.4	13.0	0.81	1.23	1.47	1.63	0.09	0.10	0.10	0.10

Table G.18: Participant 9, identification performance in %, time domain.

Model Case	IR				SA				OSFA			
	R1	R2	R3	R4	R1	R2	R3	R4	R1	R2	R3	R4
M1, VAF _M	84.5	89.0	87.7	66.1	80.9	86.9	80.2	55.6	69.5	85.3	65.9	63.3
M2, VAF _M	93.4	91.5	93.8	96.1	91.6	90.6	91.4	94.0	77.1	78.1	85.9	89.5
M3, VAF _M	97.1	89.4	94.6	95.7	95.4	88.7	94.5	94.3	85.6	82.9	87.1	92.5
G3, VAF _{G/P}	42.2	46.2	36.9	31.9	41.7	45.7	37.1	31.6	42.7	45.3	36.9	31.1

Table G.19: Participant 10, parameters identification in time domain.

Param. Model	G_{BDFT} [mm/(m/s ²)]				ω_{BDFT} [rad/s]				ζ_{BDFT} [-]				τ_{BDFT} [s]			
	M1	M2	M3	G3	M1	M2	M3	G3	M1	M2	M3	G3	M1	M2	M3	G3
IR R1	27.0	36.1	43.0	11.1	7.3	6.7	8.2	14.2	0.60	0.93	1.55	0.95	0.07	0.09	0.11	0.11
IR R2	29.9	22.2	26.3	15.7	6.7	15.7	12.3	14.2	0.83	1.99	1.99	1.97	0.09	0.14	0.12	0.11
IR R3	28.1	31.7	29.1	12.9	8.8	9.4	9.3	13.5	1.00	1.77	1.98	1.96	0.10	0.11	0.11	0.11
IR R4	21.7	20.9	33.7	11.8	7.5	8.4	9.2	14.3	0.58	0.84	2.00	2.00	0.09	0.10	0.11	0.11
SA	26.7	27.7	33.0	12.9	7.6	10.1	9.8	14.0	0.76	1.38	1.88	1.72	0.09	0.11	0.11	0.11
OSFA	22.2	25.1	25.6	10.2	7.3	7.4	7.4	13.0	0.81	1.23	1.47	1.63	0.09	0.10	0.10	0.10

Table G.20: Participant 10, identification performance in %, time domain.

Model Case	IR				SA				OSFA			
	R1	R2	R3	R4	R1	R2	R3	R4	R1	R2	R3	R4
M1, VAF _M	77.8	76.6	64.0	84.9	76.2	74.3	63.2	83.0	68.7	73.5	60.4	79.3
M2, VAF _M	93.1	87.2	93.7	88.5	86.8	86.0	89.8	85.6	79.3	78.6	91.2	81.2
M3, VAF _M	96.0	92.5	88.3	93.6	90.2	90.7	86.7	93.5	78.2	84.7	83.9	88.4
G3, VAF _{G/P}	46.0	42.9	24.5	26.5	44.9	43.2	24.0	24.9	41.1	40.2	27.1	28.2

Table G.21: Participant 11, parameters identification in time domain.

Param. Model	G_{BDFT} [mm/(m/s ²)]				ω_{BDFT} [rad/s]				ζ_{BDFT} [-]				τ_{BDFT} [s]			
	M1	M2	M3	G3	M1	M2	M3	G3	M1	M2	M3	G3	M1	M2	M3	G3
IR R1	70.6	35.6	47.4	10.4	4.2	5.7	4.1	12.4	0.84	1.16	1.13	1.78	0.08	0.10	0.09	0.08
IR R2	38.4	55.9	76.7	15.9	3.4	4.1	2.4	10.0	0.46	1.05	1.11	2.00	0.06	0.09	0.05	0.08
IR R3	28.1	69.1	63.7	18.4	4.5	3.9	3.1	10.2	0.57	1.87	1.49	1.98	0.09	0.09	0.06	0.08
IR R4	54.5	74.5	32.2	13.3	3.3	3.0	5.8	9.3	0.76	1.37	1.99	2.00	0.07	0.07	0.11	0.08
SA	47.9	58.8	55.0	14.5	3.9	4.2	3.8	10.5	0.66	1.36	1.43	1.94	0.08	0.09	0.08	0.08
OSFA	22.2	25.1	25.6	10.2	7.3	7.4	7.4	13.0	0.81	1.23	1.47	1.63	0.09	0.10	0.10	0.10

Table G.22: Participant 11, identification performance in %, time domain.

Model Case	IR				SA				OSFA			
	R1	R2	R3	R4	R1	R2	R3	R4	R1	R2	R3	R4
M1, VAF _M	85.6	88.2	84.6	87.2	79.1	85.7	67.3	81.4	51.3	52.5	59.0	46.3
M2, VAF _M	93.5	96.2	97.0	94.5	85.3	93.5	91.6	87.8	86.3	71.9	73.2	59.9
M3, VAF _M	92.4	94.0	92.9	79.2	90.0	87.7	89.3	68.4	76.2	60.8	69.2	61.8
G3, VAF _{G/P}	40.6	31.9	44.4	28.1	40.7	31.5	43.9	25.0	40.6	29.0	39.7	21.8

Table G.23: Participant 12, parameters identification in time domain.

Param. Model	G_{BDFT} [mm/(m/s ²)]				ω_{BDFT} [rad/s]				ζ_{BDFT} [-]				τ_{BDFT} [s]			
	M1	M2	M3	G3	M1	M2	M3	G3	M1	M2	M3	G3	M1	M2	M3	G3
IR R1	36.5	19.0	23.0	12.5	6.7	7.6	4.9	12.2	1.79	1.17	0.89	1.68	0.11	0.10	0.08	0.10
IR R2	14.6	18.8	24.6	9.4	5.4	10.8	5.7	13.4	0.66	1.60	1.07	1.39	0.07	0.13	0.10	0.10
IR R3	23.7	7.8	22.2	17.7	6.4	9.3	7.3	10.0	1.02	0.92	2.00	2.00	0.08	0.11	0.11	0.10
IR R4	25.9	21.4	30.0	9.9	4.1	8.4	7.1	14.3	0.68	2.00	2.00	2.00	0.05	0.12	0.12	0.10
SA	25.2	16.8	24.9	12.3	5.6	9.0	6.2	12.5	1.04	1.42	1.49	1.77	0.08	0.11	0.10	0.10
OSFA	22.2	25.1	25.6	10.2	7.3	7.4	7.4	13.0	0.81	1.23	1.47	1.63	0.09	0.10	0.10	0.10

Table G.24: Participant 12, identification performance in %, time domain.

Model Case	IR				SA				OSFA			
	R1	R2	R3	R4	R1	R2	R3	R4	R1	R2	R3	R4
M1, VAF _M	89.7	60.0	81.8	73.0	85.3	50.9	80.7	71.0	68.8	22.9	74.4	53.6
M2, VAF _M	84.6	76.9	82.0	76.0	83.1	75.0	53.6	71.6	78.7	72.5	-46.6	47.3
M3, VAF _M	89.8	90.8	85.6	94.4	86.5	87.7	78.5	93.3	84.1	87.5	60.3	89.7
G3, VAF _{G/P}	41.6	35.3	38.6	19.4	41.9	34.3	37.3	13.7	42.2	35.2	36.0	17.9

Table G.25: Participant 13, parameters identification in time domain.

Param. Model	G_{BDFT} [mm/(m/s ²)]				ω_{BDFT} [rad/s]				ζ_{BDFT} [-]				τ_{BDFT} [s]			
	M1	M2	M3	G3	M1	M2	M3	G3	M1	M2	M3	G3	M1	M2	M3	G3
IR R1	30.2	29.5	23.8	8.8	6.6	6.8	6.7	16.5	0.72	1.16	1.00	1.19	0.09	0.10	0.09	0.10
IR R2	28.5	25.8	22.3	10.4	7.0	6.2	6.3	12.9	0.78	0.87	0.83	1.97	0.10	0.08	0.09	0.10
IR R3	23.6	31.1	28.2	8.9	7.0	5.6	7.3	15.9	0.73	0.91	1.69	1.38	0.08	0.08	0.11	0.10
IR R4	19.5	25.2	33.2	8.2	6.6	5.7	6.2	14.4	0.67	1.14	1.63	1.98	0.08	0.08	0.10	0.10
SA	25.4	27.9	26.9	9.1	6.8	6.1	6.6	14.9	0.73	1.02	1.29	1.63	0.09	0.09	0.10	0.10
OSFA	22.2	25.1	25.6	10.2	7.3	7.4	7.4	13.0	0.81	1.23	1.47	1.63	0.09	0.10	0.10	0.10

Table G.26: Participant 13, identification performance in %, time domain.

Model Case	IR				SA				OSFA			
	R1	R2	R3	R4	R1	R2	R3	R4	R1	R2	R3	R4
M1, VAF _M	89.7	96.4	85.6	81.0	87.9	95.1	84.9	74.7	83.2	91.1	84.8	79.7
M2, VAF _M	96.2	96.0	93.1	95.1	95.5	95.0	91.6	87.4	94.2	93.8	88.3	89.6
M3, VAF _M	96.3	98.5	97.0	92.3	94.6	95.1	95.6	90.2	93.5	93.8	96.4	90.3
G3, VAF _{G/P}	39.0	33.7	41.8	25.9	37.3	35.5	41.2	23.3	36.0	32.2	39.2	19.4

Table G.27: Participant 14, parameters identification in time domain.

Param. Model	G_{BDFT} [mm/(m/s ²)]				ω_{BDFT} [rad/s]				ζ_{BDFT} [-]				τ_{BDFT} [s]			
	M1	M2	M3	G3	M1	M2	M3	G3	M1	M2	M3	G3	M1	M2	M3	G3
IR R1	19.0	32.5	9.4	11.9	7.0	5.0	14.3	13.8	0.61	0.91	1.99	1.99	0.08	0.07	0.13	0.10
IR R2	10.8	19.8	14.1	10.0	6.9	7.0	6.1	13.9	0.35	2.00	1.50	1.98	0.04	0.12	0.06	0.10
IR R3	9.8	13.1	23.8	14.5	11.8	6.8	5.1	11.5	1.09	0.81	1.04	1.99	0.12	0.08	0.09	0.10
IR R4	20.3	7.3	35.5	10.5	2.7	7.5	5.8	12.3	0.21	0.58	2.00	1.99	0.00	0.06	0.11	0.10
SA	15.0	18.2	20.7	11.7	7.1	6.6	7.8	12.9	0.57	1.08	1.63	1.99	0.06	0.08	0.10	0.10
OSFA	22.2	25.1	25.6	10.2	7.3	7.4	7.4	13.0	0.81	1.23	1.47	1.63	0.09	0.10	0.10	0.10

Table G.28: Participant 14, identification performance in %, time domain.

Model Case	IR				SA				OSFA			
	R1	R2	R3	R4	R1	R2	R3	R4	R1	R2	R3	R4
M1, VAF _M	67.2	61.9	66.3	70.3	63.5	58.2	36.7	17.2	66.4	39.1	1.7	22.0
M2, VAF _M	93.1	80.7	83.1	74.4	77.7	55.9	80.2	38.2	87.4	-2.0	54.8	-38.3
M3, VAF _M	85.4	70.9	85.9	81.2	47.2	33.8	79.7	72.9	-21.3	-32.5	79.7	72.8
G3, VAF _{G/P}	23.7	21.7	30.1	13.9	24.3	18.8	30.2	11.8	24.8	20.7	29.2	12.3

Table G.29: Participant 15, parameters identification in time domain.

Param. Model	G_{BDFT} [mm/(m/s ²)]				ω_{BDFT} [rad/s]				ζ_{BDFT} [-]				τ_{BDFT} [s]			
	M1	M2	M3	G3	M1	M2	M3	G3	M1	M2	M3	G3	M1	M2	M3	G3
IR R1	14.1	17.4	17.3	8.5	11.8	7.5	9.5	13.2	1.99	1.18	2.00	1.19	0.15	0.10	0.11	0.11
IR R2	18.1	15.5	24.5	8.2	6.5	6.2	5.4	16.6	0.61	0.96	0.99	2.00	0.07	0.08	0.08	0.11
IR R3	15.9	20.1	16.7	11.0	7.0	5.9	9.4	11.6	0.64	0.98	1.69	1.99	0.09	0.08	0.12	0.11
IR R4	17.9	17.4	14.3	8.5	6.5	6.2	8.9	13.3	0.96	1.09	2.00	1.98	0.11	0.09	0.12	0.11
SA	16.5	17.6	18.2	9.1	8.0	6.5	8.3	13.7	1.05	1.05	1.67	1.79	0.10	0.09	0.11	0.11
OSFA	22.2	25.1	25.6	10.2	7.3	7.4	7.4	13.0	0.81	1.23	1.47	1.63	0.09	0.10	0.10	0.10

Table G.30: Participant 15, identification performance in %, time domain.

Model Case	IR				SA				OSFA			
	R1	R2	R3	R4	R1	R2	R3	R4	R1	R2	R3	R4
M1, VAF _M	46.0	74.3	85.3	66.7	36.0	67.8	80.2	64.0	-14.7	71.8	78.7	41.7
M2, VAF _M	90.3	89.7	92.1	95.0	89.9	88.5	90.8	94.0	76.5	58.3	83.5	65.4
M3, VAF _M	91.2	94.4	94.7	89.1	90.2	85.7	94.4	75.4	65.1	92.8	77.4	6.5
G3, VAF _{G/P}	33.0	34.1	26.8	25.2	32.0	32.5	26.8	23.6	32.7	30.2	22.9	19.5

Table G.31: Participant 16, parameters identification in time domain.

Param. Model	G_{BDFT} [mm/(m/s ²)]				ω_{BDFT} [rad/s]				ζ_{BDFT} [-]				τ_{BDFT} [s]			
	M1	M2	M3	G3	M1	M2	M3	G3	M1	M2	M3	G3	M1	M2	M3	G3
IR R1	40.1	18.9	23.0	8.2	4.5	7.1	4.4	7.8	0.85	2.00	0.75	0.81	0.09	0.12	0.10	0.08
IR R2	11.6	29.9	27.2	9.4	6.6	4.9	4.8	7.8	0.40	1.97	1.25	1.02	0.05	0.11	0.09	0.08
IR R3	7.9	25.8	14.6	6.7	5.4	4.9	4.2	7.2	0.30	1.08	0.99	1.44	0.07	0.09	0.08	0.08
IR R4	17.4	27.2	22.9	5.2	10.7	4.7	3.6	10.4	1.99	1.22	0.77	1.95	0.14	0.12	0.06	0.08
SA	19.3	25.5	21.9	7.4	6.8	5.4	4.3	8.3	0.88	1.57	0.94	1.31	0.09	0.11	0.08	0.08
OSFA	22.2	25.1	25.6	10.2	7.3	7.4	7.4	13.0	0.81	1.23	1.47	1.63	0.09	0.10	0.10	0.10

Table G.32: Participant 16, identification performance in %, time domain.

Model Case	IR				SA				OSFA			
	R1	R2	R3	R4	R1	R2	R3	R4	R1	R2	R3	R4
M1, VAF _M	83.1	56.6	31.1	34.3	63.7	47.7	4.1	24.5	63.3	40.5	-19.1	6.2
M2, VAF _M	48.0	82.4	60.7	69.0	43.4	80.4	57.9	66.1	-4.7	19.7	49.5	38.6
M3, VAF _M	84.5	78.8	75.9	84.8	79.5	76.3	49.8	83.2	69.6	69.9	-41.2	57.1
G3, VAF _{G/P}	24.8	20.7	15.0	2.3	20.7	18.4	15.9	-1.4	24.1	20.7	12.9	-11.7

Table G.33: Participant 17, parameters identification in time domain.

Param.	\dot{G}_{BDFT} [mm/(m/s ²)]				ω_{BDFT} [rad/s]				ζ_{BDFT} [-]				τ_{BDFT} [s]			
	M1	M2	M3	G3	M1	M2	M3	G3	M1	M2	M3	G3	M1	M2	M3	G3
IR R1	20.3	20.0	15.4	8.3	6.1	14.9	14.6	17.4	0.48	2.00	1.99	0.80	0.06	0.14	0.15	0.13
IR R2	14.4	15.3	17.0	7.7	10.8	8.4	10.1	18.6	0.90	0.87	1.36	2.00	0.12	0.11	0.12	0.13
IR R3	9.8	17.3	15.8	8.1	14.8	10.9	14.3	17.1	0.82	1.45	2.00	2.00	0.15	0.12	0.14	0.13
IR R4	10.7	14.8	15.9	4.7	13.9	9.4	11.4	17.5	0.88	1.08	1.52	0.75	0.14	0.12	0.13	0.13
SA	13.8	16.8	16.0	7.2	11.4	10.9	12.6	17.6	0.77	1.35	1.72	1.39	0.12	0.12	0.13	0.13
OSFA	22.2	25.1	25.6	10.2	7.3	7.4	7.4	13.0	0.81	1.23	1.47	1.63	0.09	0.10	0.10	0.10

Table G.34: Participant 17, identification performance in %, time domain.

Model Case	IR				SA				OSFA			
	R1	R2	R3	R4	R1	R2	R3	R4	R1	R2	R3	R4
M1, VAF _M	68.6	76.5	60.7	78.8	60.4	73.6	55.8	73.8	65.9	67.6	38.0	51.9
M2, VAF _M	86.6	90.9	90.1	85.6	85.3	89.5	90.0	84.5	83.8	82.3	83.7	74.1
M3, VAF _M	87.1	93.2	92.6	85.7	87.2	92.8	92.4	85.7	76.9	87.3	82.4	78.1
G3, VAF _{G/P}	36.2	17.9	21.9	13.2	31.8	20.2	24.5	10.2	31.2	15.8	20.9	5.3

Table G.35: Participant 18, parameters identification in time domain.

Param.	\dot{G}_{BDFT} [mm/(m/s ²)]				ω_{BDFT} [rad/s]				ζ_{BDFT} [-]				τ_{BDFT} [s]			
	M1	M2	M3	G3	M1	M2	M3	G3	M1	M2	M3	G3	M1	M2	M3	G3
IR R1	19.8	17.7	15.9	7.0	6.3	7.6	6.9	16.3	0.50	0.68	0.92	1.97	0.08	0.09	0.09	0.10
IR R2	13.9	18.8	20.3	4.6	10.9	10.9	7.0	13.3	0.98	1.45	0.82	0.28	0.12	0.11	0.09	0.10
IR R3	19.0	18.7	15.6	7.7	8.7	9.0	11.9	16.4	0.89	1.07	2.00	1.99	0.11	0.11	0.12	0.10
IR R4	22.5	22.1	21.5	7.1	8.2	8.1	10.4	16.8	1.34	0.98	1.65	1.99	0.11	0.09	0.11	0.10
SA	18.8	19.3	18.3	6.6	8.5	8.9	9.0	15.7	0.93	1.05	1.35	1.56	0.10	0.10	0.10	0.10
OSFA	22.2	25.1	25.6	10.2	7.3	7.4	7.4	13.0	0.81	1.23	1.47	1.63	0.09	0.10	0.10	0.10

Table G.36: Participant 18, identification performance in %, time domain.

Model Case	IR				SA				OSFA			
	R1	R2	R3	R4	R1	R2	R3	R4	R1	R2	R3	R4
M1, VAF _M	86.8	72.9	81.3	87.6	78.8	69.4	81.0	82.8	82.6	60.7	79.6	77.5
M2, VAF _M	90.8	94.2	89.5	95.5	88.7	92.0	89.2	94.4	86.1	88.6	86.5	92.2
M3, VAF _M	93.6	94.3	83.1	90.7	90.8	87.6	76.1	89.5	84.1	88.2	65.1	88.0
G3, VAF _{G/P}	21.0	27.4	28.3	19.3	22.3	22.8	29.0	20.8	14.0	13.5	25.2	11.3

Table G.37: Participant 19, parameters identification in time domain.

Param.	\dot{G}_{BDFT} [mm/(m/s ²)]				ω_{BDFT} [rad/s]				ζ_{BDFT} [-]				τ_{BDFT} [s]			
	M1	M2	M3	G3	M1	M2	M3	G3	M1	M2	M3	G3	M1	M2	M3	G3
IR R1	16.8	20.4	25.8	11.2	7.4	6.7	6.5	14.6	0.42	0.81	0.75	1.98	0.08	0.09	0.09	0.11
IR R2	20.8	21.4	18.3	9.0	7.9	7.0	11.1	13.2	0.78	1.06	1.98	1.98	0.10	0.10	0.14	0.11
IR R3	24.4	17.4	19.8	12.6	8.2	7.8	7.8	13.1	1.07	0.83	1.18	1.98	0.12	0.09	0.11	0.11
IR R4	16.6	27.0	25.0	6.0	7.8	7.7	8.7	13.8	0.58	1.61	1.92	1.04	0.09	0.11	0.11	0.11
SA	19.7	21.5	22.2	9.7	7.8	7.3	8.5	13.7	0.71	1.08	1.46	1.75	0.10	0.10	0.11	0.11
OSFA	22.2	25.1	25.6	10.2	7.3	7.4	7.4	13.0	0.81	1.23	1.47	1.63	0.09	0.10	0.10	0.10

Table G.38: Participant 19, identification performance in %, time domain.

Model Case	IR				SA				OSFA			
	R1	R2	R3	R4	R1	R2	R3	R4	R1	R2	R3	R4
M1, VAF _M	87.1	83.9	83.2	79.5	81.5	83.8	80.2	78.4	76.7	83.4	81.7	75.6
M2, VAF _M	79.8	87.0	94.4	92.6	78.9	86.4	92.1	90.9	78.4	85.2	90.5	90.7
M3, VAF _M	96.6	89.0	95.4	96.8	83.6	83.0	95.0	95.1	83.2	80.1	93.6	95.3
G3, VAF _{G/P}	30.0	26.8	31.5	32.4	31.2	24.0	34.2	28.9	31.0	22.3	34.2	27.7

Table G.39: Participant 20, parameters identification in time domain.

Param. Model	G_{BDFT} [mm/(m/s ²)]				ω_{BDFT} [rad/s]				ζ_{BDFT} [-]				τ_{BDFT} [s]			
	M1	M2	M3	G3	M1	M2	M3	G3	M1	M2	M3	G3	M1	M2	M3	G3
IR R1	19.6	20.2	20.2	10.2	6.2	6.4	6.3	14.6	0.42	0.78	0.98	2.00	0.08	0.08	0.09	0.10
IR R2	20.3	17.9	24.1	8.7	6.7	9.8	8.1	12.5	0.91	1.99	2.00	1.99	0.12	0.12	0.11	0.10
IR R3	9.2	12.2	10.2	8.0	6.6	12.0	9.0	13.2	0.36	1.99	2.00	2.00	0.05	0.12	0.11	0.10
IR R4	17.8	27.5	16.3	9.9	5.4	6.0	6.8	14.3	0.51	1.22	1.11	2.00	0.08	0.10	0.10	0.10
SA	16.7	19.4	17.7	9.2	6.2	8.6	7.6	13.7	0.55	1.50	1.52	2.00	0.08	0.10	0.10	0.10
OSFA	22.2	25.1	25.6	10.2	7.3	7.4	7.4	13.0	0.81	1.23	1.47	1.63	0.09	0.10	0.10	0.10

Table G.40: Participant 20, identification performance in %, time domain.

Model Case	IR				SA				OSFA			
	R1	R2	R3	R4	R1	R2	R3	R4	R1	R2	R3	R4
M1, VAF _M	81.2	76.4	67.9	70.7	74.8	71.1	44.8	67.4	74.0	63.4	27.3	59.1
M2, VAF _M	88.1	79.6	59.6	86.7	81.2	74.5	41.8	80.5	86.1	46.8	-8.4	84.0
M3, VAF _M	90.2	92.0	63.1	88.6	82.7	89.2	15.1	87.5	88.1	83.6	-122.9	75.1
G3, VAF _{G/P}	23.7	13.3	22.9	25.4	24.1	10.9	21.3	26.6	23.4	3.4	16.5	23.5

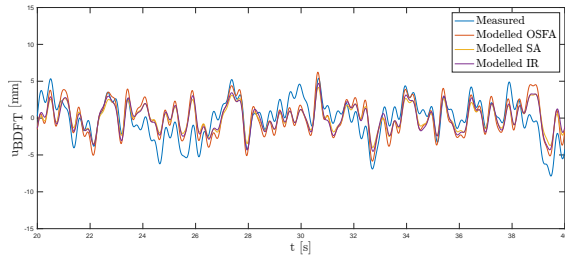
Table G.41: Participant 21, parameters identification in time domain.

Param. Model	G_{BDFT} [mm/(m/s ²)]				ω_{BDFT} [rad/s]				ζ_{BDFT} [-]				τ_{BDFT} [s]			
	M1	M2	M3	G3	M1	M2	M3	G3	M1	M2	M3	G3	M1	M2	M3	G3
IR R1	25.1	19.1	30.0	11.8	6.2	8.4	5.2	13.2	0.58	1.33	1.26	2.00	0.09	0.11	0.09	0.11
IR R2	20.5	38.2	21.6	7.7	7.8	5.3	6.9	12.9	0.88	1.47	1.30	1.38	0.11	0.10	0.12	0.11
IR R3	20.7	33.0	24.2	10.7	6.6	5.1	7.8	12.9	0.55	0.97	1.44	1.99	0.08	0.09	0.12	0.11
IR R4	21.1	28.5	29.6	14.1	6.9	5.4	5.6	11.9	0.64	1.11	1.19	1.98	0.10	0.10	0.10	0.11
SA	21.9	29.7	26.3	11.1	6.9	6.1	6.4	12.7	0.66	1.22	1.30	1.84	0.10	0.10	0.11	0.11
OSFA	22.2	25.1	25.6	10.2	7.3	7.4	7.4	13.0	0.81	1.23	1.47	1.63	0.09	0.10	0.10	0.10

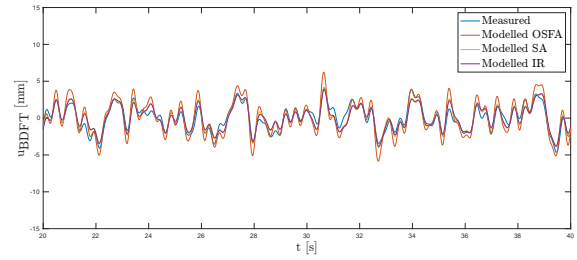
Table G.42: Participant 21, identification performance in %, time domain.

Model Case	IR				SA				OSFA			
	R1	R2	R3	R4	R1	R2	R3	R4	R1	R2	R3	R4
M1, VAF _M	90.0	65.8	69.5	77.4	87.1	63.1	68.7	77.2	82.8	64.7	66.9	75.1
M2, VAF _M	93.3	90.5	95.4	93.3	82.5	87.9	93.2	92.5	86.7	81.1	88.1	87.5
M3, VAF _M	92.3	88.7	95.7	95.1	90.9	86.3	94.9	94.2	88.5	82.0	93.9	90.7
G3, VAF _{G/P}	23.0	26.8	26.0	31.1	24.1	23.3	24.6	33.2	25.0	24.6	25.3	32.9

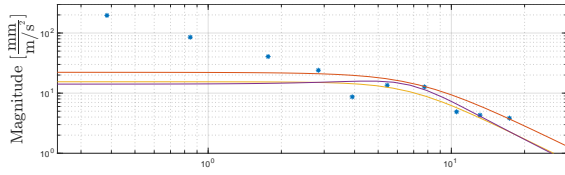
Example of modeled BDFT using the OSFA, SA and IR models



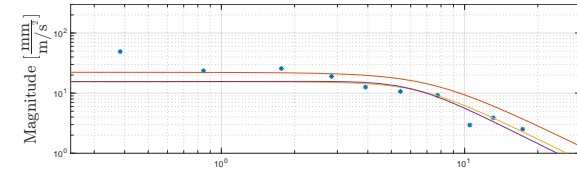
(a) Time traces of the measured and modeled BDFT, run 1.



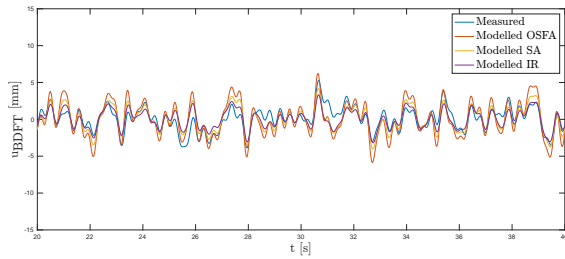
(b) Time traces of the measured and modeled BDFT, run 2.



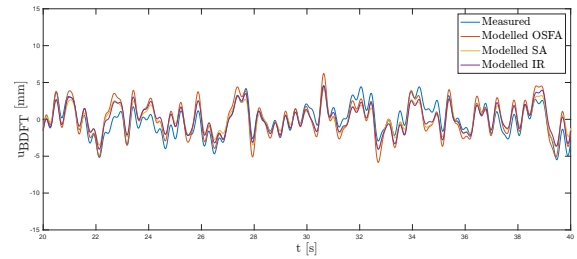
(c) BDFT estimates and frequency response of the models to the motion disturbance, run 1.



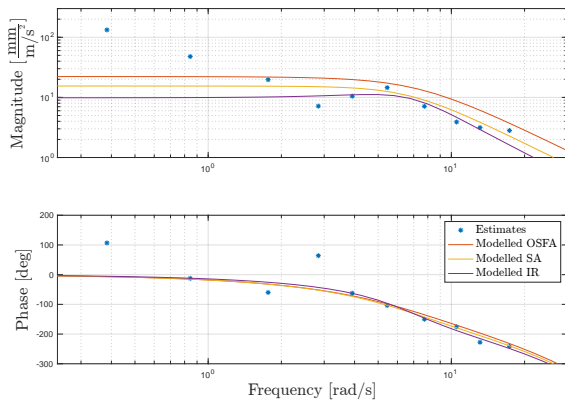
(d) BDFT estimates and frequency response of the models to the motion disturbance, run 2.



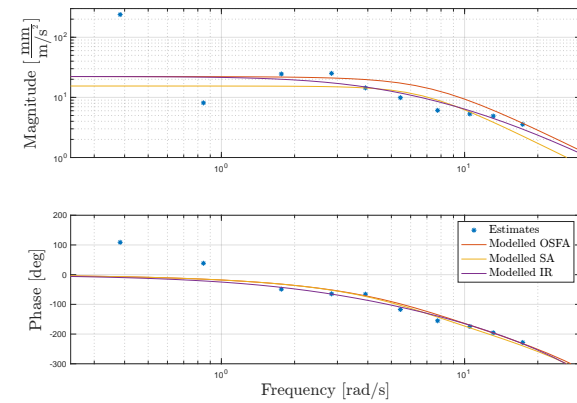
(e) Time traces of the measured and modeled BDFT, run 3.



(f) Time traces of the measured and modeled BDFT, run 4.

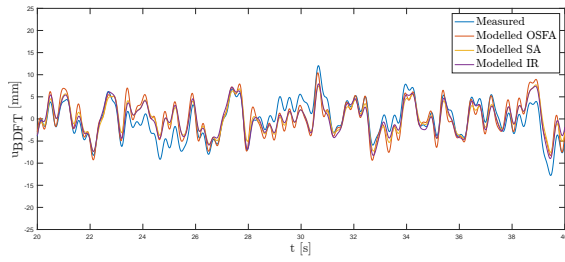


(g) BDFT estimates and frequency response of the models to the motion disturbance, run 3.

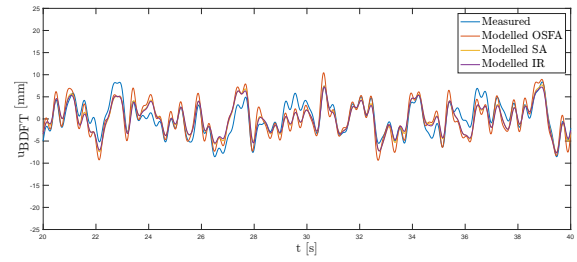


(h) BDFT estimates and frequency response of the models to the motion disturbance, run 4.

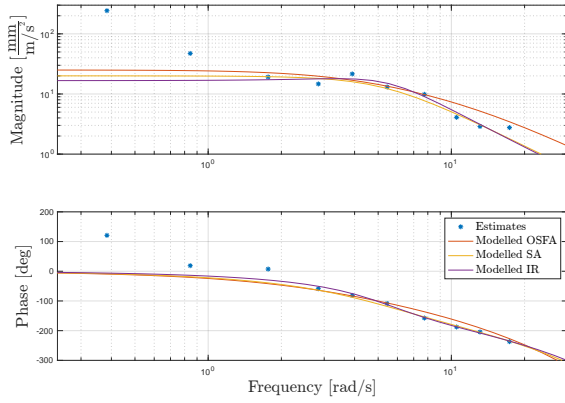
Figure G.1: Participant 1, identification dataset M1.



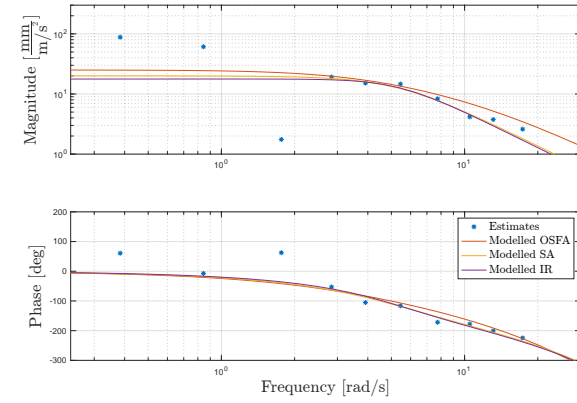
(a) Time traces of the measured and modeled BDFT, run 1.



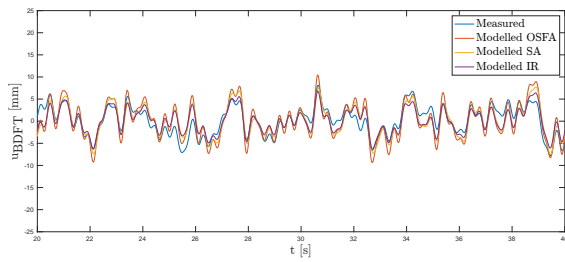
(b) Time traces of the measured and modeled BDFT, run 2.



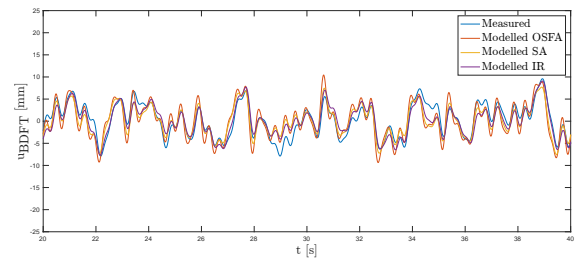
(c) BDFT estimates and frequency response of the models to the motion disturbance, run 1.



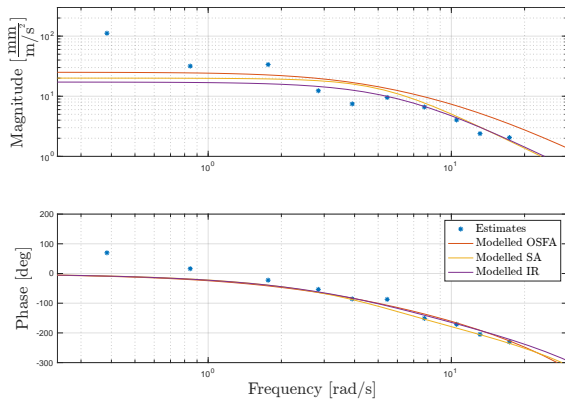
(d) BDFT estimates and frequency response of the models to the motion disturbance, run 2.



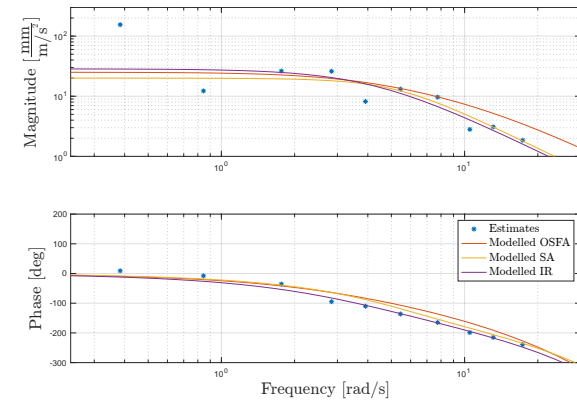
(e) Time traces of the measured and modeled BDFT, run 3.



(f) Time traces of the measured and modeled BDFT, run 4.

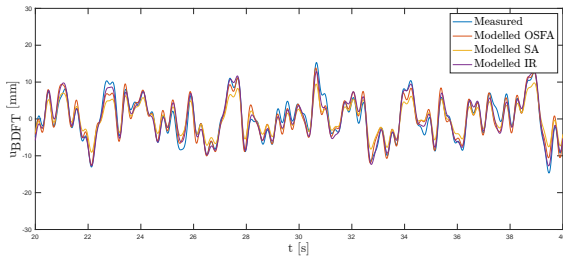


(g) BDFT estimates and frequency response of the models to the motion disturbance, run 3.

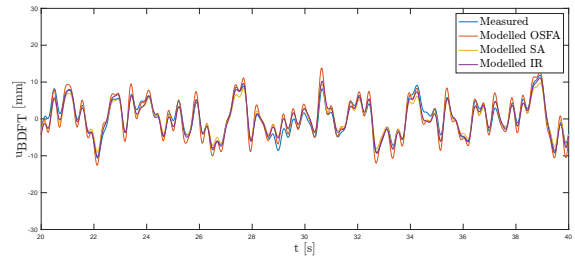


(h) BDFT estimates and frequency response of the models to the motion disturbance, run 4.

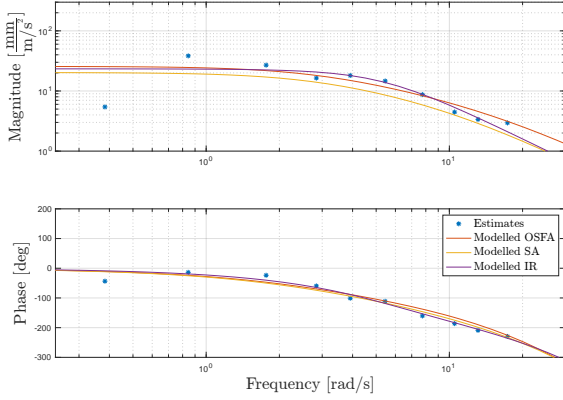
Figure G.2: Participant 1, identification dataset M2.



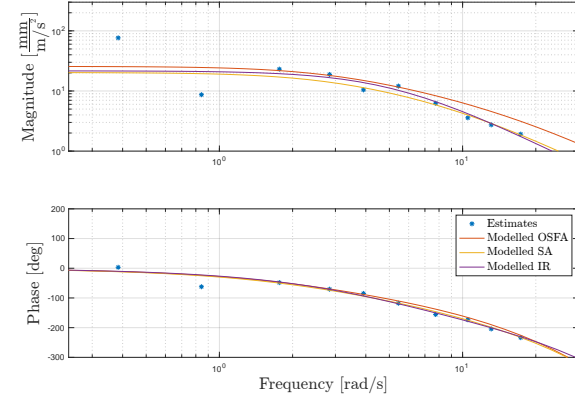
(a) Time traces of the measured and modeled BDFT, run 1.



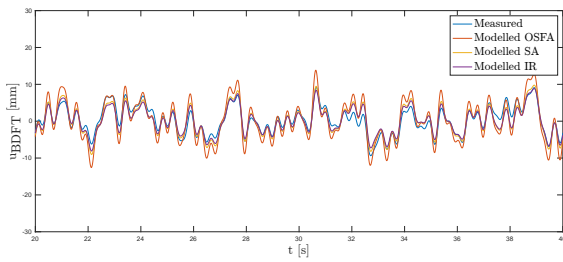
(b) Time traces of the measured and modeled BDFT, run 2.



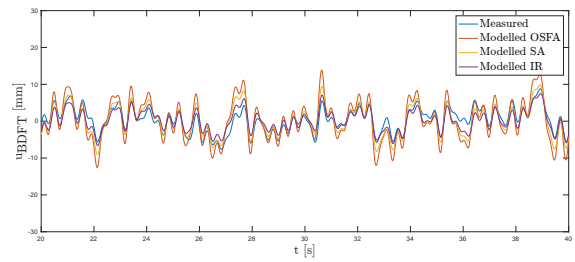
(c) BDFT estimates and frequency response of the models to the motion disturbance, run 1.



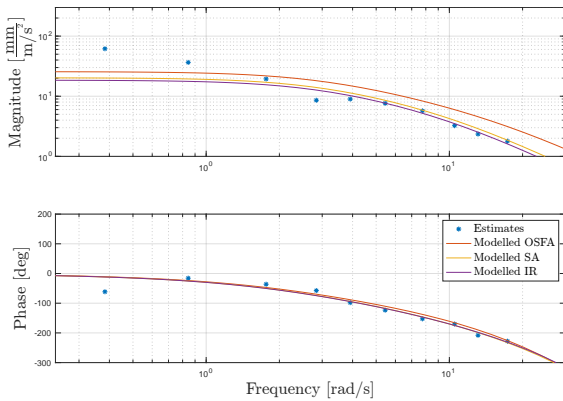
(d) BDFT estimates and frequency response of the models to the motion disturbance, run 2.



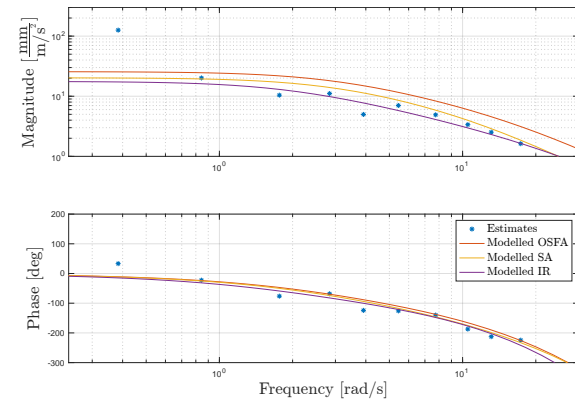
(e) Time traces of the measured and modeled BDFT, run 3.



(f) Time traces of the measured and modeled BDFT, run 4.

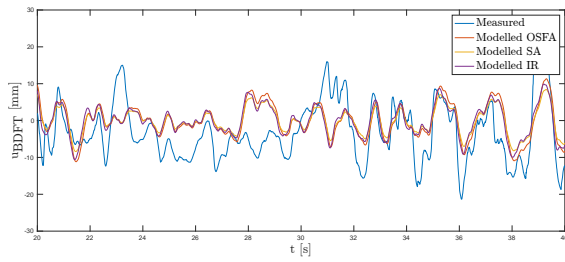


(g) BDFT estimates and frequency response of the models to the motion disturbance, run 3.

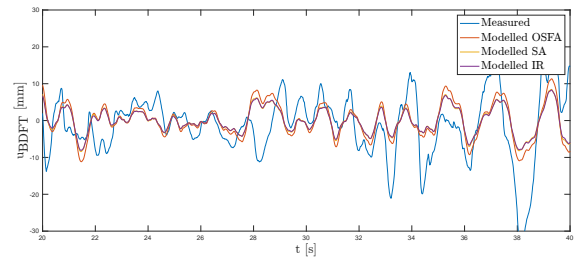


(h) BDFT estimates and frequency response of the models to the motion disturbance, run 4.

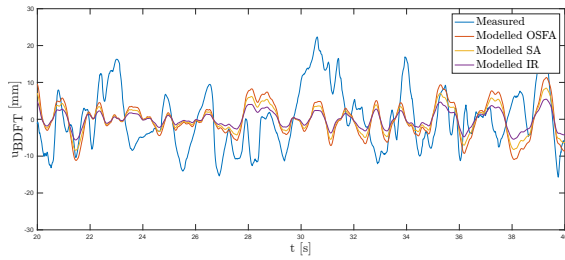
Figure G.3: Participant 1, identification dataset M3.



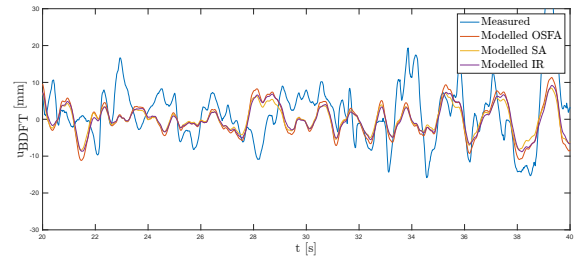
(a) Time traces of the measured and modeled BDFT, run 1.



(b) Time traces of the measured and modeled BDFT, run 2.

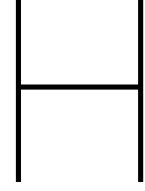


(c) Time traces of the measured and modeled BDFT, run 3.



(d) Time traces of the measured and modeled BDFT, run 4.

Figure G.4: Participant 1, identification dataset G3.



Individual Runs Cancellation Results

This appendix details the cancellation performance for each combination of motion disturbance condition and model used in the study, calculated using the cancellation index CI_M (Eq. (11) of the paper) for the multisine cases and using CI (Eq. (10) of the paper) for Gaussian and patchy conditions. Each table, containing the data of each participant individually, displays results for all four repeated runs. In addition, in Figures H.1, H.2, H.3, H.4 and H.5 an example of the time traces of the BDFT modeled using the relevant models is plotted to the measured BDFT for each motion condition, using the data from participant 1.

Table H.1: Participant 1, individual run cancellation results in %.

Model	Case	M1, CI_M				M2, CI_M				M3, CI_M				G3, CI				P3, CI			
		R1	R2	R3	R4	R1	R2	R3	R4	R1	R2	R3	R4	R1	R2	R3	R4	R1	R2	R3	R4
$H_{BDFT/M1}$	SA	-53.7	-55.6	-59.1	-77.2																
	OSFA	-50.8	-51.1	-48.1	-62.7																
$H_{BDFT/M2}$	SA					-86.7	-65.5	-57.1	-39.8												
	OSFA					-75.7	-58.7	-45.6	-27.9												
$H_{BDFT/M3}$	SA	-40.5	-40.8	-43.7	-73.1	-88.8	-57.5	-49.6	-56.2	-76.3	-82.9	-95.9	-78.5	8.1	23.1	58.6	37.1	33.6	18.6	61.2	79.4
	OSFA	-44.8	-44.4	-44.8	-77.4	-84.6	-59.4	-47.0	-42.3	-81.1	-56.9	-75.5	-59.3	45.6	61.4	127.9	96.4	85.2	60.9	127.1	147.6
$H_{BDFT/G3}$	SA													-32.8	-16.5	-6.4	-9.9	-21.9	-22.1	-5.3	7.3
	OSFA													-31.7	-12.2	5.0	-1.5	-16.3	-18.7	5.9	21.8

Table H.2: Participant 2, individual run cancellation results in %.

Model	Case	M1, CI_M				M2, CI_M				M3, CI_M				G3, CI				P3, CI			
		R1	R2	R3	R4	R1	R2	R3	R4	R1	R2	R3	R4	R1	R2	R3	R4	R1	R2	R3	R4
$H_{BDFT/M1}$	SA	-88.9	-85.0	-82.4	-86.3																
	OSFA	-89.0	-85.4	-81.4	-83.8																
$H_{BDFT/M2}$	SA					-91.4	-89.3	-93.1	-85.3												
	OSFA					-89.6	-89.9	-87.1	-82.6												
$H_{BDFT/M3}$	SA	-74.7	-69.3	-66.6	-74.9	-84.7	-88.1	-88.8	-86.3	-81.0	-92.4	-82.8	-90.9	8.7	-9.1	13.6	-13.3	15.8	12.5	39.6	41.7
	OSFA	-82.4	-77.1	-73.5	-79.6	-87.8	-91.7	-88.4	-86.0	-82.8	-89.2	-62.3	-84.1	58.5	33.6	68.3	32.7	72.2	66.5	103.9	116.3
$H_{BDFT/G3}$	SA													-31.4	-37.8	-32.3	-44.7	-34.2	-34.5	-19.7	-25.9
	OSFA													-29.5	-37.0	-30.2	-44.0	-32.4	-32.8	-15.9	-22.1

Table H.3: Participant 3, individual run cancellation results in %.

Model	Case	M1, CI_M				M2, CI_M				M3, CI_M				G3, CI				P3, CI			
		R1	R2	R3	R4	R1	R2	R3	R4	R1	R2	R3	R4	R1	R2	R3	R4	R1	R2	R3	R4
$H_{BDFT/M1}$	SA	-75.3	-86.7	-85.6	-75.4																
	OSFA	-78.9	-87.4	-82.8	-76.5																
$H_{BDFT/M2}$	SA					-91.4	-91.9	-91.0	-90.0												
	OSFA					-92.2	-89.8	-84.0	-90.3												
$H_{BDFT/M3}$	SA	-76.8	-87.6	-80.4	-73.4	-93.9	-92.7	-89.2	-92.2	-91.5	-92.6	-93.4	-95.1	36.9	6.6	5.7	43.4	19.0	24.7	45.1	36.3
	OSFA	-66.5	-77.1	-67.6	-62.5	-88.7	-86.6	-79.8	-86.8	-82.2	-91.1	-84.7	-90.5	2.8	-15.7	-16.3	5.5	-3.8	-1.8	9.4	4.4
$H_{BDFT/G3}$	SA													-45.2	-48.4	-42.5	-39.9	-49.3	-42.4	-39.4	-38.1
	OSFA													-40.3	-42.6	-38.9	-37.5	-41.4	-37.0	-36.2	-34.7

Table H.4: Participant 4, individual run cancellation results in %.

Model	Case	M1, CI_M				M2, CI_M				M3, CI_M				G3, CI				P3, CI			
		R1	R2	R3	R4	R1	R2	R3	R4	R1	R2	R3	R4	R1	R2	R3	R4	R1	R2	R3	R4
$H_{BDFT/M1}$	SA	-54.5	-55.2	-56.5	-69.6																
	OSFA	-41.8	-48.8	-49.3	-59.8																
$H_{BDFT/M2}$	SA					-84.2	-86.3	-86.1	-89.2												
	OSFA					-70.7	-81.7	-78.9	-76.0												
$H_{BDFT/M3}$	SA	-52.6	-52.9	-48.8	-65.3	-84.0	-83.8	-84.7	-88.3	-88.6	-85.3	-81.9	-90.3	20.8	47.4	9.7	-10.3	31.0	104.7	38.1	49.6
	OSFA	-52.3	-54.0	-54.2	-69.8	-79.8	-86.0	-84.4	-84.7	-74.8	-69.8	-71.9	-69.9	55.6	111.2	48.3	15.6	72.6	193.8	81.8	112.3
$H_{BDFT/G3}$	SA													-31.3	-21.9	-30.2	-33.2	-24.7	-7.2	-22.9	-26.3
	OSFA													-29.5	-13.3	-28.2	-34.4	-20.8	9.5	-18.0	-18.7

Table H.5: Participant 5, individual run cancellation results in %.

Model	Case	M1, CI_M				M2, CI_M				M3, CI_M				G3, CI				P3, CI			
		R1	R2	R3	R4	R1	R2	R3	R4	R1	R2	R3	R4	R1	R2	R3	R4	R1	R2	R3	R4
$H_{BDFT/M1}$	SA	-79.9	-88.3	-83.5	-83.4																
	OSFA	-73.4	-83.1	-80.7	-77.4																
$H_{BDFT/M2}$	SA					-90.7	-92.3	-83.9	-91.5												
	OSFA					-87.6	-87.7	-82.8	-91.0												
$H_{BDFT/M3}$	SA	-65.5	-79.3	-79.8	-79.7	-90.5	-91.3	-83.1	-91.3	-92.8	-94.3	-93.5	-93.7	15.6	-12.1	0.7	29.3	-5.1	25.6	31.3	39.3
	OSFA	-54.0	-67.4	-71.8	-71.0	-82.0	-82.4	-82.6	-89.5	-84.0	-90.3	-89.1	-93.7	5.1	-20.1	-11.0	11.0	-14.4	6.2	11.4	18.4
$H_{BDFT/G3}$	SA													-38.7	-54.5	-48.2	-32.9	-51.2	-43.8	-38.8	-25.2
	OSFA													-32.6	-46.3	-42.5	-32.7	-43.7	-42.5	-37.5	-28.4

Table H.6: Participant 6, individual run cancellation results in %.

Model	Case	M1, CI_M				M2, CI_M				M3, CI_M				G3, CI				P3, CI			
		R1	R2	R3	R4	R1	R2	R3	R4	R1	R2	R3	R4	R1	R2	R3	R4	R1	R2	R3	R4
$H_{BDFT/M1}$	SA	-75.9	-80.4	-47.3	-75.2																
	OSFA	-83.5	-76.5	-51.1	-61.6																
$H_{BDFT/M2}$	SA					-92.5	-91.2	-96.1	-89.0												
	OSFA					-85.9	-85.0	-90.4	-88.7												
$H_{BDFT/M3}$	SA	-63.0	-76.1	-57.7	-82.5	-95.3	-91.3	-96.3	-85.6	-95.7	-92.2	-77.6	-79.8	-25.3	-19.9	23.5	51.0	4.9	10.6	33.0	69.1
	OSFA	-73.5	-75.6	-69.2	-71.8	-86.0	-82.6	-89.6	-89.0	-88.7	-86.6	-81.4	-86.1	-51.8	-50.8	-22.6	-2.2	-41.7	-34.2	-27.2	-3.3
$H_{BDFT/G3}$	SA													-55.0	-55.7	-43.1	-30.7	-55.5	-48.0	-52.3	-40.3
	OSFA													-47.1	-49.0	-41.1	-31.9	-51.0	-44.4	-49.6	-41.8

Table H.7: Participant 7, individual run cancellation results in %.

Model	Case	M1, CI_M				M2, CI_M				M3, CI_M				G3, CI				P3, CI			
		R1	R2	R3	R4	R1	R2	R3	R4	R1	R2	R3	R4	R1	R2	R3	R4	R1	R2	R3	R4
$H_{BDFT/M1}$	SA	-56.3	-46.1	-41.9	-29.1																
	OSFA	-53.7	-43.5	-39.0	-9.5																
$H_{BDFT/M2}$	SA					-76.9	-67.2	-77.5	-68.7												
	OSFA					-65.1	-47.6	-67.3	-57.6												
$H_{BDFT/M3}$	SA	-50.1	-34.0	-41.2	-36.7	-81.9	-74.0	-80.9	-73.4	-80.0	-90.1	-69.8	-81.6	-27.6	5.6	-4.2	-0.7	1.6	29.6	-5.4	30.2
	OSFA	-58.0	-42.9	-43.8	-31.8	-76.3	-60.5	-76.9	-69.4	-72.2	-76.5	-64.7	-69.8	-28.2	12.3	2.4	5.1	-3.9	32.8	-2.9	36.5
$H_{BDFT/G3}$	SA													-35.5	-28.1	-29.5	-30.0	-35.3	-13.9	-33.5	-16.7
	OSFA													-32.8	-28.3	-28.0	-29.6	-37.1	-17.1	-32.7	-19.5

Table H.8: Participant 8, individual run cancellation results in %.

Model	Case	M1, CI_M				M2, CI_M				M3, CI_M				G3, CI				P3, CI			
		R1	R2	R3	R4	R1	R2	R3	R4	R1	R2	R3	R4	R1	R2	R3	R4	R1	R2	R3	R4
$H_{BDFT/M1}$	SA	-58.0	-73.8	-67.4	-78.3																
	OSFA	-44.9	-69.0	-68.5	-69.6																
$H_{BDFT/M2}$	SA					-84.2	-71.2	-65.6	-41.1												
	OSFA					-72.6	-59.4	-48.6	-34.5												
$H_{BDFT/M3}$	SA	-56.9	-62.2	-55.6	-68.1	-81.2	-80.5	-85.9	-82.1	-92.7	-91.2	-86.9	-78.6	18.6	12.3	29.1	16.9	50.7	37.5	60.2	67.6
	OSFA	-51.3	-66.3	-66.4	-70.7	-78.6	-68.5	-63.8	-54.6	-83.7	-57.9	-65.2	-75.4	143.8	111.3	158.4	134.0	210.2	160.1	224.8	246.5
$H_{BDFT/G3}$	SA													-29.9	-24.5	-20.8	-26.0	-22.2	-17.3	-14.0	-13.7
	OSFA													-19.9	-16.6	-5.4	-15.1	-6.1	-4.9	7.4	10.2

Table H.9: Participant 9, individual run cancellation results in %.

Model	Case	M1, CI_M				M2, CI_M				M3, CI_M				G3, CI				P3, CI			
		R1	R2	R3	R4	R1	R2	R3	R4	R1	R2	R3	R4	R1	R2	R3	R4	R1	R2	R3	R4
$H_{BDFT/M1}$	SA	-79.6	-86.9	-80.5	-76.4																
	OSFA	-65.9	-74.9	-73.7	-72.2																
$H_{BDFT/M2}$	SA					-94.2	-86.8	-83.5	-72.5												
	OSFA					-78.4	-72.0	-92.8	-94.5												
$H_{BDFT/M3}$	SA	-67.8	-78.1	-78.8	-75.4	-87.4	-80.9	-91.1	-89.2	-91.3	-39.1	-91.5	-32.8	95.7	42.7	61.9	57.3	63.7	20.6	67.3	36.8
	OSFA	-54.2	-65.1	-69.2	-66.8	-73.5	-67.9	-90.3	-95.3	-86.6	-71.4	-92.6	-67.8	12.8	-14.5	0.1	0.3	1.6	-30.1	1.8	-15.6
$H_{BDFT/G3}$	SA													-41.7	-45.7	-37.1	-31.6	-39.5	-54.9	-38.9	-42.8
	OSFA													-42.7	-45.3	-36.9	-31.1	-40.2	-53.1	-38.9	-41.5

Table H.10: Participant 10, individual run cancellation results in %.

Model	Case	M1, CI_M				M2, CI_M				M3, CI_M				G3, CI				P3, CI			
		R1	R2	R3	R4	R1	R2	R3	R4	R1	R2	R3	R4	R1	R2	R3	R4	R1	R2	R3	R4
$H_{BDFT/M1}$	SA	-62.8	-82.9	-84.1	-86.3																
	OSFA	-68.0	-79.5	-82.2	-86.2																
$H_{BDFT/M2}$	SA					-81.2	-90.1	-80.8	-88.3												
	OSFA					-78.0	-86.6	-72.2	-86.6												
$H_{BDFT/M3}$	SA	-61.7	-73.3	-81.5	-88.2	-82.4	-88.0	-74.1	-91.7	-91.0	-90.3	-93.2	-94.7	-8.6	-3.5	59.3	64.7	37.6	68.0	68.1	55.8
	OSFA	-58.8	-65.0	-71.9	-78.1	-73.2	-81.3	-66.0	-83.1	-82.2	-81.1	-83.2	-84.5	-29.6	-26.8	14.9	17.5	4.8	23.0	22.5	11.9
$H_{BDFT/G3}$	SA													-44.9	-43.2	-24.0	-24.9	-28.0	-20.0	-24.1	-28.0
	OSFA													-41.1	-40.2	-27.1	-28.2	-28.4	-23.7	-27.0	-30.1

Table H.11: Participant 11, individual run cancellation results in %.

Model	Case	M1, CI_M				M2, CI_M				M3, CI_M				G3, CI				P3, CI			
		R1	R2	R3	R4	R1	R2	R3	R4	R1	R2	R3	R4	R1	R2	R3	R4	R1	R2	R3	R4
$H_{BDFT/M1}$	SA	-67.1	-76.4	-81.8	-59.1																
	OSFA	-60.6	-44.2	-66.1	-38.1																
$H_{BDFT/M2}$	SA					-90.8	-90.7	-93.3	-87.9												
	OSFA					-62.1	-62.2	-72.0	-63.3												
$H_{BDFT/M3}$	SA	-58.8	-53.0	-74.4	-75.1	-88.4	-84.5	-93.6	-88.8	-93.2	-84.9	-95.4	-92.8	97.0	51.5	19.8	39.7	25.1	112.5	62.0	112.2
	OSFA	-57.1	-43.9	-66.7	-53.1	-65.0	-62.8	-75.4	-67.1	-82.1	-64.8	-79.3	-73.0	-2.5	-4.2	-28.7	-0.1	-34.8	27.7	7.7	30.1
$H_{BDFT/G3}$	SA													-40.7	-31.5	-43.9	-25.0	-47.2	-21.1	-23.1	-20.7
	OSFA													-40.6	-29.0	-39.7	-21.8	-42.9	-20.0	-20.8	-19.6

Table H.12: Participant 12, individual run cancellation results in %.

Model	Case	M1, CI_M				M2, CI_M				M3, CI_M				G3, CI				P3, CI			
		R1	R2	R3	R4	R1	R2	R3	R4	R1	R2	R3	R4	R1	R2	R3	R4	R1	R2	R3	R4
$H_{BDFT/M1}$	SA	-74.9	-67.6	-63.7	-37.9																
	OSFA	-74.1	-55.4	-55.4	-19.1																
$H_{BDFT/M2}$	SA					-79.7	-87.6	-78.1	-75.4												
	OSFA					-85.8	-81.5	-72.1	-64.1												
$H_{BDFT/M3}$	SA	-70.8	-65.3	-61.8	-42.2	-88.1	-91.5	-81.4	-68.2	-89.6	-89.7	-81.3	-60.9	-13.1	-3.9	-26.4	28.8	2.7	22.0	26.8	40.4
	OSFA	-75.6	-68.2	-63.1	-40.5	-89.2	-88.7	-78.9	-67.9	-84.9	-84.7	-79.3	-45.6	1.7	7.5	-12.7	51.7	17.4	44.0	52.3	72.6
$H_{BDFT/G3}$	SA													-41.9	-34.3	-37.3	-13.7	-29.6	-24.0	-17.5	-7.1
	OSFA													-42.2	-35.2	-36.0	-17.9	-31.0	-27.3	-21.4	-12.4

Table H.13: Participant 13, individual run cancellation results in %.

Model	Case	M1, CI_M				M2, CI_M				M3, CI_M				G3, CI				P3, CI			
		R1	R2	R3	R4	R1	R2	R3	R4	R1	R2	R3	R4	R1	R2	R3	R4	R1	R2	R3	R4
$H_{BDFT/M1}$	SA	-84.5	-84.4	-78.6	-74.5																
	OSFA	-89.5	-80.5	-84.2	-77.2																
$H_{BDFT/M2}$	SA					-90.8	-91.4	-87.7	-84.2												
	OSFA					-87.4	-94.3	-92.0	-86.9												
$H_{BDFT/M3}$	SA	-81.3	-72.5	-80.5	-74.8	-85.4	-95.9	-92.0	-90.9	-94.7	-94.5	-93.3	-96.0	37.3	114.4	63.0	136.7	74.5	106.8	101.6	143.7
	OSFA	-80.7	-69.8	-79.8	-73.6	-82.7	-96.2	-92.5	-91.5	-93.6	-94.4	-91.4	-96.7	20.5	84.4	41.7	105.8	52.8	79.1	74.3	112.7
$H_{BDFT/G3}$	SA													-45.4	-35.5	-41.2	-23.3	-39.2	-30.8	-35.5	-16.6
	OSFA													-43.6	-32.2	-39.2	-19.4	-36.9	-28.7	-33.2	-13.2

Table H.14: Participant 14, individual run cancellation results in %.

Model	Case	M1, CI_M				M2, CI_M				M3, CI_M				G3, CI				P3, CI			
		R1	R2	R3	R4	R1	R2	R3	R4	R1	R2	R3	R4	R1	R2	R3	R4	R1	R2	R3	R4
$H_{BDFT/M1}$	SA	-70.9	-50.9	-49.9	-58.8																
	OSFA	-72.4	-63.9	-62.1	-51.0																
$H_{BDFT/M2}$	SA					-80.1	-72.4	-58.7	-64.2												
	OSFA					-87.5	-81.4	-5.9	-51.3												
$H_{BDFT/M3}$	SA	-68.2	-56.5	-66.2	-51.0	-75.4	-68.2	-58.8	-62.3	-88.8	-80.9	-91.0	-85.2	-3.8	13.3	-23.4	8.0	3.5	40.4	49.6	77.1
	OSFA	-73.8	-65.0	-73.9	-50.5	-83.4	-77.8	-28.2	-57.2	-79.4	-70.7	-90.4	-79.9	28.8	55.9	-4.0	38.5	38.6	89.3	108.3	145.1
$H_{BDFT/G3}$	SA													-24.3	-18.8	-30.2	-11.8	-20.1	3.7	6.0	20.5
	OSFA													-24.8	-20.7	-29.2	-12.3	-20.9	2.2	4.5	17.2

Table H.15: Participant 15, individual run cancellation results in %.

Model	Case	M1, CI_M				M2, CI_M				M3, CI_M				G3, CI				P3, CI			
		R1	R2	R3	R4	R1	R2	R3	R4	R1	R2	R3	R4	R1	R2	R3	R4	R1	R2	R3	R4
$H_{BDFT/M1}$	SA	-79.5	-70.9	-82.4	-68.8																
	OSFA	-83.2	-50.4	-80.5	-38.5																
$H_{BDFT/M2}$	SA					-84.5	-81.4	-89.0	-78.2												
	OSFA					-64.7	-71.7	-82.9	-59.2												
$H_{BDFT/M3}$	SA	-70.7	-65.0	-71.0	-59.0	-83.2	-79.3	-88.3	-77.3	-72.7	-90.7	-81.0	-43.4	-21.0	4.9	-0.6	14.1	-0.3	6.4	33.2	30.5
	OSFA	-82.5	-62.0	-77.5	-46.6	-72.3	-77.4	-88.5	-69.2	-4.3	-68.6	-32.6	56.9	11.8	83.2	71.5	96.8	60.8	74.9	141.6	120.7
$H_{BDFT/G3}$	SA													-32.4	-32.5	-26.8	-23.6	-27.1	-24.6	-17.5	-14.4
	OSFA													-33.2	-30.2	-22.9	-19.5	-25.1	-21.9	-10.8	-9.3

Table H.16: Participant 16, individual run cancellation results in %.

Model	Case	M1, CI_M				M2, CI_M				M3, CI_M				G3, CI				P3, CI			
		R1	R2	R3	R4	R1	R2	R3	R4	R1	R2	R3	R4	R1	R2	R3	R4	R1	R2	R3	R4
$H_{BDFT/M1}$	SA	-6.9	-41.9	14.8	-39.1																
	OSFA	4.1	-27.5	36.9	-34.7																
$H_{BDFT/M2}$	SA					-41.2	-60.2	-68.5	-65.5												
	OSFA					-41.2	-56.3	-27.0	-72.6												
$H_{BDFT/M3}$	SA	6.0	-31.3	4.2	-22.5	-45.5	-58.5	-71.5	-66.3	-74.4	-80.4	-87.2	-63.7	5.2	-1.8	18.5	51.5	10.0	34.7	31.2	9.4
	OSFA	-0.5	-32.7	16.8	-28.6	-43.3	-62.0	-45.5	-72.7	-71.6	-86.8	-71.6	-38.8	8.9	4.0	37.1	78.1	21.2	56.0	52.2	20.0
$H_{BDFT/G3}$	SA													-20.7	-18.4	-15.9	1.4	-11.3	-10.6	-17.3	-20.2
	OSFA													-24.1	-20.7	-12.9	11.7	-9.9	-5.7	-13.7	-21.2

Table H.17: Participant 17, individual run cancellation results in %.

Model	Case	M1, CI_M				M2, CI_M				M3, CI_M				G3, CI				P3, CI			
		R1	R2	R3	R4	R1	R2	R3	R4	R1	R2	R3	R4	R1	R2	R3	R4	R1	R2	R3	R4
$H_{BDFT/M1}$	SA	-63.6	-70.9	-68.5	-81.4																
	OSFA	-46.2	-73.7	-67.6	-81.4																
$H_{BDFT/M2}$	SA					-79.6	-91.1	-88.6	-72.8												
	OSFA					-79.0	-88.1	-91.4	-69.4												
$H_{BDFT/M3}$	SA	-54.7	-73.7	-68.1	-74.6	-76.7	-86.8	-84.2	-69.8	-86.0	-88.8	-92.0	-82.8	-20.5	8.9	3.4	18.6	21.1	24.6	34.5	3.0
	OSFA	-48.3	-72.9	-57.9	-68.1	-76.5	-85.1	-87.7	-66.2	-86.1	-79.2	-87.9	-78.4	10.4	56.7	53.0	61.2	84.2	88.7	104.2	37.7
$H_{BDFT/G3}$	SA													-31.8	-20.2	-24.5	-10.2	-19.6	-15.5	-12.1	-16.4
	OSFA													-31.2	-15.8	-20.9	-5.3	-12.5	-9.1	-4.2	-14.1

Table H.18: Participant 18, individual run cancellation results in %.

Model	Case	M1, CI_M				M2, CI_M				M3, CI_M				G3, CI				P3, CI			
		R1	R2	R3	R4	R1	R2	R3	R4	R1	R2	R3	R4	R1	R2	R3	R4	R1	R2	R3	R4
$H_{BDFT/M1}$	SA	-68.3	-73.0	-61.7	-70.6																
	OSFA	-62.2	-75.3	-48.6	-67.9																
$H_{BDFT/M2}$	SA					-87.3	-81.5	-91.7	8.6												
	OSFA					-86.7	-84.8	-91.7	29.0												
$H_{BDFT/M3}$	SA	-62.3	-64.8	-59.2	-61.2	-85.5	-77.2	-85.6	-42.1	-92.3	-93.7	-91.3	-88.3	43.9	48.6	20.2	49.1	69.2	47.9	53.6	50.7
	OSFA	-53.2	-65.3	-41.0	-57.3	-84.9	-81.2	-86.9	-1.3	-84.7	-92.7	-86.8	-85.2	95.6	104.4	64.3	104.1	139.2	105.2	119.9	107.1
$H_{BDFT/G3}$	SA													-22.3	-22.8	-29.0	-20.8	-20.9	-20.4	-26.6	-20.6
	OSFA													-14.0	-13.5	-25.2	-11.3	-8.2	-11.6	-17.0	-11.6

Table H.19: Participant 19, individual run cancellation results in %.

Model	Case	M1, CI_M				M2, CI_M				M3, CI_M				G3, CI				P3, CI			
		R1	R2	R3	R4	R1	R2	R3	R4	R1	R2	R3	R4	R1	R2	R3	R4	R1	R2	R3	R4
$H_{BDFT/M1}$	SA	-79.6	-60.1	-72.0	-83.9																
	OSFA	-75.1	-57.5	-71.3	-84.6																
$H_{BDFT/M2}$	SA					-92.0	-93.4	-63.9	-93.1												
	OSFA					-93.2	-93.8	-56.6	-90.4												
$H_{BDFT/M3}$	SA	-60.0	-60.7	-65.6	-81.6	-90.2	-91.7	-68.4	-94.5	-94.3	-86.5	-92.1	-92.6	18.8	59.3	16.5	57.9	7.7	33.0	44.5	102.4
	OSFA	-56.6	-55.8	-63.2	-78.9	-90.6	-91.8	-64.0	-92.0	-94.0	-86.3	-91.0	-90.8	31.4	77.1	29.3	78.7	21.5	48.9	63.6	130.6
$H_{BDFT/G3}$	SA													-31.2	-24.0	-34.2	-28.9	-35.9	-27.3	-27.7	-15.3
	OSFA													-31.0	-22.3	-34.2	-27.7	-36.8	-27.0	-27.2	-13.5

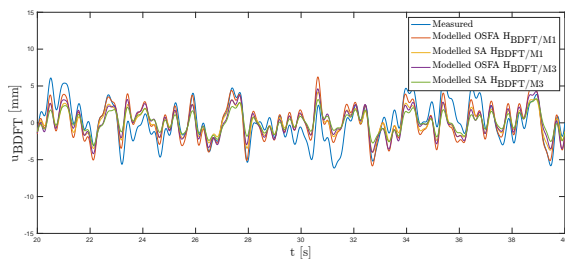
Table H.20: Participant 20, individual run cancellation results in %.

Model	Case	M1, CI_M				M2, CI_M				M3, CI_M				G3, CI				P3, CI			
		R1	R2	R3	R4	R1	R2	R3	R4	R1	R2	R3	R4	R1	R2	R3	R4	R1	R2	R3	R4
$H_{BDFT/M1}$	SA	-73.1	101.2	-60.7	-59.2																
	OSFA	-69.7	179.8	-46.6	-40.1																
$H_{BDFT/M2}$	SA					-78.1	-79.1	-6.8	-31.6												
	OSFA					-82.4	-81.0	131.2	39.5												
$H_{BDFT/M3}$	SA	-48.5	11.8	-54.1	-60.4	-72.6	-76.1	-50.4	-54.8	-83.3	-85.6	-88.5	-81.4	-4.6	25.9	8.5	-0.2	-4.5	26.9	85.4	69.7
	OSFA	-56.2	85.3	-50.9	-58.5	-81.6	-84.5	65.9	-0.5	-86.0	-86.2	-82.9	-39.3	42.4	110.4	82.6	66.0	56.5	119.1	213.4	191.0
$H_{BDFT/G3}$	SA													-24.1	-10.9	-21.3	-26.6	-26.1	-14.8	19.3	9.0
	OSFA													-23.4	-3.4	-16.5	-23.5	-22.8	-8.3	34.0	21.4

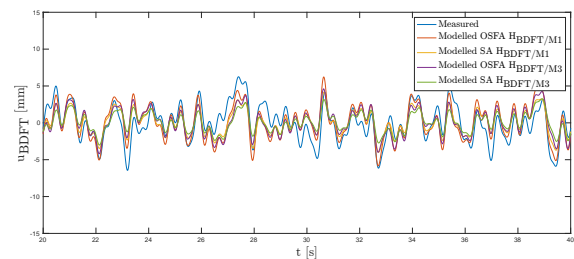
Table H.21: Participant 21, individual run cancellation results in %.

Model	Case	M1, CI_M				M2, CI_M				M3, CI_M				G3, CI				P3, CI			
		R1	R2	R3	R4	R1	R2	R3	R4	R1	R2	R3	R4	R1	R2	R3	R4	R1	R2	R3	R4
$H_{BDFT/M1}$	SA	-71.4	-53.4	-52.8	-84.3																
	OSFA	-74.4	-60.1	-55.8	-83.2																
$H_{BDFT/M2}$	SA					-89.9	-80.9	-91.6	-80.1												
	OSFA					-91.5	-83.1	-86.8	-76.4												
$H_{BDFT/M3}$	SA	-66.3	-63.9	-47.7	-70.3	-88.5	-83.6	-90.0	-81.6	-91.3	-86.1	-86.2	-95.7	58.0	60.2	66.9	22.4	26.8	47.7	20.5	74.7
	OSFA	-69.4	-66.8	-50.6	-71.5	-89.8	-84.2	-86.3	-78.4	-91.1	-85.2	-86.6	-93.8	47.8	49.4	55.5	14.3	19.2	35.3	12.1	63.7
$H_{BDFT/G3}$	SA													-24.1	-23.3	-24.6	-33.2	-25.1	-34.6	-34.8	-21.7
	OSFA													-25.0	-24.6	-25.3	-32.9	-25.4	-36.3	-35.0	-22.4

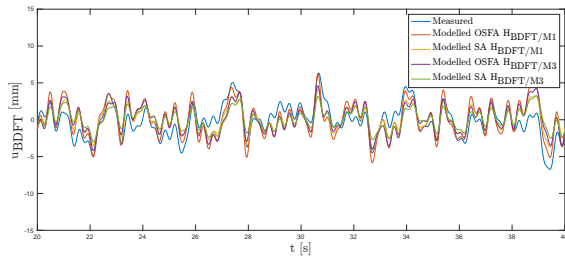
Example of modeled and measured BDFT time traces using the evaluation dataset



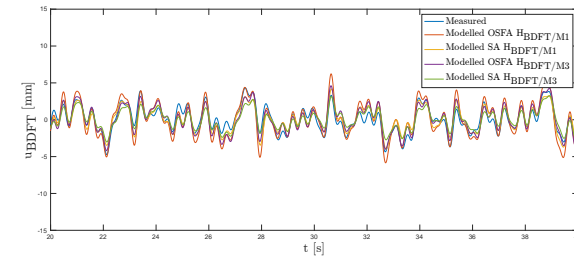
(a) Time traces of the measured and modeled BDFT, run 1.



(b) Time traces of the measured and modeled BDFT, run 2.

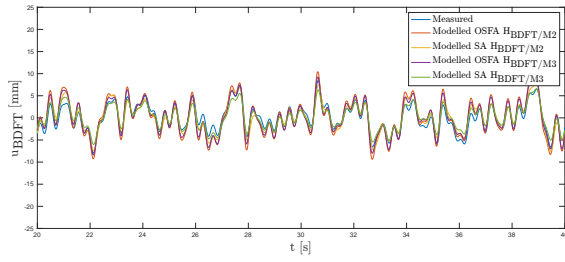


(c) Time traces of the measured and modeled BDFT, run 3.

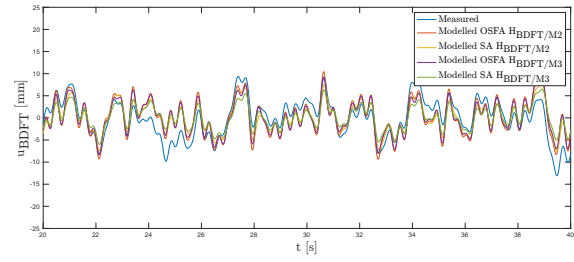


(d) Time traces of the measured and modeled BDFT, run 4.

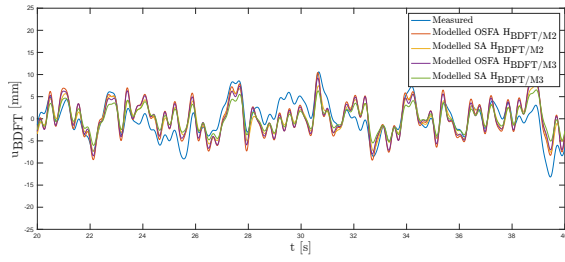
Figure H.1: Participant 1, evaluation dataset M1.



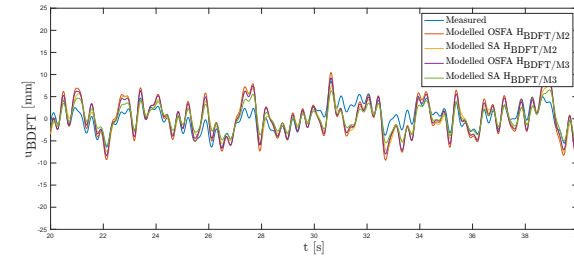
(a) Time traces of the measured and modeled BDFT, run 1.



(b) Time traces of the measured and modeled BDFT, run 2.

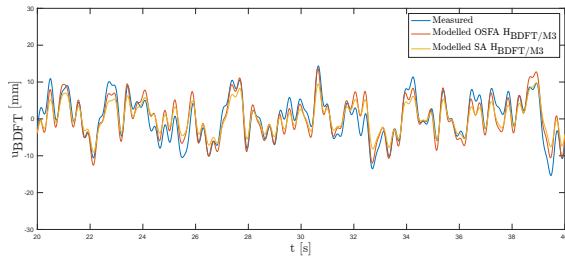


(c) Time traces of the measured and modeled BDFT, run 3.

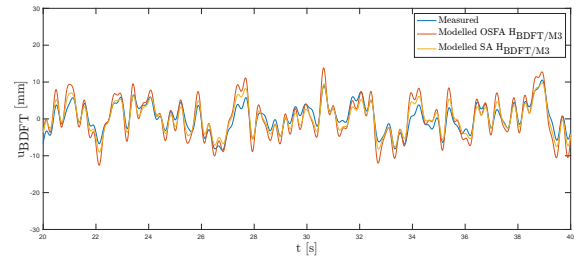


(d) Time traces of the measured and modeled BDFT, run 4.

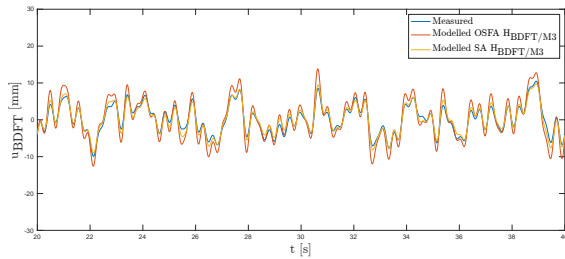
Figure H.2: Participant 1, evaluation dataset M2.



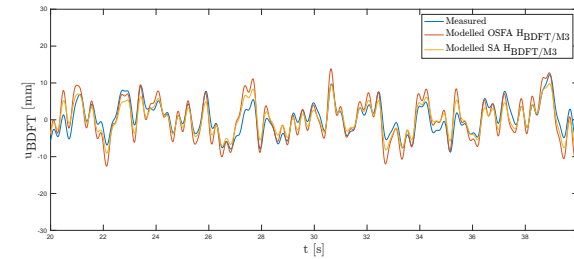
(a) Time traces of the measured and modeled BDFT, run 1.



(b) Time traces of the measured and modeled BDFT, run 2.

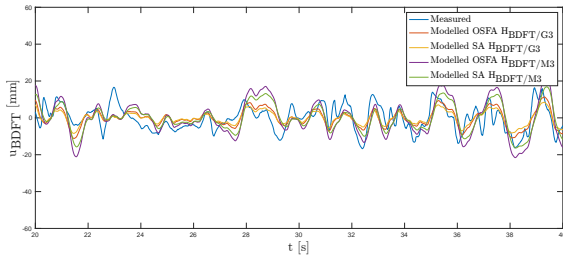


(c) Time traces of the measured and modeled BDFT, run 3.

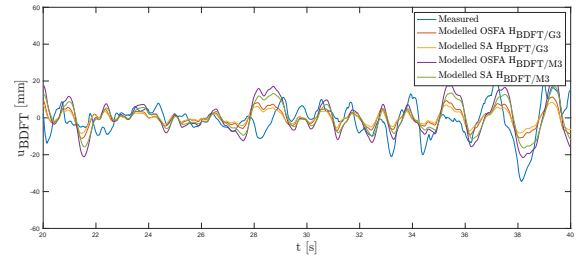


(d) Time traces of the measured and modeled BDFT, run 4.

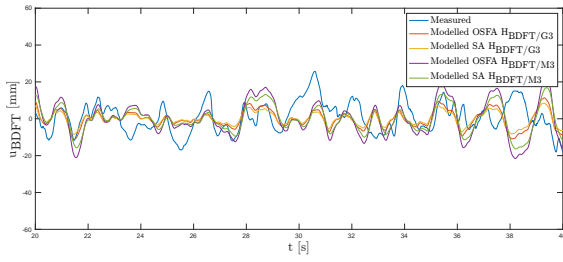
Figure H.3: Participant 1, evaluation dataset M3.



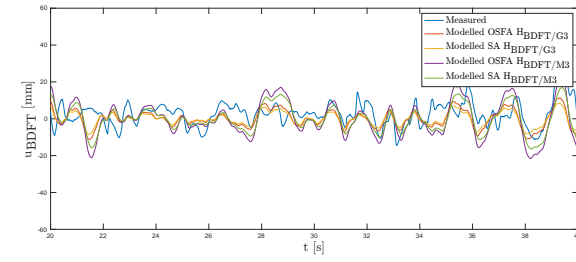
(a) Time traces of the measured and modeled BDFT, run 1.



(b) Time traces of the measured and modeled BDFT, run 2.

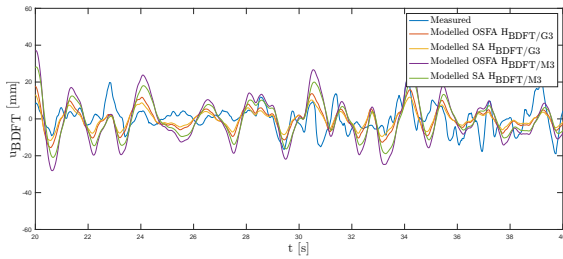


(c) Time traces of the measured and modeled BDFT, run 3.

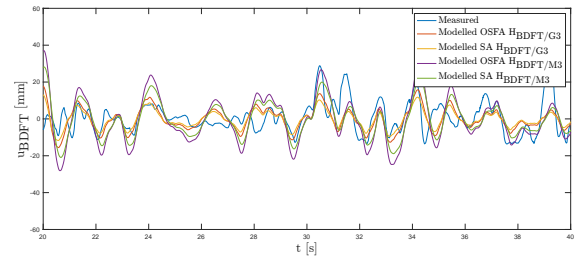


(d) Time traces of the measured and modeled BDFT, run 4.

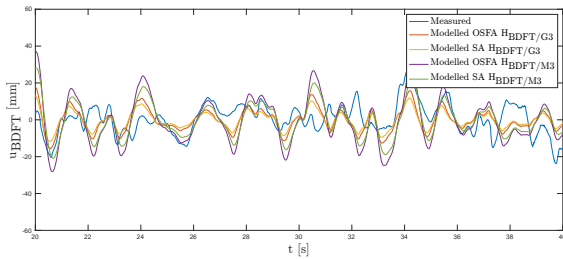
Figure H.4: Participant 1, evaluation dataset G3.



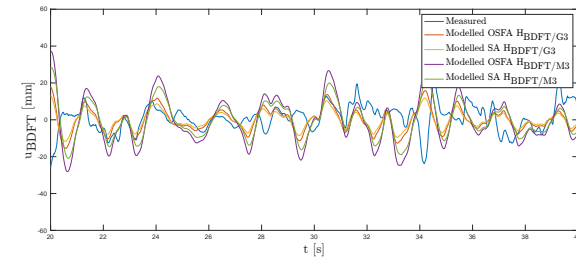
(a) Time traces of the measured and modeled BDFT, run 1.



(b) Time traces of the measured and modeled BDFT, run 2.



(c) Time traces of the measured and modeled BDFT, run 3.



(d) Time traces of the measured and modeled BDFT, run 4.

Figure H.5: Participant 1, evaluation dataset P3.

Performance in Gaussian and Patchy Turbulence at Medium and Low Intensity

Section IV.E discussed results for the Gaussian and patchy turbulence conditions across motion intensities in comparison to results from the multisine condition. This appendix completes the results discussed showing model identification performance of the OSFA, SA and IR models, for the G2 condition in Figure I.1 and for the G1 condition in Figure I.2. In addition, cancellation performance for the lower intensity Gaussian and patchy cases is shown using the models identified from the Gaussian condition in Figures I.3 and I.5 and using the models identified from the multisine condition in Figures I.4 and I.6.

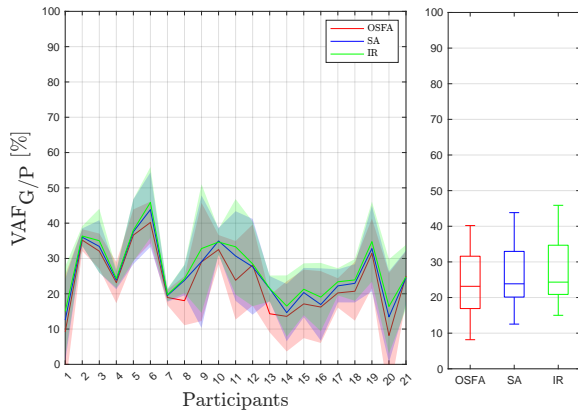


Figure I.1: Performance of the OSFA, SA and IR $H_{BDFT/G2}$ models for the identification of BDFT from the G2 data (time domain approach, VAF evaluated on the full frequency spectrum).

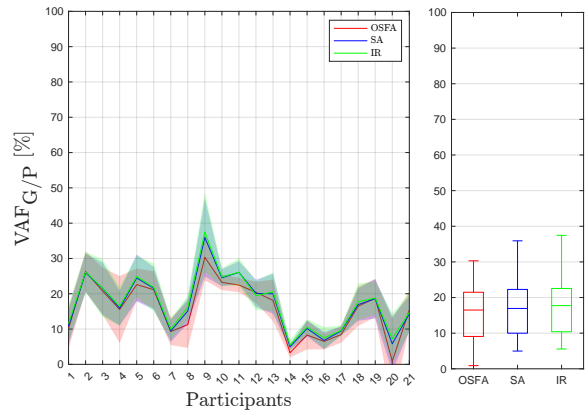


Figure I.2: Performance of the OSFA, SA and IR $H_{BDFT/G1}$ models for the identification of BDFT from the G1 data (time domain approach, VAF evaluated on the full frequency spectrum).

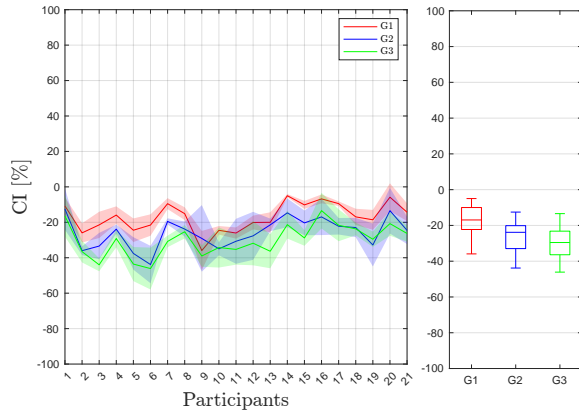


Figure I.3: Cancellation performance of model $H_{BDFT/G3}$ on BDFT occurring in G3 conditions, of model $H_{BDFT/G2}$ on BDFT occurring in G2 conditions and of model $H_{BDFT/G1}$ on BDFT occurring in G1 conditions (time domain approach, SA model, CI evaluated on the full frequency spectrum).

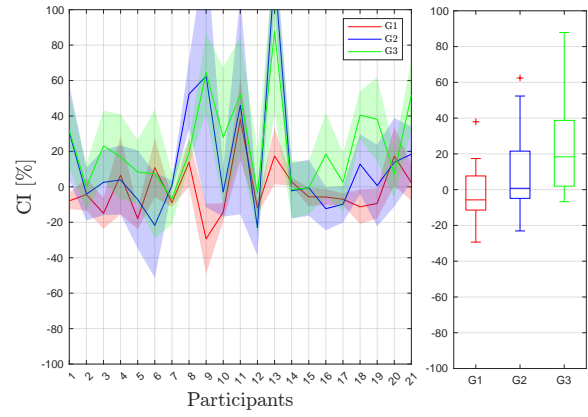


Figure I.4: Cancellation performance of model $H_{BDFT/M3}$ on BDFT occurring in G3 conditions, of model $H_{BDFT/M2}$ on BDFT occurring in G2 conditions and of model $H_{BDFT/M1}$ on BDFT occurring in G1 conditions (time domain approach, SA model, CI evaluated on the full frequency spectrum).

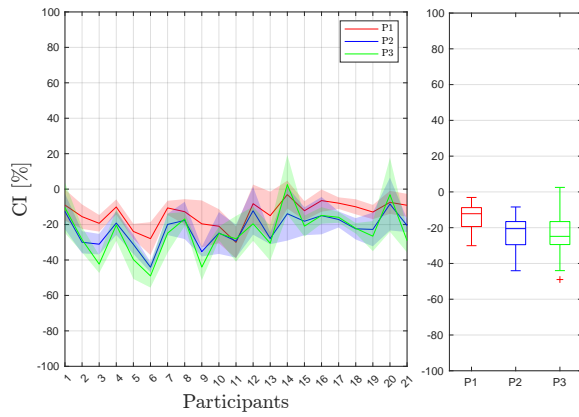


Figure I.5: Cancellation performance of model $H_{BDFT/G3}$ on BDFT occurring in P3 conditions, of model $H_{BDFT/G2}$ on BDFT occurring in P2 conditions and of model $H_{BDFT/G1}$ on BDFT occurring in P1 conditions (time domain approach, SA model, CI evaluated on the full frequency spectrum).

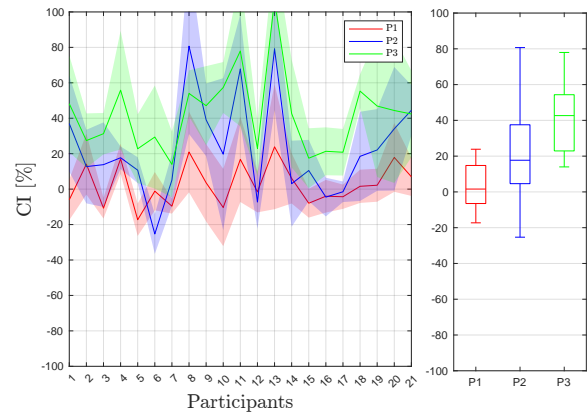


Figure I.6: Cancellation performance of model $H_{BDFT/M3}$ on BDFT occurring in P3 conditions, of model $H_{BDFT/M2}$ on BDFT occurring in P2 conditions and of model $H_{BDFT/M1}$ on BDFT occurring in P1 conditions (time domain approach, SA model, CI evaluated on the full frequency spectrum).

Bibliography

- [1] A. Khoshnawisadeh. Model-based mitigation of biodynamic feedthrough for touchscreen dragging tasks in turbulence. Master's thesis, Unpublished. Delft University of Technology, 2020. URL <http://resolver.tudelft.nl/uuid:b84fefaa-51e3-4a93-a38a-d6c44b078fd7>.
- [2] H. Avsar, J. E. Fischer, and T. Rodden. Mixed method approach in designing flight decks with touch screens: A framework. In *2016 IEEE/AIAA 35th Digital Avionics Systems Conference (DASC)*, pages 1–10. IEEE, 2016. doi: 10.1109/dasc.2016.7778066.
- [3] W. Rouwhorst, R. Verhoeven, M. Suijkerbuijk, T. Bos, A. Maij, M. Vermaat, and R. Arents. Use of touch screen display applications for aircraft flight control. In *2017 IEEE/AIAA 36th Digital Avionics Systems Conference (DASC)*, pages 1–10. IEEE, 2017. doi: 10.1109/dasc.2017.8102060.
- [4] S. R. Dodd, J. Lancaster, S. Grothe, B. DeMers, B. Rogers, and A. Miranda. Touch on the flight deck: The impact of display location, size, touch technology & turbulence on pilot performance. In *2014 IEEE/AIAA 33rd Digital Avionics Systems Conference (DASC)*, pages 2C3–1. IEEE, 2014. doi: 10.1109/dasc.2014.6979570.
- [5] N. van Zon. Evaluation of a touch-based navigation display for lateral weather avoidance. Master's thesis, Unpublished. Delft University of Technology, 2017. URL <http://resolver.tudelft.nl/uuid:73381717-51d8-4183-a299-df2f59e295de>.
- [6] G. Stuyven, H. Damveld, and C. Borst. Concept for an avionics multi touch flight deck. *SAE International Journal of Aerospace*, 5(2012-01-2120):164–171, 2012. doi: 10.4271/2012-01-2120.
- [7] A. Alapetite, R. Fogh, D. Zammit-Mangion, C. Zammit, I. Agius, M. Fabbri, M. Pregnotato, and L. Becouarn. Direct tactile manipulation of the flight plan in a modern aircraft cockpit. In *Proc. of HCI Aero*, 2012. URL https://www.researchgate.net/profile/Alexandre-Alapetite/publication/260297675_Direct_tactile_manipulation_of_the_flight_plan_in_a_modern_aircraft_cockpit/links/00b7d530b16b6dc72e000000/Direct-tactile-manipulation-of-the-flight-plan-in-a-modern-aircraft-cockpit.pdf.
- [8] M. Mertens and H. J. Damveld. An avionics touch screen-based control display concept. In *Head- and Helmet-Mounted Displays XVII; and Display Technologies and Applications for Defense, Security, and Avionics VI*, volume 8383, page 83830L. International Society for Optics and Photonics, 2012. doi: 10.1117/12.919217.
- [9] J. Gauci, N. Cauchi, K. Theuma, D. Zammit-Mangion, and A. Muscat. Design and evaluation of a touch screen concept for pilot interaction with avionic systems. In *2015 IEEE/AIAA 34th Digital Avionics Systems Conference (DASC)*, pages 3C2–1. IEEE, 2015. doi: 10.1109/dasc.2015.7311398.
- [10] C. B. Watkins, C. Nilson, S. Taylor, K. B. Medin, I. Kuljanin, and H. B. Nguyen. Development of touchscreen displays for the gulfstream g500 and g600 symmetry™ flight deck. In *2018 IEEE/AIAA 37th Digital Avionics Systems Conference (DASC)*, pages 1–10. IEEE, 2018. doi: 10.1109/dasc.2018.8569532.
- [11] L. V. Coutts, K. L. Plant, M. Smith, L. Bolton, K. J. Parnell, J. Arnold, and N. A. Stanton. Future technology on the flight deck: assessing the use of touchscreens in vibration environments. *Ergonomics*, 62(2):286–304, 2019. doi: 10.1080/00140139.2018.1552013.
- [12] S. Kaminani. Human computer interaction issues with touch screen interfaces in the flight deck. In *2011 IEEE/AIAA 30th Digital Avionics Systems Conference*, pages 6B4–1. IEEE, 2011. doi: 10.1109/dasc.2011.6096098.

- [13] D. Harris. *Human performance on the flight deck*. CRC Press, 2011. doi: 10.1201/9781315252988.
- [14] J. Venrooij, M. Mulder, M. M. Van Paassen, M. Mulder, and D. A. Abbink. A review of biodynamic feedthrough mitigation techniques. *IFAC Proceedings Volumes*, 43(13):316–321, 2010. doi: 10.3182/20100831-4-fr-2021.00056.
- [15] D. Tao, J. Zeng, K. Liu, and X. Qu. Effects of control-to-display gain and operation precision requirement on touchscreen operations in vibration environments. *Applied Ergonomics*, 91:103293, 2021. doi: 10.1016/j.apergo.2020.103293.
- [16] B. Jacobson. A novel fitts' law: Evaluating touch-based interfaces in atmospheric turbulence. Master's thesis, Unpublished. Delft University of Technology, 2021. URL <http://resolver.tudelft.nl/uuid:2404d466-fbc9-4cca-ba54-097413df9eea>.
- [17] X. Mobertz. A cybernetic analysis of biodynamic effects in turbulence on touchscreen continuous-dragging tasks. Master's thesis, Unpublished. Delft University of Technology, 2017. URL <http://resolver.tudelft.nl/uuid:ef39b0cc-0674-4c7e-8871-70612499daec>.
- [18] A. Degani, E. A. Palmer, and K. G. Bauersfeld. “soft” controls for hard displays: Still a challenge. In *Proceedings of the Human Factors Society Annual Meeting*, volume 36, pages 52–56. SAGE Publications Sage CA: Los Angeles, CA, 1992. doi: 10.1177/154193129203600114.
- [19] K. North and H. D Souza. Acoustic pulse recognition enters touch-screen market. *Information Display*, 22(12):22, 2006.
- [20] S. Heo and G. Lee. Force gestures: augmenting touch screen gestures with normal and tangential forces. In *Proceedings of the 24th annual ACM symposium on User interface software and technology*, pages 621–626, 2011. doi: 10.1145/2047196.2047278.
- [21] A. Cockburn, D. Masson, C. Gutwin, P. Palanque, A. Goguey, M. Yung, C. Gris, and C. Trask. Design and evaluation of braced touch for touchscreen input stabilisation. *International Journal of Human-Computer Studies*, 122:21–37, 2019. doi: 10.1016/j.ijhcs.2018.08.005.
- [22] H. Avsar. *Exploring potential benefits and challenges of touch screens on the flight deck*. PhD thesis, University of Nottingham, 2017.
- [23] D. R. Jones. Three input concepts for flight crew interaction with information presented on a large-screen electronic cockpit display. Technical report, NASA, 1990.
- [24] E. L. Hutchins, J. D. Hollan, and D. A. Norman. Direct manipulation interfaces. *Human-computer interaction*, 1(4):311–338, 1985. doi: 10.1201/b15703-5.
- [25] J. A. Ballas, C. L. Heitmeyer, and M. A. Pérez-Quiñones. Evaluating two aspects of direct manipulation in advanced cockpits. In *Proceedings of the SIGCHI conference on human factors in computing systems*, pages 127–134, 1992. doi: 10.1145/142750.142770.
- [26] M. A. Smith, K. L. Plant, K. J. Parnell, R. A. Wynne, and N. A. Stanton. P-28: Investigating the usability of touchscreen interfaces in a turbulent flight deck—for panning and numeric data entry tasks. In *SID Symposium Digest of Technical Papers*, volume 51, pages 1438–1441. Wiley Online Library, 2020. doi: 10.1002/sdtp.14158.
- [27] A. Cockburn, C. Gutwin, P. Palanque, Y. Deleris, C. Trask, A. Coveney, M. Yung, and K. MacLean. Turbulent touch: Touchscreen input for cockpit flight displays. In *International Conference for Human-Computer Interaction (CHI 2017)*, pages 6742–6753, 2017. doi: 10.1145/3025453.3025584.
- [28] A. Alapetite, E. Møllenbach, A. Stockmarr, and K. Minakata. A rollercoaster to model touch interactions during turbulence. *Advances in Human-Computer Interaction*, 2018, 2018. doi: 10.1155/2018/2698635.

- [29] D. B. Beringer and M. J. Bowman. Operator behavioral biases using high-resolution touch input devices. In *Proceedings of the Human Factors Society Annual Meeting*, volume 33, pages 320–322. SAGE Publications Sage CA: Los Angeles, CA, 1989. doi: 10.1177/154193128903300518.
- [30] FAA. Controls for flight deck systems - ac bo: 20-175. Technical report, U.S. Department of Transportation Federal Aviation Administration, 2011.
- [31] G. Grabski and T. Robinson. Enhancing the visual performance of touch screen displays. *SID Symposium Digest of Technical Papers*, 44(1):1509—1512, 2013.
- [32] J. Venrooij. Relating biodynamic feedthrough to neuromuscular admittance: Understanding the effect of acceleration disturbances on manual control performance. Master's thesis, Unpublished. Delft University of Technology, 2009. URL <http://resolver.tudelft.nl/uuid:3087158a-0b38-49fc-bb76-f90c871f371a>.
- [33] R. W. McLeod and M. J. Griffin. Review of the effects of translational whole-body vibration on continuous manual control performance. *Journal of Sound and Vibration*, 133(1):55–115, 1989. doi: 10.1016/0022-460x(89)90985-1.
- [34] H.-J. Kim and B. J. Martin. Biodynamic characteristics of upper limb reaching movements of the seated human under whole-body vibration. *Journal of applied biomechanics*, 29(1):12–22, 2013. doi: 10.1123/jab.29.1.12.
- [35] G. E. Conway, J. L. Szalma, B. M. Saxton, J. M. Ross, and P. A. Hancock. The effects of whole-body vibration on human performance: A meta-analytic examination. In *Proceedings of the Human Factors and Ergonomics Society Annual Meeting*, volume 50, pages 1741–1745. SAGE Publications Sage CA: Los Angeles, CA, 2006. doi: 10.1177/154193120605001704.
- [36] M. Lone and A. Cooke. Review of pilot models used in aircraft flight dynamics. *Aerospace Science and Technology*, 34:55–74, 2014. doi: 10.1016/j.ast.2014.02.003.
- [37] N. J. Mansfield. *Human response to vibration*. CRC press, 2004. doi: 10.1201/b12481.
- [38] M. Wiertelowski and V. Hayward. Mechanical behavior of the fingertip in the range of frequencies and displacements relevant to touch. *Journal of biomechanics*, 45(11):1869–1874, 2012. doi: 10.1016/j.jbiomech.2012.05.045.
- [39] J. Venrooij, M. M. Van Paassen, M. Mulder, D. A. Abbink, M. Mulder, F. C. Van Der Helm, and H. H. Bühlhoff. A framework for biodynamic feedthrough analysis—part i: Theoretical foundations. *IEEE transactions on cybernetics*, 44(9):1686–1698, 2014. doi: 10.1109/tcyb.2014.2311043.
- [40] X. Bi, Y. Li, and S. Zhai. Fitts law: modeling finger touch with fitts' law. In *Proceedings of the SIGCHI Conference on Human Factors in Computing Systems*, pages 1363–1372, 2013. doi: 10.1145/2470654.2466180.
- [41] K. A. Rider and B. J. Martin. Effects of ride motion on the speed and accuracy of in-vehicle pointing tasks. In *Proceedings of the Human Factors and Ergonomics Society Annual Meeting*, volume 49, pages 1119–1123. SAGE Publications Sage CA: Los Angeles, CA, 2005. doi: 10.1037/e577362012-004.
- [42] H. Abrahamsson and L. Karlsson. Case study: Digitization of a user interface: Investigating the use of a touch screen in helicopter 14, 2020.
- [43] J. Lancaster, B. De Mers, B. Rogers, A. Smart, and S. Whitlow. 57.3: The effect of touch screen hand stability method on performance & subjective preference in turbulence. In *SID Symposium Digest of Technical Papers*, volume 42, pages 841–844. Wiley Online Library, 2011. doi: 10.1889/1.3621464.
- [44] S. Dodd, J. Lancaster, B. DeMers, and S. Boswell. Multi-touch touch screens on the flight deck: The impact of display location, display inclination angle and gesture type on pilot performance. In *2019 IEEE/AIAA 38th Digital Avionics Systems Conference (DASC)*, pages 1–10. IEEE, 2019. doi: 10.1109/dasc43569.2019.9081723.

- [45] J. R. Lewis. Technical report: literature review of touch-screen research from 1980 to 1992. *Unclassified IBM Technical Report*, 54:694, 1993.
- [46] S. Pauchet, C. Letondal, J.-L. Vinot, M. Causse, M. Cousy, V. Becquet, and G. Crouzet. Gazeform: dynamic gaze-adaptive touch surface for eyes-free interaction in airliner cockpits. In *Proceedings of the 2018 Designing Interactive Systems Conference*, pages 1193–1205, 2018. doi: 10.1145/3196709.3196712.
- [47] J. A. Mulder, J. C. van der Vaart, W. H. J. J. van Staveren, Q. P. Chu, and M. Mulder. *Aircraft Responses to Atmospheric Turbulence: Lecture Notes AE4304*. TU Delft, 2016.
- [48] P. M. T. Zaal, D. M. Pool, Q. P. Chu, M. M. Van Paassen, M. Mulder, and J. A. Mulder. Modeling human multimodal perception and control using genetic maximum likelihood estimation. *Journal of Guidance, Control, and Dynamics*, 32(4):1089–1099, 2009. doi: 10.2514/1.42843.
- [49] F. M. Nieuwenhuizen. *Changes in pilot control behaviour across Stewart platform motion systems*. PhD thesis, Delft University of Technology, The Netherlands, 2012.
- [50] P. A. Davidson. *Turbulence: an introduction for scientists and engineers*. Oxford University Press, 2004. doi: 10.1093/acprof:oso/9780198722588.001.0001.
- [51] J. M. Wallace and P. V. Hobbs. *Atmospheric science: an introductory survey*, volume 92. Elsevier, 2006. URL <https://books.google.nl/books?id=HZ2wNtDOU0oC>.
- [52] H. A. Panovsky and J. A. Dutton. *Atmospheric turbulence: Models and methods for engineering applications*. Wiley, 1984.
- [53] S. B. Pope. *Turbulent Flows*. Cambridge University Press, 2000. doi: 10.1017/cbo9780511840531.
- [54] H. L. Dryden. A review of the statistical theory of turbulence. *Quarterly of Applied Mathematics*, 1(1):7–42, 1943. doi: 10.1090/qam/8209.
- [55] T. Von Karman. Progress in the statistical theory of turbulence. *Proceedings of the National Academy of Sciences of the United States of America*, 34(11):530, 1948. doi: 10.1073/pnas.34.11.530.
- [56] G. A. J. Van de Moesdijk. The description of patchy atmospheric turbulence, based on a non-gaussian simulation technique. *Delft University of Technology, Department of Aeronautical Engineering, Report VTH-192*, 1975. URL <http://resolver.tudelft.nl/uuid:d9060267-cef5-4955-982a-1a7b5da25d90>.
- [57] S. Haykin and M. Moher. *Introduction to analog and digital communications*. Wiley, 2007.
- [58] M. Lam. A comparative study between display augmentation and control augmentation for tunnel-in-the-sky displays. Master’s thesis, Unpublished. Delft University of Technology, 2003.
- [59] O. Stroosma, M. M. Van Paassen, and M. Mulder. Using the simona research simulator for human-machine interaction research. In *AIAA modeling and simulation technologies conference and exhibit*, page 5525, 2003. doi: 10.2514/6.2003-5525.
- [60] P. M. T. Zaal, D. M. Pool, M. Mulder, and M. M. Van Paassen. Multimodal pilot control behavior in combined target-following disturbance-rejection tasks. *Journal of guidance, control, and dynamics*, 32(5):1418–1428, 2009. doi: 10.2514/6.2009-6027.
- [61] C. A. A. M. Van Der Linden. Dasmatt-delft university aircraft simulation model and analysis tool: A matlab/simulink environment for flight dynamics and control analysis. *Series 03: Control and Simulation 03*, 1998.
- [62] T. Von Karman and L. Howarth. On the statistical theory of isotropic turbulence. *Proceedings of the Royal Society of London. Series A-Mathematical and Physical Sciences*, 164(917):192–215, 1938. doi: 10.1098/rspa.1938.0013.

- [63] O. H. Gerlach. Calculation of the response of an aircraft to random atmospheric turbulence: Part i. symmetric motions. Technical report, Delft University of Technology, 1966. URL <http://resolver.tudelft.nl/uuid:a0d7df8d-f375-46f1-9af5-6021257506f8>.
- [64] O. H. Gerlach and M. Baarspul. Calculation of the response of an aircraft to random atmospheric turbulence: Part ii. asymmetric motions. Technical report, Delft University of Technology, 1968. URL <http://resolver.tudelft.nl/uuid:f9ae7a61-dcb8-4b7a-9e42-000be6b478b9>.
- [65] G. A. J. Van de Moesdijk. Non-gaussian structure of the simulated turbulent environment in piloted flight simulation. *Technische Hogeschool Delft, Vliegtuigbouwkunde, memorandum m-304*, 1978. URL <http://resolver.tudelft.nl/uuid:b5e66aad-6a6e-44e8-af4d-58d51684c515>.
- [66] H. Press. Atmospheric turbulence environment with special reference to continuous turbulence. Technical report, ADVISORY GROUP FOR AERONAUTICAL RESEARCH AND DEVELOPMENT PARIS (FRANCE), 1957.
- [67] O. H. Gerlach and J. Schuring. Mathematical model of external disturbances acting on an aircraft during an ils approach and landing. Technical report, Delft University of Technology, 1970. URL <http://resolver.tudelft.nl/uuid:37288b76-59f2-4a56-a5dd-058891f484ce>.
- [68] J. C. Houbolt, R. Steiner, and K. G. Pratt. *Dynamic response of airplanes to atmospheric turbulence including flight data on input and response*, volume 199. National Aeronautics and Space Administration, 1964.
- [69] M. Mulder, D. M. Pool, D. A. Abbink, E. R. Boer, P. M. T. Zaal, F. M. Drop, K. van der El, and M. M. van Paassen. Manual control cybernetics: State-of-the-art and current trends. *IEEE Transactions on Human-Machine Systems*, 48(5):468–485, 2017. doi: 10.1109/thms.2017.2761342.
- [70] W. L. Golding. Turbulence and its impact on commercial aviation. *Journal of Aviation/Aerospace Education & Research*, 11(2):8, 2002. doi: 10.15394/jaaer.2002.1301.
- [71] EASA. *Easy Access Rules for All Weather Operations (CS-AWO)*. European Aviation Safety Agency (EASA), February 2018.
- [72] Flying qualities of piloted aircraft. *US Department of Defense MIL-STD-1797A*, 1990.
- [73] A. R. Veldhuijzen. Integrating flight path oriented control with the tunnel-in-the-sky display. Master's thesis, Unpublished. Delft University of Technology, 2002.
- [74] O. Stroosma. *The SIMONA Research Simulator's Motion Software*, 2019.
- [75] C. C. Morris, C. Sultan, J. A. Schetz, and R. K. Kapania. State variance-based approach to flight dynamic constraints in multidisciplinary design optimization. *Journal of Guidance, Control, and Dynamics*, 40(5):1206–1220, 2017. doi: 10.2514/1.G002278.
- [76] W. Widowati and H. Muhammad. Linear parameter-varying versus linear time-invariant reduced-order controller design for turboprop aircraft dynamics. *ITB Journal of Engineering Science*, 44(2):169-186, 2012. doi: 10.5614/itbj.eng.sci.2012.44.2.5.
- [77] B. Gouverneur, J. A. Mulder, M. M. R. van Paassen, O. Stroosma, and E. Field. Optimisation of the SIMONA research simulator's motion filter settings for handling qualities experiments. In *AIAA Modeling and Simulation Technologies Conference and Exhibit*. American Institute of Aeronautics and Astronautics, jun 2003. doi: 10.2514/6.2003-5679.
- [78] A. Khoshnewisazadeh and D. M. Pool. Mitigation of biodynamic feedthrough for touchscreens on the flight deck. *International Journal of Human-Computer Interaction*, pages 1–13, 2021. doi: 10.1080/10447318.2021.1890490.